Compact and broadband antenna system at UHF

by

Nerijus Riauka

A Doctoral Thesis submitted in partial fulfilment of the requirements for the award of

Doctor of Philosophy of Loughborough University

June 2010

Mano brangiems Tėvams

(Dedicated to my dear Parents)

ABSTRACT

The aim of this research was to study a novel, broadband, low cost, low profile and a high-medium gain antenna in the UHF band. This has been achieved through numerical modelling, theoretical investigation and physical measurements. In this study two commercially available antenna systems are investigated in order to compare and establish potential deficiencies in the UHF antenna systems. A number of disadvantages are resolved within a novel antenna system design. The parametric study is performed for each element of the novel antenna system in order to optimise its overall performance.

The indoor and outdoor measurements have been carried out in house, in order to validate the predicted results. The novel antenna system is compared to the most popular and commercially available UHF antenna systems. The study demonstrates that the novel antenna system has clear advantages such as broadband, balanced, compact and low cost when compared to the commercial antenna designs studied here. The comparison of the manufacturers' data to the measured results shows a good match, validating the outdoor measurements technique used in this research.

Keywords: Broadband, Low Cost, Low profile, UHF, printed dipole antenna (PDA), DTV, DVB-T, tapered balun, broadband balun.

ACKNOWLEDGEMENTS

I would like to thank, first and foremost, my supervisor, Prof. Yiannis Vardaxoglou, for his generosity, support and critical guidance through my research and during the completion of this thesis.

I would also like to thank the Electrical and Electronic Engineering Department for funding this research project. I am grateful to Antrum Ltd for hardware support and ancillary components.

I would like to acknowledge other members of WiCR and CMRC research groups and the staff members of the Department of Electronic and Electrical Engineering for their assistance, continued interest and encouragements.

I offer my sincere appreciation to my parents and my brother. Last but not least I would like to thank my wife, Jelena, who constantly offered love, companionship and support during the research and the writing up stage.

PUBLICATIONS FROM THE RESEARCH:

Conference papers:

N. Riauka, A. Chauraya, and J. C. Vardaxoglou, “Compact antenna integrated into flat plate FSS”, IEEE APS 2008, 5-11 July 2008, San Diego, CA, AP-S/URSI 2008.

N. Riauka, A. Chauraya, and J. C. Vardaxoglou, “Wideband Planar Metamaterial Inspired Antenna Analysis and Design”. IEEE International Symposium on Antennas and Propagation - June 2009, North Charleston, South Carolina, USA.

Yiannis (J) Vardaxoglou, R. D. Seager, N. Riauka, A. Chauraya, and P deMaagt, “Metamaterial Based Antennas with Super- and Sub-strates” 3rd European Conference on Antennas and Propagation (EUCAP) - March 2009 in Berlin, Germany.

J.(Yiannis) C. Vardaxoglou, A.Chauraya, R.D.Seager, N.Riauka, G.K.Palikaras and P. deMaagt, “Towards Metasurfaces for Wideband Systems” 39th European Microwave Conference (EuMC)- August 2009, Rome, Italy.

Journal papers:

N. Riauka, A. Chauraya and J. C. Vardaxoglou “Novel, broadband and low cost Printed dipole antenna for UHF band”, IEEE Transactions Antennas and Propagation, 2010.*****

N. Riauka, A. Chauraya, and J. C. Vardaxoglou “High gain, broadband and low cost antenna system for DVB-T“, IEEE Microwave and Wireless Components Letters (MWCL), 2010.*

PATENTS:

Metamaterial based TV Antenna Patent, Antrum Limited, UK File No. 0823272.0GB, patent pending, 2010.

***Journal papers have been prepared and will be submitted once the patent is published.**

CONTENTS

1. Introduction **1**

1.1 Introduction to UHF Antennas **1**
1.2 Deficiencies in Existing UHF Antennas **2**
1.3 Research objectives **3**
1.4 Thesis Overview **4**
1.5 References **7**

2. Vertically stacked dipole antenna (VSDA) system **11**

2.1 Introduction **11**
2.2 CST's MicroStripes 7.5 ..... **13**
2.3 AWR Microwave office 2009 ..... **14**
2.4 Vertically stacked dipole antenna **15**
2.4.1 Structure of the VSDA antenna system balun **16**
2.4.2 Broadband balun equivalent circuit **20**
2.4.3 VSDA antenna system radiating element **23**
2.4.4 VSDA antenna system with ground plane **27**
2.5 Conclusions **32**
2.6 References **34**

3. Yagi-Uda antenna (YUA) system **36**

3.1 Introduction **36**
3.2 Yagi-Uda antenna (YUA) system **38**
3.2.1 YUA system balun **32**
3.2.2 YUA system driven element **44**
3.3 Yagi Antenna Parametric Study **45**
3.3.1 Adjusting the parasitic element length due to the YUA performance **46**
3.3.2 Changing the air gap distance between the balun and the radiating element with parasitic element **48**

3.3.3 Changing the air gap distance between the balun and the radiating element without parasitic element **53**
3.3.4 Changing V-shape dipoles arms angle **58**
3.3.5 Changing V-shape dipoles base length **64**
3.4 Conclusions **70**
3.5 References **72**

4. Printed Dipole Antenna (PDA) **75**

4.1 Introduction **75**
4.2 Printed dipole antenna structure **77**
4.3 Printed dipole antenna simulations **80**
4.3.1 Printed dipole antenna design **81**
4.3.2 Printed dipole antenna with extended feeding line **88**
4.3.3 Printed dipole antenna with stretched balun **89**
4.3.4 Printed dipole antenna with parasitic element (PDAwP) **95**
4.3.5 Optimised printed dipole antenna with parasitic element (OPDAwP) **101**
4.4 Manufactured PDA prototypes **110**
4.4.1 Manufactured PDAwP **111**
4.4.2 Manufactured OPDAwP **112**
4.5 Conclusions **115**
4.6 References **118**

5. PDA with reflector system **121**

5.1 Introduction **121**
5.2 Ground plane analysis **123**
5.2.1 Perfect electric conductor (PEC) **124**
5.2.2 Periodic structure analysis **125**
5.2.3 Elliptical ground plane **133**
5.3 Results for PDA with ground plane **136**
5.3.1 Results for PDAwP placed over ground plane **137**
5.3.2 Results for OPDAwP placed over ground plane **144**
5.3.3 Directivity results for various PDA configurations **150**

5.4 Outdoor measurements....152
5.4.1 Dipole Calibration....153
5.4.2 Measurements setup....157
5.4.3 Measurements....163
5.4.3.1 Return loss measurements....164
5.4.3.2 Radiation patterns measurements....164
5.4.3.3 Gain measurements....167
5.4.4 Comparative measurements....170
5.5 Conclusions....174
5.6 References....176

6. Conclusions and Future Work....179

6.1 Review of the research study....179
6.2 Future Work....185
6.3 References....186

Appendices

Appendix A Transforming 50Ω to 75 Ω....188
Appendix B Microstrip transition to parallel strip....191
Appendix C EM field distribution in microstrip and parallel strip transmission lines....193
Appendix D Manufactured dipoles....194
Appendix E The path phase difference (φ)....195
Appendix F The Gain calculation data....196
References....198

NOMENCLATURE

LIST OF FIGURES

Chapter 2

Figure 2.1 Picture of the VSDA system: A- ground plane, B- V shape dipole, C-balun box.....**15**
Figure 2.2 The structure of the VSDA balun **16**
Figure 2.3 VSDA system balun dimensions.....**17**
Figure 2.4 Return loss and input impedance results of the VSDA system balun with 75Ω **17**
Figure 2.5 VSDA system balun surface currents at different frequencies and phases **19**
Figure 2.6 VSDA system balun surface currents directions at 650MHz **20**
Figure 2.7 VSDA system balun equivalent circuit **20**
Figure 2.8 Structure of the VSDA system balun and the return loss results.....**21**
Figure 2.9 VSDA system balun phase results.....**22**
Figure 2.10 VSDA system dimensions without ground plane **23**
Figure 2.11 VSDA system simulations and measurements results over frequency.....**24**
Figure 2.12 Simulated 3D Co-polar radiation patterns of the VSDA system.....**26**
Figure 2.13 VSDA system dimensions with ground plane **27**
Figure 2.14 VSDA system with ground plane simulations and measurements comparison of return loss over frequency.....**28**
Figure 2.15 Simulated 3D Co-polar radiation patterns of the VSDA system with GP **29**
Figure 2.16 Comparison of VSDA system simulations and measurement results with and without ground plane.....**30**

Chapter 3

Figure 3.1 Yagi – Uda antenna configuration **38**
Figure 3.2 52 elements Yagi - Uda antenna system **39**
Figure 3.3 The structure of the YUA system balun **40**
Figure 3.4 The YUA system balun dimensions **41**
Figure 3.5 Return loss and input impedance results of the YUA system balun with 75Ω load ..**42**
Figure 3.6 The YUA system balun surface currents distribution **43**

Figure 3.7 The YUA system balun surface currents direction at 650MHz **44**

Figure 3.8 Diagram of the YUA system radiating element: a) Top view, b) Side view.....**44**

Figure 3.9 Structure of the YUA system with parasitic element **46**

Figure 3.10 YUA system return loss behaviour changing parasitic element length over the frequency **47**

Figure 3.11 Increasing the air gap separation between the YUA system balun and radiating element **48**

Figure 3.12 The capacitance of the flat, parallel metallic plates **49**

Figure 3.13 The YUA system with parasitic element simulation results **51**

Figure 3.14 The YUA system with parasitic element measurement results **52**

Figure 3.15 Increasing the air gap separation between the YUA system balun and radiating element **53**

Figure 3.16 The YUA system without parasitic element simulation results **55**

Figure 3.17 The YUA system without parasitic element measurement results **56**

Figure 3.18 YUA system without parasitic element simulation and measurement comparison, when the air gap distance is 1.0mm **57**

Figure 3.19 Changing the YUA system dipole arms angle ϕ **58**

Figure 3.20 The YUA system simulated return loss results changing dipoles arms angle ϕ from $0°$ to $45°$ each $5°$ **59**

Figure 3.21 Radiation patterns changing dipoles arms angle $\phi = 0° - 20°$ **60**

Figure 3.22 Radiation patterns changing dipole arms angle $\phi = 30° - 45°$ **61**

Figure 3.23 The directivity results over the YUA system dipoles arms angle ϕ **63**

Figure 3.24 Changing the YUA system dipole base length from *x-2cm* to *x+14cm* **64**

Figure 3.25 Return Loss over frequency changing YUA base length from x-2cm to x+14cm ...**65**

Figure 3.26 The YUA system radiation patterns changing base length from x to x+6cm **66**

Figure 3.27 The YUA system radiation patterns changing base length x+8cm to x+14cm **67**

Figure 3.28 Directivity values of the YUA system changing base length **69**

Chapter 4

Figure 4.1 General PDA structure **77**

Figure 4.2 Configuration of the back to back transition from microstrip to parallel strip line **78**

Figure 4.3 Structure of the PDA : A) top view; B) bottom view **81**

Figure 4.4 Simulated results of the PDA **82**
Figure 4.5 Surface currents distribution of the PDA **84**
Figure 4.6 PDA balun surface currents directions at 650MHz ϕ=20° **85**
Figure 4.7 PDA E,H-plane co-polar and x-polar radiation patterns **87**
Figure 4.8 Structure of the PDA with extended feeding line **88**
Figure 4.9 Return loss results of the PDA with extended feeding line **89**
Figure 4.10 Structure of the PDA with stretched balun **90**
Figure 4.11 Simulated results of the PDA with stretched balun **91**
Figure 4.12 Printed dipole antenna surface currents at different frequencies **92**
Figure 4.13 Printed Dipole antenna E,H-plane co-polar and x-polar radiation patterns **93**
Figure 4.14 Top view of the PDAwP **95**
Figure 4.15 Bottom view of the PDAwP **95**
Figure 4.16 Simulated PDA with parasitic element results **97**
Figure 4.17 PDA simulation results at different frequencies **98**
Figure 4.18 Simulated radiation pattern results of the PDAwP **99**
Figure 4.19 Structure of the OPDAwP **101**
Figure 4.20 Simulated OPDAWP results **102**
Figure 4.21 Dimensions of the OPDAwP **103**
Figure 4.22 Simulated OPDAwP surface currents at 470MHz and 550MHz **104**
Figure 4.23 Simulated OPDAwP surface currents at 650MHz 750MHz and 850MHz **105**
Figure 4.24 Simulated surface current directions of OPDAwP at 650MHz **106**
Figure 4.25 Simulated OPDAwP radiation patterns **108**
Figure 4.26 The directivity values comparison **109**
Figure 4.27 OPDAwP efficient coefficient and gain simulation results **110**
Figure 4.28 Manufactured PDAwP model compared to one pound coin **111**
Figure 4.29 The simulation and measurement results of the PDAwP **112**
Figure 4.30 Manufactured OPDAwP model compared to one pound coin **112**
Figure 4.31 The simulation and measurement results of the OPDAwP **113**
Figure 4.32 PDAs covered with antioxidant rubber coating **114**

Chapter 5

Figure 5.1 Radiating antenna placed very close to a perfect electric conductor **123**
Figure 5.2 An antenna placed at $\lambda/4$ distance from ground plane **124**
Figure 5.3 Phase change of the antenna placed at $\lambda/4$ distance from ground plane **124**
Figure 5.4 Picture of the galvanised mesh roll **125**
Figure 5.5 Single cell analysis **126**
Figure 5.6 4x4 cells analysis **126**
Figure 5.7 a) Simulated reflection phase results; b) single cells structure **126**
Figure 5.8 The dimensions of the ground planes **127**
Figure 5.9 Simulated return loss of the dipoles placed over different size ground plane **128**
Figure 5.10 E,H-planes co-polar radiation patterns of the dipole placed over various GP **130**
Figure 5.11 Simulated F/B results of the dipole placed over various size GP **131**
Figure 5.12 Simulated directivity values for the dipole placed over various GP **132**
Figure 5.13 Surface current distribution at various phases **134**
Figure 5.14 Structure of various PDA **136**
Figure 5.15 Predicted results of the PDAwP placed above the ground plane **137**
Figure 5.16 Radiation patterns of the PDAwP placed over the ground plane **139**
Figure 5.17 Predicted results of the PDAwP placed parallel to the ground plane **140**
Figure 5.18 Radiation patterns of the OPDAwP placed parallel to the ground plane **141**
Figure 5.19 Comparison of the simulations and measurements **143**
Figure 5.20 Predicted results of the OPDAwP placed above the ground plane **144**
Figure 5.21 Radiation patterns of the OPDAwP placed over the ground plane **145**
Figure 5.22 Predicted results of the OPDAwP placed parallel to the ground plane **146**
Figure 5.23 Radiation patterns of the OPDAwP placed parallel to the ground plane **147**
Figure 5.24 Comparison of the simulations and measurements **149**
Figure 5.25 Predicted directivity results of the various PDA **150**
Figure 5.26 Diagram of the balun **153**
Figure 5.27 Manufactured dipole at 470MHz frequency **154**
Figure 5.28 Simulated and measured dipole radiation patterns **155**
Figure 5.29 Measured return loss of the five dipole set of pairs **156**
Figure 5.30 Measurement set up on the roof of a three storey building **157**
Figure 5.31 The outdoor measurements setup **158**
Figure 5.32 Adapter which holds and connects the dipole and the cable **159**

Figure 5.33 Attenuation results in the outdoors measurements **159**
Figure 5.34 Connectors and cables used in outdoors measurements **160**
Figure 5.35 The PDAwP placed above the ground plane front, side and corner views **163**
Figure 5.36 Indoor measured results of the various PDA systems **164**
Figure 5.37 Measured radiation patterns for the PDAwP placed above the ground plane at 470MHz, 550MHz, 650MHz and 750MHz **165**
Figure 5.38 Measured radiation pattern for the PDAwP placed above the ground plane at 850MHz **166**
Figure 5.39 PDAwP$\perp$GP$\angle$20° **167**
Figure 5.40 PDAwP$\perp$GP$\angle$45° **167**
Figure 5.41 Gain results of the PDA system **169**
Figure 5.42 Measured results of the various antenna **171**
Figure 5.43 Measured return loss of the various UHF antennas **172**

LIST OF TABLES

Chapter 2

Table 2.1 HPBW values of the VSDA system without ground plane **25**
Table 2.2 HPBW values of the VSDA system with ground plane **30**

Chapter 3

Table 3.1 The HPBW values changing the dipole arms angle ϕ **62**
Table 3.2 The HPBW values changing the dipole base length x **68**

Chapter 4

Table 4.1 The dimensions of the PDA with stretched balun **90**
Table 4.2 The dimensions of the PDAwP **96**

Chapter 5

Table 5.1 The HPBW values for various ground plane **129**

Table 5.2 HPBW values of the various PDAwP configurations **142**
Table 5.3 The bandwidth values of the various PDAwP configurations **142**
Table 5.4 HPBW values of the various OPDAwP configurations **148**
Table 5.5 The bandwidth values of the various OPDAwP configurations **148**
Table 5.6 Predicted directivity results of the various PDA **150**
Table 5.7 Attenuation results in measurements **160**
Table 5.8 The HPBW values of the PDAwP⊥GP **166**
Table 5.9 Predicted and measured results of the different PDA systems variations **168**
Table 5.10 Data of the bought UHF antennas and PDAwP placed above the GP **170**
Table 5.11 The bandwidth results for varies UHF antenna systems **173**

ABBREVIATIONS

Abbreviation	Expansion
2D	Two Dimensional
3D	Three Dimensional
AMC	Artificial Magnetic Conductor
ANT	Antenna
AUT	Antenna Under Test
BW	Bandwidth
CST	Computer Simulation Technology
CW	Continuous Wave
DE	Driven Element
DR	Dynamic Range
DTV	Digital TV
DVB-T	Digital Video Broadcasting Terrestrial
DVB-S	Digital Video Broadcasting Satellite
EM	Electromagnetic
F/B	Front to Back ratio
FF	Far Field
FSPL	Free Space Path Loss
FSS	Frequency Selective Surface

GP	Ground Plane
HIS	High Impedance Surface
HPBW	Half Power Beam Width
LPDA	Log Periodic Dipole Array
MoM	Method of Moments
OPDAwP	Optimised Printed Dipole Antenna with Parasitic
PCB	Printed Circuit Board
PDA	Printed Dipole Antenna
PDAwP	Printed Dipole Antenna with Parasitic
PEC	Perfect Electric Conductor
Rx	Receiver
TLM	Transmission Line Matrix
Tx	Transmitter
UHF	Ultra High Frequency
VNA	Vector Network Analyser
VSDA	Vertically Stacked Dipole Array
Wi-Fi	Wireless Fidelity
WiMAX	Worldwide Interoperability for Microwave Access
YUA	Yagi Uda antenna

SYMBOLS

Symbol	Denotes
λ_0	Wavelength [m]
BW	Bandwidth [percents]
c	Speed of light in vacuum $[m \cdot s^{-1}]$
C	Capacitance [F]
C_{eff}	Effective Capacitance [F]
d	Distance [m]
D_a	Largest dimension of an aperture [m]
dB	Decibels
ε_r	Relative Permittivity
ε_0	Free space Permittivity $\approx 8.854 \cdot 10^{-12}$ $[F \cdot m^{-1}]$
e_r	Mismatch efficiency
e_{Ant}	Antenna efficiency
e_{Rad}	Radiation efficiency
φ	Phase [deg]
f	Frequency [Hz]
ϕ	Angle [deg]

G_{Tx}	Gain of a transmitter antenna [dBi]
G_{Rx}	Gain of a receiver antenna [dBi]
Γ	Reflection coefficient
H_n	Height [m] (n=1, 2, 3, 4)
L_n	Length [m] (n=1, 2, 3, 4)
L	Inductance [H]
μ_r	Relative Permeability
μ_0	Free space Permeability $= 4\pi \cdot 10^{-7}\ [H \cdot m^{-1}]$
π	Mathematical constant ≈ 3.141593
P_{Tx}	Transmitted power [dBm]
P_{Rx}	Received power [dBm]
R	Resistance [Ω]
S_{11}	Return loss [dB]
θ	Incident angle of the ground [deg]
ω	Angular frequency $= 2\pi \cdot f\ [rad \cdot s^{-1}]$
W_n	Width [m] (n=1, 2, 3, 4, 5, 6)
w'	Effective width [m]
x	Dipole arm Length [m]
X	Reactance [Ω]
Z	Impedance [Ω]

Chapter 1

Introduction

1.1 Introduction to UHF Antennas

The ultra high frequency (UHF) designates a range of electromagnetic waves with frequencies between 300MHz and 3000MHz. A major disadvantage of the UHF is its limited broadcast range and the reception, often referred to as line-of-sight between the transmission antenna and the reception antenna. A number of public safety and business communications are handled on the UHF [1, 2]. The simplest antennas for the UHF band are as follows: the $\lambda_0/2$ dipole, the bowtie dipole, the folded dipole, and the loop. However, these types of antennas are low gain and they serve as a driven element (DE) in the antenna systems [1-3]. In order to increase the directionality and the gain values, dipoles are commonly stacked horizontally (collinearly) [4, 5], vertically

(broadside) [6-11] and in echelon (end-fire) [12-20]. To increase the gain even more (i.e. up to 3dB), the ground planes of various size and type are used: flat metal sheet reflectors, corner reflectors, screen reflectors, parabolic reflectors. The most popular high gain antenna systems in the UHF band are the Yagi-Uda antenna (YUA), the vertically stacked dipole antenna (VSDA) and the Log periodic dipole arrays (LPDA). These antenna systems achieve the high gain, broad bandwidth and narrow beamwidth mainly due to the number of elements, their structure and alignment. However, these antenna systems have also disadvantages.

1.2 Deficiencies in Existing UHF Antennas

The main deficiencies of the YUA, the LPDA and the VSDA systems are:

- their complex structure,
- limited bandwidth (not covering the whole band of 470MHz-850MHz with 10dB return loss),
- large dimensions,
- heavy structures,
- not perfectly balanced through whole band
- expensive manufacturing,
- installation complexity,
- balun is a separate element of the antenna system,

- the radiation patterns are not consistent over the whole frequency range,
- might require a fair amount of the regular maintenance.

1.3 Research objectives

The aim of this research was to come up with a viable alternative to the Yagi that overcome some (preferably all) of the above mentioned disadvantages. Through my literature search I found that printed balun can be integrated into the printed dipole antenna (PDA) structure, making it a single structure, which is low profile, low weight and also serves as a support to the antenna. Furthermore, the antenna bandwidth can be improved by introducing parasitic elements in close proximity. The antenna system low profile and low wind loading can be enhanced by using Metamaterials.

A number of popular and commercially available UHF antenna systems have been assessed by transferring the antenna geometries into an electromagnetic wave solver tool.

Another research goal was to compare the simulated results with the measurements and to improve the performance by carrying out a number of parametric studies. To the best of our knowledge there are not many publications done on the high gain, low profile and broadband antennas for the UHF band. Therefore, the main task was to develop a balanced, broadband, low cost and low profile with medium to high gain antenna, which would outperform the conventional (commercially available) antennas.

1.4 Thesis structure

Chapter 1 presents an outline of the work in the thesis, and serves as the main introduction of the research work described in Chapters 2 to 5. The advantages and the disadvantages of the UHF antennas systems are discussed and lead to the creation of the research objectives.

Chapter 2 describes the VSDA system analysis. A number of simulations were performed for various parts of the antenna. The investigation concentrated on the balun components, dimensions and the antenna overall operation. Balun is one of the most important parts of the antenna system. It transforms the unbalanced input to the antenna to the balanced input. To perform the π balancing effect, the surface currents at the symmetrical points of the antenna must be equal and have the opposite directions. An equivalent circuit, using lumped elements, for the balun was developed to examine the π phase shift performance over the UHF band. This section also compares the simulated and the measured return loss results, discusses the predicted radiation patterns, the directivity and the gain values [21].

Chapter 3 describes the analysis of the commercially available Yagi – Uda antenna system: the balun and the radiating element. A parametric study was carried out in order to investigate and improve the performance of the balun loaded with a radiating element. Firstly, the parasitic element effect on the balun return loss is investigated. Secondly, the antenna performance through simulation and

measurements is analysed by changing the radiating element separation distance from the balun. Thirdly, the YUA system dipole analysis and optimization is performed by changing the dipole arms angle and base length. The improvements are analysed through the predicted return loss, the radiation patterns and the directivity results [21-24].

Chapter 4 introduces and describes the methodology for the innovation of the balanced, broadband and low cost radiating element for the UHF antenna system. The theoretical explanation of a general Printed Dipole Antenna (PDA) design is described and analysed. Moreover, the methodology of the parametric study was carried out in order to improve the PDA performance. Various types of different PDA structures are suggested and described. Two best PDA prototypes (the Printed dipole antenna with parasitic and the Optimised printed dipole antenna with parasitic) were manufactured. The comparison between the predicted and the measured results were discussed as well as these antennas were prepared for outdoor usage.

Chapter 5 presents the comparison of the measured and the simulated results of the PDA placed over the various ground planes. A parametric study was carried out in order to optimise the flat plate reflectors for the outdoors UHF communications. The predicted return loss, the directivity and radiation patters results are shown for the Printed Dipole Antenna with Parasitic (PDAwP) and the Optimised Printed Dipole Antenna with Parasitic (OPDAwP) placed over the ground plane. For validation of the predicted results, outdoor measurements were carried out. The antenna under test

(AUT) was PDAwP placed over three different types of the ground plane. For comparison purpose, three types of commercially available Yagi UHF antennas with different number of elements were bought. The gain values of these antennas were measured and compared with available datasheets in order to evaluate the measuring method and the PDA system.

Chapter 6 summarises the research, concludes the work presented in this thesis and also discusses the possible future work. Consideration is also given to improvements that could be implemented to antenna design. The pilot study provides the potential areas and applications for future work.

1.5 References

[1] Y.T. Lo, S.W. Lee ”Antenna handbook”, New York, USA, Van Nostrand Reinhold, 1993.

[2] A.W. Rudge, K.Milne, A.D. Olver, P.Knight “The handbook of antenna design”, volumes1 and 2, Page Bros Ltd, Norfolk,1986.

[3] C. Balanis, “Antenna Theory, Analysis, and Design”, 2nd ed. New York, USA, Wiley, 1997.

[4] Joglekar, P.J. "Curtain Arrays of Horizontal Dipoles", Electromagnetic Compatibility, IEEE Transactions on , vol.EMC-15, no.3, pp.147-148, Aug. 1973.

[5] Litva, J.; Yuan Zhuang; Liang, A. "Modelling study of coaxial collinear antenna array," Electrical and Computer Engineering, 1993. Canadian Conference on, vol., no., pp.920-924 vol.2, 14-17 Sep 1993.

[6] Kawakami, H.; Sato, G. "Metal-bar supported full-wave dipole antennas (four-bay) with a screen-type reflector plate," Antennas and Propagation Society International Symposium, 1988. AP-S. Digest, vol., no., pp.816-819 vol.2, 6-10 Jun, 1988.

[7] Page, H. "The measured performance of horizontal dipole transmitting arrays", Electrical Engineers - Part III: Radio and Communication Engineering, vol.92, no.18, pp.68-79, June 1945.

[8] King, R.; Sandler, S. "The theory of broadside arrays", Antennas and Propagation, IEEE Transactions on, vol.12, no.3, pp. 269- 275, May 1964.

[9] King, H. "Directivity of a broadside array of isotropic radiators," Antennas and Propagation, IRE Transactions on, vol.7, no.2, pp.197-198, April 1959.

[10] Tai, C. "The optimum directivity of uniformly spaced broadside arrays of dipoles," Antennas and Propagation, IEEE Transactions on, vol.12, no.4, pp. 447- 454, Jul 1964.

[11] Harrison, C.W., Jr. "A Theory for Three-Element Broadside Arrays," Proceedings of the IRE, vol.34, no.4, pp. 204p- 209p, April 1946.

[12] Sahaya, J.; Raj, K.; Poongodi, C. "Echelon, Collinear, H-shaped and V-shaped dipole Arrays for MIMO Systems," Microwave Conference, 2007. APMC 2007. Asia-Pacific , vol., no., pp.1-4, 11-14 Dec. 2007.

[13] Yen, J. "Coupled surface waves and broadside arrays of end-fire antennas," Antennas and Propagation, IRE Transactions on, vol.9, no.3, pp.296-304, May 1961.

[14] Brown, J.; Spector, J.O. "The radiating properties of end-fire aerials," Proceedings of the IEE - Part B: Radio and Electronic Engineering, vol.104, no.13, pp.27-34, January 1957.

[15] Guo-wei Yao; Zheng-hui Xue; Wei-ming Li; Zhong-kai Liu "Multi-feed compared with single-feed end-fire antenna," Antennas, Propagation and EM Theory, 2008. ISAPE 2008. 8th International Symposium on, vol., no., pp.240-243, 2-5 Nov. 2008.

[16] Brown, J.; Spector, J.O. "End-fire aerials," Electrical Engineers, Journal of the Institution of, vol.3, no.25, pp.16-17, January 1957.

[17] Kahn, W. "End-fire hybrid array antennas," Antennas and Propagation, IEEE Transactions on, vol.32, no.1, pp. 36- 43, Jan 1984.

[18] Mushiake, Y. "A theoretical analysis of the multi-element end-fire array with particular reference to the Yagi-Uda antenna," Antennas and Propagation, IRE Transactions on, vol.4, no.3, pp.441-444, July 1956.

[19] Papas, C.H.; King, R. "The Radiation Resistance of End-Fire and Collinear Arrays," Proceedings of the IRE, vol.36, no.6, pp. 736- 741, June 1948

[20] Feilong Liao; Chengyou Yin "MPIE-MOM analysis of the horizontal LPDA array over ground plane," Antennas, Propagation and EM Theory, 2008. ISAPE 2008. 8th International Symposium on, vol., no., pp.278-281, 2-5 Nov. 2008.

[21] N. Riauka, A. Chauraya, and J. C. Vardaxoglou, “Compact antenna integrated into flat plate FSS”, IEEE APS 2008, 5-11 July 2008, San Diego, CA, AP-S/URSI 2008, pp1-4.

[22] N. Riauka, A. Chauraya, and J. C. Vardaxoglou, “Wideband Planar Metamaterial Inspired Antenna Analysis and Design”. IEEE International Symposium on Antennas and Propagation - June 2009, North Charleston, South Carolina, USA.

[23] Yiannis (J) Vardaxoglou, R. D. Seager, N. Riauka, A. Chauraya, and P deMaagt, “Metamaterial Based Antennas with Super- and Sub-strates” 3rd European Conference on Antennas and Propagation (EUCAP) - March 2009 in Berlin, Germany.

[24] J.(Yiannis) C. Vardaxoglou, A.Chauraya, R.D.Seager, N.Riauka, G.K.Palikaras and P. deMaagt, “Towards Metasurfaces for Wideband Systems” 39th European Microwave Conference (EuMC)- August 2009, Rome, Italy.

Chapter 2

Vertically stacked dipole antenna (VSDA) system

2.1 Introduction

To the best of the author knowledge only limited published information is available for consolidated and practical high gain, broadband VSDA systems. Therefore, one of the initial research goals was to analyse the commercially available UHF antenna by assessing its performances using electromagnetic wave solver software. Another goal was to compare them to measured results in order to find out the discrepancy of predicted results and most importantly to get familiar with the disadvantages of these types of antenna systems. The Vertically stacked dipole antenna (VSDA) system was chosen to be investigated due to its popularity and overall acceptable performance through the UHF band.

This chapter presents the VSDA system results with a number of simulations for various parts of the antenna: i.e. the balun surface current and the return loss, the balun equivalent circuit, the driven element system and the VSDA placed above the ground plane, see Figure 2.1. The software tools based on a transmission line matrix (TLM) method and a Method of Moments (MoM) were used to obtain the predicted results, which are described in section 2.2 and section 2.3 respectively.

The VSDA system structure and analysis details are discussed in section 2.4. The investigation has concentrated on the balun components, dimensions and the antenna overall operation. An equivalent circuit for the balun was developed to examine the π phase shift performance over the UHF band. This section also compares the simulated and the measured return loss results of the radiating element to the results of the radiating element placed above the ground plane. The predicted radiation patterns reveal the real nature of the VSDA system performance at various frequencies. Conclusions are summarised in section 2.5.

2.2 CST's MicroStripes 7.5

In this research the simulation software played an important part in the design and the evaluation of the UHF antenna structure. The MicroStripes software (a product of the Computer Simulation Technology (CST)) was chosen as suitable tool for this purpose.

The CST's MicroStripes produces the 3D electromagnetic analysis and design of devices and structures required for the UHF range [1]. The solver technology is based on a multi-grid formulation of the time-domain Transmission-Line Matrix (TLM) method. The time is divided into discrete time steps and voltage pulses travel along the lines and scatter at the centre of the node. Electric and magnetic fields are then calculated from the voltages and the currents on the lines at each step. The time domain results are converted to frequency domain using Fourier transformations.

The created 3D model is used to produce the geometric model design and to define the electromagnetic parameters and components. The user assigns materials to the components, input excitations and output to the model and generates the workspace and mesh around the antenna. The mesh is dependent upon the operation frequency and the dielectric material in the model and significantly affects the computation time.

After the model formation the data is saved into the so-called TLM files. This file is then used to determine the electromagnetic response of the model and derives the desired results.

The antenna parameters examined in this research were the return loss, the efficiency, the impedance, E, H-plane co-polar and x-polar far field radiation patterns. In order to obtain them, the time domain output file is taken through a response predictor tool, which extends an incomplete time response trying to predict resonant frequencies, a wave resolver tool calculates the S-parameters. The efficiency and far field pattern are calculated using the Near to Far tool [1,2].

2.3 AWR Microwave office 2009

To develop the equivalent circuit of the balun the AWR Microwave office was used. AWR is a 2Dimensional (2D) electromagnetic simulator, which uses Method of Moments (MoM) technique. This package employs EMSight as its electromagnetic simulator. EMSight is a Windows based EM and linear circuit simulator for analysing the behaviour of circuits and structures at high frequencies. EMSight is capable of analysing arbitrary circuits incorporating interconnecting vias on an unlimited number of dielectric layers with unlimited number of materials, geometries and ports [3, 4].

2.4 Vertically stacked dipole antenna

The VSDA system was bought from a local UHF antenna supplier. All antenna dimensions were measured and accurately transformed into the simulation packaged. The main components of the VSDA system are the radiating element (Figure 2.1 B), the balun (Figure 2.1 C) and the ground plane (Figure 2.1 A).

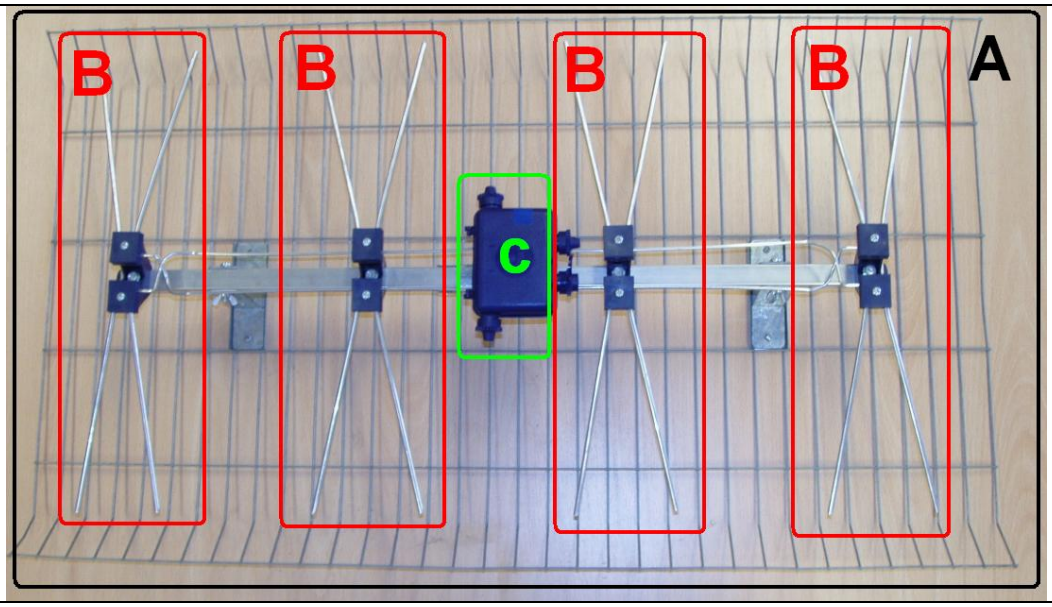

Figure 2.1 Picture of the VSDA system: A- ground plane, B- V shape dipole, C-balun box

In this section the geometry of the VSDA system is presented. The antenna system's basic properties such as the return loss, the input impedance, the radiation patterns and the surface current distribution are considered.

2.4.1 Structure of the VSDA system balun

The balun design was obtained by measuring the dimensions of the VSDA system balun using the digital microscope. The top and bottom views of the analysed balun design are shown in Figure 2.2.

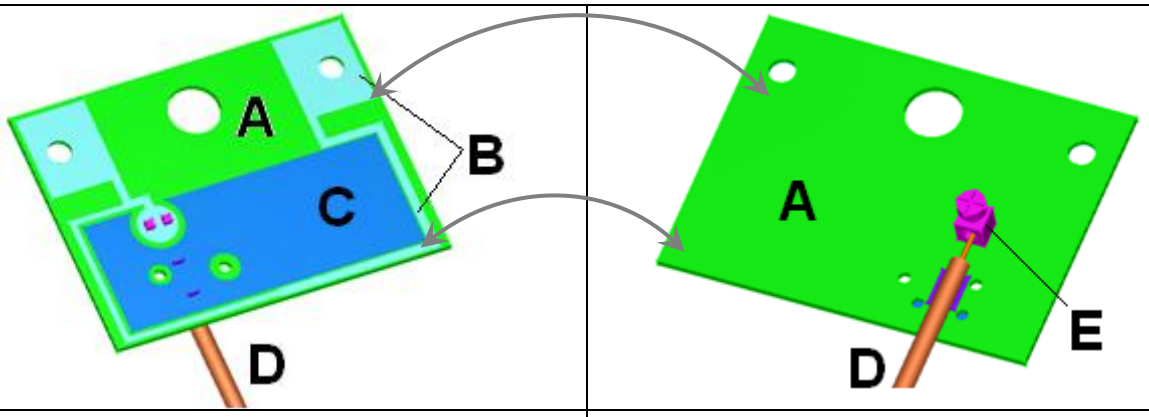

Top view of the balun | Bottom view of the balun

Figure 2.2 The structure of the VSDA balun

The substrate used in simulations was FR4 with a 4.5 permittivity. It is represented by **A** in Figure 2.2. All other surfaces consist of the metal (Cu) with a $5.8 \cdot 10^7$ S/m conductivity and are represented by **B** and **C** in Figure 2.2. The input to the balun is connected to the 75Ω coaxial cable (**D** in Figure 2.2). The connector which holds the coaxial cable inner corresponds to **E** in Figure 2.2.

The balun dimensions are 51mm x 66.5mm x 1.2mm. The diagram for the VSDA system balun dimensions is shown in Figure 2.3.

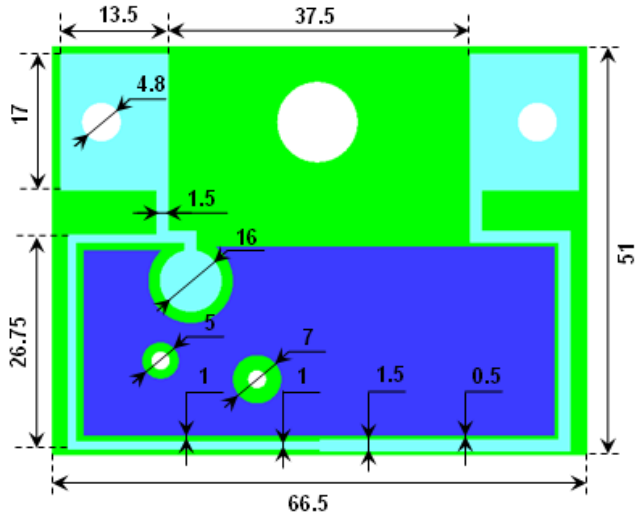

Figure 2.3 VSDA system balun dimensions (all dimensions in mm)

The simulated return loss and the input impedance, obtained by using the AWR Microwave office software [3, 4] are shown in Figure 2.4. The loaded balun achieved the broadband match of the 75Ω over the desired frequency band. Figure 2.4 contains: a) the return loss of the VSDA balun, and b) corresponds to the input impedance values.

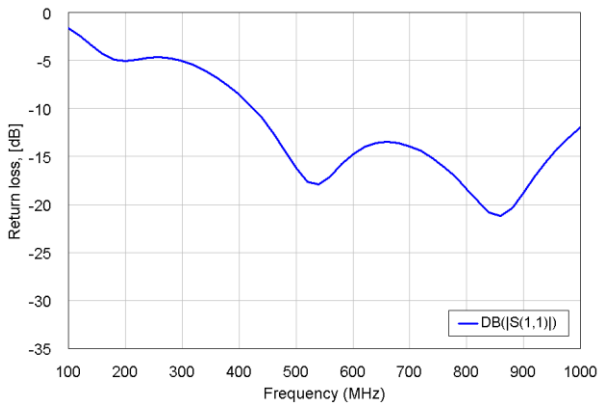

a) Return loss

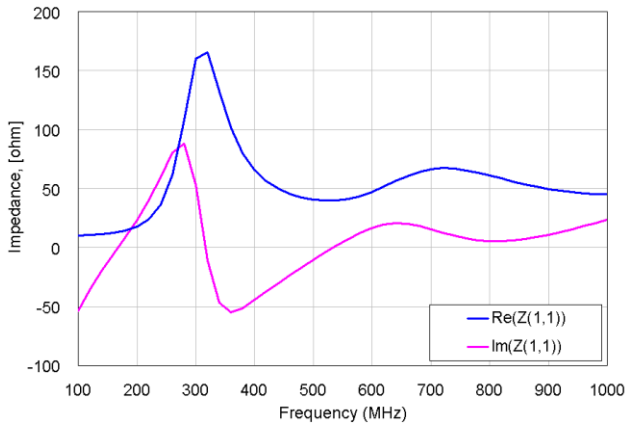

b) Input impedance

Figure 2.4 Return loss and input impedance results of the VSDA system balun with 75Ω load

A balun (balanced to unbalanced) is a transformer connected between a load and an unbalanced source or vice versa. An unbalanced line has just one conductor; the current in it returns via a common ground or earth path. The balanced line has two conductors, with equal currents, but in opposite directions (phase difference between them is 180°) [5, 6].

To analyse the balun, a surface current distribution is investigated at various frequencies and phases. The surface currents distributions of the balun are shown in Figure 2.5 at different frequencies and two phases: when the surface currents are maximum and when they are minimum. In the first picture the red circles highlight the area which indicates that the balun is perfectly balancing the surface currents from the frequency of 470MHz. Since the surface currents are equal at the symmetrical points, the same colour represents identical surface currents values. Figure 2.6 shows that the surface currents are in opposite directions, performing 180° phase difference. It is a broadband (470MHz – 850MHz) operating balun.

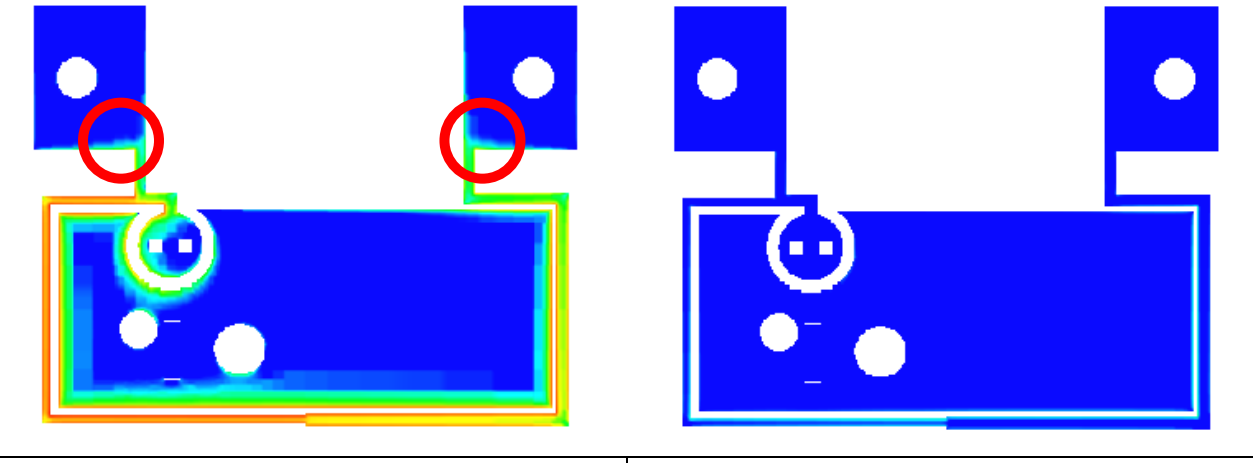

470 MHz ϕ=50° | 470 MHz ϕ=140°

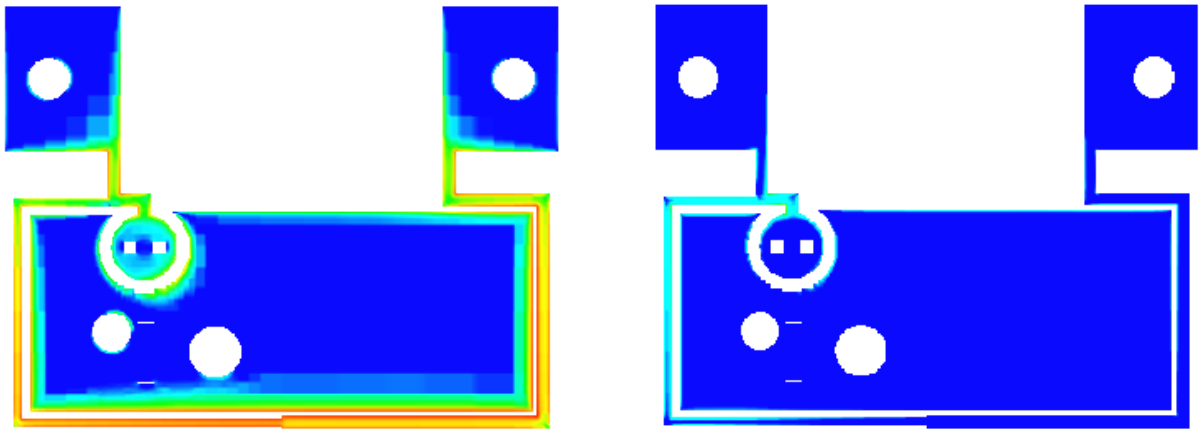

650 MHz ϕ=0° | 650 MHz ϕ=90°

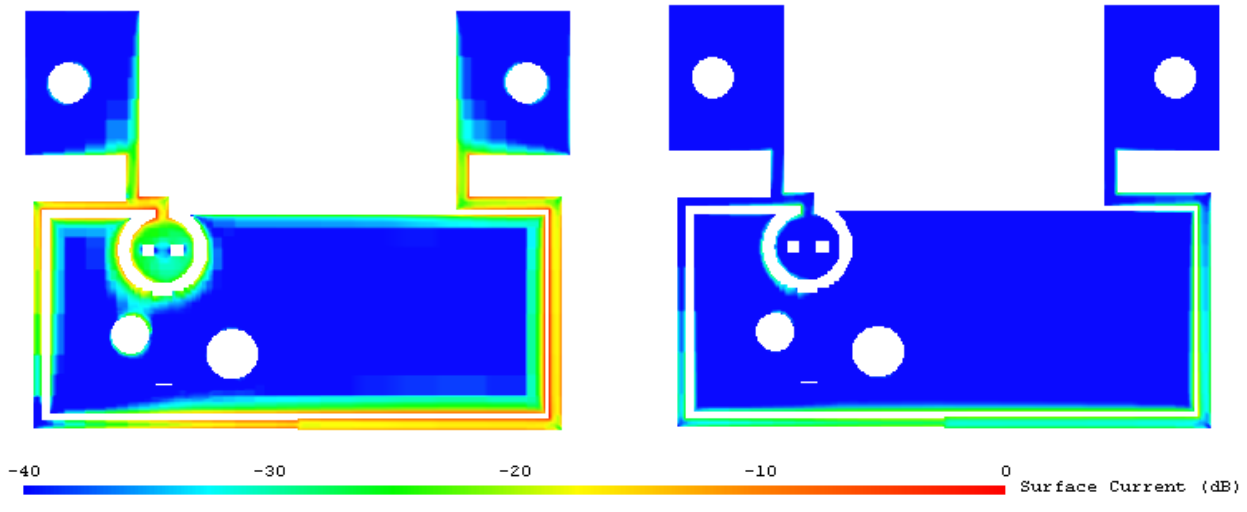

850 MHz ϕ=100° | 850 MHz ϕ=190°

Figure 2.5 VSDA system balun surface currents at different frequencies and phases

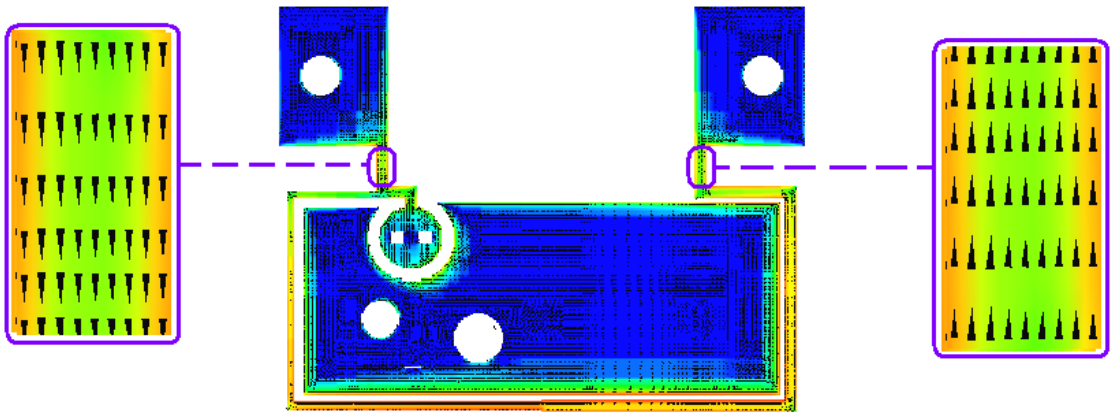

Figure 2.6 VSDA system balun surface currents directions at 650MHz

2.4.2 Broadband balun equivalent circuit

In order to explain the VSDA system balun operation, the equivalent circuit was created by using the AWR Microwave office 2009 [3, 4]. The equivalent circuit with lumped elements (capacitance, inductance and resistance) is shown in Figure 2.7. The input to the balun is unbalanced. However, the 180° phase transformation is achieved between the Port 3 and the Port 2.

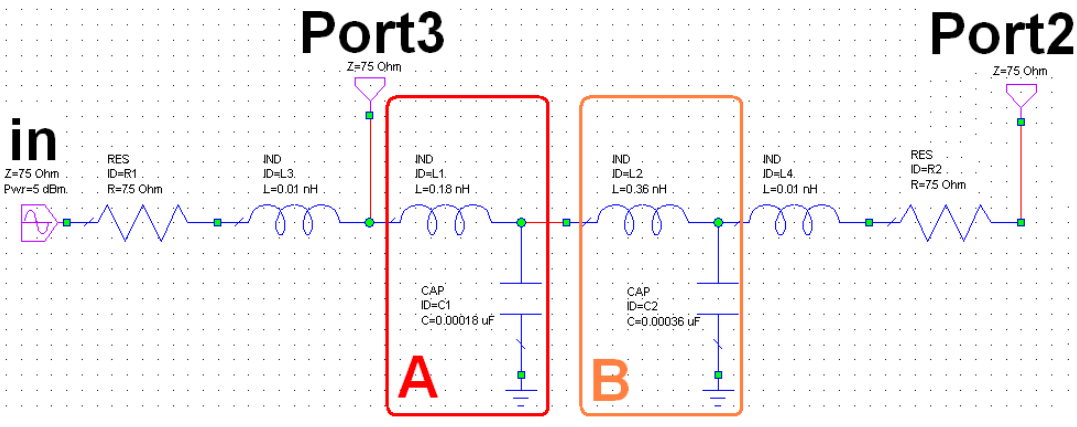

Figure 2.7 VSDA system balun equivalent circuit

The structure of the balun and the return loss results of the equivalent circuit are shown in Figure 2.8.

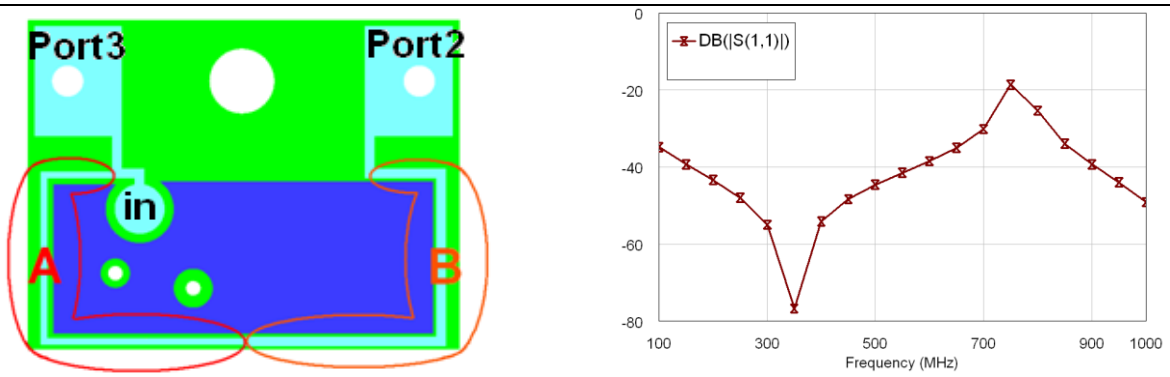

Figure 2.8 Structure of the VSDA system balun and the return loss results

The printed inner line of the PCB balun in the left down corner of Figure 2.8 corresponds to the **A**-side and the **B**-side of the equivalent circuit (Figure 2.7). The **B**-side's capacitance and inductance values are twice bigger than the **A**-side's. This is explained by the fact that in the PCB the gap between the inner and the outer of the B-side is twice smaller than the **A**-side's. Also the **B**-side's inner printed line's width is twice bigger than the **A**-side's.

This balun equivalent circuit contains two resonant parallel LC pairs. The first parallel LC pair resonates at 880 MHz (and is represented as the **A**-side) and the second resonates at 350 MHz (and corresponds to the **B**-side).

$$f_1 = \frac{1}{2\pi\sqrt{LC}} = \frac{1}{2\pi\sqrt{(0.18\cdot10^{-9}H)\cdot(0.18\cdot10^{-9}F)}} = 880\ MHz$$

$$f_2 = \frac{1}{2\pi\sqrt{LC}} = \frac{1}{2\pi\sqrt{(0.35\cdot10^{-9}H)\cdot(0.35\cdot10^{-9}F)}} = 350\ MHz$$

The phase behaviour of the VSDA system balun through the frequency is illustrated in Figure 2.9.

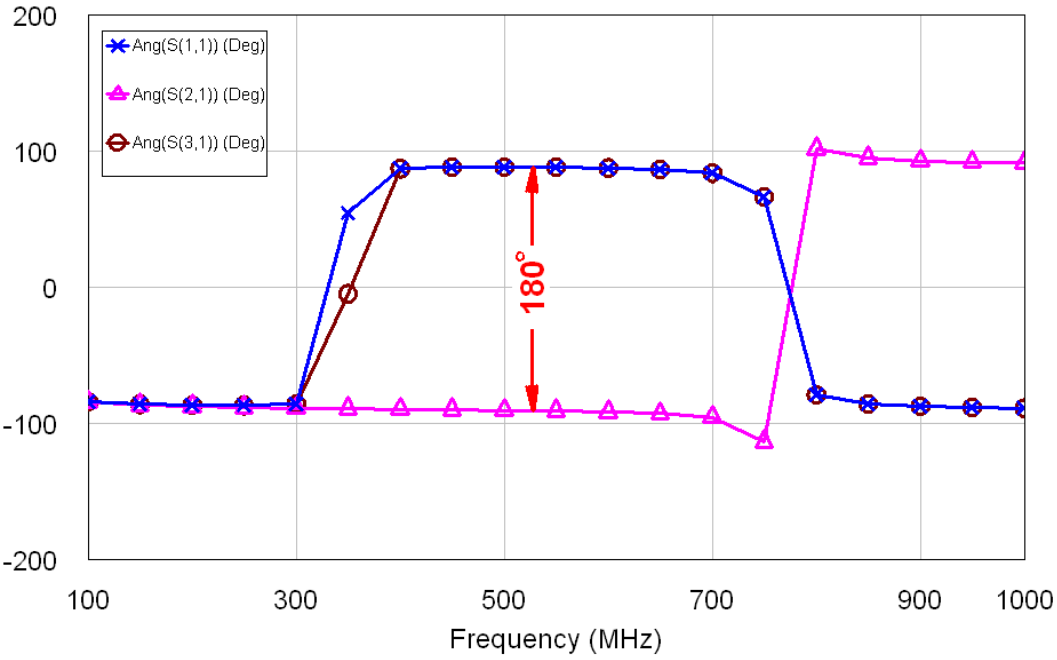

Figure 2.9 VSDA system balun phase results

The broadband phase shift of 180° was achieved between the balun Port 3 and the Port 2 over the desired frequency band. They are represented by the S(1,3) Deg and the S(1,2) Deg respectively in Figure 2.9 The equivalent circuit achieves the balance phenomena between the Port 2 and Port 3 from 420MHz up to the frequency of 920MHz.

2.4.3 VSDA system radiating element

The VSDA system balun is loaded with the radiating element structure (Figure 2.10). It consists of four V-shape dipoles placed symmetrically along the horizontal axis at the same distances of 200mm between the centre points. The radiating element's structure is connected to the twin wire which is fed by the broadband balun.

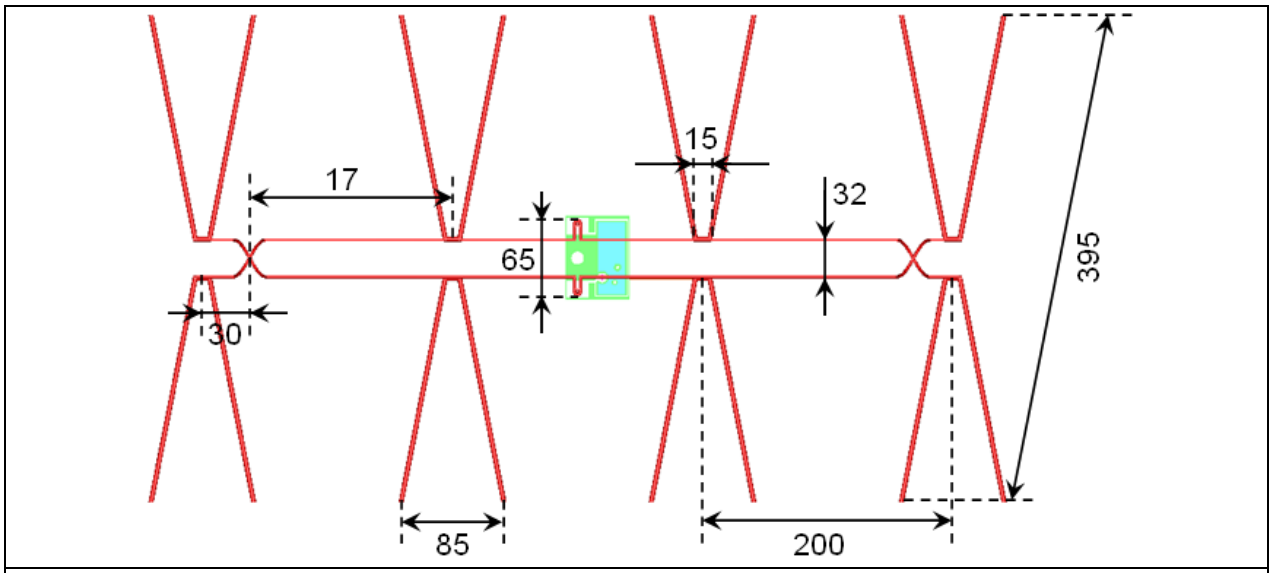

Figure 2.10 VSDA system dimensions without ground plane (All dimensions in mm)

The first and the last pairs of V-shape dipoles are switched over at both ends of the radiating element. The crossover transmission line ensures the correct signal phasing. The resulting antenna produces a highly directional radiation pattern, not in the line of the elements as in a Yagi Uda, but broadside or perpendicular to the plane of the array. Similar to the collinear, the broadside is bi-directional in radiation, but the

radiation pattern has a very narrow beamwidth and the high gain [7, 8]. The whole radiating element structure dimensions are equal to 685mm x 388mm.

The simulated and measured return loss results are shown in Figure 2.11. The measurements took place in the anechoic chamber by using Anritsu 37397D vector network analyzer (VNA) [9]. However, the measurements were made with 50Ω VNA and 50Ω calibration kit. The results illustrated in Figure 2.10 are normalised to 75Ω. For the 50Ω reference transformation to 75Ω the MATLAB [10] code was used. It was derived using the equations shown in Appendix A.

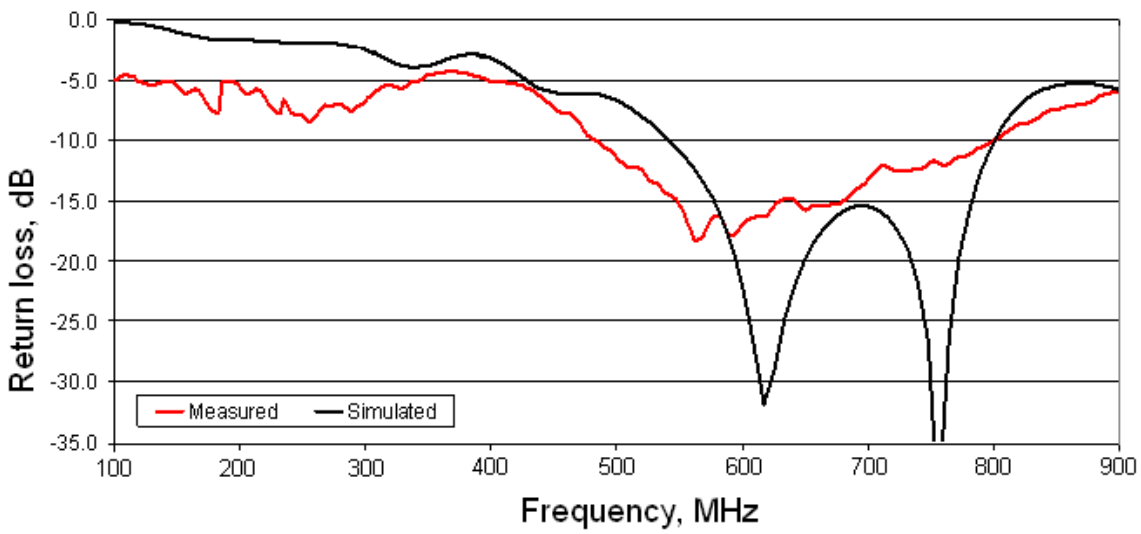

Figure 2.11 VSDA system simulations and measurements results over frequency

The measured results proved to be better than the predicted ones. The simulated Bandwidth is 37% and the measured Bandwidth is 48% at –10 dB in the return loss.

To evaluate the VSDA system performance, the radiation patterns were created, using CST's MicroStripes 7.5 [1, 2]. The predicted 3Dimensional (3D) co-polar radiation

patterns and directivity values (D) are shown in Figure 2.12. They are represented at various frequencies: i.e. 470MHz, 550MHz, 650MHz, 750 and 850MHz. The co-polar E, H-planes radiation patterns of the VSDA system without the ground plane become more directive as the frequency increases. The Half Power Beam Width (HPBW) at five different frequencies is shown in Table 2.1.

HPBW, deg	**470MHZ**		**550MHz**		**650MHz**		**750MHz**		**850MHz**	
	E-plane	**H**-plane	**E**-plane	**H**-plane	**E**-plane	**H**-plane	**E**-plane	**H**-plane	**E**-plane	**H**-plane
VSDA system without GP	58°	61°	41°	46°	38°	44°	34°	38°	28°	30°

Table 2.1 HPBW values of the VSDA system without ground plane

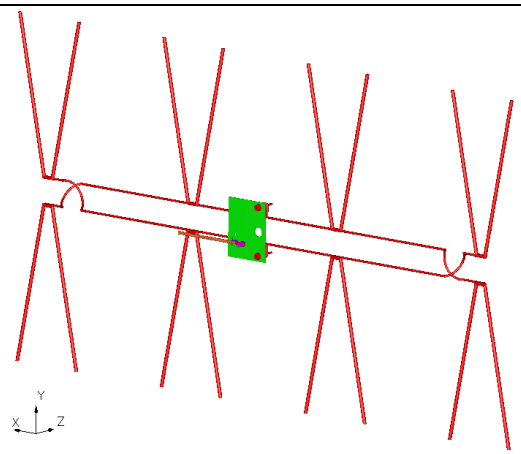

VSDA system without ground plane

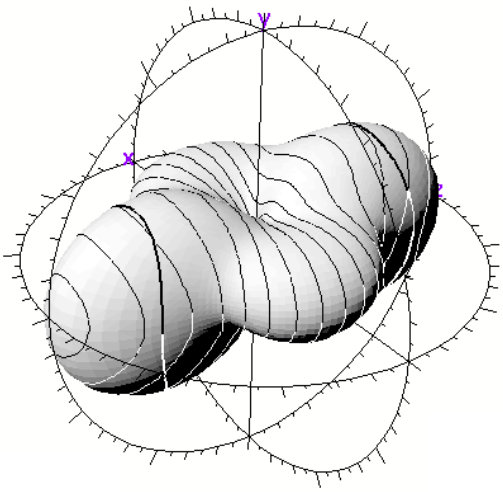

470 MHz D=5.4dBi

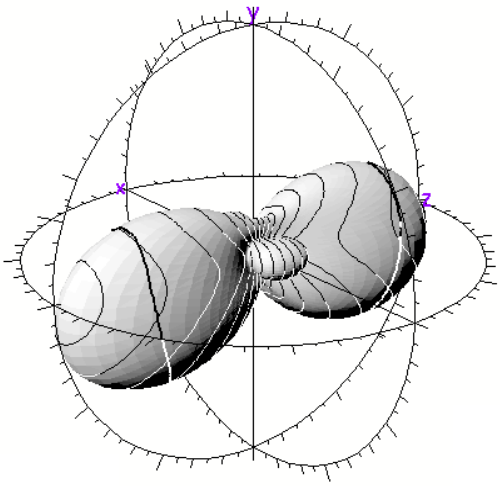

550 MHz D=8.4dBi

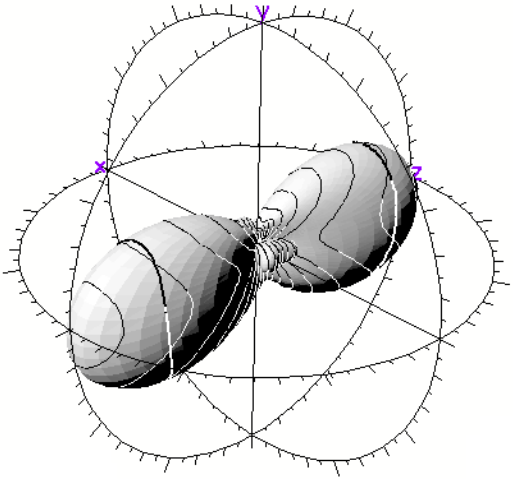

650 MHz D=9.6dBi

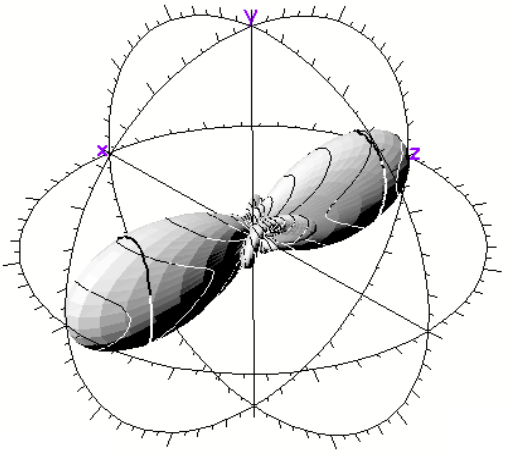

750 MHz D=10.7dBi

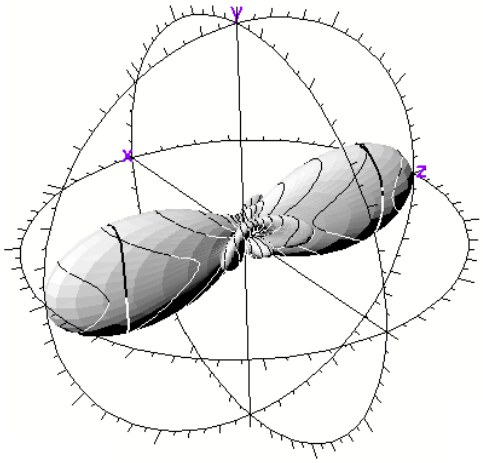

850 MHz D=11.8dBi

Figure 2.12 Simulated 3D Co-polar radiation patterns of the VSDA system

2.4.4 VSDA system with ground plane

The VSDA system match and directionality is improved by adding the ground plane at 80mm ($\lambda_0/8$) distance from the radiating element system (Figure 2.13). The groundplane dimensions are 720mm x 408 mm. It was made from a solid aluminium strips crossing at the vertical and the horizontal axis. The groundplane vertical sides are bended at $40°$ to achieve more directional beams.

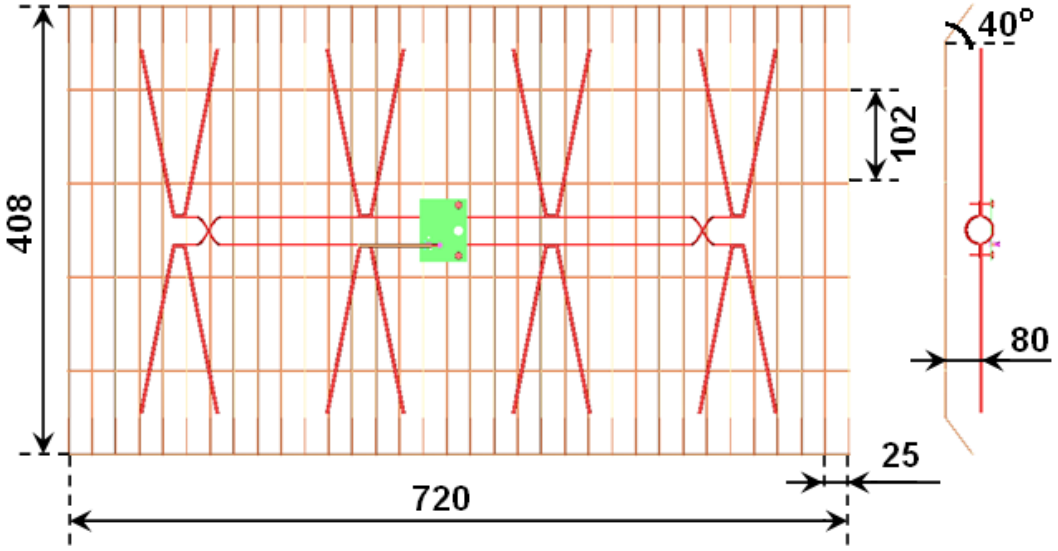

Figure 2.13 VSDA system dimensions with ground plane (All dimensions in mm)

The predicted and measured results of the return loss of the VSDA system are shown in Figure 2.14. There is a discrepancy between the measured and the predicted results. However, a visible trace of a similar performance can be noticed. The disagreement could be caused by a rectangular mesh used in the simulation.

In terms of the measurement comparison, the VSDA system with the ground plane has a deeper resonant up to -28dB, and its Bandwidth is equal to 50% compared to the VSDA without ground plane, these results also were reported in [11].

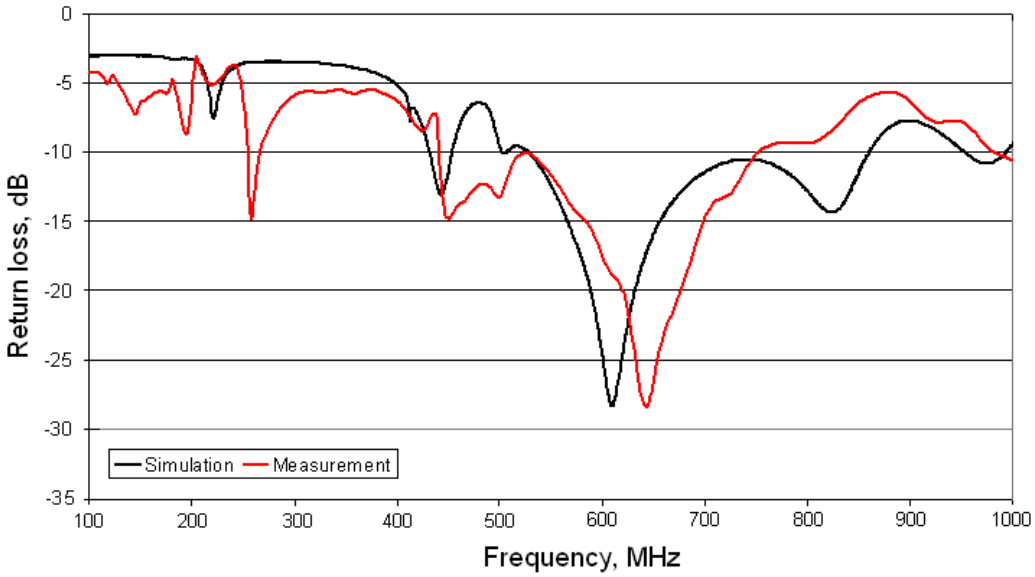

Figure 2.14 VSDA system with ground plane simulations and measurements comparison of return loss over frequency

To evaluate the VSDA system propagation performances in case when the balun is loaded with four V-shape dipoles and placed over the ground plane, the 3D co-polar radiation patterns and directivity values were simulated and analysed (Figure 2.15).

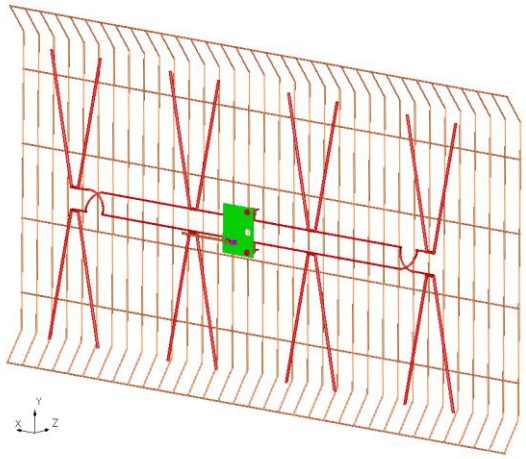

VSDA system with ground plane

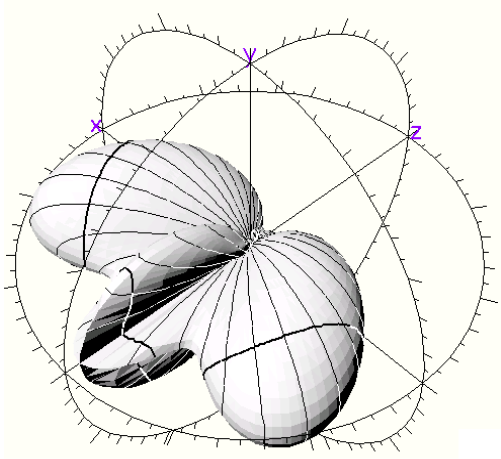

470 MHz D=7.2dBi

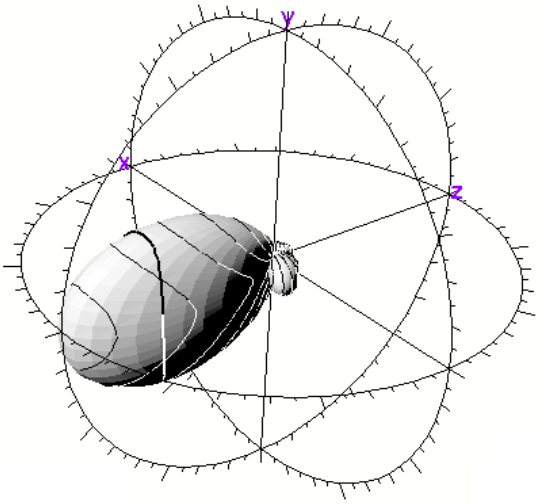

550 MHz D=12.4dBi

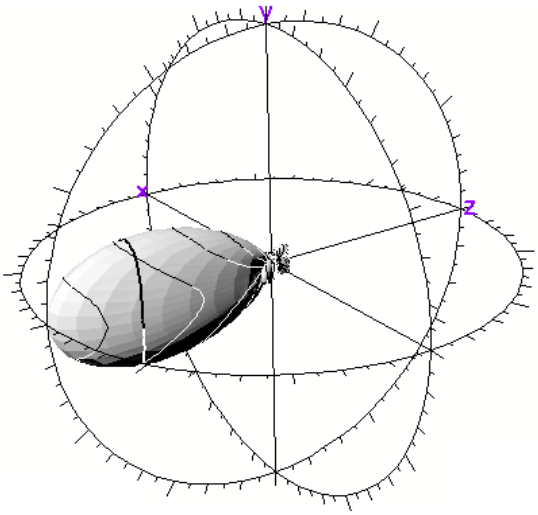

650 MHz D=12.9dBi

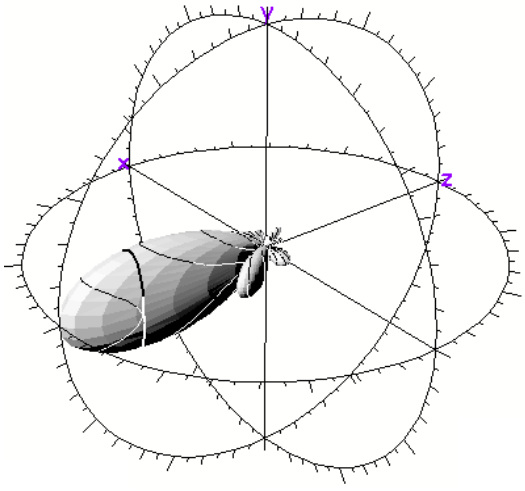

750 MHz D=14.7dBi

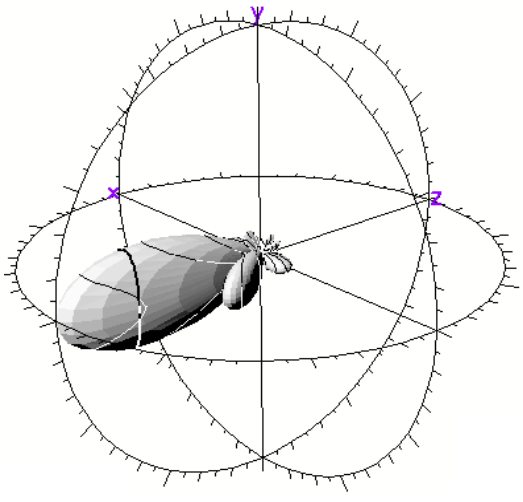

850 MHz D=15.6dBi

Figure 2.15 Simulated 3D Co-polar radiation patterns of the VSDA system with GP

The Half Power Beam Width (HPBW) values for the E, H- planes at various frequencies are shown in Table 2.2. The Front-to-Back ratio varies from 20dB to 26dB throughout the operating band.

HPBW, deg	470MHZ		550MHz		650MHz		750MHz		850MHz	
	E-plane	**H**-plane	**E**-plane	**H**-plane	**E**-plane	**H**-plane	**E**-plane	**H**-plane	**E**-plane	**H**-plane
VSDA system with GP	74°	90°	51°	53°	48°	46°	42°	45°	28°	31°

Table 2.2 HPBW values of the VSDA system with ground plane

The comparison of the simulation results for the directivity (shown in dotted line) and the gain (shown in solid line) values, with and without the ground plane, are represented in Figure 2.16. The return loss results, included in Gain values, are from measurements.

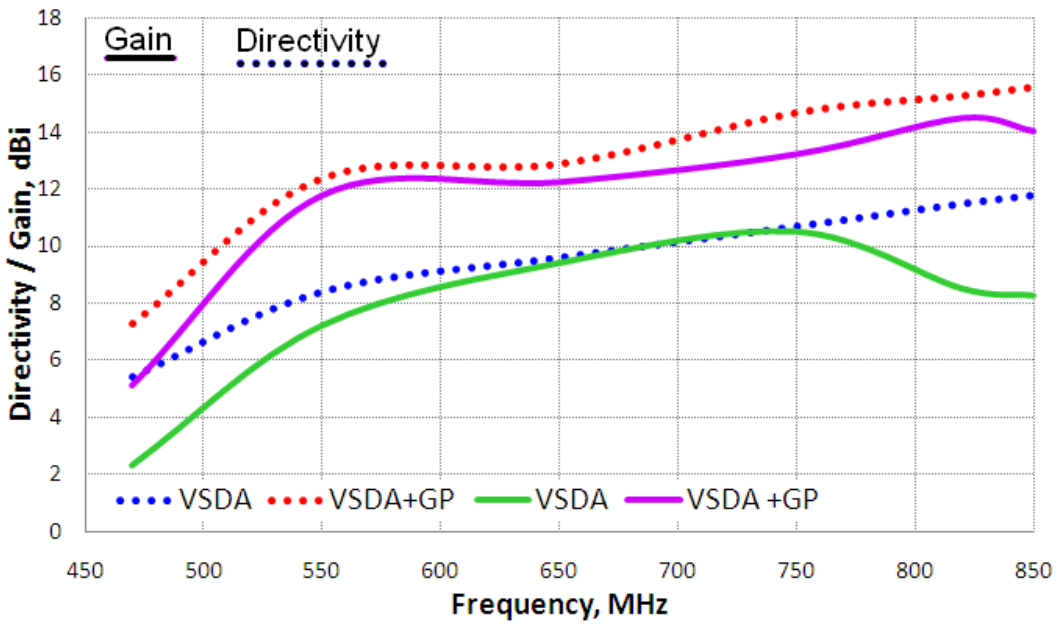

Figure 2.16 Comparison of VSDA system simulations and measurement results with and without ground plane (GP)

At the lower frequency of 470 MHz the directivity difference with and without the ground plane is only 2dB. However, the gain difference is 2.8dB. On the other hand, at the highest frequency of 850 MHz the directivity difference with and without the ground plane is 3.8dB. But in this case the gain difference is 5.8dB. The VSDA system has very directional beams. Nevertheless, the radiation patterns acquire quite large side lobes at the lower frequency (Figure 2.15), due to the close ground plane distance to the driven element system. At the highest frequency radiation patterns have high directivity, see Figure 2.15, however the measured return loss is only -7dB at 850MHz (Figure 2.14).

2.5 Conclusions

This chapter summarised the investigation on one of the most popular and high gain commercially available UHF antennas.

The Vertically stacked dipole antenna (VSDA) system structure consisted of three main parts: the balun, the radiating element and the ground plane. In the first part of this chapter the balun performance was investigated in terms of the return loss, the input impedance, the surface currents and the equivalent circuit using lumped elements. The balance effect was achieved between the frequencies of 420MHz and 920MHz.

The radiating element of the VSDA system consisted of four V-shape dipoles placed along the vertical axis at the same distance of $\lambda_0/4$ and fed by wire pair. More directional beams and higher gain values can be achieved by switching over the first and the last pairs of the V-shape dipoles at both ends of the radiating element. A good agreement between the predicted and measured return loss results was achieved. The measured VSDA system bandwidth was equal to 48% at 10 dB in the return loss.

The simulated radiation patterns of the VSDA system were similar to the $\lambda_0/2$ dipole. They remained relatively consistent over the frequency band.

To increase the directivity and gain values, the four V-shape dipoles fed from the broadband balun were placed above the wire ground plane at $\lambda_0/8$ distance. The VSDA with GP system achieved high directionality pencil beams in E and H planes. However, large side lobes appeared in the lower frequency band (470MHz-520MHz), since the ground plane was placed too close towards the radiating element. The best

performance of this antenna system type was achieved in the middle band of 550MHz-750MHz, when the radiation patterns were very directional and the return loss was very low (from -10dB to -28db). At the higher frequency band of 800MHz-850MHz the VSDA system lost the match and the return loss increased up to -7dB. The HPBW values (for the VSDA system placed over the ground plane) were: 28° for the E-plane and 31° for the H-plane at 850MHz.

The VSDA system placed above the ground plane achieved a medium overall performance with a mean gain value of 9.5dBi over the frequency band of 470MHz-850MHz.

2.6 References:

[1] CST's MicroStripes website: http://www.cst.com/.aspx

[2] MicroStripes Reference Manual, Release 5.5, issue 2, copyright 1994-2000 Kimberley Communications Limited, Electromagnetic Division of Flomerics.

[3] AWR Microwave office website: http://web.awrcorp.com/

[4] EMSight, "User Manual", Applied Wave Research. Inc., CA, USA.

[5] A.W. Rudge, K.Milne, A.D. Olver, P.Knight "The handbook of antenna design", volumes1 and 2, Page Bros Ltd, Norfolk,1986.

[6] C. Balanis, "Antenna Theory, Analysis, and Design", 2nd ed. New York, Wiley, 1997.

[7] J.F. Kiang "Radiation properties of coaxial colinear antennas" IEEE Trans. Antennas Propagat APS vol.1, Page(s): 244 - 247 1997.

[8] T. J. Judasz and B. B. Balsley, "Improved theoretical and experimental models for the coaxial colinear antenna," IEEE Trans. Antennas Propagat., vol.AP-37, pp.289-296, March 1989.

[9] Anritsu 37XXXD Series Vector Network Analyzer Operation Manual, 30 September 2007, UK; Anritsu 37XXXD Series Vector Network Analyzer Programming Manual, 30 September 2007, UK.

[10] MATLAB webpage: http://www.mathworks.com/products/matlab/

[11] N. Riauka, A. Chauraya, and J. C. Vardaxoglou, “Compact antenna integrated into flat plate FSS”, IEEE APS 2008, 5-11 July 2008, San Diego, CA, AP-S/URSI 2008, pp1-4.

Chapter 3

Yagi - Uda antenna (YUA) system

3.1 Introduction

This chapter presents the Yagi – Uda antenna (YUA) system analysis. The YUA system is horizontally polarised, directional, and capable of operating over the broad bandwidth. The broadband and high gain characteristics of these antennas have made them very popular in the UHF commercial communication systems. Moreover, these types of antennas maintain relatively consistent radiation patterns over the operating frequency. On the other hand, they tend to have a very large and complicated structure in order to achieve the broadband performances and the high gain pencil beams. The structural complexity will ultimately affect the antennas price and installation, therefore,

it becomes an obvious disadvantage of such devices. The YUA system consists of the balun, the radiating element, the reflector and a number of directors.

This chapter is organised in the following way: section 3.2 commences with analysis of the commercially available YUA system balun and the radiating element. The return loss and the input impedance of the YUA system balun was predicted by using the AWR Microwave software [1, 2].

Section 3.3 describes the parametric study carried out to investigate and improve the balun loaded with radiating element performance. Firstly, the parasitic element effect to the balun return loss was investigated. In sections 3.3.2 and 3.3.3 the balun performance was analysed by changing the radiating element distance from the balun. Measurements were performed to evaluate the predicted results of the return loss [3].

Section 3.3.4 commences with the YUA system dipole analysis and optimization. The gradual change of the dipole arms angle (ϕ) was performed. The predicted results of the return loss, the radiation patterns and the directivity were also discussed [4-6].

The last parametric study step of the YUA system dipole is described in section 3.3.5. The V-shape dipoles base length was changed and the predicted results were evaluated through the return loss, the radiation patterns and the directivity values [4-6].

Achieved results and conclusions are described in section 3.4.

3.2 Yagi – Uda antenna (YUA) system

The Yagi-Uda antenna was invented in 1926 by Shintaro Uda with the collaboration of Hidetsugu Yagi. It is a directional antenna designed to maximize the reception over long distances. Three types of element are termed, i.e. the driving element (DE), the reflector and the directors (Figure 3.1). Only the DE is connected directly to the feeder. Other elements couple to the transmitter power through the local electromagnetic fields which induce currents in them [7-10].

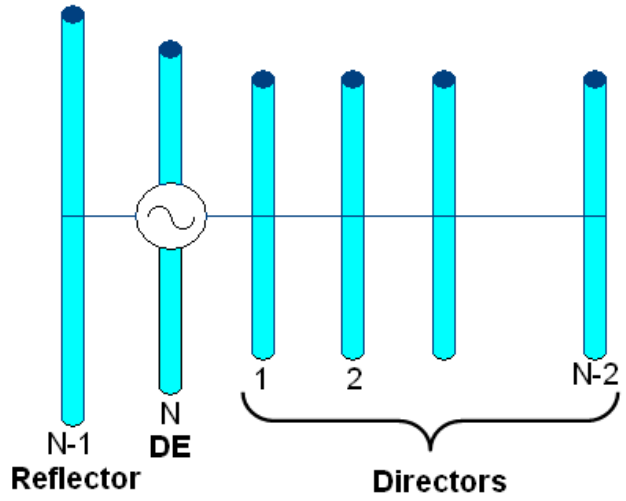

Figure 3.1 Yagi – Uda antenna configuration

The driven element is typically resonant when its length is slightly less than $\lambda_0 / 2$ ($0.4\lambda_0$ - $0.49\lambda_0$). In order to broadband the Yagi - Uda, individual elements are split into two in an approximation of a primitive biconical antenna [9, 11, 12]. Also the directional radiation patterns can be achieved by incorporating the corner reflector into the antenna

system [9]. The structure of the broad band and high gain 52 element Yagi – Uda antenna (commercially available for the UHF reception) is shown in Figure 3.2.

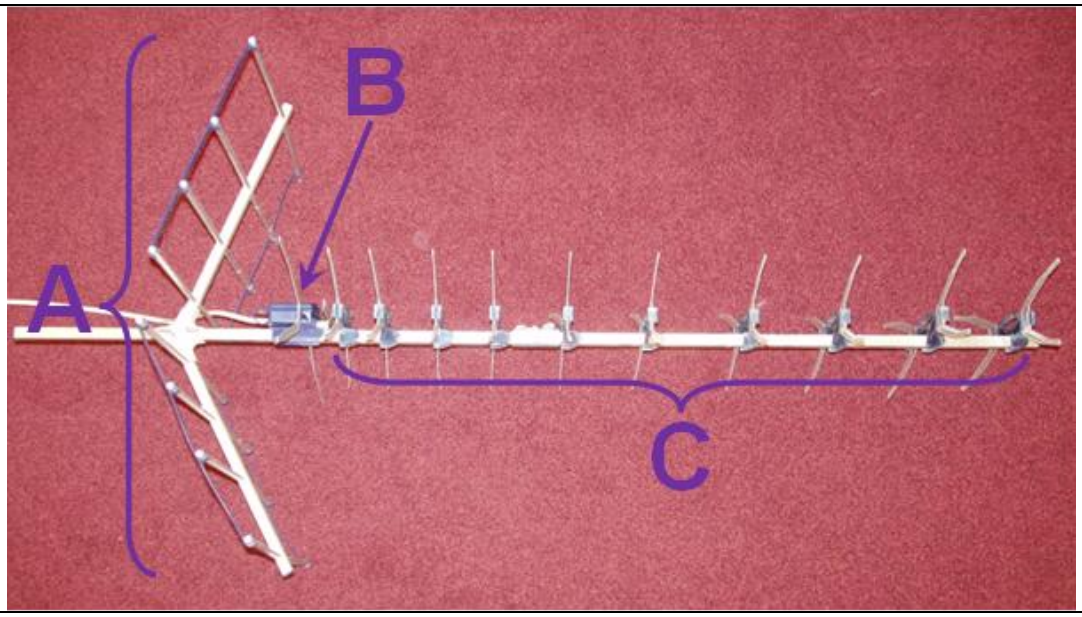

Figure 3.2 52 elements Yagi - Uda antenna system

In this figure A represents the corner reflector, B corresponds to the driven element system and C shows ten directors. The broadband balun and the radiating element are analysed in more details in sections 3.2.1 and 3.2.2 respectively.

3.2.1 YUA system balun

The balun structure of the YUA system is more complicated and smaller compared to the VSDA system balun, analysed in Chapter 2 (section 2.4.1). The balun design was obtained by measuring the dimensions of the YUA system balun with a digital microscope. The top and the bottom views of the YUA system balun structure are shown in Figure 3.3. A 1.6mm FR4 material with a 4.5 permittivity was used as a substrate. It is represented by **A** in Figure 3.3. The balun consists of two parts: the printed copper patch connected to the inner (**B** in Figure 3.3) and the copper patch connected to the outer (**C** in Figure 3.3). This balun type is similar to the one investigated earlier in Chapter 2 (section 2.4.1).

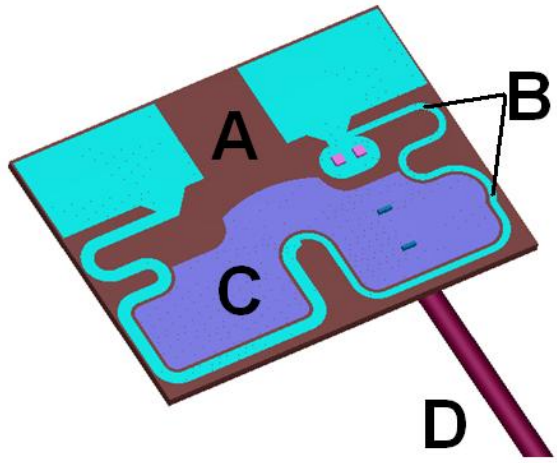

Top view of the balun

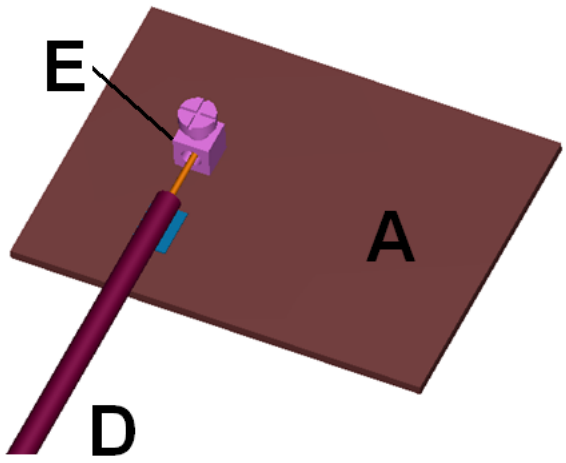

Bottom view of the balun

Figure 3.3 The structure of the YUA system balun

All conductor surfaces consist of the metal (Cu) with a $5.8 \cdot 10^7$ S/m conductivity. The input to the balun is connected to the $75\,\Omega$ coaxial cable (**D** in Figure 3.3). The connector which holds the coaxial cable inner corresponds to **E** in Figure 3.3. The PCB is covered with an antioxidant material to prevent the metal oxidation. Hence, the balun outputs are not physically contacting the radiating element, but rather coupling on to it. The balun dimensions are 57.5mm x 53mm x 1.6mm and its structure is shown in Figure 3.4.

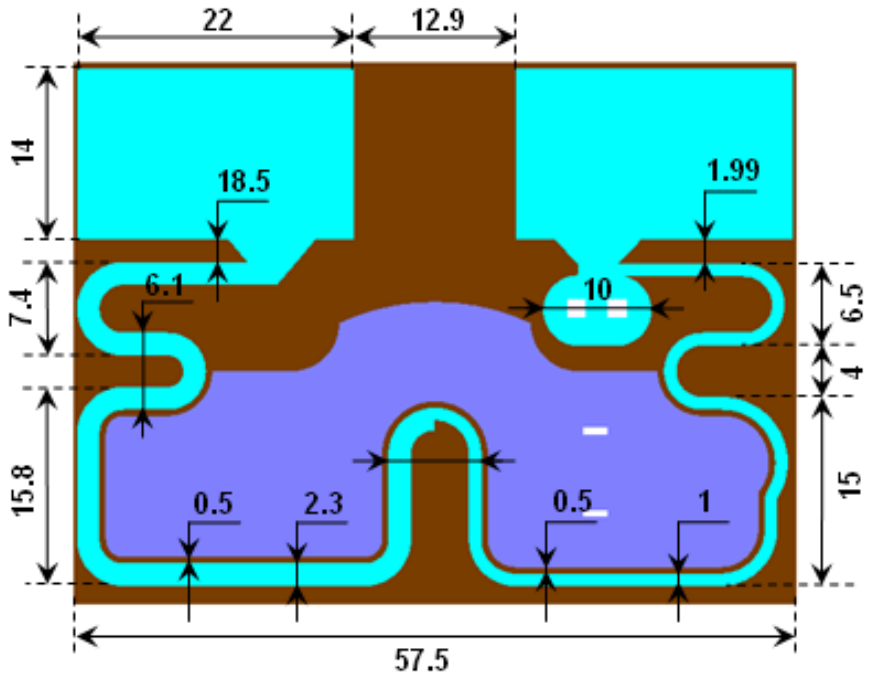

Figure 3.4 The YUA system balun dimensions (all dimensions in mm)

The return loss and the input impedance values of the YUA system balun are shown in Figure 3.5. The terminal impedance of the YUA system balun is equal to $75\,\Omega$ similar to the VSDA system balun, analysed in Chapter 2 (section 2.4.1).

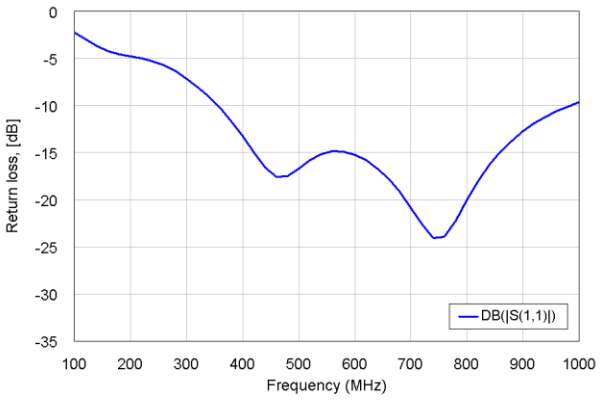

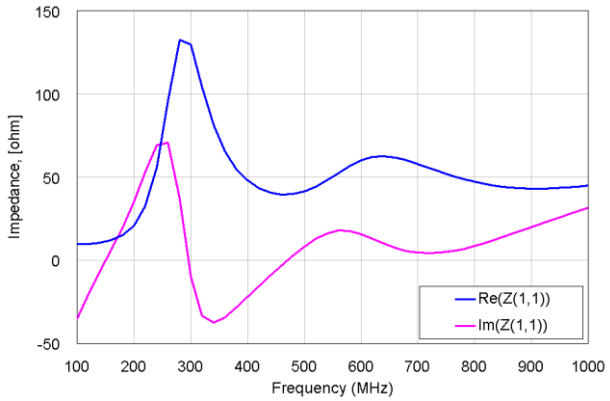

Figure 3.5 Return loss and input impedance results of the YUA system balun with 75Ω load

The YUA system's balun has a broader bandwidth than the VSDA balun, investigated in section 2.4.1. The YUA balun achieves 10dB return loss from 350MHz, and the VSDA balun only at 420MHz. Also the YUA balun is protected from corrosion.

To evaluate the YUA system balun performance, the surface current distribution was analysed at various frequencies. The CST MicroStripes [13, 14] EM software was used to obtain these results. Figure 3.6 illustrates the surface currents distribution at different frequencies and various phases. The pink ellipses in the first picture (Figure 3.6) indicate that the balun has same surface current values at symmetrical points. Figure 3.7 represents the YUA balun surface current directions at 650MHz. They are opposite, which means they performs $180°$ phase shift. It is a broadband operating balun from 470MHz to 850MHz.

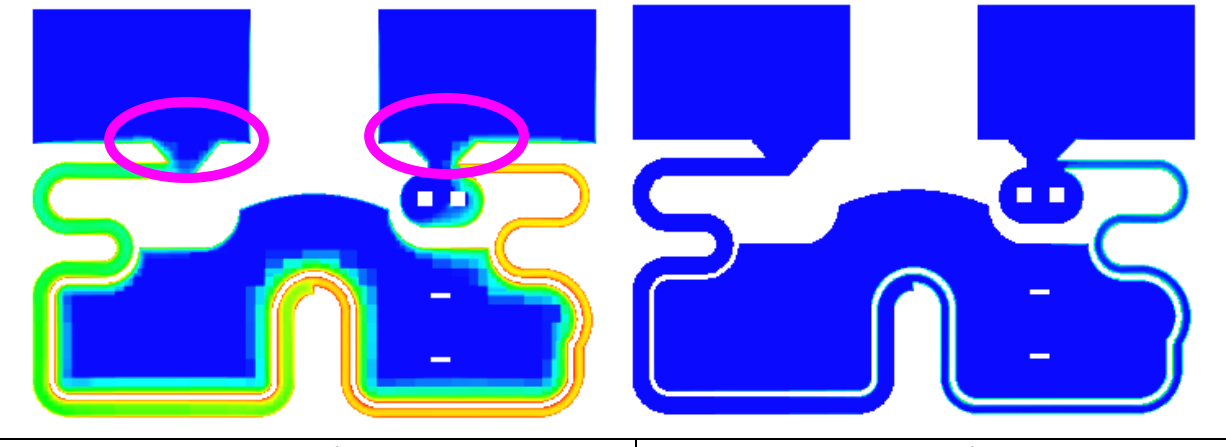

470 MHz ϕ=230° | 470 MHz ϕ=320°

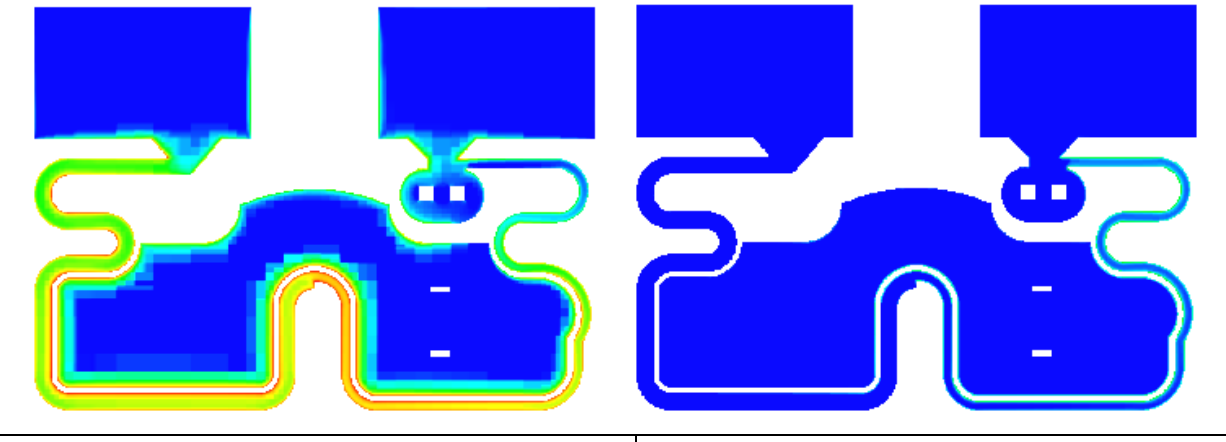

650 MHz ϕ=170° | 650 MHz ϕ=260°

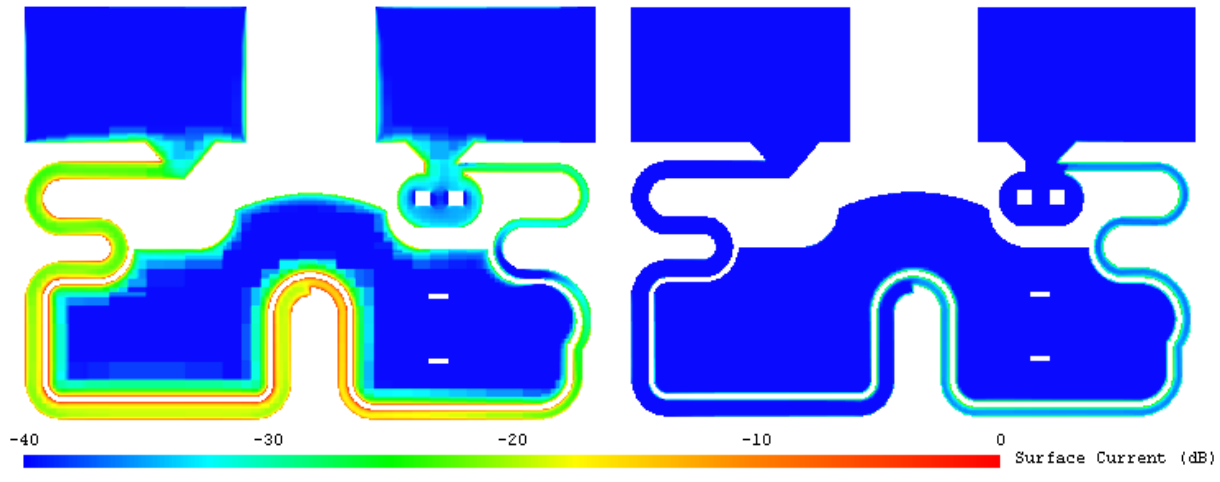

850 MHz ϕ=40° | 850 MHz ϕ=130°

Figure 3.6 The YUA system balun surface currents distribution

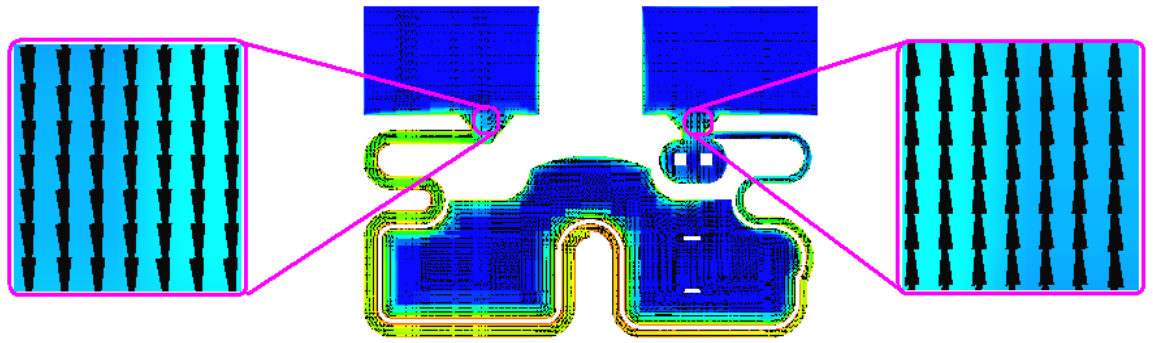

Figure 3.7 The YUA system balun surface currents direction at 650MHz

3.2.2 YUA system driven element

The YUA system balun is loaded with a V-shape dipole, radiating element, which resonates and converts the electricity into the electromagnetic waves. The structural diagram of the YUA system radiating element is shown in Figure 3.8.

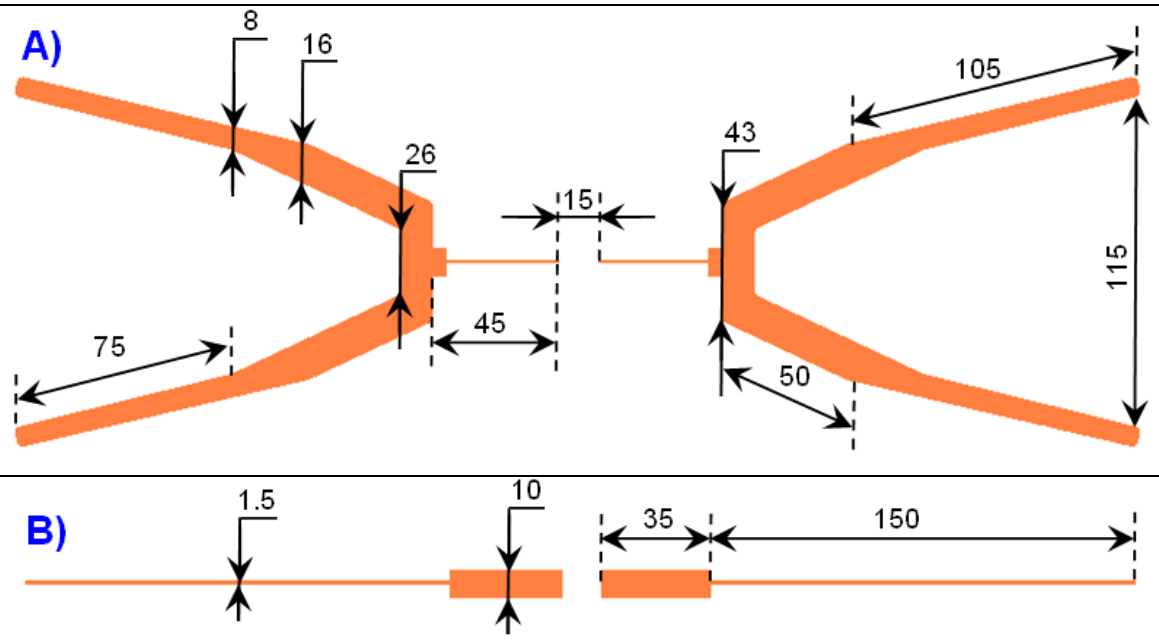

Figure 3.8 Diagram of the YUA system radiating element: a) Top view, b) Side view (Dimensions in mm)

3.3 YUA system parametric study

It was decided to tune the YUA system with the broadband balun and a pair of V-shape dipoles. In order to improve the return loss, the bandwidth and boost the directivity, a parametric study was carried out. The results are presented in the following sections. The methodology included:

- Adjusting the parasitic element length due to the YUA performance.
- Changing the air gap distance between the balun and the radiating element with a parasitic element.
- Changing the air gap distance between the balun and the radiating element without a parasitic element.
- Changing V-shape dipoles arms angle.
- Changing V-shape dipoles base length.

3.3.1 Parasitic element length change

In these simulations the parasitic element length of the YUA system was changed from 100% to 0% (the later correspond to the total element removal from the antenna structure). The dimensions of the parasitic element of the YUA system are shown in Figure 3.9. The parasitic element dimensions for the simulations were:

- 140mm x 14mm x 1.5mm – 100%
- 105 mm x 14mm x 1.5mm - 75%
- 91 mm x 14mm x 1.5mm - 65%
- 70 mm x 14mm x 1.5mm - 50%
- 14 mm x 14mm x 1.5mm - 10%
- Without parasitic element - 0%

The simulations were performed for the case when the balun output is connected to the input of the radiating element, without any air gap separation.

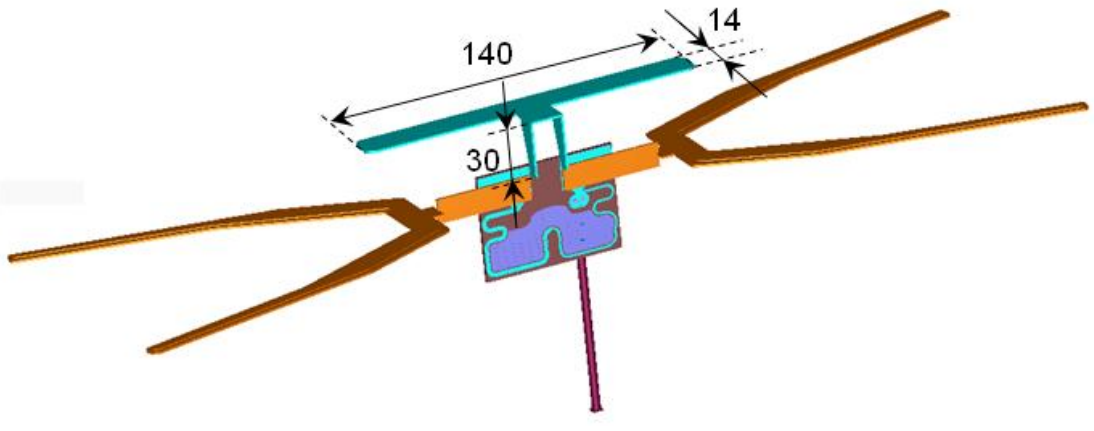

Figure 3.9 Structure of the YUA system with parasitic element (dimensions in mm)

The predicted results for the changes above are shown in Figure 3.10. Two resonant frequencies can be seen: the first resonance is at 219MHz and the second resonance depends on the change of the parasitic element length, shifting from 718MHz to 803MHz. When the parasitic element is removed, the second resonance shifts to 826MHz. These results show that it is possible to increase the second resonant frequency by 100MHz.

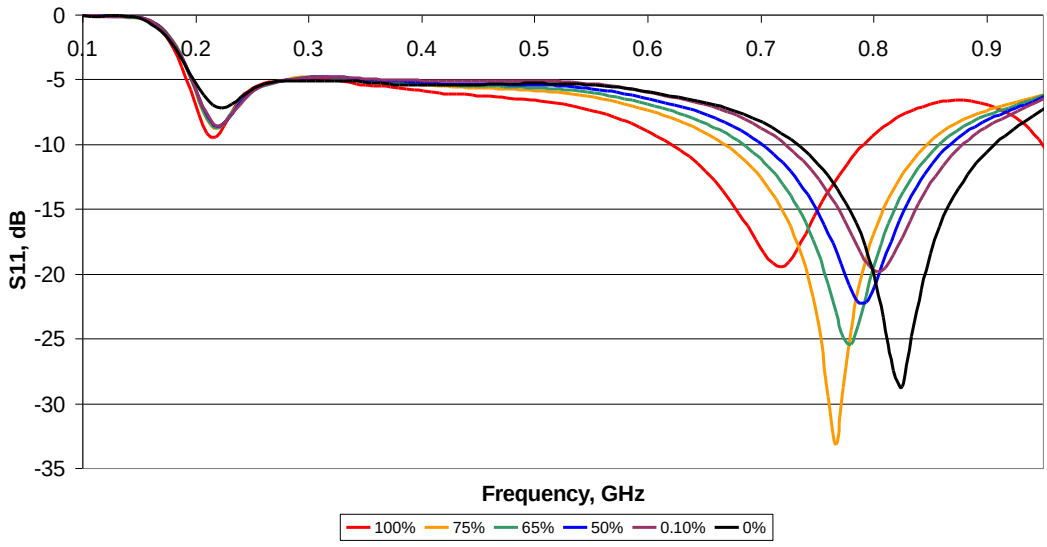

Figure 3.10 YUA system return loss behaviour changing parasitic element length over the frequency

3.3.2 Changing the air gap distance between the balun and the radiating element with parasitic element

The second part of the YUA systems optimisations begins by changing the air gap distance between the balun and the radiating element [3]. This process is shown in figure 3.11. The radiating element was moved from the balun in order to make an air gap separation.

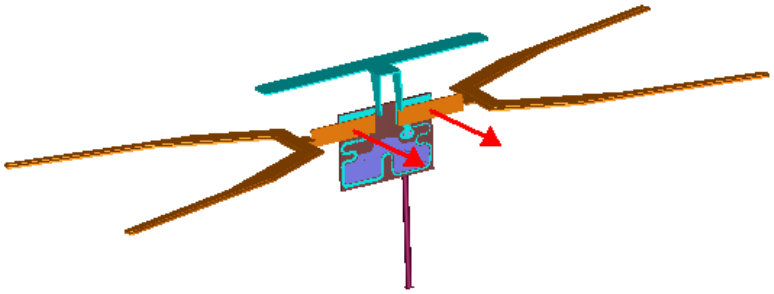

Figure 3.11 Increasing the air gap separation between the YUA system balun and radiating element

The air gap separation distance is altered from 0.0mm to 1.0mm (parasitic element on its top). The increase of the air gap distance between the YUA balun and the radiating element represents an extra effective capacitance (C_{eff}) value. It can be approximated to the capacitance of the flat, parallel metallic plates for the area ***A*** and the separation ***d*** (Figure 3.12).

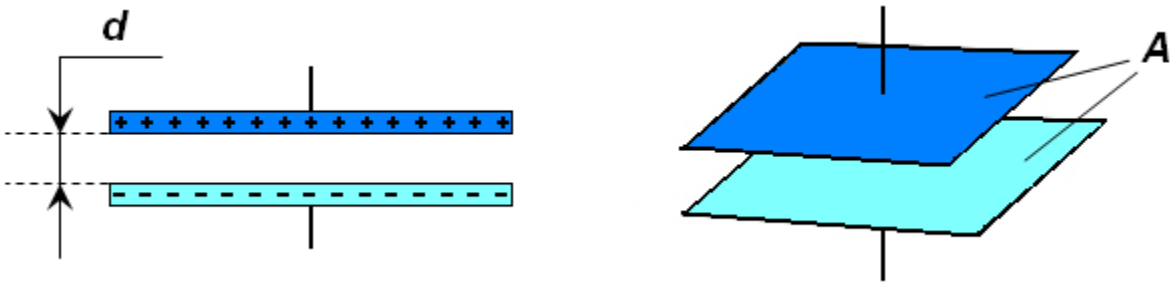

Figure 3.12 The capacitance of the flat, parallel metallic plates

The capacitance value (C) is expressed by following equation:

$$C = \frac{\varepsilon \cdot A}{d} \qquad \text{eq. 3.1}$$

Where ε is the permittivity of the insulating material or dielectric between the metallic plates. The capacitance (C) value varies from 27pF to 2.7pF when the separation gap varies from 0.1mm to 1mm. The added extra capacitance value adjust the input impedance value at different frequency and, therefore, changing the return loss response. The reactance (X) and impedance (Z) of a capacitor can be expressed as fallows (eq. 3.2 and eq.3.3):

$$X = \frac{1}{\omega \cdot C} = -\frac{1}{2\pi \cdot f \cdot C} \qquad \text{eq.3.2}$$

$$Z = \frac{1}{j\omega \cdot C} = -\frac{j}{2\pi \cdot f \cdot C} \qquad \text{eq.3.3}$$

The predicted return loss results of the YUA system with parasitic element are shown in Figure 3.13.There are two resonances at the 219MHz and at the 718MHz frequencies. Increasing the air gap separation distance between the balun and radiating element, the first resonant is shifted towards the upper frequency and the second

resonant moves to the lower frequency. The coupling between the radiating element and the balun increases the YUA system bandwidth up to 64.4% (when the air gap distance equal to 1mm). In order to evaluate the predicted results, measurements were made by changing the air gap separation distance of the YUA system with parasitic element from 0.0mm to 2.0mm by 0.2mm step. The return loss measurements were carried out using the Marconi Instruments Reflection analyzer [15] in anechoic chamber, shown in figure 3.14. The red solid line (with 1.0mm air gap separation distance) represents the best separation distance between the balun and the radiating element, when the YUA system has the parasitic element on top.

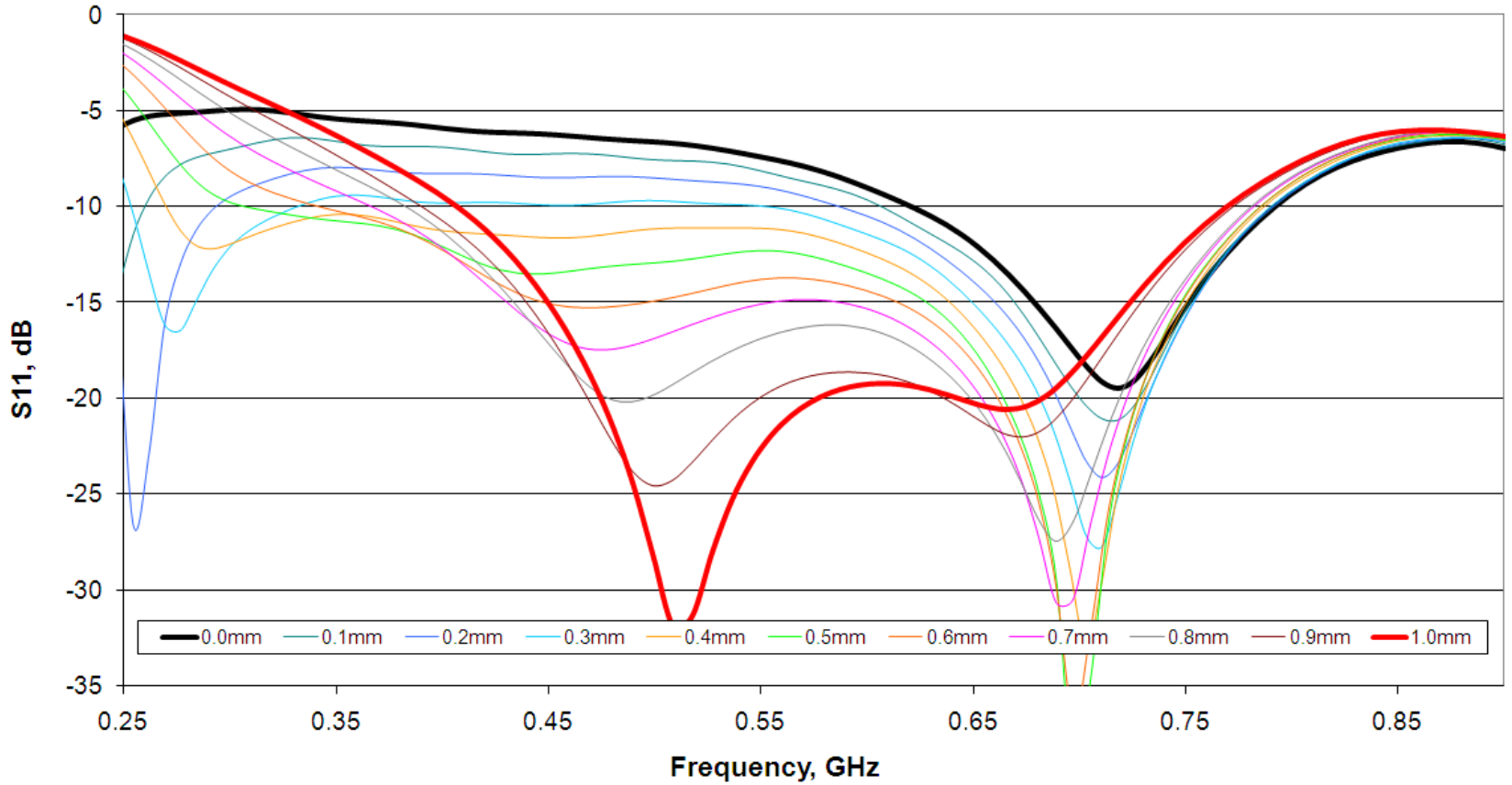

Figure 3.13 The YUA system with parasitic element simulation results

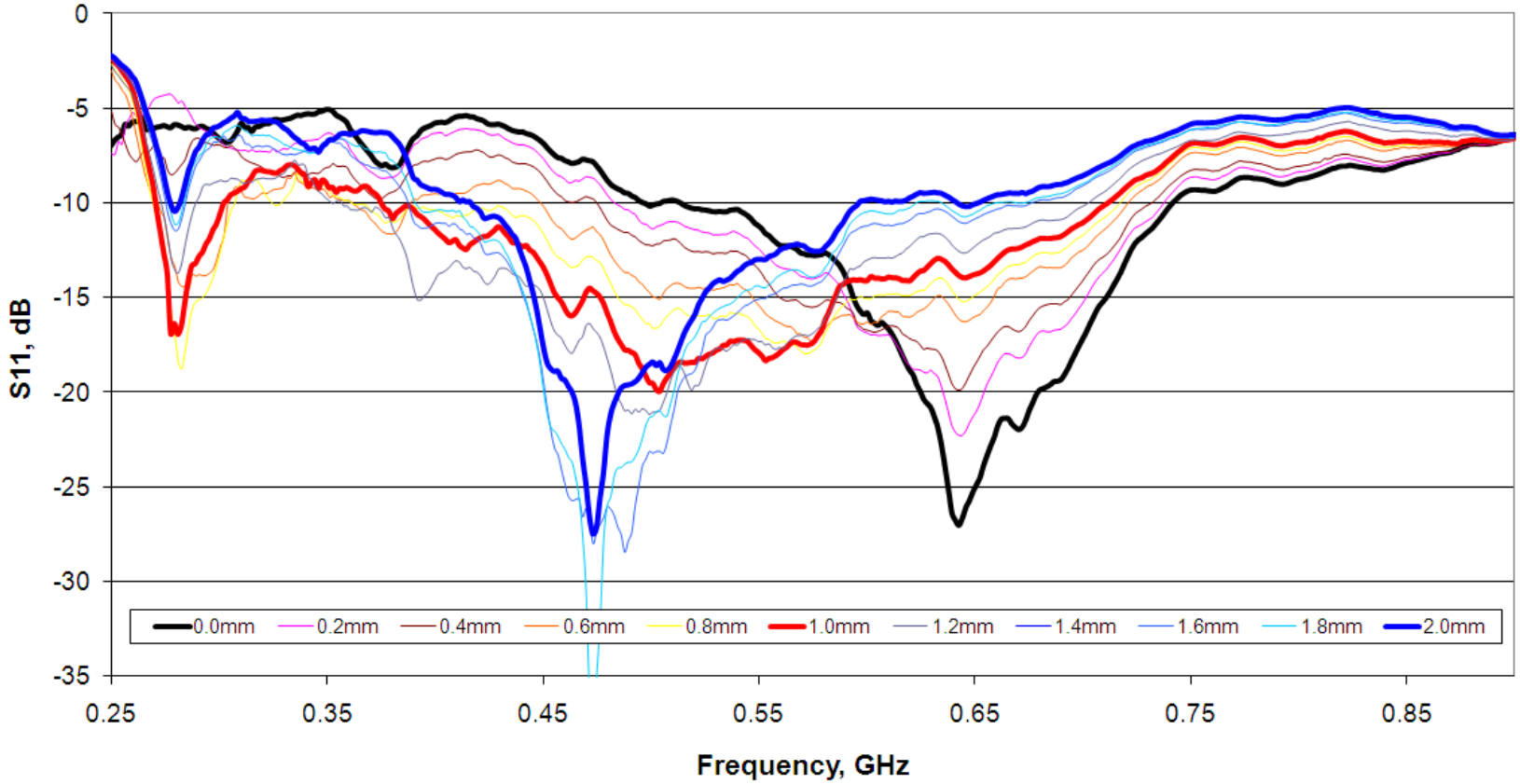

Figure 3.14 The YUA system with parasitic element measurement results

3.3.3 Changing the air gap distance between the balun and the radiating element without parasitic element

The next tuning part of the Yagi – Uda antenna system starts by changing the air gap distance between the balun and the radiating element without the parasitic element (Figure 3.15) [3].

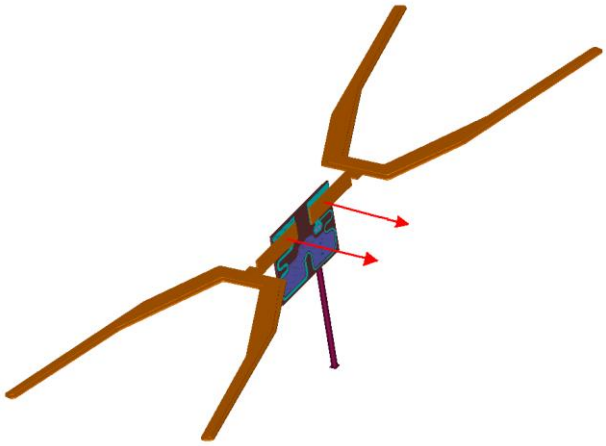

Figure 3.15 Increasing the air gap separation between the YUA system balun and radiating element

The air gab distance in simulations is changed from 0.0mm to 2.0mm with a 0.1mm step. The simulation results are shown in Figure 3.16. There are two resonances at the 219MHz and the 826MHz frequency respectively. Increase in the air gap separation distance between the YUA system balun and the radiating element makes the first resonant shift towards the upper frequency. Similarly to the previous example,

the same change of the distance gap results in the second resonant movement towards the lower frequency.

To evaluate the predicted results, measurements were carried out (Figure 3.17). The red line corresponds to the best antenna performance over the bandwidth. When the air gap between the balun and the antenna radiating element is equal to 1.0mm, the BW is 78%.

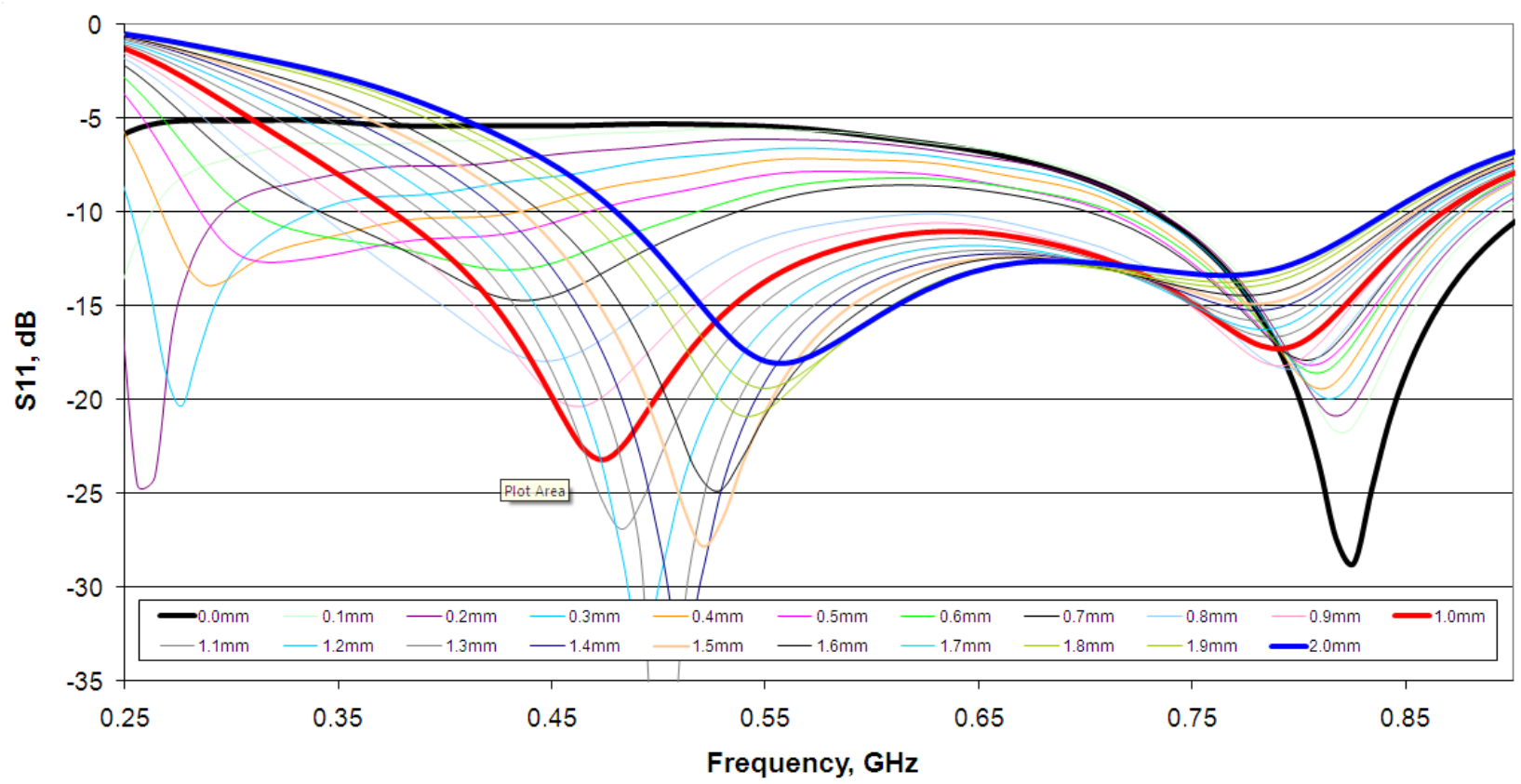

Figure 3.16 The YUA system without parasitic element simulation results

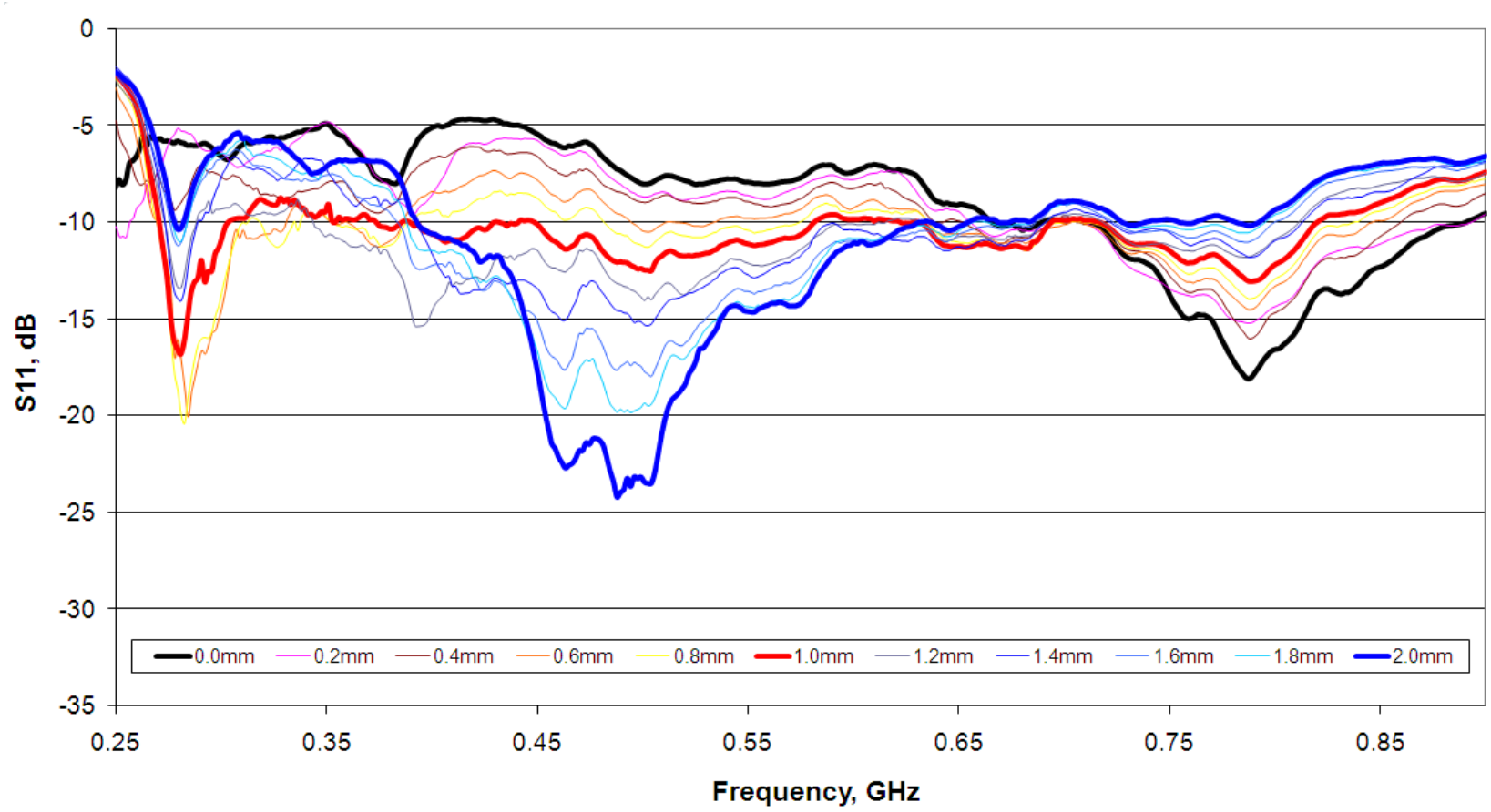

Figure 3.17 The YUA system without parasitic element measurement results

Figure 3.18 shows the comparison of the results obtained by the simulation and the measurements (the YUA system without the parasitic element), when the air gap separation distance is equal to 1.0mm. It can be seen from this Figure that the measurement results has reasonable agreement with those obtained by the simulation.

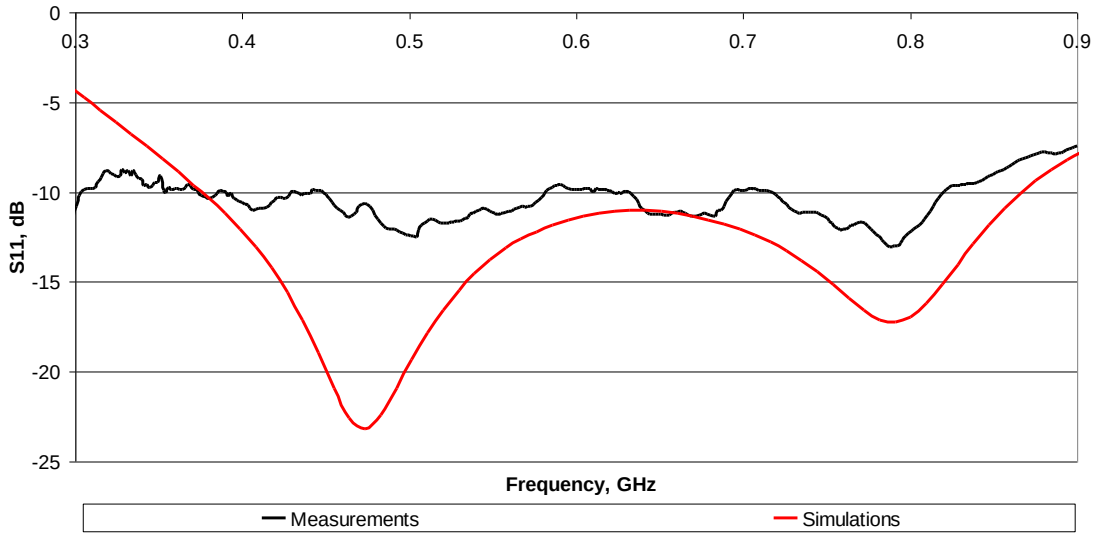

Figure 3.18 YUA system without parasitic element simulation and measurement comparison, when the air gap distance is 1.0mm

The best return loss and bandwidth values were achieved in this part of the parametric study. Therefore, for the next YUA system optimisation stages (section 3.3.4 Changing V-shape dipoles arms angle and section 3.3.5 Changing V-shape dipoles base length) the same air gap separation distance of 1mm will be used.

3.3.4 Changing V-shape dipoles arms angle

The next YUA system optimization step involves the V-shape dipoles arms angle ϕ change from $0°$ to $45°$ (Figure 3.19) [4-6]. The air gap between the balun and the radiating element is kept 1.0mm [3].

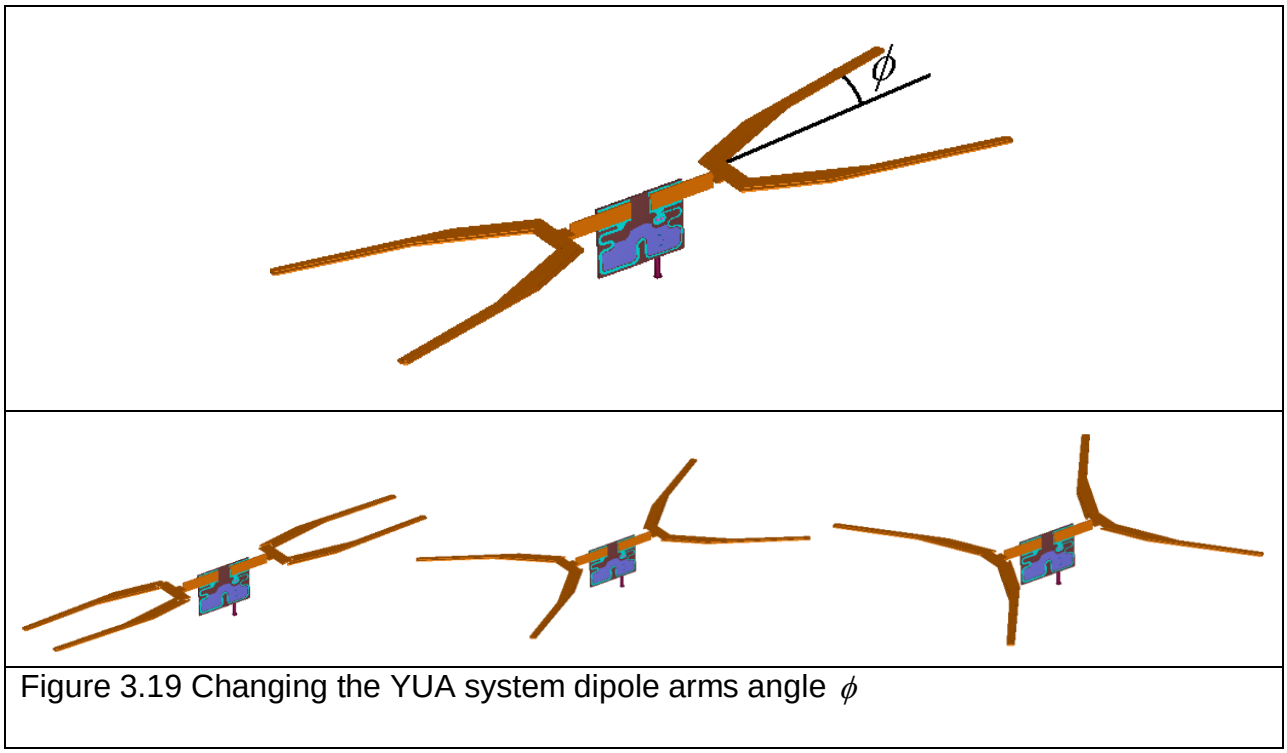

Figure 3.19 Changing the YUA system dipole arms angle ϕ

Ten different V-shape dipole arm angles were simulated starting from 0° to 45° with a 5° step, in order to optimise the E, H-plane co-polar radiation patterns and achieve a higher directivity. The simulated return loss response is shown in Figure 3.20. The bandwidth is equal to 89% when the YUA system dipole arm angle is $0°$. The black line represents a $45°$ angle with the bandwidth equal to 78.8% at 10 dB line of return loss.

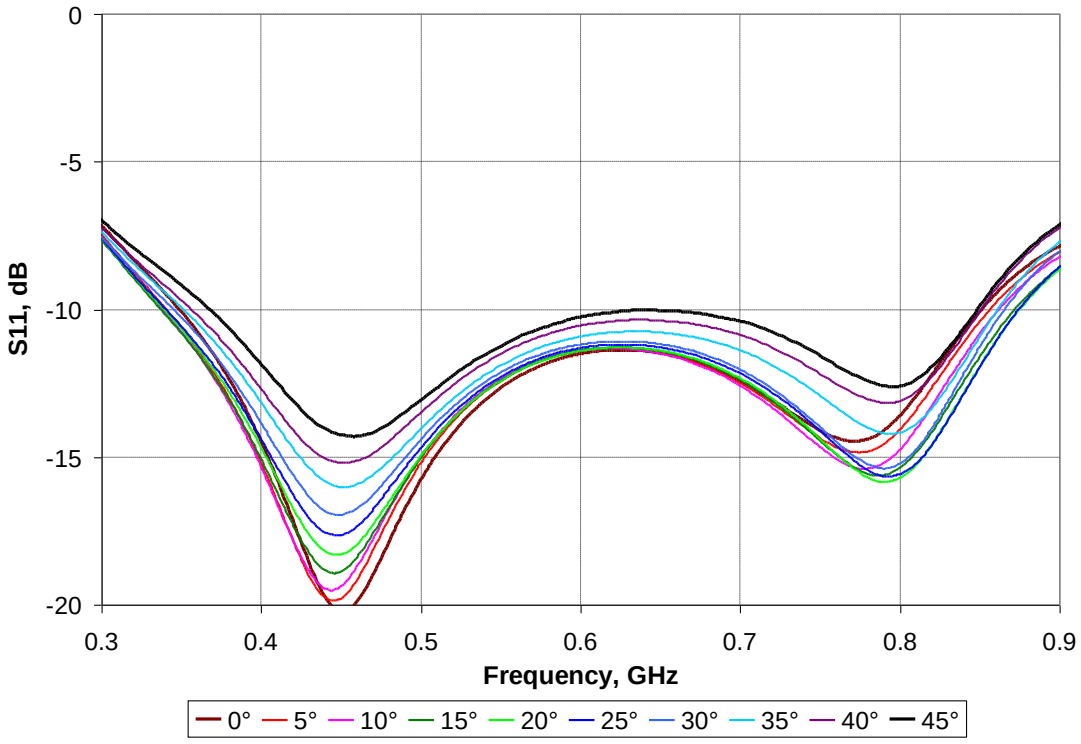

Figure 3.20 The YUA system simulated return loss results changing dipoles arms angle ϕ from $0°$ to $45°$ each $5°$

The next two figures (Figure 3.21 and Figure 3.22) show the E, H - planes co-polar radiation patterns and the directivity values of the YUA system for different dipole arm angle (ϕ).

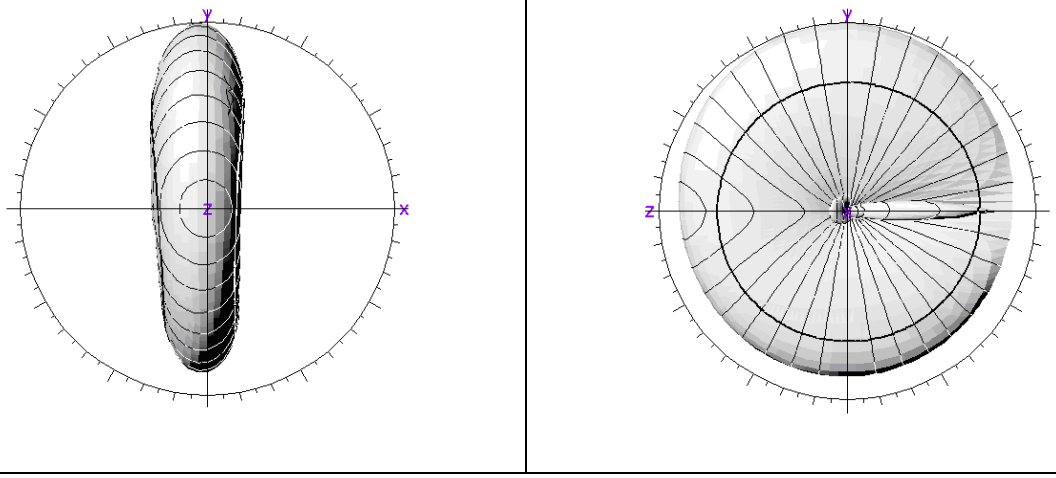

ϕ=0° D= 4.8dBi

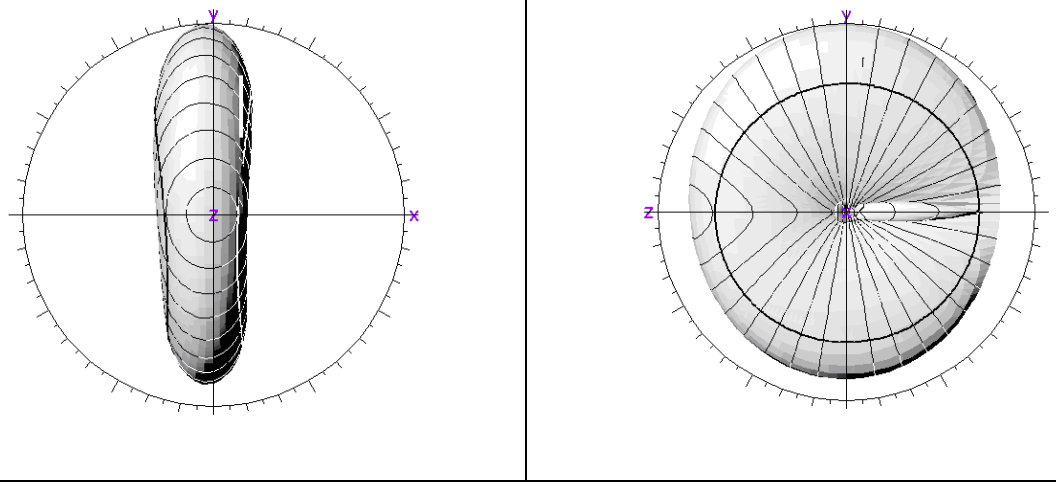

ϕ=10° D= 4.9dBi

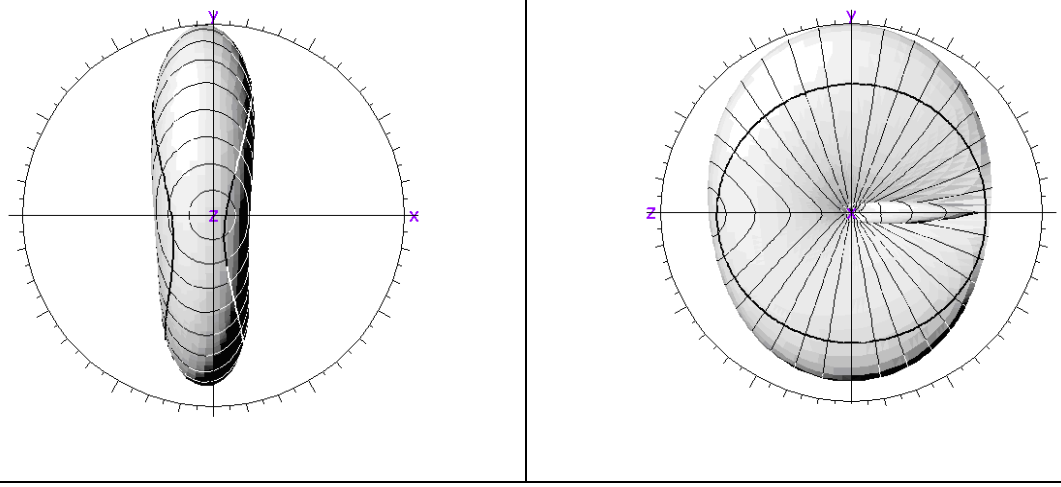

ϕ=20° D= 5dBi

Figure 3.21 Radiation patterns changing dipoles arms angle $\phi = 0° - 20°$

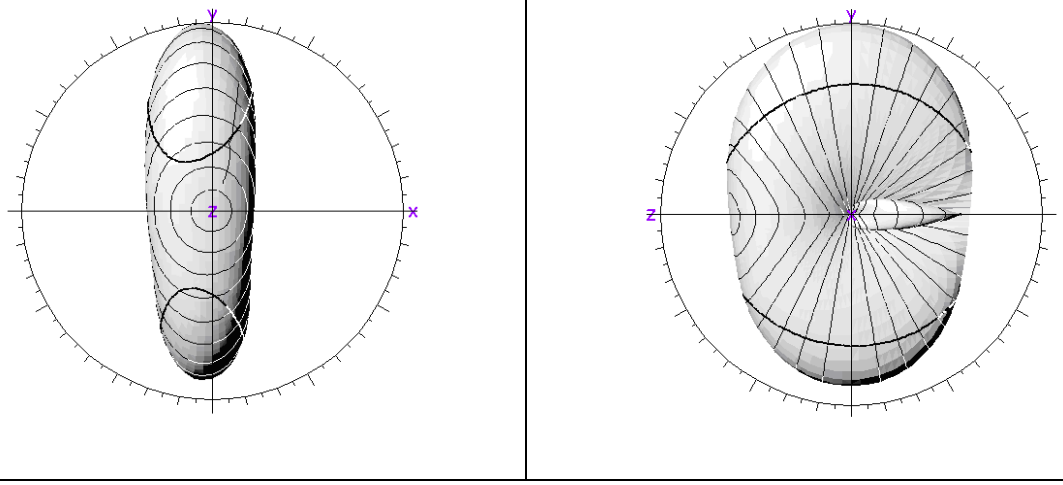

ϕ=30° D= 5.04dBi

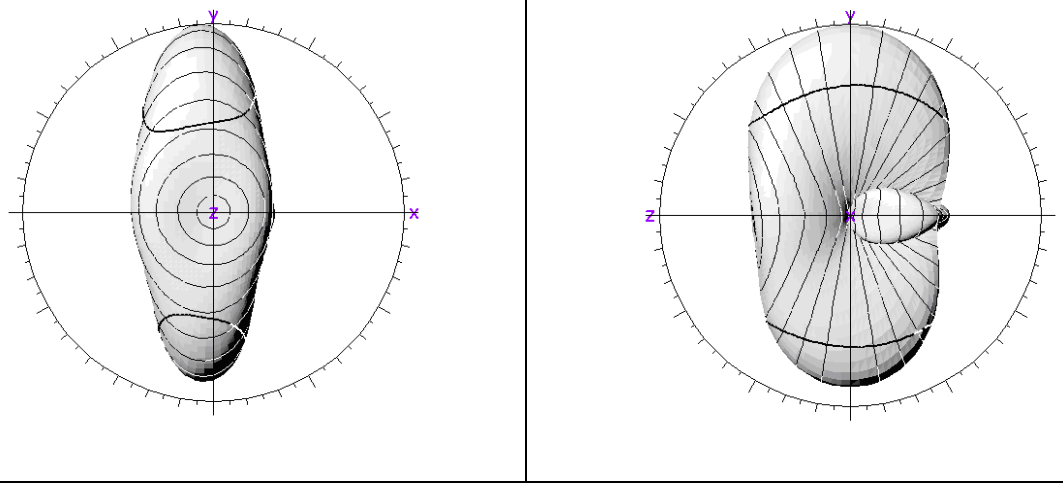

ϕ=40° D=4.9 dBi

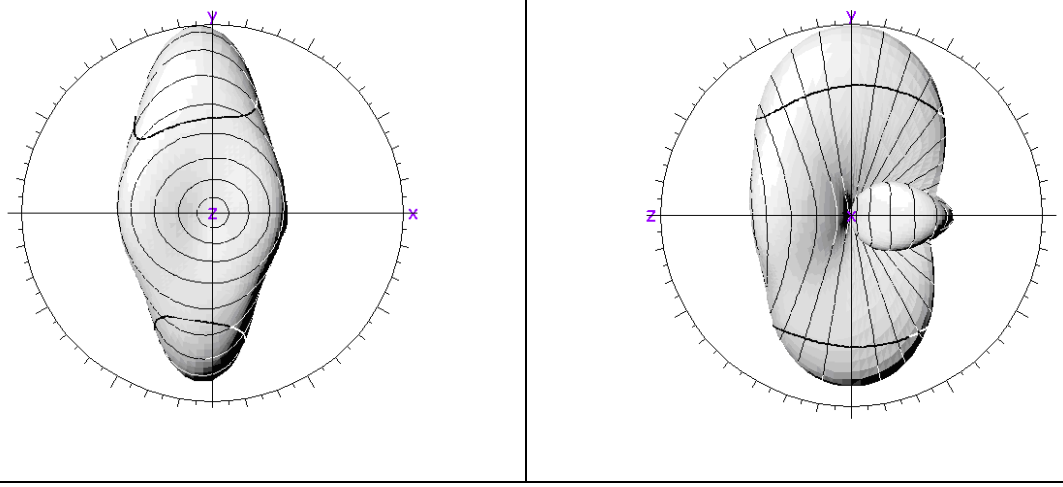

ϕ=45° D= 4.5dBi

Figure 3.22 Radiation patterns changing dipole arms angle ϕ =30° - 45°

The Half Power Beam Width (HPMW) at five different frequencies is shown in Table 3.1.

ϕ=0°		ϕ=10°		ϕ=20°		ϕ=30°		ϕ=40°		ϕ=45°	
E-plane	**H**-plane	**E**-plane	**H**-plane	**E**-plane	**H**-plane	**E**-plane	**H**-plane	**E**-plane	**H**-plane	**E**-plane	**H**-plane
43°	180°	44°	180°	46°	180°	48°	126°	49°	92°	51°	87°

Table 3.1 The HPBW values changing the dipole arms angle ϕ

It can be noticed that the E-plane radiation patterns become wider when frequency increases from 43° to 51°. However, the H-plane radiation patterns change from omni - directional patterns to directional from a 25° angle.

Figure 3.23 shows the simulated directivity values of the YUA system dipole arm angle (ϕ) at two different frequencies, i.e. 500MHz and 800MHz. The directivity decreases from 2.9dBi to 2.6dBi at a lower frequency. However, at a higher frequency the directivity increases from 4.8dBi to 5.1dBi till the YUA system dipole arm reaches $25°$ angle and then starts to decrease to 4.5dBi.

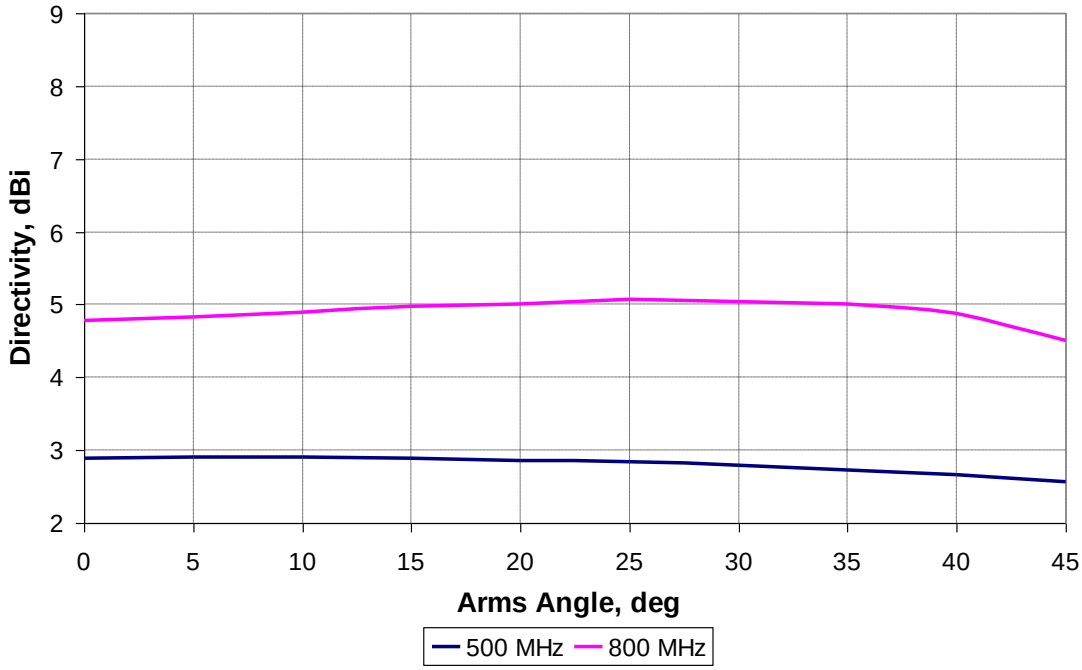

Figure 3.23 The directivity results over the YUA system dipoles arms angle ϕ

Based on the acquired simulation results, the optimum YUA system dipole arm angle is $25°$. The next section commences with a parametric study of changing the dipole base length, when the dipole arm angle is $25°$ and the coupling gap separation between the balun and the radiating element is 1mm.

3.3.5 Changing V-shape dipole base length

The last step of the YUA system parametric study investigates the V-shape dipole base length change impact on the directivity values at different frequencies [4-6]. Figure 3.24 illustrates the YUA system with various dipole base length values x from the interval of -2cm to +14cm.

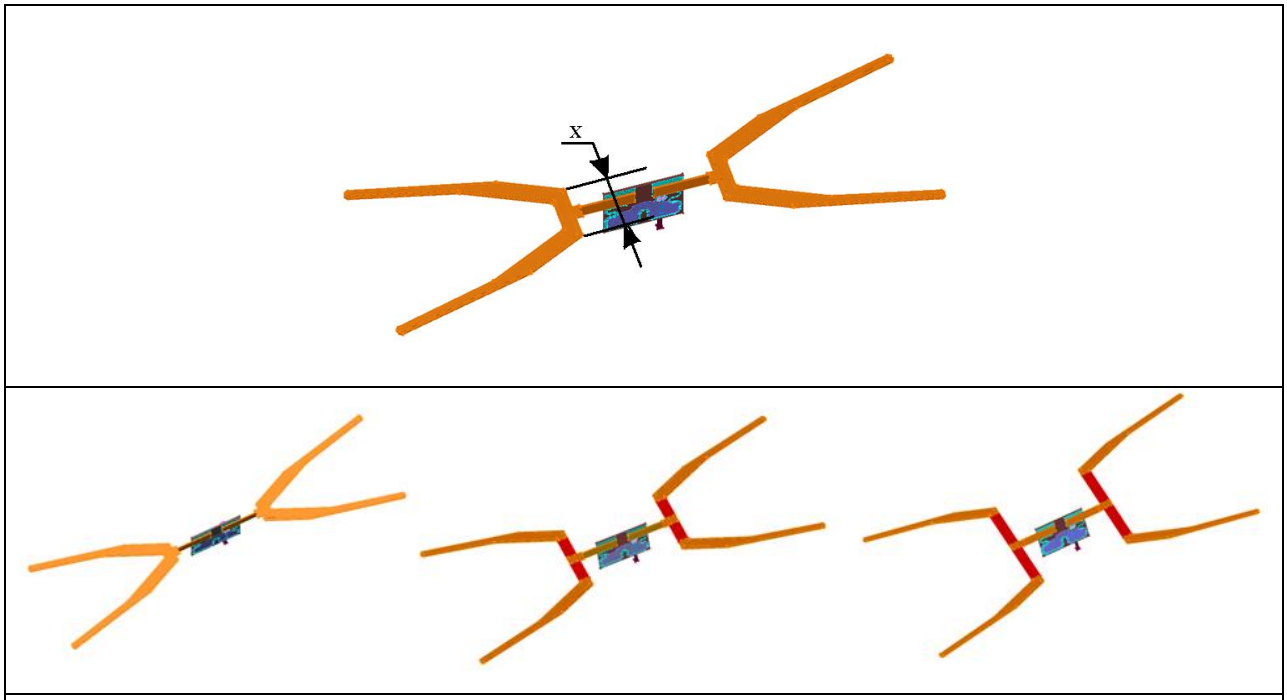

Figure 3.24 Changing the YUA system dipole base length from *x-2cm* to *x+14cm*

The return loss values for changed V-shape dipole base length vary (Figure 3.25). The thick brown line represents the *x-2* base length and has the bandwidth of 81% at 10dB return loss. At *x-12* base length the YUA system has the bandwidth of

67.6%. The second (highest) resonant of the YUA system becomes mismatched and the broadband operation disappears when the base length dimensions are increased.

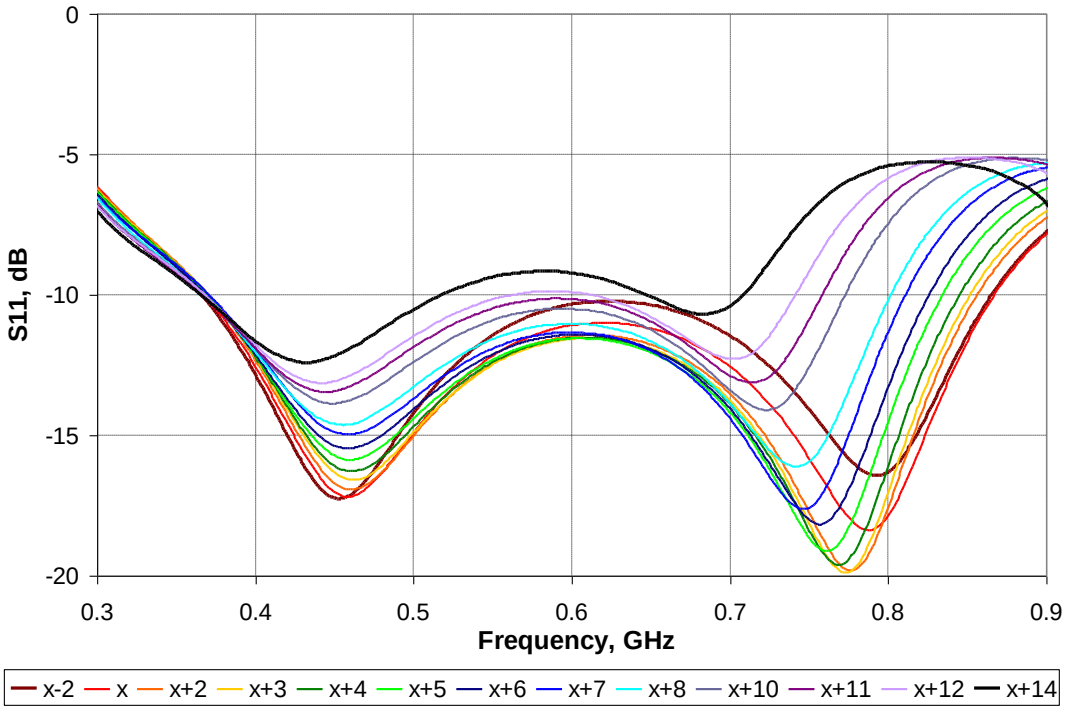

Figure 3.25 Return Loss over frequency changing YUA base length from x-2cm to x+14cm

To analyse the YUA system performance the E-plane and the H-plane co-polar radiation patterns for changed V-shape dipole arm base length were simulated. The results are shown in Figure 3.26 and Figure 3.27.

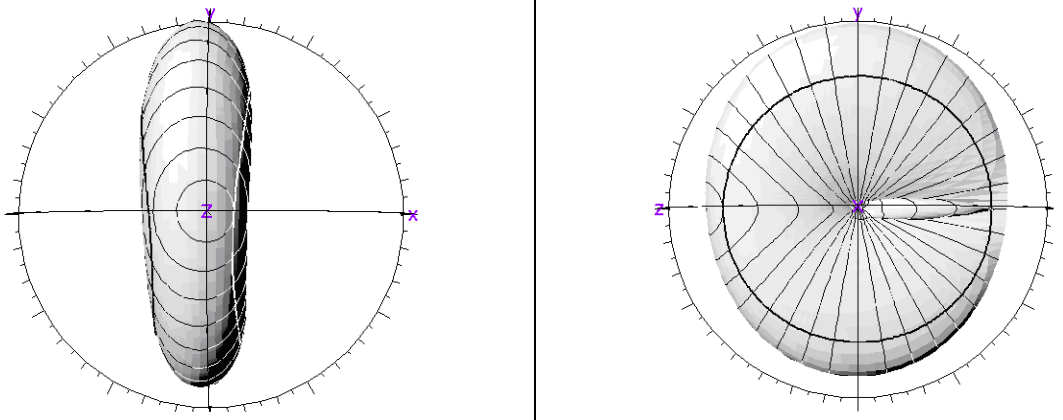

Base length x-2cm D= 4.7dBi

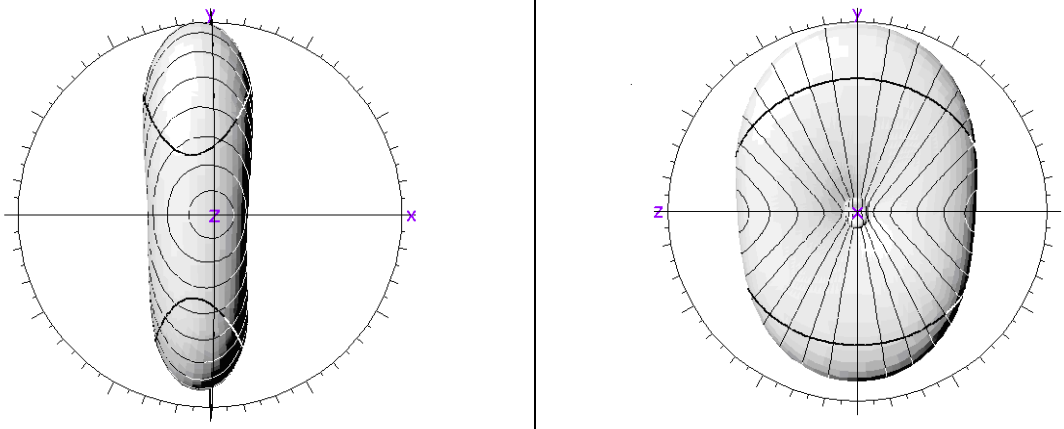

Base length x+2cm D= 5.4dBi

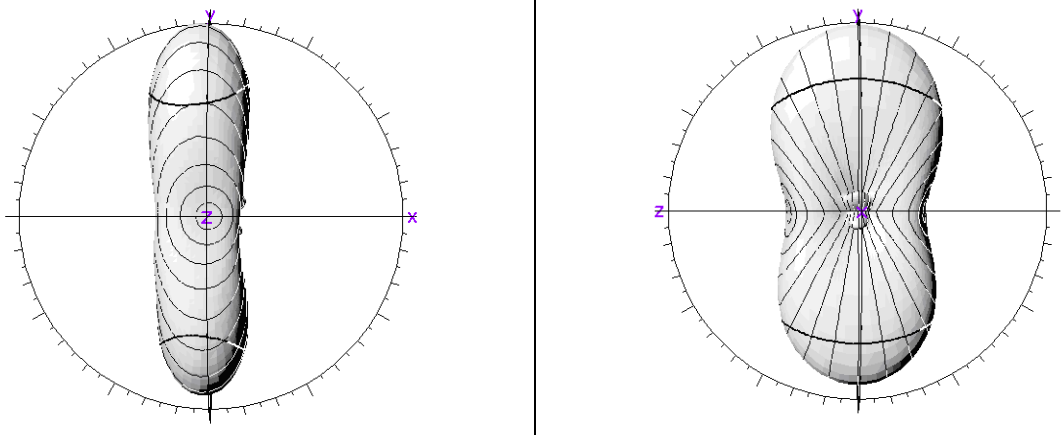

Base length x+6cm D= 6.6dBi

Figure 3.26 The YUA system radiation patterns changing base length from x to x+6cm

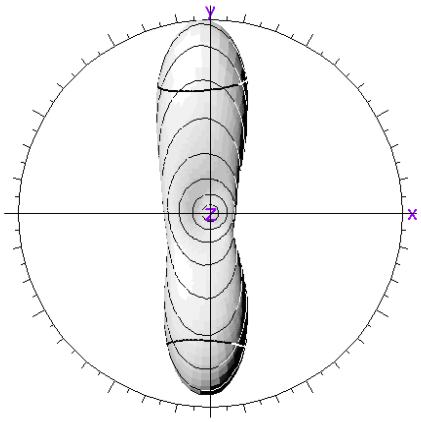
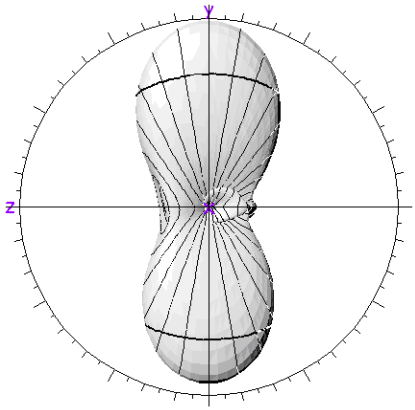

Base length x+8cm D= 7.5dBi

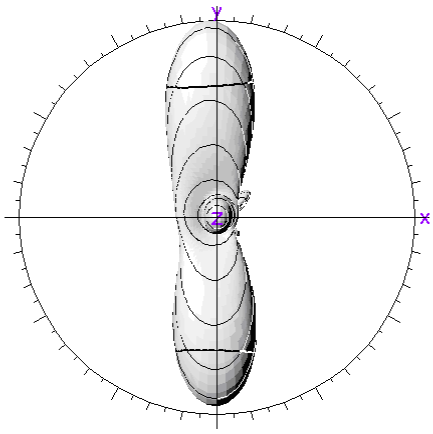
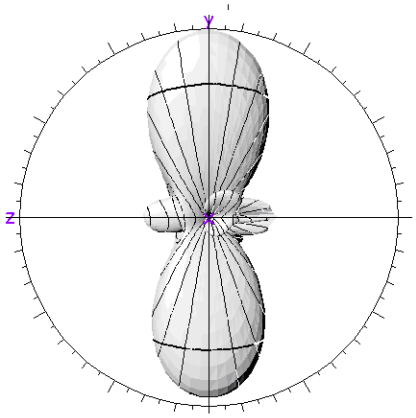

Base length x+10cm D= 8.2dBi

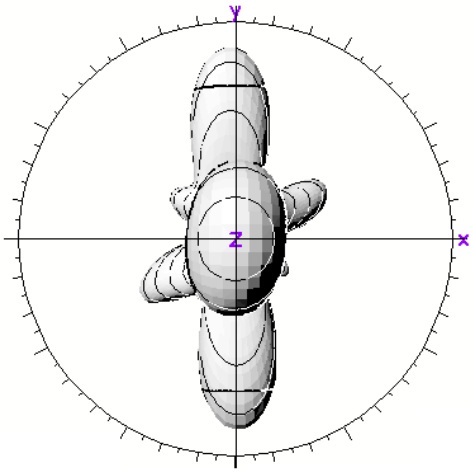
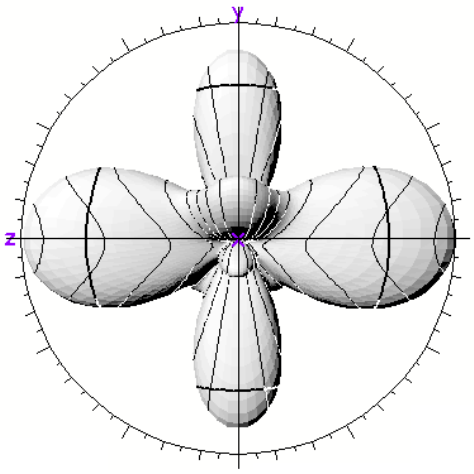

Base length x+14cm D= 7.3dBi

Figure 3.27 The YUA system radiation patterns changing base length from x+8cm to x+14cm

The Half Power Beam Width (HPMW) at five different frequencies is shown in Table 3.2.

x-2cm		x+2cm		x+6cm		x+8cm		x+10cm		x+14cm	
E-plane	**H**-plane	**E**-plane	**H**-plane	**E**-plane	**H**-plane	**E**-plane	**H**-plane	**E**-plane	**H**-plane	**E**-plane	**H**-plane
46°	180°	46°	124°	42°	78°	40°	63°	38°	53°	34°	80°

Table 3.2 The HPBW values changing the dipole base length x

The base length change from *x-2*cm to *x+14*cm results in a 12° directionality increase of the E-plane radiation patterns. The side lobes start to appear from *x+12*cm. This causes deterioration in the antenna performance.

Figure 3.28 shows the directivity values of various YUA system dipole base lengths at two different frequencies, i.e. 500MHz and 800MHz. The directivity increases from 2.8dBi to 3.9dBi throughout all base length variations at the lower frequency. However, at the higher frequency of 800MHz it increases from 4.8dBi with *x-2cm* base length to 8.2dBi with *x+10 cm* base length. The radiation patterns start to acquire unwanted side lobes at *x+11 cm,* which causes the poor antenna performance.

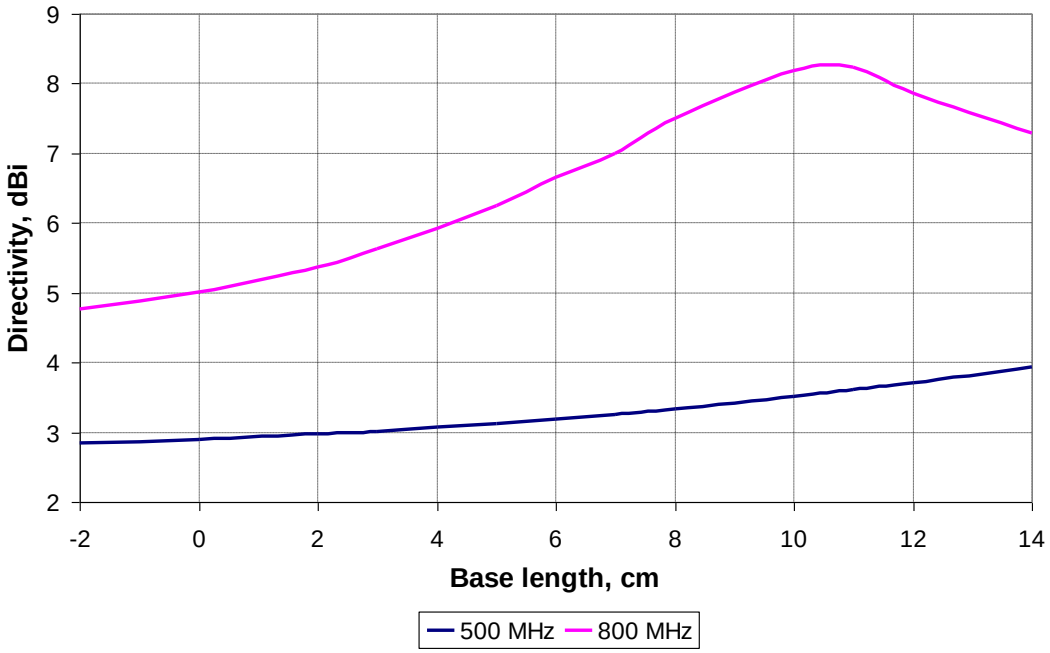

Figure 3.28 Directivity values of the YUA system changing base length

Therefore, the optimal configuration of the YUA system is achieved when the dipole base length is equal to *x+11cm* with the directivity of 3.6dBi at 500MHz and the directivity of 8.23dBi at 800MHz. In this case the achieved bandwidth is 69.3%.

3.4 Conclusions

In this chapter the performance of the YUA system was investigated. The YUA system balun achieved a better match over the desired UHF frequency band than the VSDA system balun, analysed in Chapter 2. The YUA balun achieved a 10dB return loss from 350MHz. In comparison, the VSDA balun achieved the same return loss value only at 420MHz. Another advantage of the YUA balun is its protection from corrosion. The surface currents revealed the broadband balun operation with the phase shift of 180° at various frequencies. Therefore, it was decided to carry out the parametric study in order to improve the bandwidth and the directivity of the YUA system.

The first parametric study stage commenced with the analysis of changing the parasitic element dimensions, placed above the YUA system. The return loss results showed that it is possible to move the second resonant frequency by 100 MHz towards the lower frequency by adding the parasitic element.

Section 3.3.2 described the coupling gap effect on the antenna performance with the parasitic element placed on the top of the antenna. A constant change of the air gap separation distance between the balun and the radiating element added an extra capacitance value, therefore, changing the antenna return loss performances. The first resonant was shifted to the higher band and the second resonant was shifted to the lower frequency band by increasing the separation distance. The achieved optimum air gap separation is 1mm and the YUA system with the parasitic achieved the bandwidth of 64.4% [3].

A 78% bandwidth was achieved during the YUA systems parametric study, when the balun was loaded with a V-shape dipole with an air gap separation of 1.0mm without the parasitic element. The measurements were carried out in order to evaluate the predicted results. A reasonable agreement between the predicted and the measurement results was obtained for the YUA system with and without the parasitic element [3].

Section 3.3.4 described the parametric study done by changing the arm angle of the YUA system. Different arm angles influenced the return loss, the radiation patterns and the directivity values. The achieved optimal YUA system V-shape dipole arm angle is $25°$ with a maximum directivity of 5.1dBi at the higher frequency band [4-6].

Finally, section 3.3.5 described the analysis of the YUA system V-shape dipole base length. It was changed from *x-2cm* to *x+14cm*. The optimised base length was *x+11cm* with directivity value of 8.2dBi. Further increase in the base length revealed large side lobes increase by 37° (in the H-plane). The resulting optimal YUA system without the parasitic element had the following configuration: the air gap separation of 1mm, the dipole arm angle equal to $25°$ and the base length equal to *x+12cm* [4-6].

The overall YUA system is a complex and expensive structure with large dimensions. In order to overcome these problems, the next chapter describes the methodology for innovation of the balanced, broadband and low cost radiating element for UHF antenna system.

3.5 References:

[1] AWR Microwave office website: http://web.awrcorp.com/

[2] EMSight, “User Manual”, Applied Wave Research. Inc., CA, USA.

[3] N. Riauka, A. Chauraya, and J. C. Vardaxoglou, “Compact antenna integrated into flat plate FSS”, IEEE APS 2008, 5-11 July 2008, San Diego, CA, AP-S/URSI 2008.

[4] N. Riauka, A. Chauraya, and J. C. Vardaxoglou, “Wideband Planar Metamaterial Inspired Antenna Analysis and Design”. IEEE International Symposium on Antennas and Propagation - June 2009, North Charleston, South Carolina, USA.

[5] Yiannis (J) Vardaxoglou, R. D. Seager, N. Riauka, A. Chauraya, and P deMaagt, “Metamaterial Based Antennas with Super- and Sub-strates” 3rd European Conference on Antennas and Propagation (EUCAP) - March 2009 in Berlin, Germany.

[6] J.(Yiannis) C. Vardaxoglou, A.Chauraya, R.D.Seager, N.Riauka, G.K.Palikaras and P. deMaagt, “Towards Metasurfaces for Wideband Systems” 39th European Microwave Conference (EuMC)- August 2009, Rome, Italy.

[7] S. Uda, "High angle radiation of short electric waves". Proceedings of the IRE, vol. 15, pp. 377-385, May 1927.

[8] H .Yagi, “Beam transmission of ultra short waves”, Proceedings of the IRE, vol. 16, pp. 715-740, June 1928.

[9] C. A. Balanis, “Antenna Theory Analysis and Design”, 2nd ed., New York: Wiley, 1996.

[10] G. A. Thiele, “Analysis of Yagi- Uda type antennas,” IEEE Trans. Antennas Propagat., vol. AP-17, pp. 24–31, Jan. 1969.

[11] Nagasawa, K., Matsuzuka, I., “Radiation field consideration of biconical horn antenna with different flare angles”, Antennas and Propagation, IEEE Transactions on AP., Volume: 36 Issue: 9, Sept.1988, pp: 1306 -1310.

[12] P. D. P. Smith, “The conical dipole of wide angle,” J. Appl. Phys., vol. 19, Jan. 1948.

[13] CST’s MicroStripes website: http:// www.cst.com/ Content/Products/ MST/ Overview.aspx

[14] MicroStripes Reference Manual, Release 5.5, issue 2, copyright 1994-2000 Kimberley Communications Limited, Electromagnetic Division of Flomerics.

[15] Marconi Instruments RF and Microwave Test Sets 6200A Series Operating Manual, 1 May 1996, UK; Marconi Instruments RF and Microwave Test Sets 6200A Series GPIB Operating Manual, 6 June 1996, UK.

Chapter 4

Printed dipole antenna (PDA)

4.1 Introduction

Previous chapters discussed two types of the UHF antenna systems (the VSDA system and the YUA system) in detail. The parametric study was carried out to optimise the YUA system (Chapter 3). The aim of this chapter is to describe the methodology for the innovation of the balanced, broadband and low cost radiating element for the UHF antenna system. The printed dipole antenna (PDA) was chosen as a primary radiating element.

Printed microstrip antennas have been commonly used for decades. Their popularity can be explained by their low profile, the low cost of fabrication and the light weight, as well as their compatibility with the microwave integrated circuit. In most cases

these advantages compensate for their main electrical disadvantages such as the poor polarization purity, the narrow bandwidth, and the limited power handling capabilities. However, these antennas wide application is limited by mentioned disadvantages [1-3].

The printed dipole antenna benefits from the capability to achieve a larger bandwidth, using a set of parasitic elements. It also occupies less space in the substrate compared to the conventional patch antenna [1-3]. The balun is integrated into the antenna structure, which would be a way to improve the antenna cost rather than having a separate PCB balun box as in convention antennas. The input connector, the balun and the radiating element is a single structure and serves as a support for the antenna. Also, it simply can be mounted and fixed to the other bodies by using the input connector.

This chapter is organised in the following way: section 4.2 commences with the theoretical explanation of the general PDA design, where the main PDA parts are described and analysed.

Section 4.3 describes the methodology of the parametric study carried out to improve the PDA performances. Various types of different PDA structures were suggested and analysed.

Finally, the PDA prototypes were manufactured, coated and prepared for the outside measurements. The comparison of the predicted and measured return loss values is shown in section 4.4. Achieved results and conclusions are discussed in final section 4.5.

4.2 Printed dipole antenna structure

The general PDA structure is shown in Figure 4.1. The main parts are: the tapered balun (A), the parallel strip transmission line, matching section (B) and the driven element (C). The top layer is highlighted in cyan and the bottom layer is shown in blue colour.

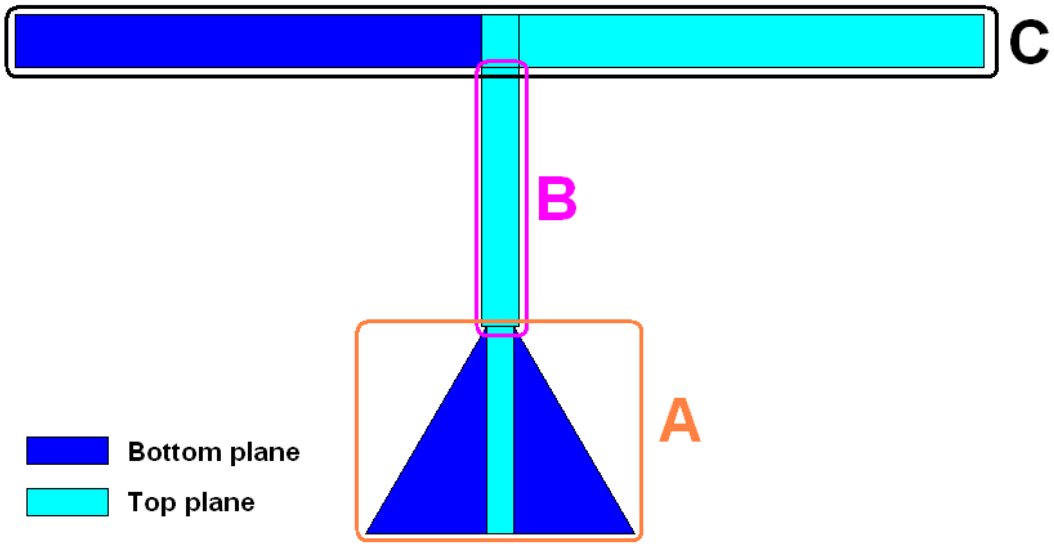

Figure 4.1 General PDA structure

The balun is created by using the microstrip line transformation to the parallel strip line as the balancing transition. The main equation for the characteristic impedance (Z_m) of the microstripe line and of the parallel strip line are shown in Appendix B.

The tapered baluns are frequently used as the balanced transmission line to feed various printed antennas [5, 6] or in microwaves mixers [7, 8]. The concept of using tapered balun was introduced by Duncan and Minerva in 1959 [8]. They used baluns to

excite the wide band balanced aerials. The balun was designed as the impedance transformer from the unbalanced to balanced line, relied on a gradual change of the cross section of the transmission line.

Three wideband transitions (step tapered, linearly tapered and circularly tapered) between the microstrip line and the strip line are shown in Figure 4.2 [9-12].

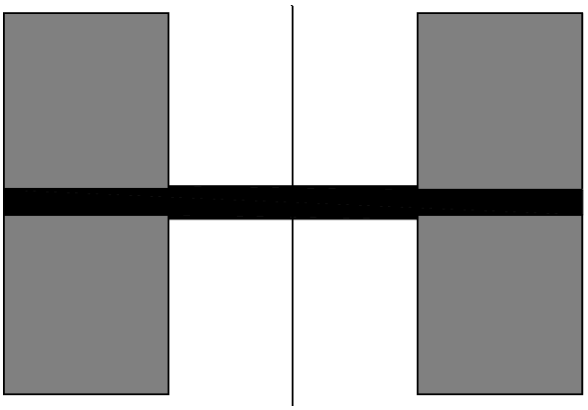

a) Step tapered transmission

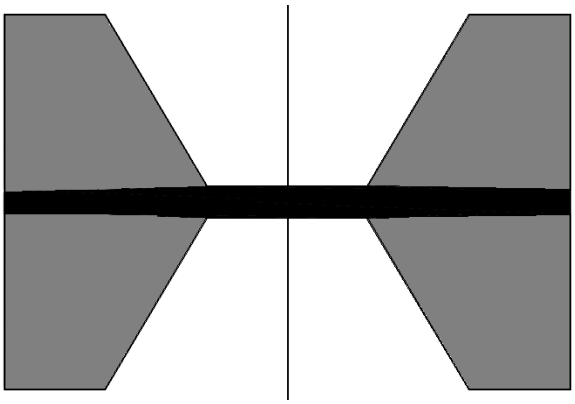

b) Linearly tapered transmission

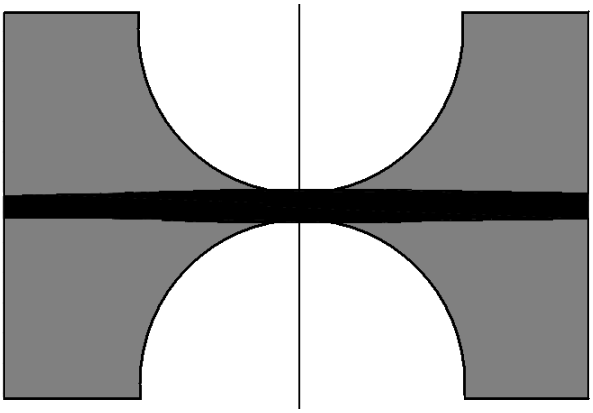

c) Circularly tapered transmission

Figure 4.2 Configuration of the back to back transition from microstrip to parallel strip line

A good transition should have a smooth electromagnetic field transition and broadband impedance matching. The EM field distribution of the microstripe line and of the parallel strip line is shown in Appendix C.

S-parameters of three configurations of the back to back transition from the microstrip to the parallel strip line differences are mainly due to the small discontinuities of the electromagnetic fields at the transitions. They are determined by the tapered surface strip smoothness. Circularly and linearly tapered transitions, used to perform a wide band operation, are reported in [9, 11].

The driven element is $\lambda_0 / 2$ dipole. Its radiation resistance is equal to $73\,\Omega$. In printed dipole antennas the increase in the width of the printed arms is identical to the increase in the radius of an equivalent wire dipole. This is a well known technique for the bandwidth widening of wire dipoles. However, the radiation efficiency might decrease by applying this technique [14, 15].

4.3 Printed dipole antenna simulations

This section describes the steps of innovating the PDA for the UHF. Previous analytic calculations were used as a starting point. In order to improve the return loss, the operating frequency band and to achieve the higher directivity, the parametric study was carried out and the results are presented in the following sections. The methodology included:

- Printed dipole antenna design
- Printed dipole antenna with extended feeding line
- Printed dipole antenna with stretched balun
- Printed dipole antenna with parasitic element (PDAwP)
- Optimised printed dipole antenna with parasitic element (OPDAwP)

4.3.1 Printed dipole antenna design

The printed dipole antenna was designed in a 3D simulation software tool CST MicroStripes [13]. The first PDA design is shown in Figure 4.3. All dimensions are represented in millimetres. The top view is shown in the A) part and the bottom view is represented in the B) part. As it was described in previous section 4.2, the PDA consists of the following components: the broadband balun, the parallel strip line and the radiating element.

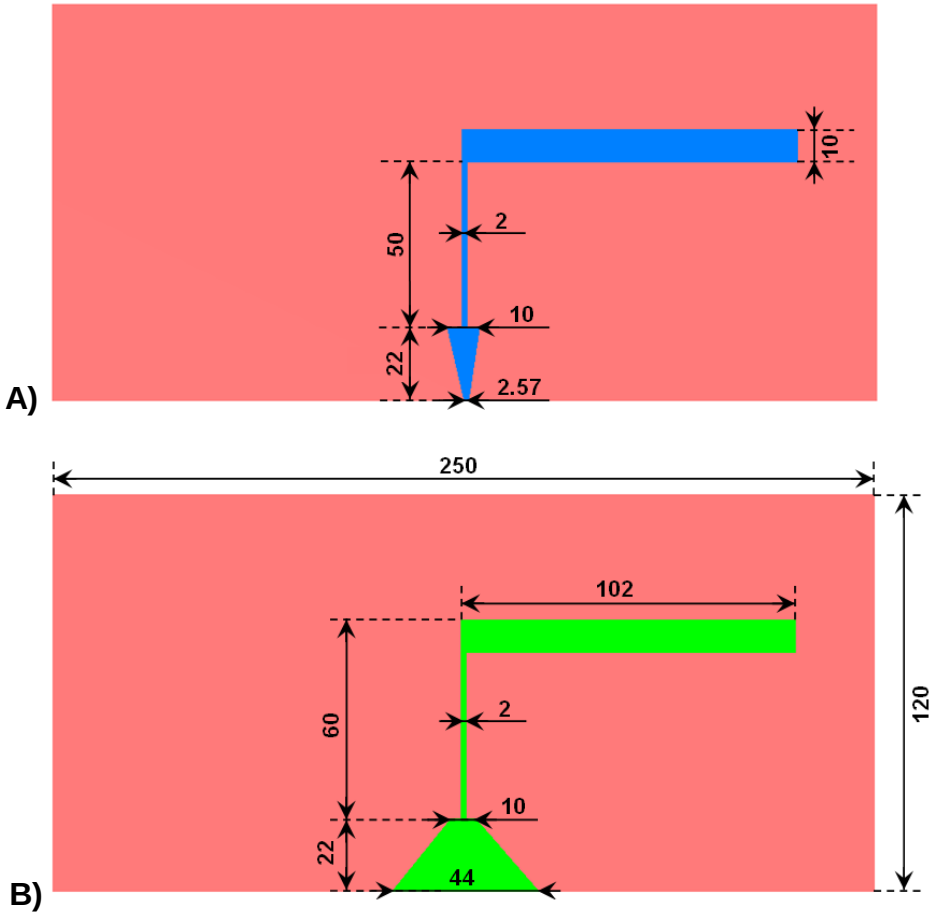

Figure 4.3 Structure of the PDA : A) top view; B) bottom view (all dimensions in mm)

The overall antenna dimensions are 120mm x 250mm. The substrate, chosen for these simulations, is FR4 with a permittivity of 4.9 and a thickness of 1.52mm. The simulated return loss results are shown in Figure 4.4. The PDA was exited using the strip line which connects the balun top and the bottom via wire. The PDA input was designed to match $50\,\Omega$. However, represented results are normalised to $75\,\Omega$.

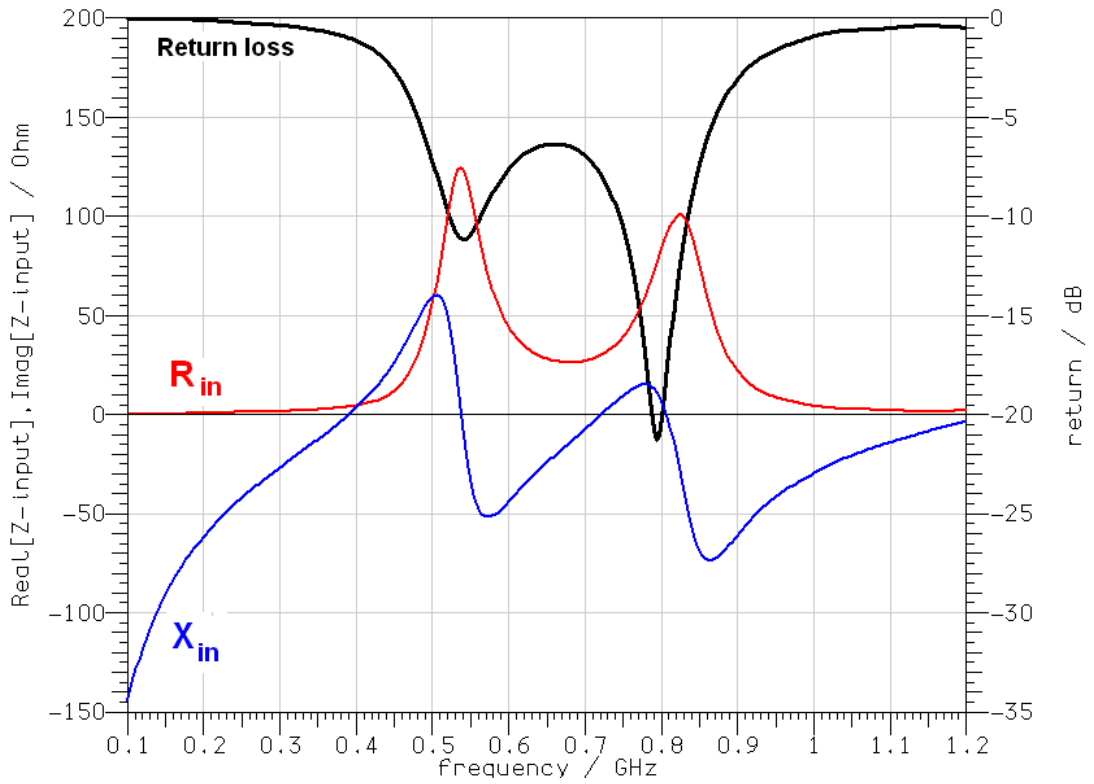

Figure 4.4 Simulated results of the PDA

The real and the imaginary parts of the input impedance are represented in R_{in} and X_{in} respectively. The PDA structure contains two resonances; the first match (resonant) is at 550MHz -11dB (return loss) and the second appears at 790MHz -21dB (return loss).

The surface current distribution plots are produced for five different frequencies (i.e. 470MHz, 550MHz, 650MHz, 750MHz and 850MHz). The balun balancing phenomena can be proved by two criteria. Firstly, the surface current distribution must have the same value at symmetrical points of the input to the radiating element. Secondly, the direction of the surface current distribution at these points must be opposite. The surface current distribution at each frequency (470MHz, 550MHz etc.) is shown for two phases: when the surface current distribution is maximum and when it is equal or close to zero. These plots are shown in Figure 4.5.

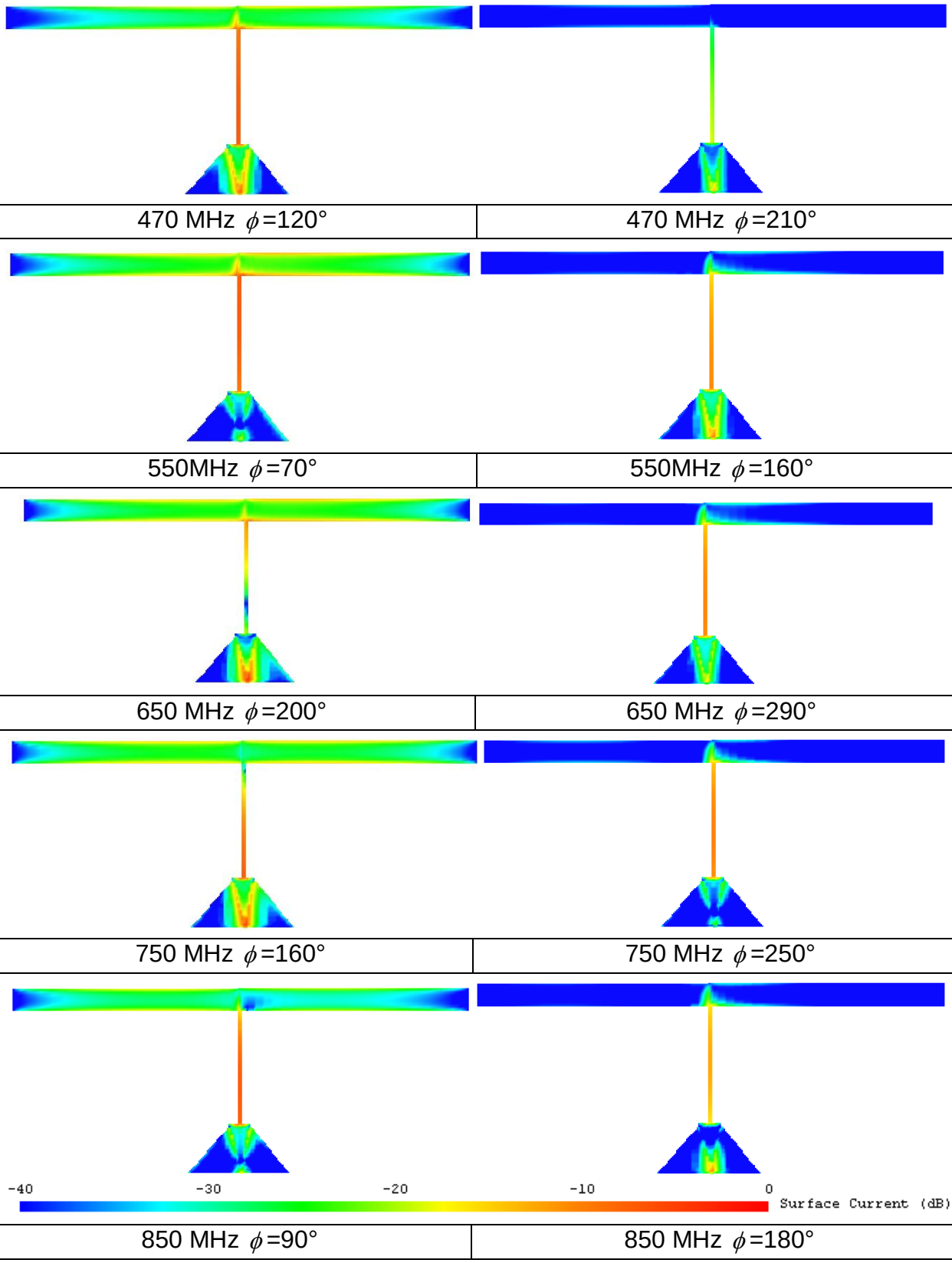

470 MHz ϕ=120°	470 MHz ϕ=210°
550MHz ϕ=70°	550MHz ϕ=160°
650 MHz ϕ=200°	650 MHz ϕ=290°
750 MHz ϕ=160°	750 MHz ϕ=250°
850 MHz ϕ=90°	850 MHz ϕ=180°

Figure 4.5 Surface currents distribution of the PDA

The direction of the surface currents distribution is plotted at 650MHz and shown in Figure 4.6. It is opposite at the symmetrical places of the balun output.

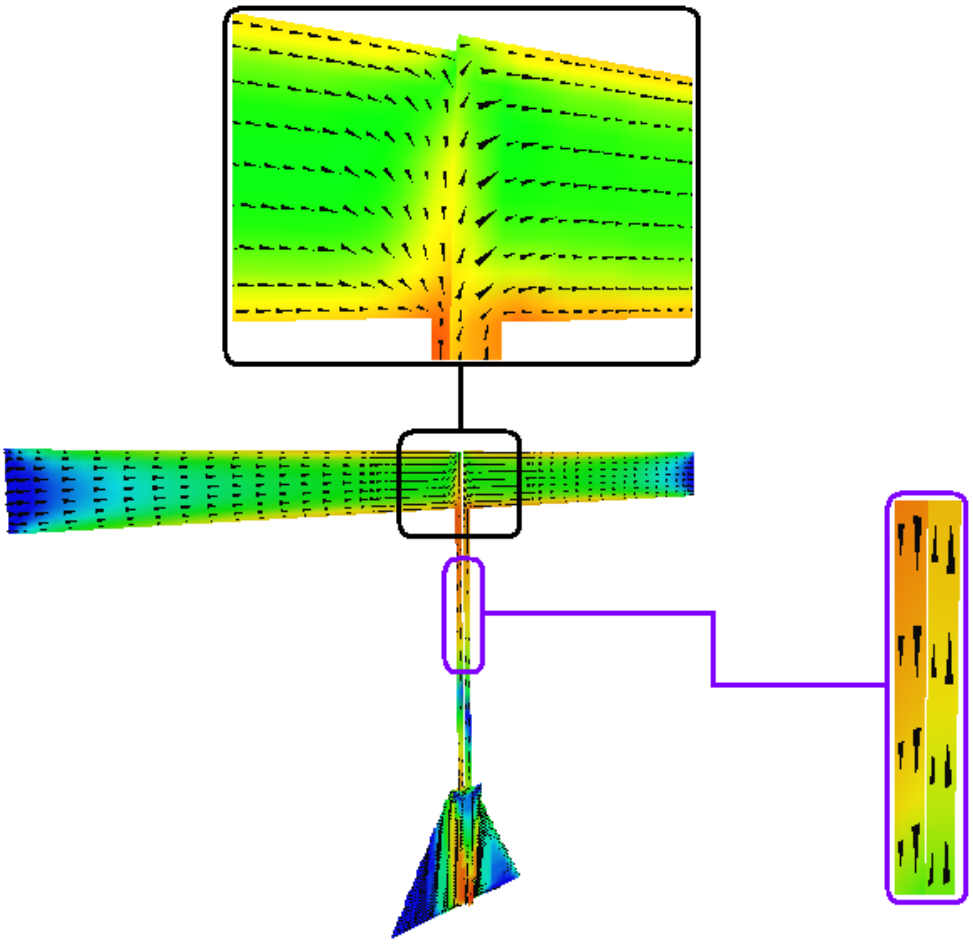

Figure 4.6 PDA balun surface currents directions at 650MHz ϕ=20°

Illustrations (Figure 4.5) indicate that the broadband balun is working from 470MHz to 750MHz. The visible surface currents mismatch appears at 850MHz (the surface current values are not identical for the left and the right sides of the radiating element).

The PDA radiation patterns were simulated. The E, H - planes co-polar and x-polar radiation patterns are shown in Figure 4.7. The E-plane co-polar radiation patterns have the shape of figure eight through all frequencies and the H-plane co-polar radiation patterns are omnidirectional. The x-polar radiation pattern peak is small (from -17dB to -40dB) at all five frequencies. These radiation patterns are identical to the $\lambda_o / 2$ wire dipole patterns [14]. However, previously shown broadband balun surface currents mismatch at 850MHz also appears on the radiation pattern. It should be noted that the E-plane co-polar radiation pattern at 850MHz is not symmetrical (Figure 4.7).

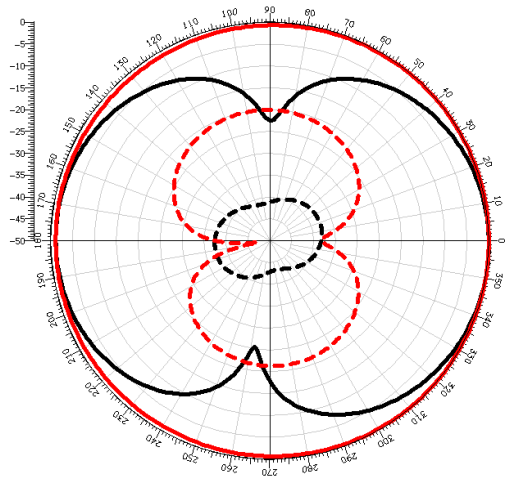

470MHz

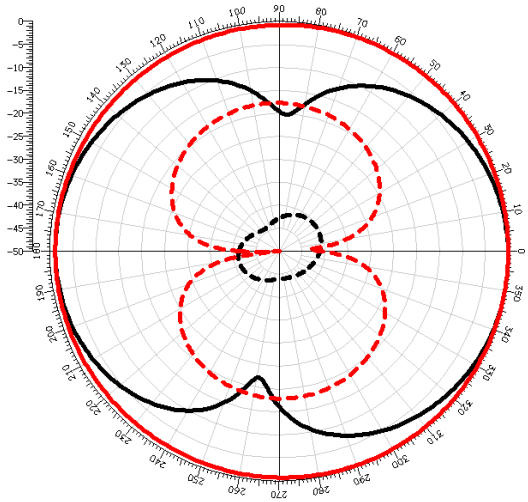

550 MHz

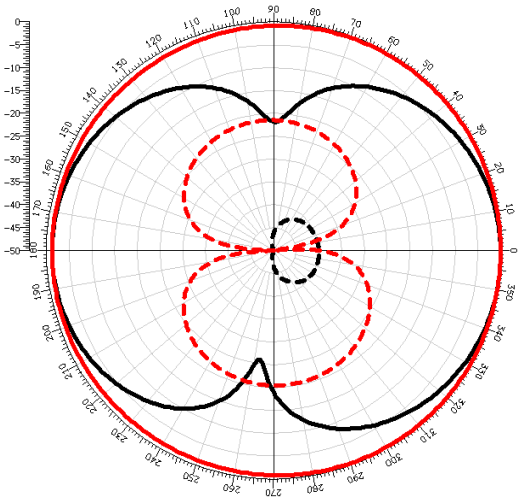

650 MHz

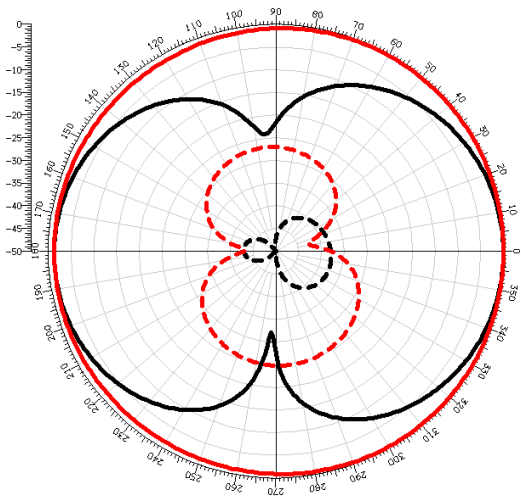

750 MHz

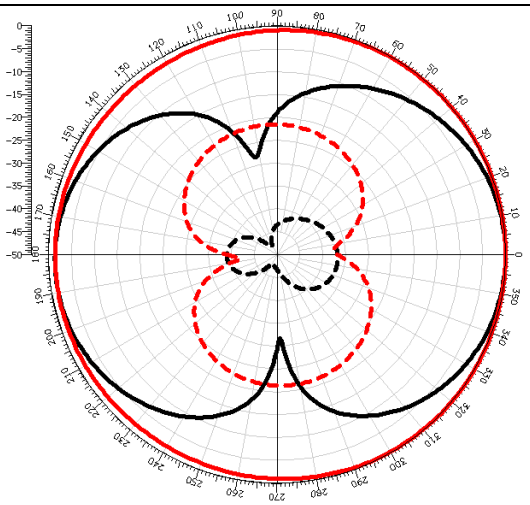

850 MHz

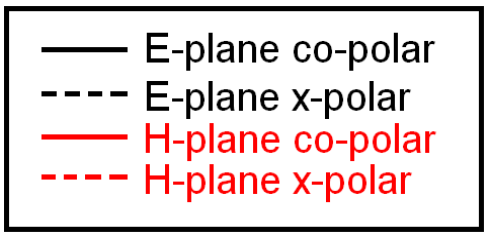

Figure 4.7 PDA E,H-plane co-polar and x-polar radiation patterns

4.3.2 Printed dipole antenna with extended feeding line

In a previously created PDA structure (section 4.3.1) the distance from the input of the antenna to the centre of the radiating element was 77mm. In order to simplify the structure of the PDA placed over the ground plane, the distance from the input to the radiating element should be close to $\lambda_o / 4$. The microstrip line with the length of 38mm and the input impendence of 75Ω was connected to the input of the PDA. The structure of such PDA configuration is shown in Figure 4.8.

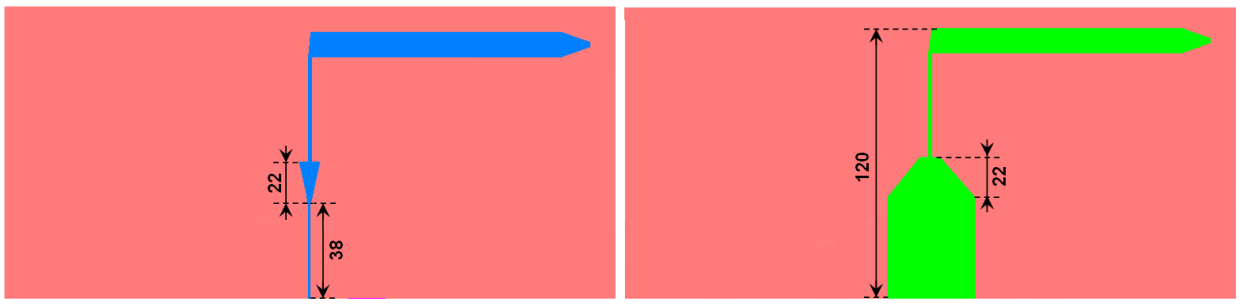

Figure 4.8 Structure of the PDA with extended feeding line

The predicted return loss results along with the real and the imaginary parts of the input impedance are shown in Figure 4.9. The PDA return loss results contain two resonances: the first is -28dB at 542 MHz and the second is -11dB at 900MHz. The simulated radiation patterns of the E - plane and the H - plane remain similar to the ones analysed in section 4.3.1 (the E-plane co-polar radiation patterns have the shape of figure eight and the H-plane co-polar radiation patterns are omnidirectional).

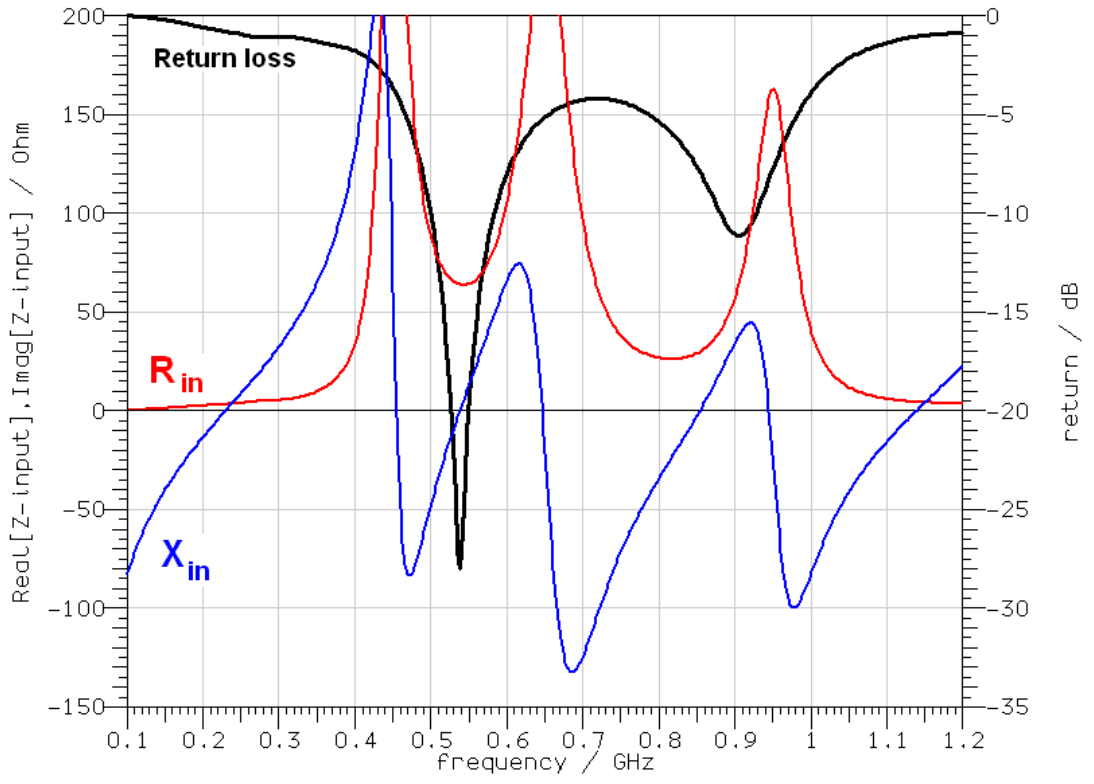

Figure 4.9 Return loss results of the PDA with extended feeding line

4.3.3 Printed dipole antenna with stretched balun

In order to improve the PDA bandwidth, the parametric study was carried out through numerous simulations. Figure 4.10 illustrates the top and the bottom views of the structure with amended PDA variables.

The PDA input was designed to match 75Ω impedance. The FR4 overall dimensions are 275mm x 160mm. The PDA dipole length is 220mm. It was designed to resonate at 681MHz in a free space and at 550MHz in the FR4 substrate.

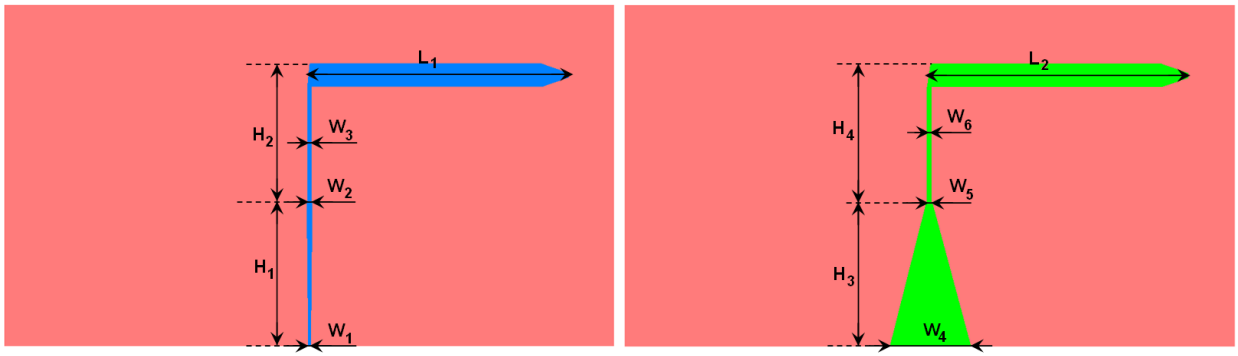

Figure 4.10 Structure of the PDA with stretched balun

The optimum dimensions of the amended variables are represented in Table 4.1. The change of the variable W_1 adjusts the characteristic impedance of the input to the antenna, which should be matched to the $75\,\Omega$. However, the W_4 is equal to 35mm and is wide enough to act as the microstripe infinite ground. The width at the tapered balun ends is equal to 2.5mm. The parallel strip lines (W_3,W_6) have identical dimensions and are equal to 2.1mm.

Variables	W_1	W_2	W_3	W_4	W_5	W_6	H_1	H_2	H_3	H_4	L_1	L_2
Value, mm	1.2	2.5	2.1	35	2.5	2.1	62	48	62	48	112	112

Table 4.1 The dimensions of the PDA with stretched balun

The predicted results of the PDA with stretched balun are shown in Figure 4.11. The predicted results contain the return loss, the real and the imaginary parts of the input impedance and impedance characteristic of the excited port. Figure 4.11 shows the case when at the 550 MHz frequency the imaginary part goes through zero and the

real part is close to the 75Ω, causing the resonant to occur. The closer these values are to the theoretical ones the smaller the return loss is.

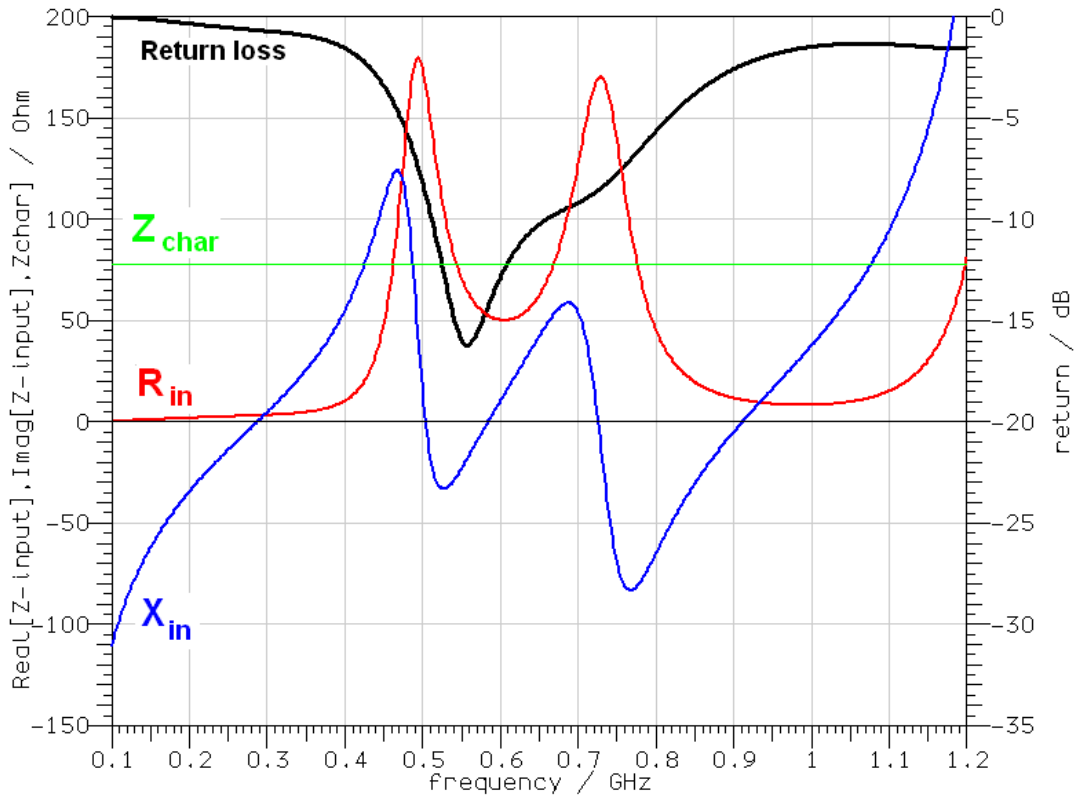

Figure 4.11 Simulated results of the PDA with stretched balun

The calculated bandwidth is 26% at 10dB of return loss. The predicted surface current distribution at various frequencies is shown in Figure 4.12. It is clearly noticeable that the broadband balun is balanced at 470MHz, 650MHz and 850MHz frequency points. The inset picture shows that the surface currents are the same magnitude (same colour) at the same phase and in the same place.

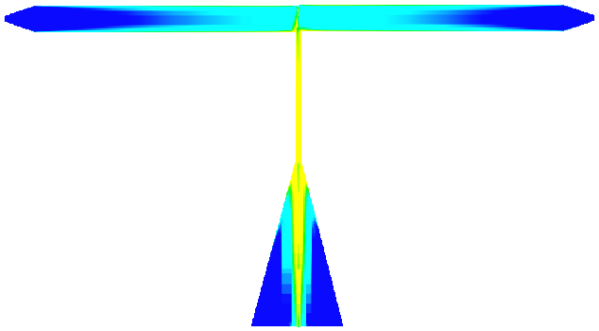

470 MHz

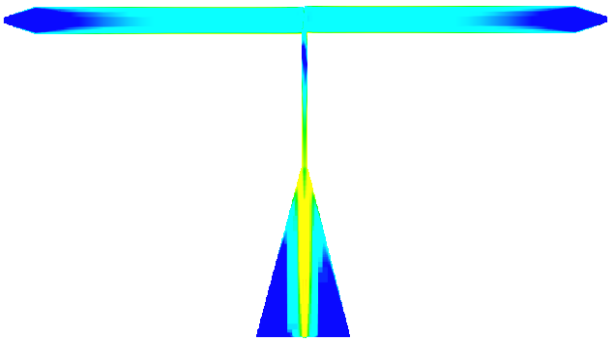

850 MHz

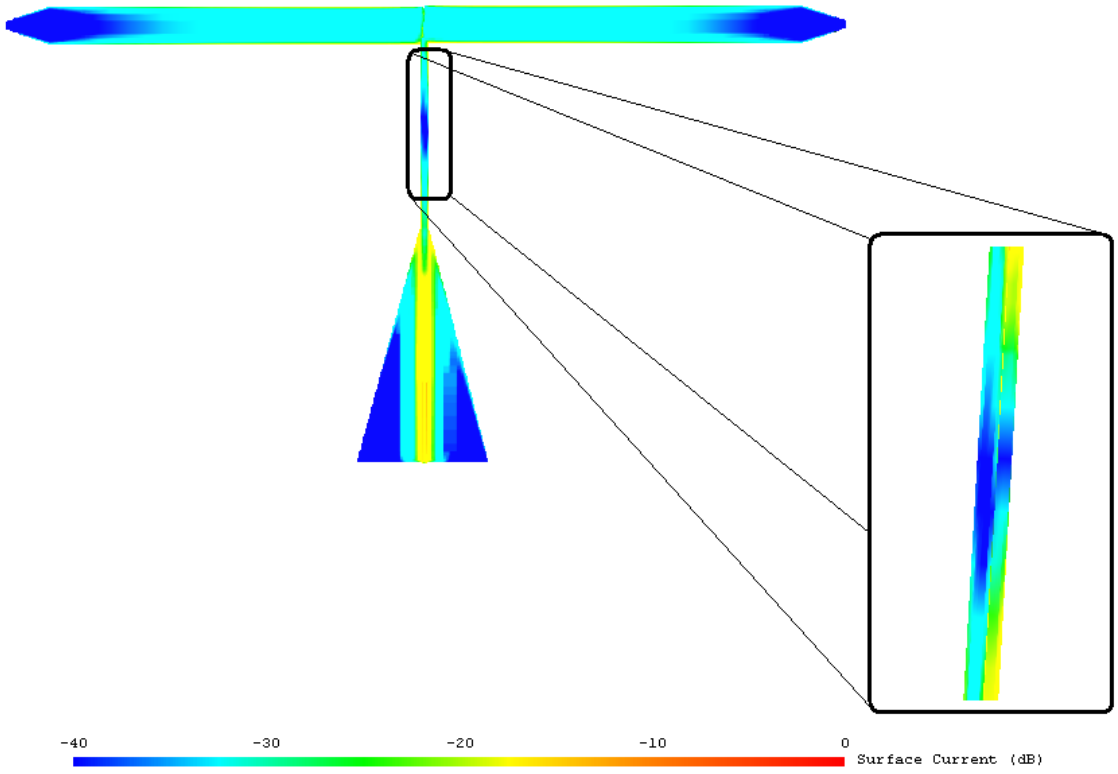

650 MHz

Figure 4.12 Printed dipole antenna surface currents at different frequencies

To evaluate the PDA radiation properties E-plane and H-plane co-polar and x-polar radiation patterns were simulated. They are shown in Figure 4.13. As it was expected, the radiation performances are identical to the ideal wire dipole in a free space. The PDA maintains relatively consistent radiation patterns over frequency (470MHz - 850MHz). The directivity at 470MHz is equal to 2.238dBi and at 850MHz is equal to 2.912dBi.

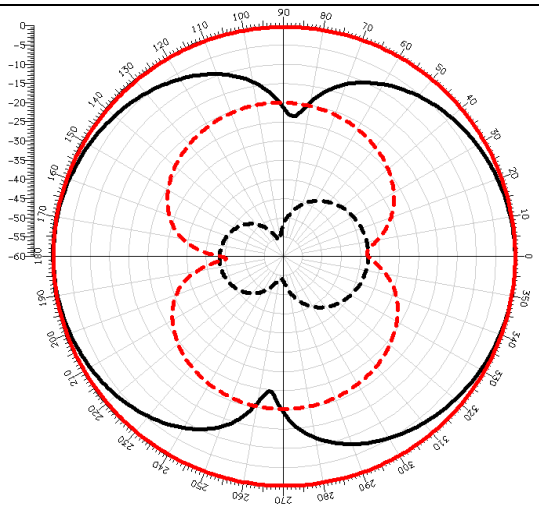

470MHz

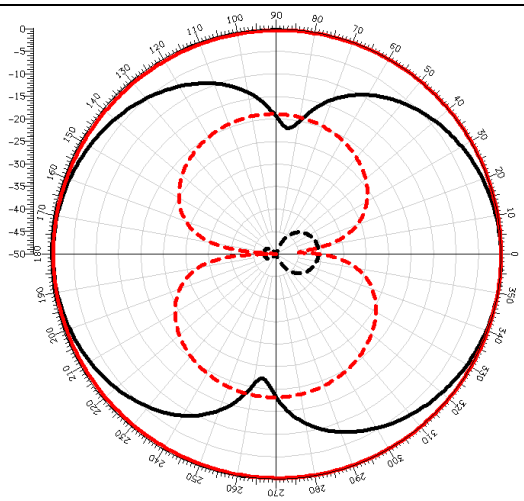

550 MHz

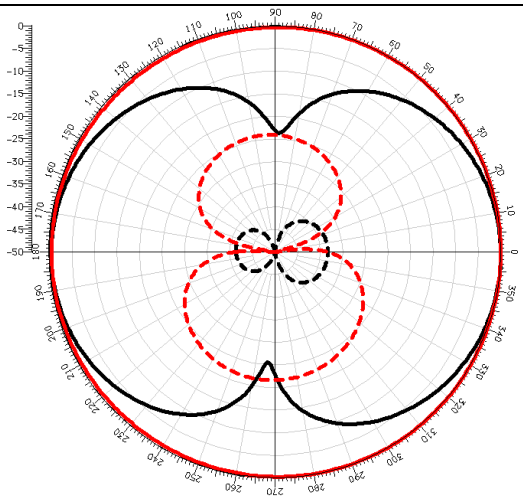

650 MHz

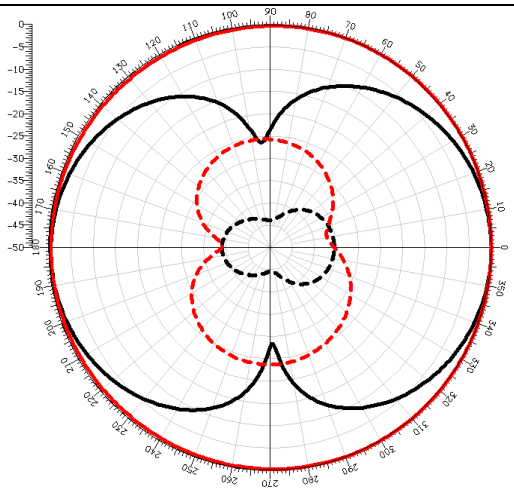

750 MHz

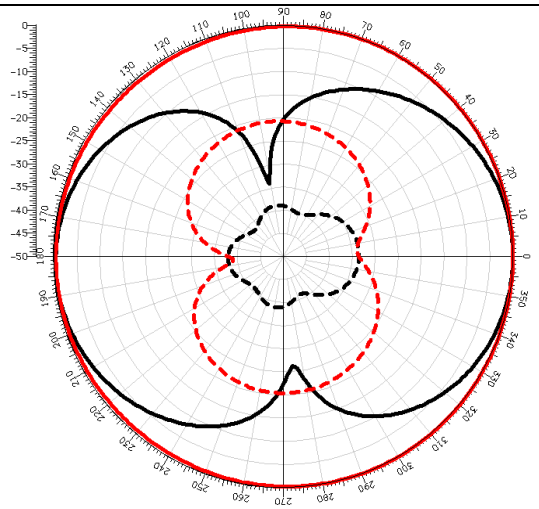

850 MHz

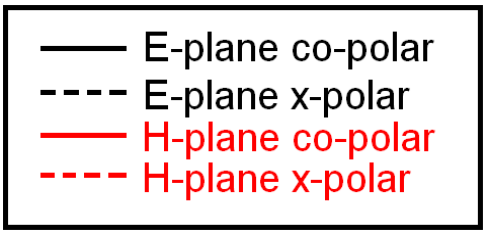

Figure 4.13 Printed Dipole antenna E,H-plane co-polar and x-polar radiation patterns

4.3.4 Printed dipole antenna with parasitic element (PDAwP)

The radiation pattern, the gain and the return loss can be improved by introducing the parasitic element to the antenna structure. The parasitic element can be described as a radiating element not driven by a feed line but coupled to a directly fed radiator [15]. The use of parasitic elements in close proximity to the dipole arms has been proposed by Evtioushkine et al [16]. In this case the bandwidth was boosted from 39% to 56% by introducing the parasitic elements, suspended over a ground plane configuration [17].

In order to improve the PDA with the stretched balun matching performances from 650 MHz to 850 MHz frequency, the parasitic element was introduced. The top and the bottom dimensions of the printed dipole antenna with the parasitic (PDAwP) are shown in Figure 4.14 and Figure 4.15 respectively.

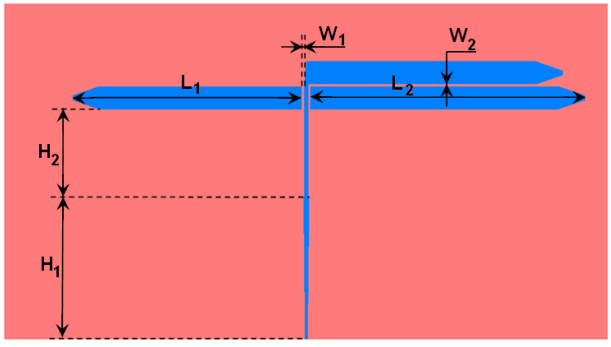

Figure 4.14 Top view of the PDAwP

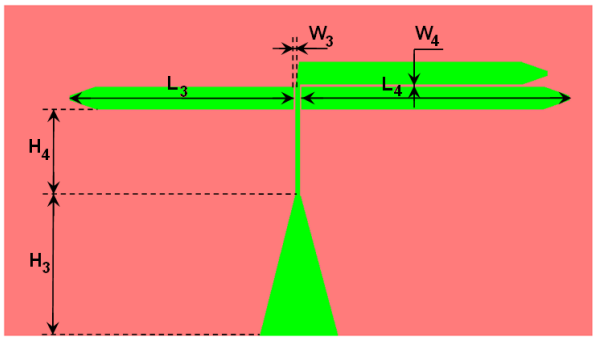

Figure 4.15 Bottom view of the PDAwP

The parasitic element dimensions, placement and separation gaps were chosen by performing a number of experiments with a manufactured prototype and initially with a copper tape. The optimised prototype with a copper tape parasitic element was transformed into the simulations. The more detailed and accurate parametric study was carried out through simulations. The values of the amended variables of the PDAwP are represented in Table 4.2.

Variable	W_1	W_2	W_3	W_4	H_1	H_2	H_3	H_4	L_1	L_2	L_3	L_4
Value, mm	1	1	1	1	42	27	42	27	100	120	100	120

Table 4.2 The dimensions of the PDAwP

The simulated results of the PDAwP are shown in Figure 4.16. The graph contains the return loss results, the real and the imaginary parts of the impedance and the input port impedance characteristic, equal to 75Ω. The PDAwP was matched from 500 MHz to 850MHz. The PDAwP prototype bandwidth has increased twice compared to the original PDA and is equal to 52% at 10dB of return loss. The maximum achieved match is -35dB at 720MHz.

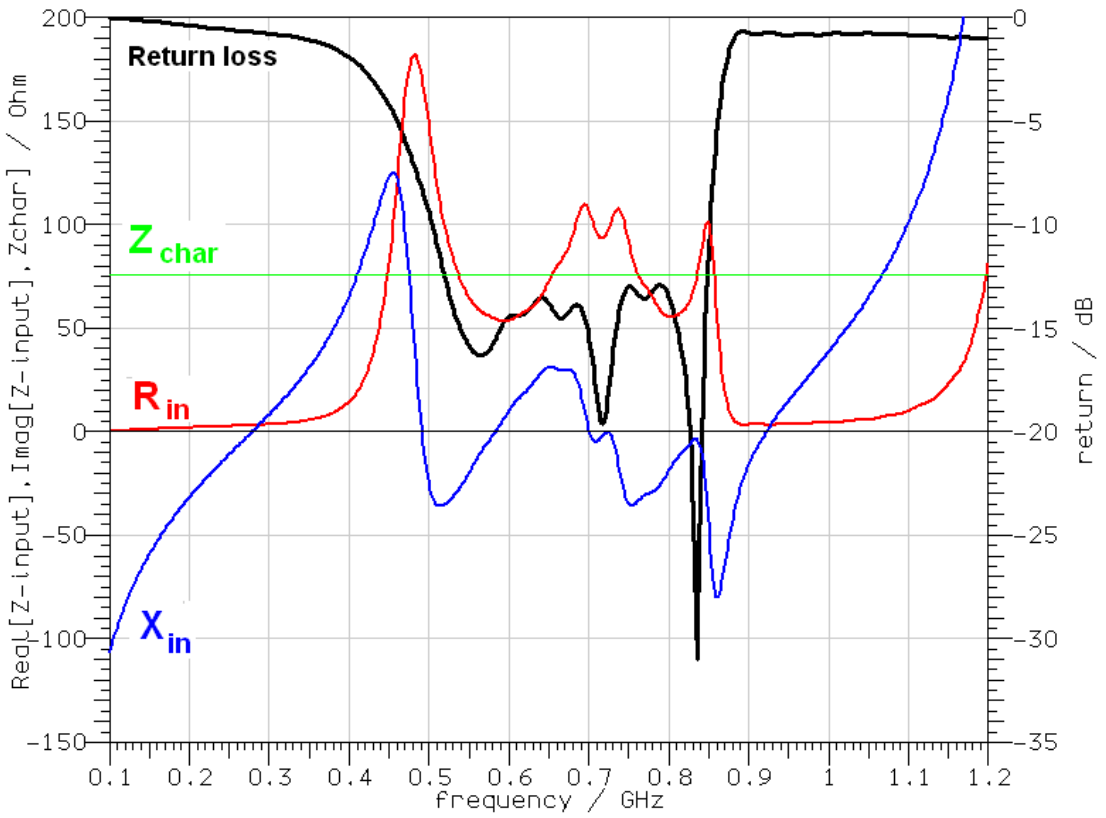

Figure 4.16 Simulated PDA with parasitic element results

The surface currents distribution at two frequencies (i.e. 470MHz and 850MHz) is shown in Figure 4.17. A visible effect of the parasitic element appears at the higher frequency band (i.e. 800-850). The parasitic element is placed very close (i.e. 1mm separation) to a directly fed radiator. The surface currents are coupled to a passive element and it starts to resonate.

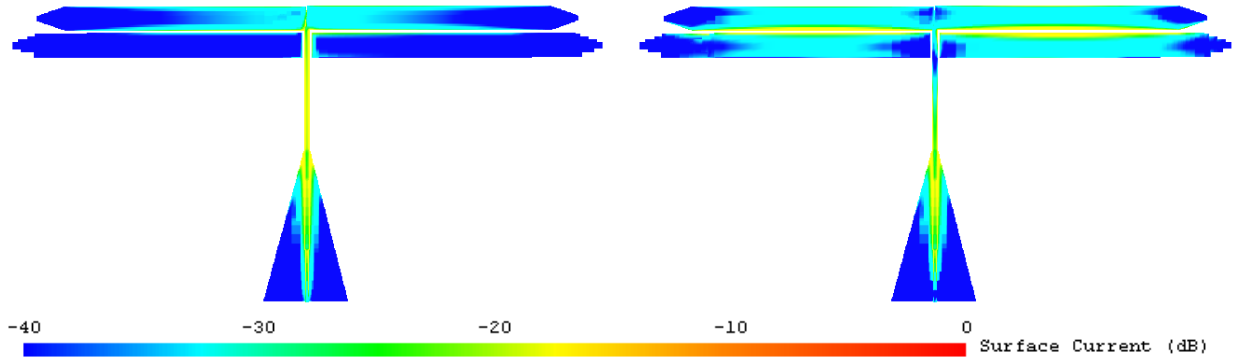

Surface currents at 470MHz	Surface currents at 850MHz

Figure 4.17 PDA simulation results at different frequencies

However, it was discovered that the additional parasitic element in the PDAwP system, has a negative effect on the radiation patterns. This phenomenon appeared in the frequency band from 800MHz to 850HMz (Figure 4.18) in the E-plane and the H-plane co-polar radiation patterns. In this frequency band the *y* axis propagation direction is reflected backwards to the antenna feeding direction. The parasitic element resonates and radiates electromagnetic waves due to the coupling from the directly fed radiating element. The exited radiating element has larger electrical length than the parasitic element. Therefore, the radiation from the passive element is reflected from the exited element.

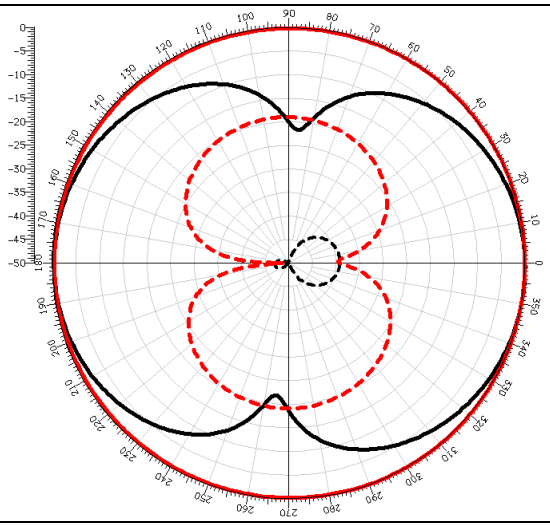

470 MHz

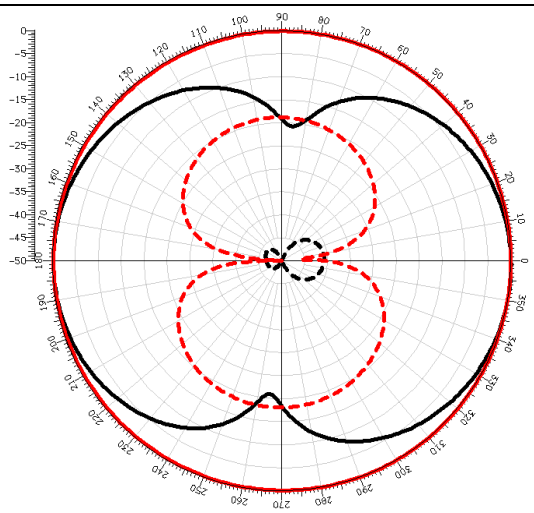

550 MHz

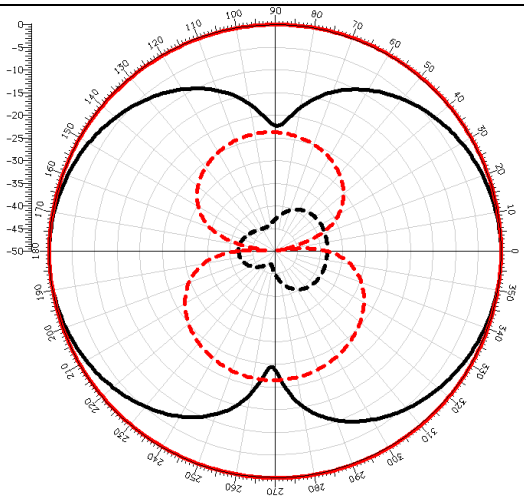

650 MHz

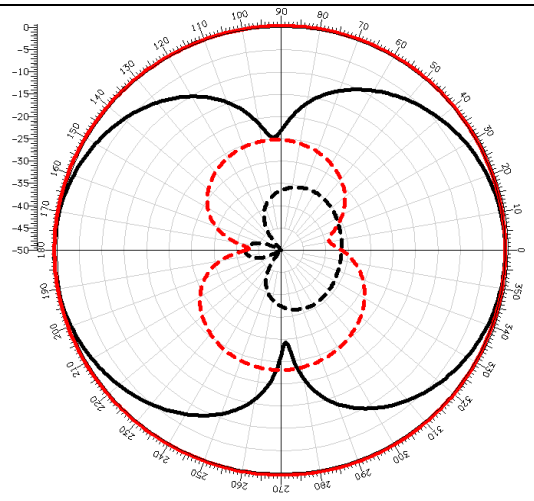

750MHz

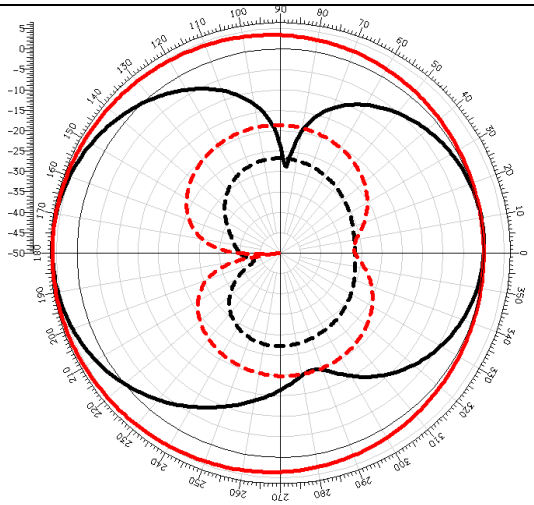

E-plane co-polar at 850MHz

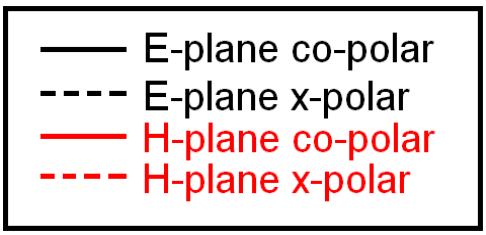

H-plane co-polar at 850MHz

Figure 4.18 Simulated radiation pattern results of the PDAwP

The PDAwP achieves 5.2dBi directivity at the highest frequency point of 850MHz. This value is 3.2dBi higher than the conventional PDA directivity. This is an improvement in comparison to the previous PDA model without a parasitic element (section 4.3.3), even despite the fact that the parasitic element is alternating the direction of the radiation and the radiation patterns at higher frequency of 850MHz.

4.3.5 Optimised printed dipole antenna with parasitic element (OPDAwP)

The optimised version of the PDA prototype was created to eliminate the previously discovered negative phenomenon of the parasitic element. The desired results were achieved by placing the parasitic element on the top of the radiating element with a separation of 1mm from the exited element. The substrate was etched into a more compact shape, without changing the electromagnetic properties of the printed dipole antenna. The structure of the optimised printed dipole antenna with the parasitic (OPDAwP) is shown in Figure 4.19.

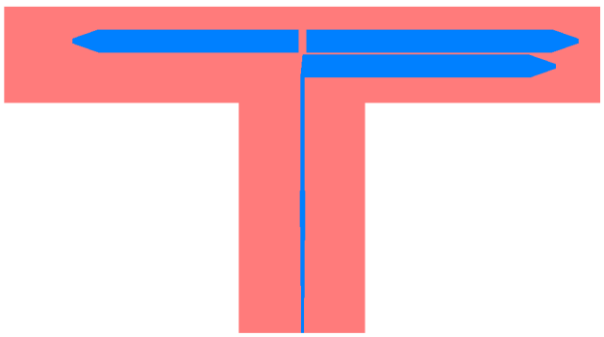

Top view

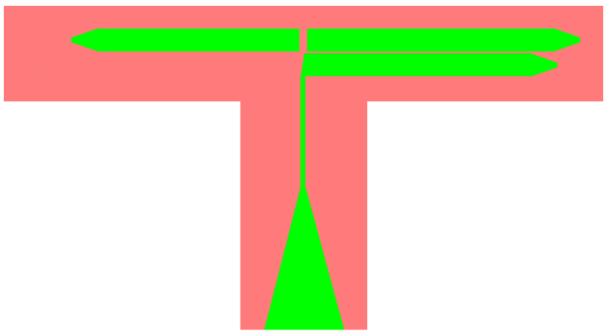

Bottom view

Figure 4.19 Structure of the OPDAwP

This OPDAwP was optimised to work within 470MHz - 850MHz band. The achieved bandwidth is 52.9% which is 0.9% larger than the bandwidth of the PDAwP. The OPDAwP return loss results are shown in Figure 4.20.

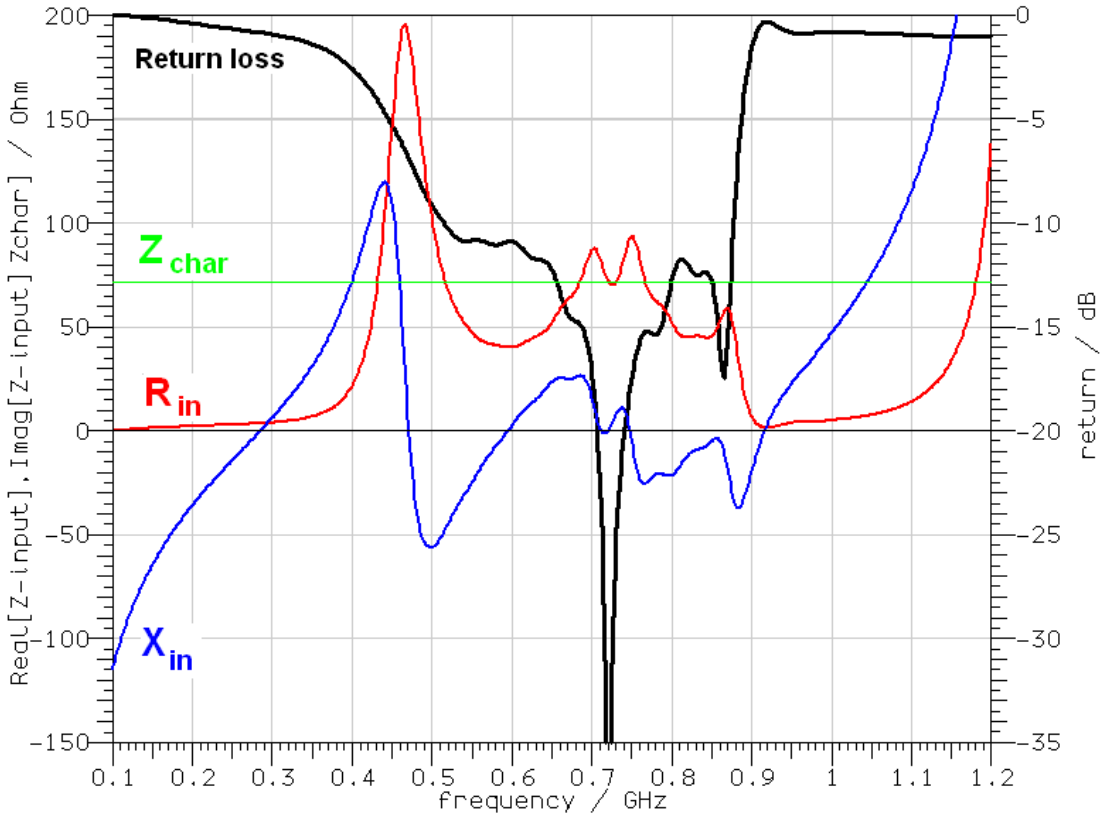

Figure 4.20 Simulated OPDAwP results

The OPDAwP dimensions are shown in millimetres in Figure 4.21. The balun starts with a microstrip line. Its bottom is wide enough to behave as the infinitive ground and the top strip width is 1.2mm. Therefore, the input impedance characteristic is equal to 74.47Ω, see Appendix B eq.13 - eq.20 (when $\varepsilon_r = 4.9$, $W = 1.2mm$, $t = 0.035mm$, $h = 1.52mm$). The gradual microstrip transformation to the parallel strip line finishes with a width of 2.5mm and the impedance is transformed to 66.25Ω. The following impedance transformation is of the parallel strip line. The width was changed to 2.1mm with a 74.58Ω impedance response. However, the impedance of the parallel strip line matches the dipole radiation resistance, which is equal to 73Ω [14].

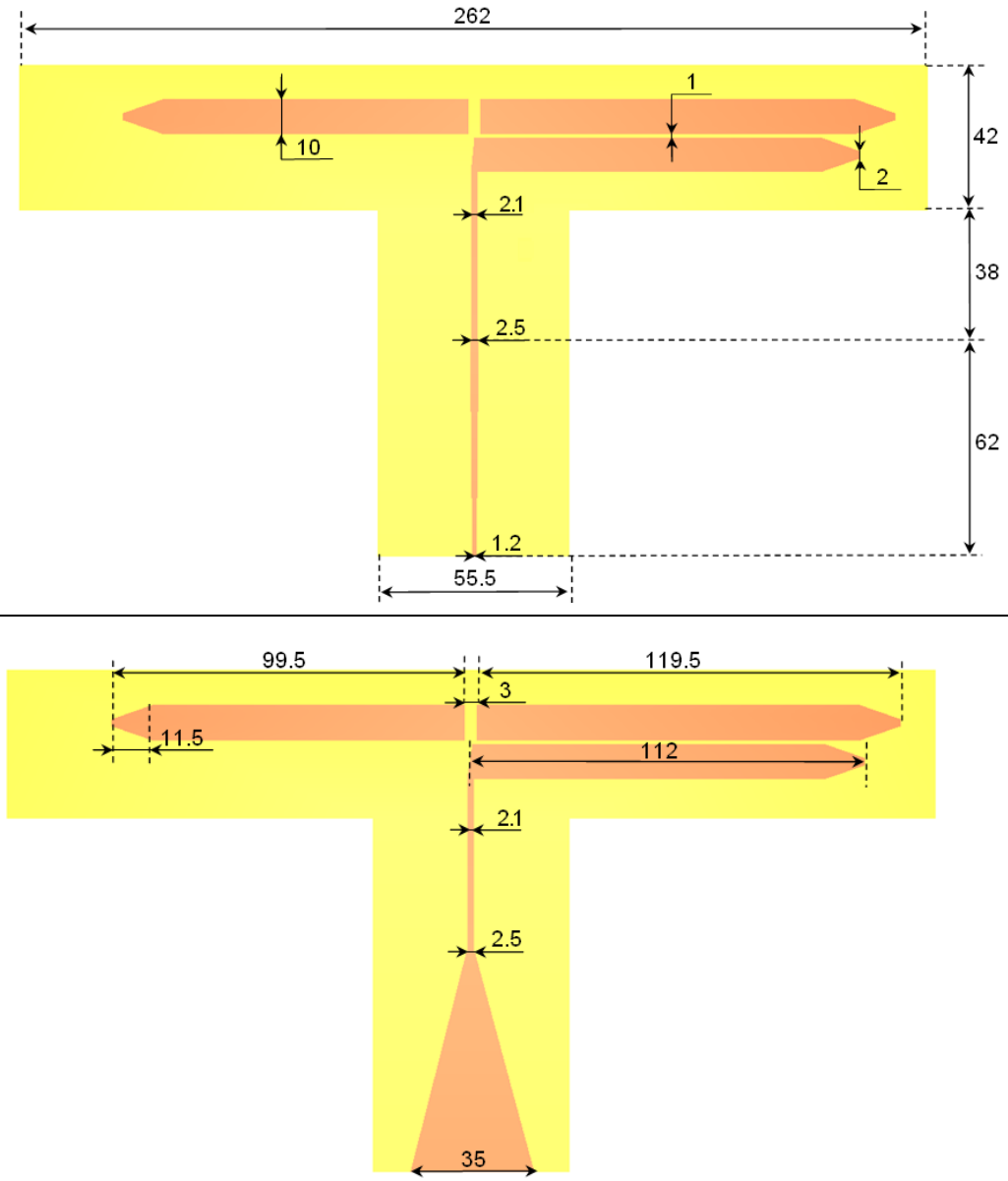

Figure 4.21 Dimensions of the OPDAwP

The OPDAwP substrate dimensions are 262mm x 142mm. The printed dipole antenna volume is equal to $0.262m \cdot 0.142m \cdot 0.0158\text{m} = 0.5 \cdot 10^{-3} m^3$. The gap between the resonating dipole and the parasitic element is equal to 1mm.

To analyse the balun balancing phenomenon, the surface current distribution of the OPDAwP at various frequencies were simulated. The distribution is represented at five different frequencies (i.e. 470MHz, 550MHz, 650MHz, 750MHz and 850MHz). Results for the first two frequencies (i.e. 470MHz and 550MHz) are represented in Figure 4.22. For other frequencies (i.e. 650MHz, 750MHz and 850MHz) the surface current distribution is shown in Figure 4.23.

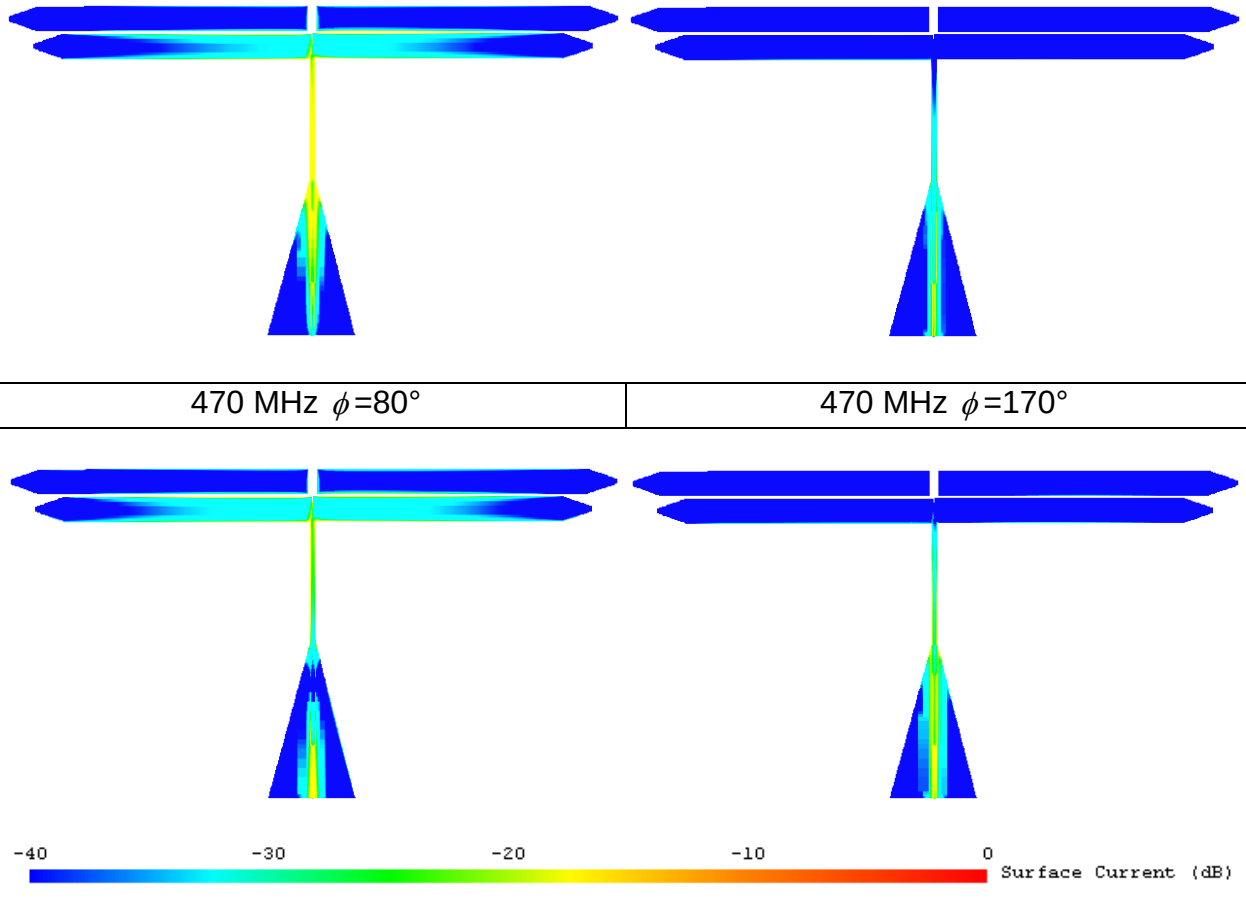

470 MHz ϕ=80°	470 MHz ϕ=170°
550 MHz ϕ=20°	550 MHz ϕ=110°

Figure 4.22 Simulated OPDAwP surface currents at 470MHz and 550MHz

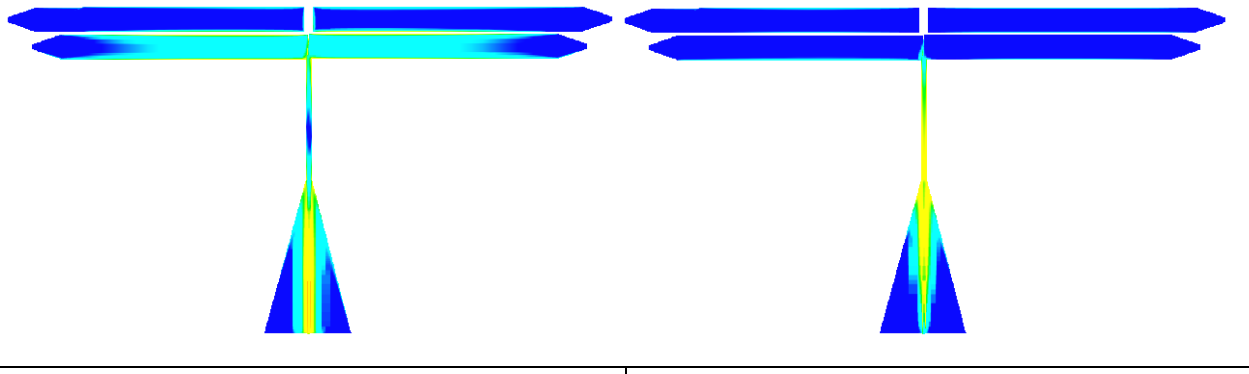

650 MHz ϕ=40° | 650 MHz ϕ=130°

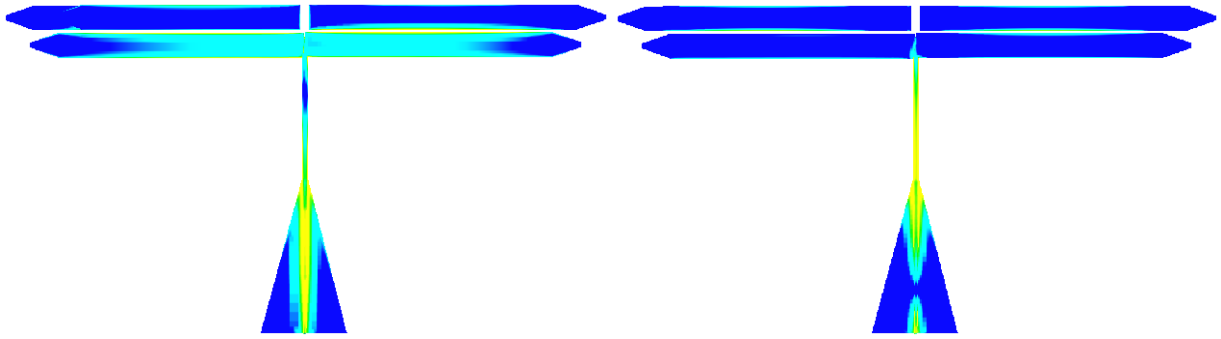

750 MHz ϕ=210° | 750 MHz ϕ=300°

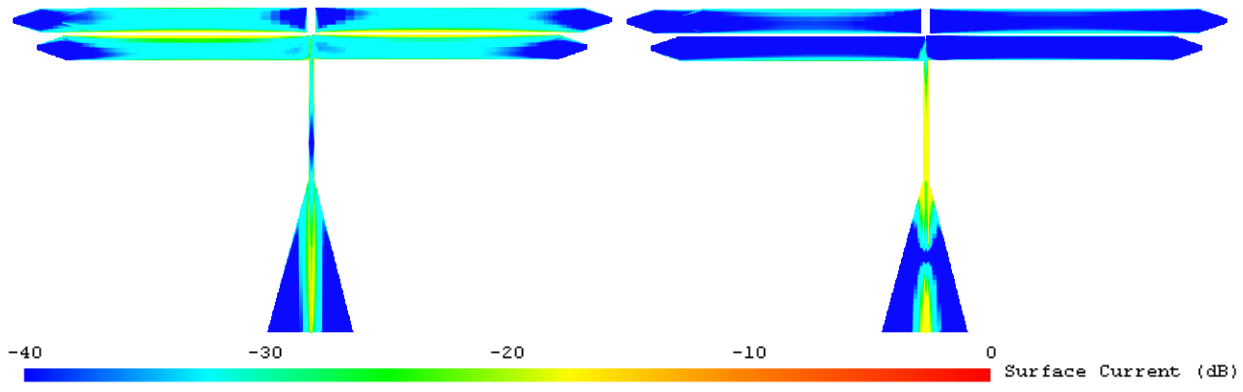

850 MHz ϕ=110° | 850 MHz ϕ=200°

Figure 4.23 Simulated OPDAwP surface currents at 650MHz 750MHz and 850MHz

Figure 4.24 illustrates the direction of the OPDAwP surface currents at central frequency of 650MHz. It should be noted that their direction is the same at the symmetrical points of the OPDAwP dipole, however at the parallel strip line these direction are opposite.

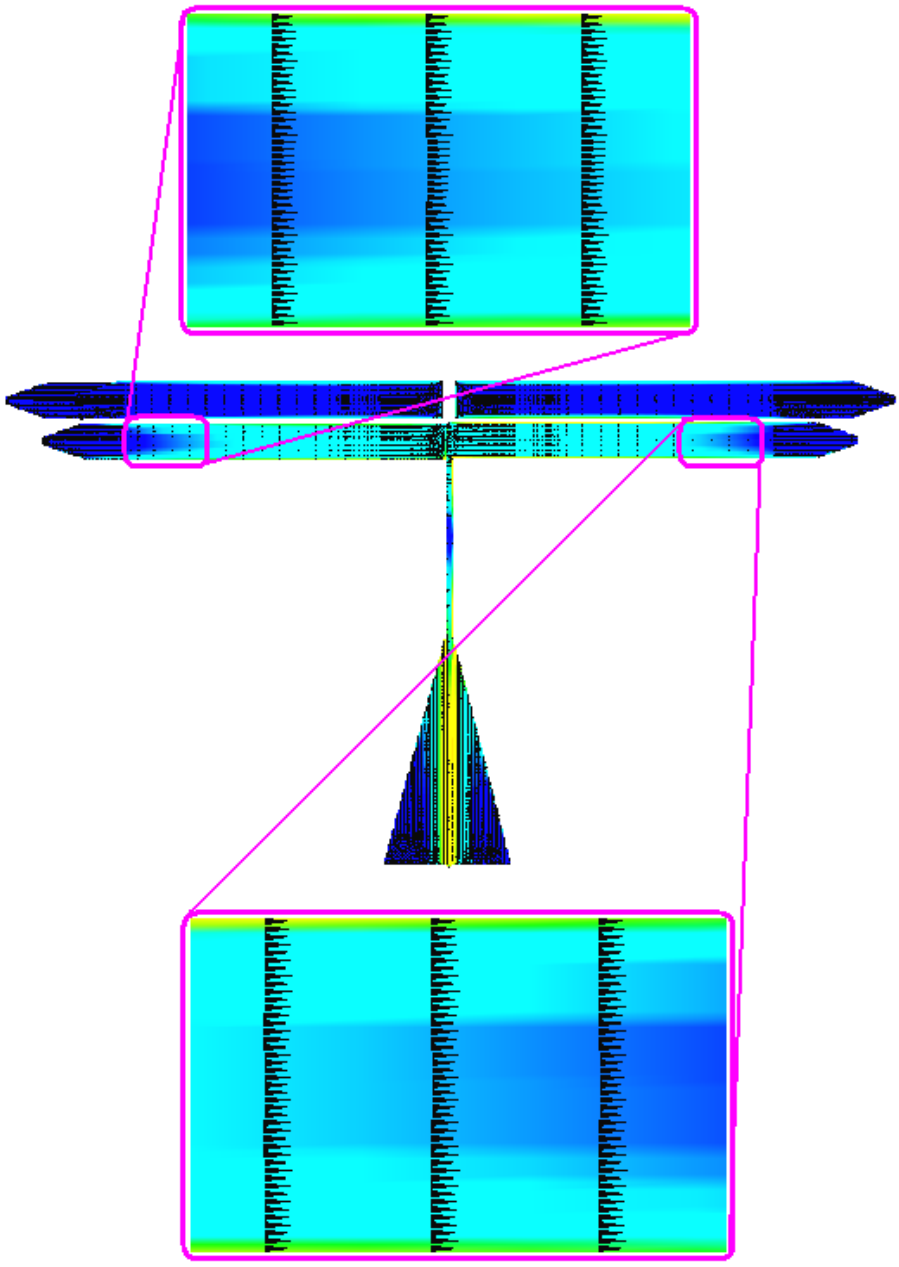

Figure 4.24 Simulated surface current directions of OPDAwP at 650MHz

The radiation patterns play an important role in describing any antenna operation. The E- plane and the H- plane, co-polar and x-polar radiation patters of the OPDAwP are shown in Figure 4.25. The first four pictures illustrate the E-plane, the H-plane co-polar and x-polar 3D radiation patterns at following frequencies: 470MHz, 550MHz, 650MHz and 750MHz. They are similar to the ones stated in the theory for the $\lambda_0/2$ wire dipole. At the E-plane the OPDAwP acquires the radiation patterns in a shape of the figure eight. At the H-plane it acquires the omnidirectional radiation patterns [14]. However, the patterns at 800MHz-850MHz are alternated by the parasitic element, coupled from the exited active element. As it was described in previous section 4.3.4, the active element reflects the parasitic element radiation. In the case when the parasitic element is placed on the top of the radiating element, the radiation is reflected forward the OPDAwP and the gain of the antenna is increased by 2.5dB.

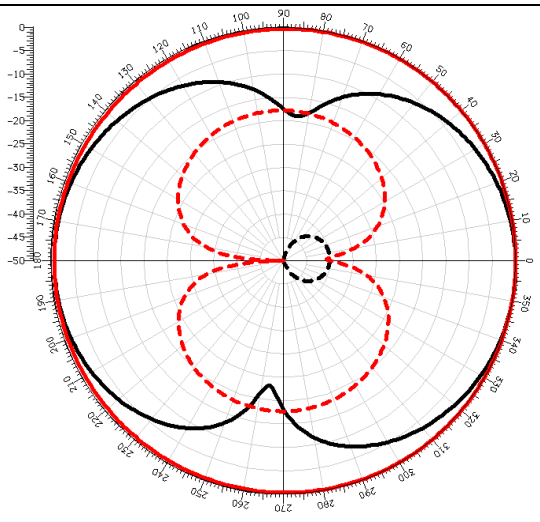

470 MHz

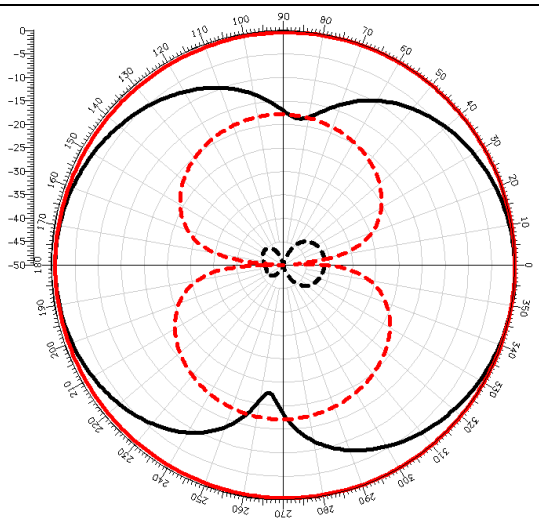

550 MHz

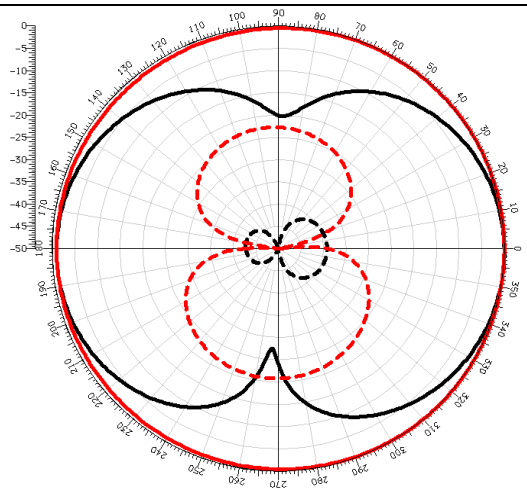

650 MHz

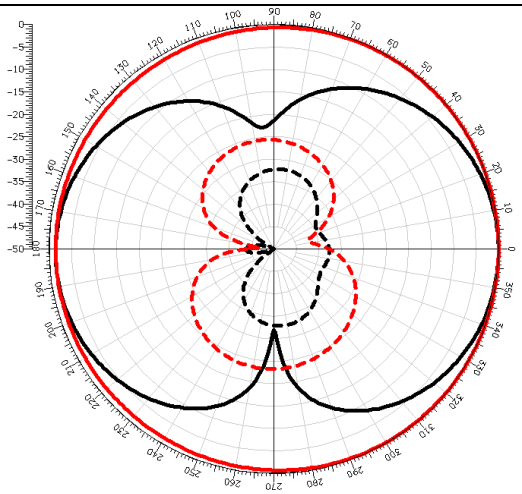

750 MHz

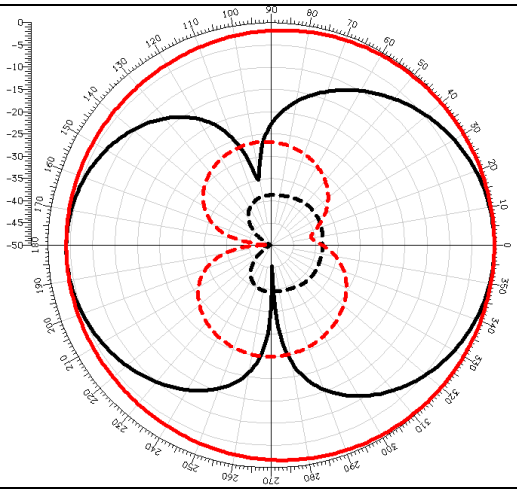

850 MHz

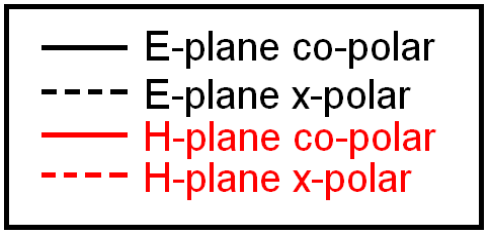

Figure 4.25 Simulated OPDAwP radiation patterns

The PDA, the PDAwP and the OPDAwP directivity values are compared in Figure 4.26.

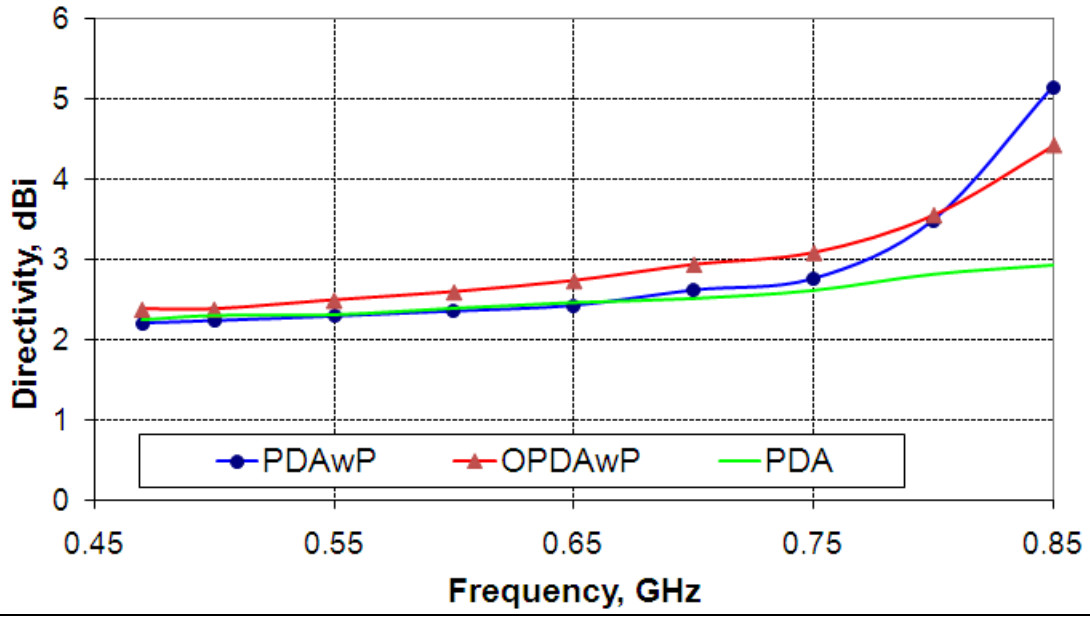

Figure 4.26 The directivity values comparison

The OPDAwP gain and antenna efficient coefficient values are shown in Figure 4.27. The coefficient values vary from 0.88 to 0.97. The antenna efficiency is calculated by using the following equation, integrated into the simulation package [13, 18]:

$$e_{Ant} = e_r \cdot e_{Rad} \qquad \text{eq.4.9}$$

where e_r is the mismatch efficiency $(1-|\Gamma|^2)$ and e_{Rad} is the radiation efficiency (conduction and dielectric losses [14]).

The OPDAwP gain value has increased from 1.2dBi to 4.1 dBi throughout the frequency band (Figure 4.27). The gain values are calculated in the following way: Gain = Directivity + Mismatch-Loss + Radiation-Efficiency [18].

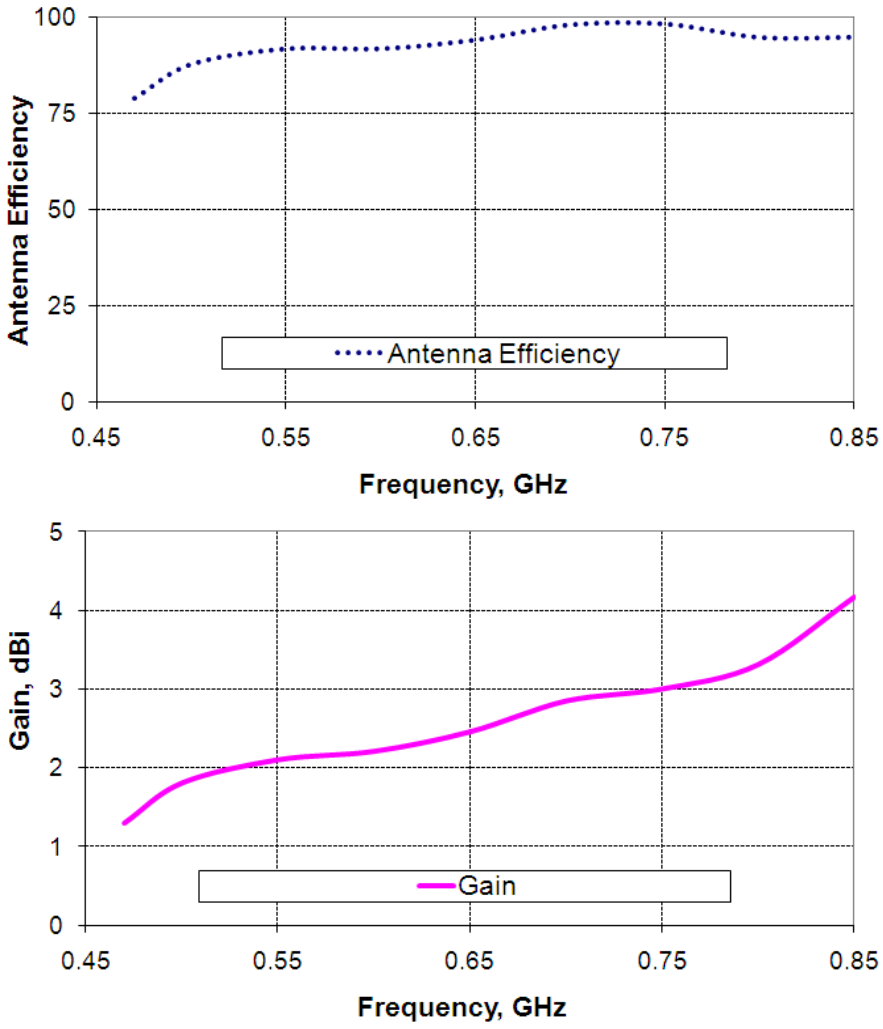

Figure 4.27 OPDAwP efficient and gain simulation results

4.4 Manufactured PDA prototypes

In this section two types of the manufactured PDA systems are described (the PDAwP and the OPDAwP). The measurements were carried out by using the ANRITSU

MS2026A portable vector network analyzer (VNA) [20] in the anechoic chamber. The VNA calibration was performed by using the 75Ω Rosenberger F-type socket calibration kit (model 74CK10A-170) [21]. The F - type female sockets of 75Ω were chosen to be used as connectors in these PDA prototypes. Also The FR4 substrate with the permittivity of 4.9 and the thickness of 1.52 was used in the manufacturing. Finally, the prototypes were covered by a special rubber coating.

4.4.1 Manufactured PDAwP

The manufactured prototype of the PDAwP is illustrated in Figure 4.28. The physical antenna size is compared to the one pound coin.

PDAwP top view

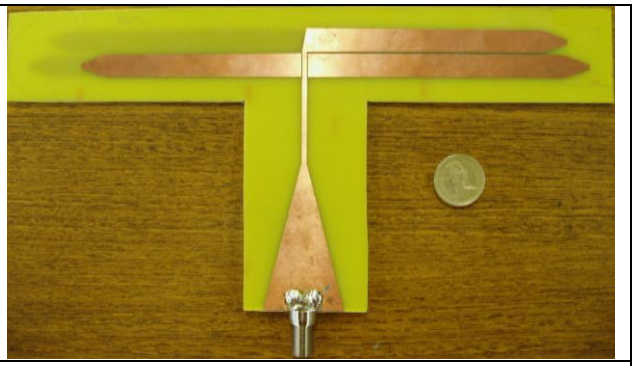

PDAwP bottom view

Figure 4.28 Manufactured PDAwP model compared to one pound coin

The return loss comparison of the simulated and measured results is shown in Figure 4.29. The measurement results achieve the bandwidth of 54.8%, which is 2.8% higher than the bandwidth of the simulation results for the PDAwP. The antenna match starts at 490MHz and finishes at 860MHz.

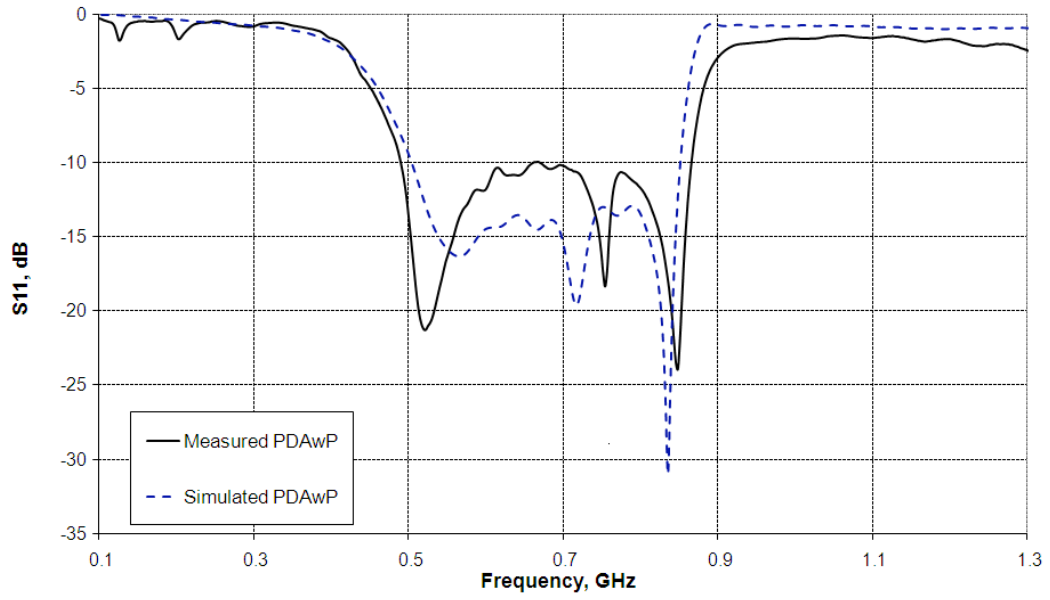

Figure 4.29 The simulation and measurement results of the PDAwP

4.4.1 Manufactured OPDAwP

This section describes the OPDAwP prototype of the dipole antenna. Several examples of this prototype were manufactured. The top and the bottom views of the manufactured OPDAwP are shown in Figure 4.30.

OPDAwP top view	OPDAwP bottom view

Figure 4.30 Manufactured OPDAwP model compared to one pound coin

The measurement results are compared to the simulated ones in Figure 4.31. The measured OPDAwP bandwidth is equal to 56.8%, which is 3.9% larger than the simulated bandwidth. The minimum measured return loss value at 524MHz is -26 and at 756Hz is about -32dB.

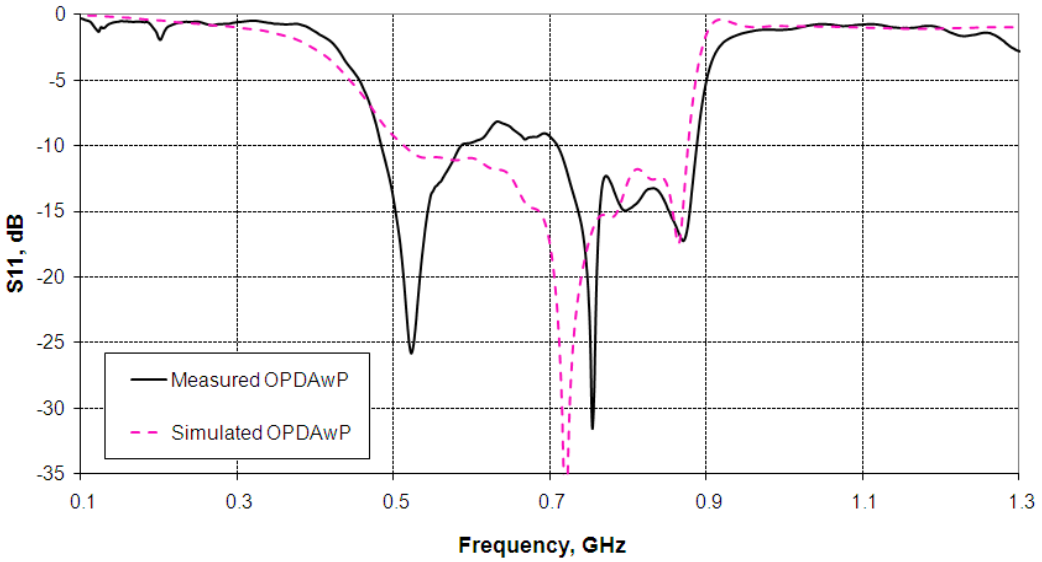

Figure 4.31 The simulation and measurement results of the OPDAwP

The printed dipole antenna will be used outside for the UHF band propagations. Hence, it needs to be safely covered in an antioxidant material. This would prevent the copper oxidation, which eventually may lead to decreased antenna performance.

A “Plasti Dip” multi-purpose rubber coating (Performix brand) was used to cover the manufactured antennas (Figure 4.32). Each printed dipole antenna used about 80g of rubber coating, which resulted in a 0.14mm layer thickness on each side.

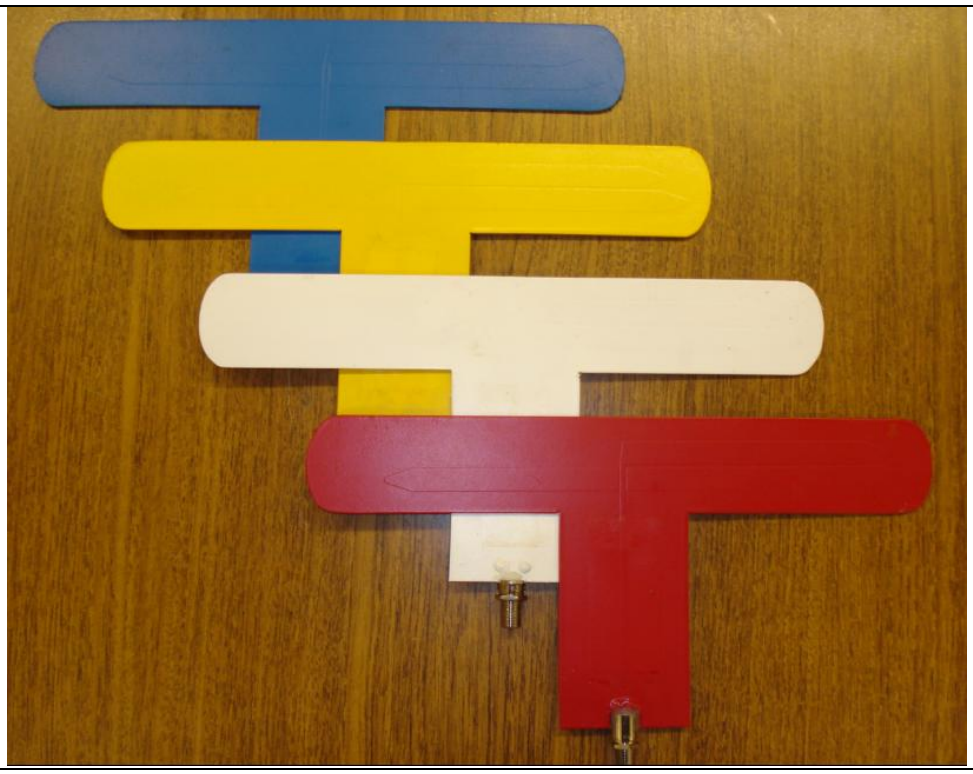

Figure 4.32 PDAs covered with antioxidant rubber coating

The rubber coating had a loading effect on the PDA. As a result, the matching band was shifted to a lower frequency by 10-15MHz.

4.5 Conclusions

The methodology for the innovation of the balanced, broadband and the low cost radiating element was developed. The printed dipole antenna structure was analysed and the main PDA parts explained. The impedance transformation was gradually discussed throughout the whole PDA design.

Section 4.3 described the main steps of the PDA innovating for the UHF. In order to improve the return loss, the operating frequency band and to achieve the higher directivity, the parametric study was carried out and the results were presented in the following sections.

The PDA with the broadband balun, the parallel strip line and the radiating element was introduced. The simulated results were discussed in section 4.3.1. The dual resonance was acquired at 550MHz and at 790MHz. The surface current distribution for the maximum and zero values was shown at various frequencies. Results indicated that the broadband balun is balancing the input to the radiating element from 470MHz to 750MHz. However, the surface current distribution mismatch appeared at 850MHz.

The PDA with the extended feeding line was described in section 4.3.2. It was created in order to simplify the connection with the ground plane. The distance from the radiating element to the ground plane should be close to $\lambda_o / 4$. The microstrip line with the length of 38mm and the input impendence of $75\,\Omega$ was connected to the input of the PDA.

In order to improve the PDA bandwidth, the parametric study was carried out through numerous simulations. The PDA with the stretched balun was introduced in section 4.3.3. The achieved bandwidth was 26%. The PDA maintained relatively consistent radiation patterns in the frequency interval from 470MHz to 850MHz. They were similar to the radiation patterns of the $\lambda_0/2$ wire dipole [14]. The directivity at 470MHz was equal to 2.238dBi and at 850MHz was equal to 2.912dBi.

Section 4.3.4 introduced the parasitic element. The radiation pattern, the directivity and the return loss were improved by implementing the passive element to the PDA structure. The use of the parasitic element in a close proximity to the dipole arms resulted in a PDAwP bandwidth increase to 52%. The directivity of the PDAwP achieved 5.2dBi value at 850MHz, which is 3.3dB higher than the conventional PDA directivity value at same frequency. However, the parasitic element had a negative effect on the radiation patterns. This phenomenon appeared in the frequency band from 800MHz to 850HMz radiation patterns. It was caused by the coupled passive element resonance at the high frequency, when its radiation was reflected backwards to the PDAwP. However, this issue was resolved in the following section.

In section 4.3.5 the PDA model was optimized by performing numerous simulations. The identical parasitic element was placed 1mm above the resonant element. This improved the radiation patterns at higher frequency (800MHz -850MHz) and also resulted in the bandwidth increase by 0.9%. The simulated antenna efficiency varied from 88% to 97.7%, which was a very good performance. The obtained OPDAwP directivity and gain values were as high as 4.3dBi and 4.1dBi respectively.

The PDAwP and the OPDAwP prototypes were manufactured and S_{11} measured in an anechoic chamber. The manufactured prototypes return loss results were better than the simulated ones. The PDAwP bandwidth was improved by 2.8% and the OPDAwP bandwidth was improved by 3.9%. In order to enable the outside range measurements, it was necessary to create the antioxidant layer for the whole antenna coverage. The Plasti Dip" multi-purpose rubber coating was used to cover the whole printed dipole antenna with a 0.14mm thickness layer. This initially resulted in the loading effect on the PDA. The antennas matching band was shifted to a lower frequency by 10-15MHz.

The PDAwP and the OPDAwP systems initially had a broad bandwidth with a low gain. The next chapter describes the methodology for optimisation of the ground plane and its placement under the PDAwP and the OPDAwP, in order to improve the antenna systems directivity, gain and bandwidth values.

4.6 References

[1] G. Kumar, K.P. Ray, “Broadband microstrip antennas”, Artech House, Norwood, MA, 2003, pp 14-15, 89-111.

[2] D.M. Pozar, “Considerations for millimetre wave printed antennas”, IEEE Trans Antennas Propogat AP-31(1983), 740-747.

[3] K.R. Carver, J.W.Mink, “Microstrip antenna technology”, IEEE Trans Antennas Propogat AP-29 (1981), 2-24.

[4] W.C. Wilkinson “ A class of printed circuit antennas”, IEEE Antennas Propagat Soc Int Symp Dig 12 (1974), 270-273.

[5] R. Garg, P. Bhartia, I. Bahl, and A. Ittipiboon “Microstrip Antenna Design Handbook”, Norwood, MA: Artech House, 2001.

[6] N. Fourikis, N. Lioutas, and N. V. Shuley, “Parametric study of the co and x-polarization characteristics of tapered planar and antipodal slot antennas,” Proc. Inst. Elect. Eng., pt. H, vol. 140, pp. 17–22, Feb.1993.

[7] M. A. Smith, K. J. Anderson, and A. M. Pavio, “Decade-band mixer covers 3.5 to 35 GHz,” Microwave J., pp. 163–171, Feb. 1986.

[8] J.W. Duncan, V.P. Minerva: “100: 1 Bandwidth balun transformer”, Proc. IRE, 1960, 48, pp. 156-164.

[9] B. Climer, “Analysis of suspended microstrip taper baluns,” Proc. Inst. Elect. Eng., pt. H, vol. 135, pp. 65–69, Apr. 1988.

[10] C. Y. Ho, “New analysis techniques builds better baluns,” Microwave RF, pp. 99–102, 1985.

[11] S.G. Kim, K.Chang, “Ultra wide -Band Transitions and New Microwave Components Using Double-Sided Parallel-Strip Lines”, IEEE transactions on Microwave theory and Techniques vol. 52 pp.2148-2152, September, 2004.

[12] M.A. Campbell, M. Okoniewski, C. Fear “Ultra-wideband microstrip to parallel strip balun with constant characteristic impedance”, EMTS 2007 International URSI Commission B - Electromagnetic Theory Symposium, July 26-28, 2007, Ottawa, Canada.

[13] CST’s MicroStripes website: http://www.cst.com/ Content/ MST/ Overview.aspx.

[14] C. A. Balanis “Antenna theory analysis and design” 2nd edition, New York, Wiley, 1997.

[15] A.W. Rudge, K.Milne, A.D. Olver, P.Knight “The handbook of antenna design”, volumes1 and 2, Page Bros Ltd, Norfolk,1986.

[16] G.A Evtioushkine, J.W Kim and K.S. Han “Very wideband printed dipole antenna array”, Elelctron Lett 34 (1998), 2292-2293.

[17] T.G. Vasiliadis, E.G. Vaitsopoulos, and G.D. Sergiadis “A wideband printed dipole antenna with optimised tapered feeding balun for ISM and FWA bands” Microwave Opt Technol Lett 43 (2004), 437-441.

[18] CST MICROSTRIPES Reference Manual, release 2009.

[19] AWR Microwave Office 2009 website: http://web.awrcorp.com/.

[20] Anritsu VNA Master MS2024A - MS2026A User’s Guide, 2 November 2005, UK; Anritsu VNA Master MS2024A/MS2026A and MS2034A/MS2036A Programming Manual, 24 October 2006, UK.

[21] Rosenberger website: http://www.rfmw.com/rosenberger/?src=adwords&pid=241.

Chapter 5

Printed dipole antenna (PDA) with reflector system

5.1 Introduction

Chapter 4 discussed a novel, balanced, broadband and low cost printed dipole antenna (PDA). This type of a driven element achieves relatively consistent radiation patterns over the UHF band. Based on its performance, the PDA was used as a radiating element in an UHF antenna system. This chapter presents the comparison of the measured and the simulated results, when the PDA is placed over a gridded ground plane.

Section 5.2 describes the parametric study which was carried out in order to investigate the size and compositions of various ground planes. The reflectors with various size, shape and structure were analysed.

Section 5.3 commences with the simulation results of the PDAwP and the OPDAwP placed over the ground plane. The directivity, the radiation pattern and the return loss values were evaluated and compared when the PDA was placed over the ground plane and in parallel to the ground plane.

In order to validate the predicted radiation patterns and the gain values, indoors and outdoors measurements were carried out and described in section 5.4. The measurements were performed on the concrete roof of the three floors building. The antenna under test (AUT) was PDAwP placed over three different types of ground planes. The first type was a flat wire mesh ellipse ground plane. The second type was a wire mesh ellipse ground plane, bended at an angle of 20° and the final type was the same structure ground plane, angled at 45°. For comparison purpose, three types of commercially available Yagi UHF antennas with different number of elements were bought from Kathrein Ltd [1]. The gain values of these antennas were measured and compared with available datasheets in order to evaluate the measuring method and the PDA system.

Results and conclusions are discussed in final section 5.5.

5.2 Ground plane analysis

Many antennas implement a flat plate metal sheet as the reflector or a ground plane [2]. The ground planes are used to redirect radiation into the forward direction. In this way they increase the antenna gain and also improve the interference with nearside objects, placed behind the antenna. Most of the reflectors are electric conductors with the property of reversing the phase of the reflected waves.

5.2.1 Perfect electric conductor (PEC)

Theoretically, a perfect electric conductor (PEC) placed over the radiating antenna changes the reflected wave phase to $180°$. When the radiating antenna is brought very close to the PEC (i.e. closer than $\lambda/4$); such placement can result in a destructive interference, as shown in Figure 5.1.

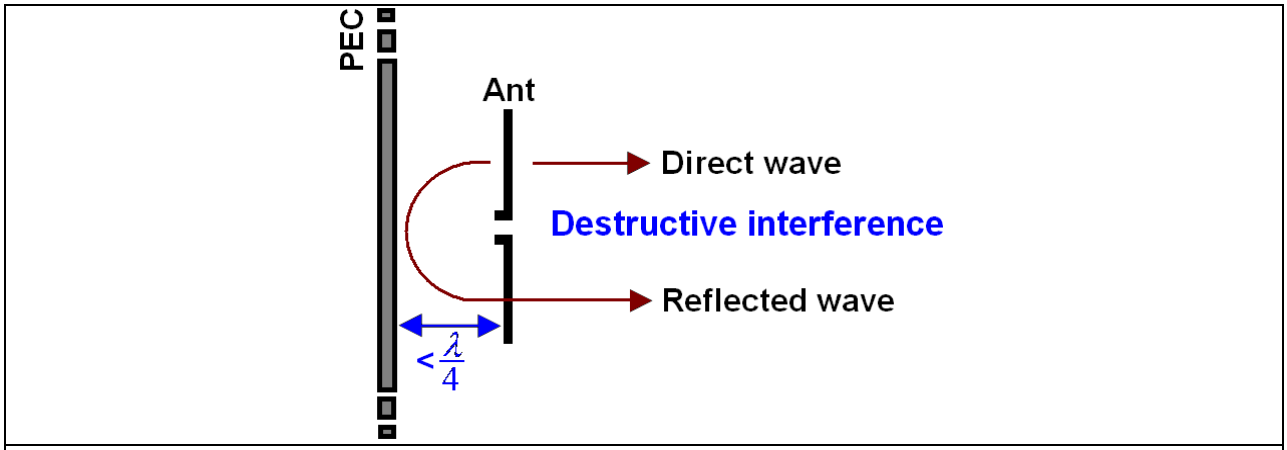

Figure 5.1 Radiating antenna placed very close to a perfect electric conductor

The radiation is being reduced due to the image currents. They are generated by the perfect electric conductor, which cancels out the currents in the antenna. To solve this problem the radiating antenna must be placed at $\lambda/4$ distance from the PEC, as shown in Figure 5.2.

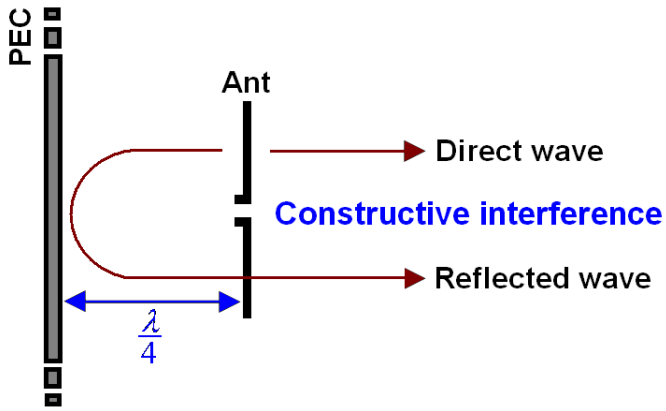

Figure 5.2 An antenna placed at $\lambda/4$ distance from ground plane

The total phase shift from antenna, i.e. to the PEC and back to the antenna, is equivalent to the one complete cycle (Figure 5.3), which creates constructive interference [3] (90°+180°+90°=360°).

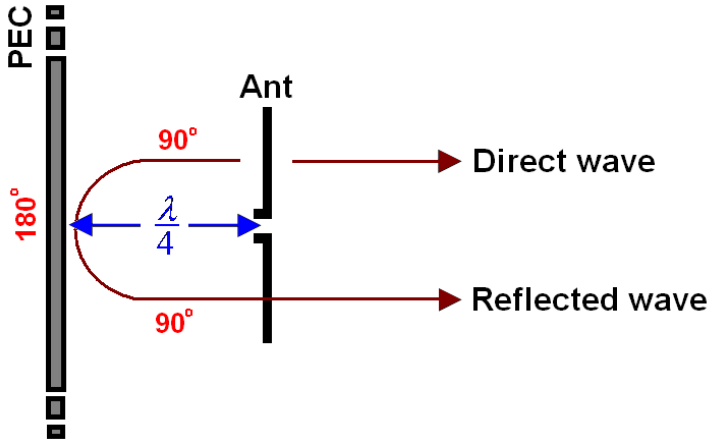

Figure 5.3 Phase change of the antenna placed at $\lambda/4$ distance from ground plane

The total size of the antenna system should be at least one quarter of the wavelength thickness, in order to radiate efficiently. The distance could be reduced by using the artificial magnetic conductors (AMC) or the high impedance surfaces (HIS). However, they have limited bandwidth.

5.2.2 Periodic structure analysis

The designing of the ground plane for the outdoor antenna system requires meeting several important conditions: i.e. having a good conductivity, using a material which does not oxidise and is light weight, having low wind loading, low profile and being inexpensive to manufacture with a reasonably good front - to - back ratio (F/B). To design a light weight and low wind loading antenna system, the PEC needs to be implemented with periodic air perforations, known as the frequency selective surfaces (FSS). However, it is quite expensive to fabricate such structures. A commercially available galvanised wire mesh meets these conditions. This material also has the advantages of being low cost, antioxidant and would be strong enough in structure, see Figure 5.4.

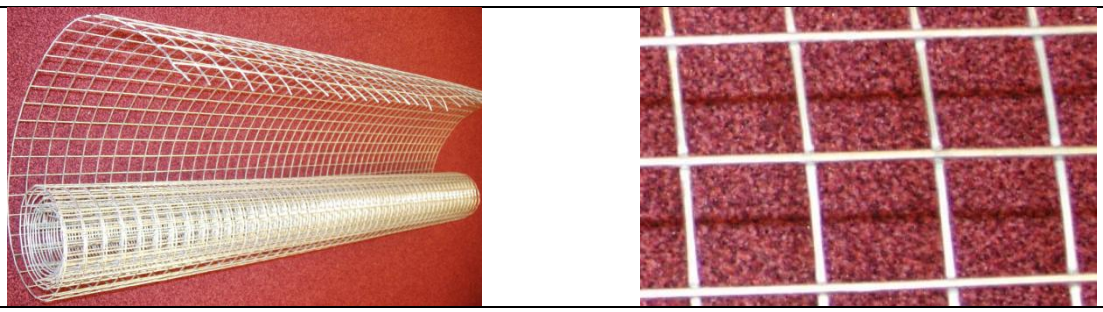

Figure 5.4 Picture of the galvanised mesh roll

The CST MicroStripes electromagnetic simulation package [4] was used to analyse such ground plane structure. Three types of prediction results were simulated: PEC, single cell of the periodic structure and 4x4 cells. The structure was exited by a waveguide placed in close proximity to the periodic surface, as shown in Figure 5.5 and Figure 5.6. The boundary conditions for the incident wave were absorbing, for the other axis the boundary conditions were wrap around.

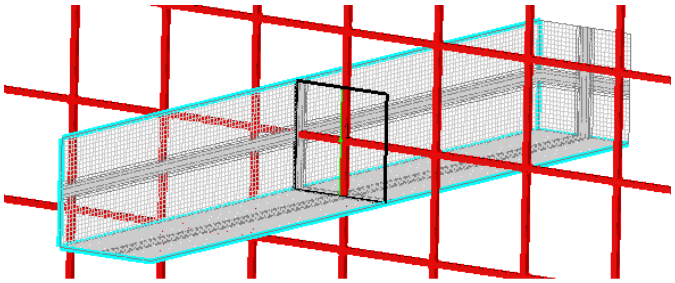

Figure 5.5 single cell analysis

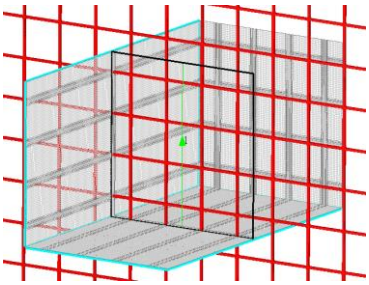

Figure 5.6 4x4 cells analysis

The simulated results of the reflection phase are shown in Figure 5.7 for different types of ground plane structures. The distance between the excited waveguide and the analysed surface was 2mm. The reflected wave phase of the PEC includes the phase of the travelling wave throughout the distance of 4mm between the nodes. Therefore, the results discrepancy varies in this phase.

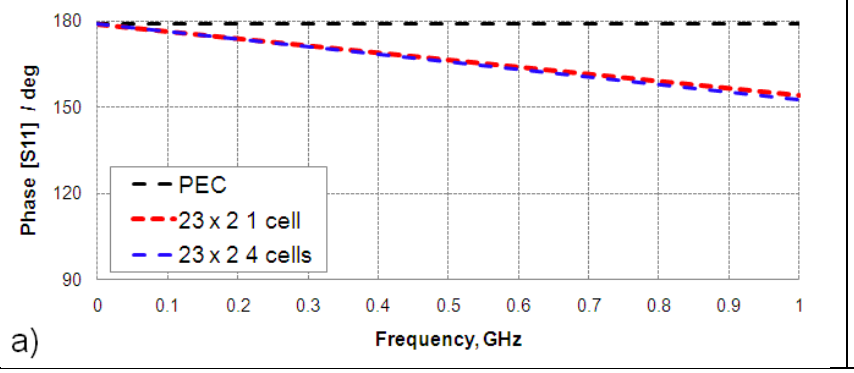

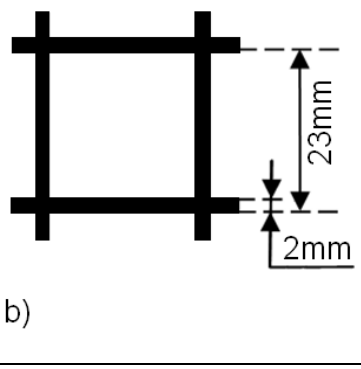

Figure 5.7 a) Simulated reflection phase results; b) single cells structure

The simulated PEC phase line is the reference for the comparison to the periodically perforated surface reflection phase. The blue and the red lines represent the reflected wave phase shift of the periodic structure with dimensions of single cells 23mm x 2mm (Figure 5.7). These lines are almost identical, which suggests that the analysing method of a single cell is optimal. The periodic structure performs $167°$ phase inversion of the reflected wave at 470MHz, $162°$ phase inversion at the centre frequency 650MHz and $156°$ phase inversion at the highest frequency point. This phase change of the reflected wave will result in the distance increase between the radiating element and the FSS ground plane by $\lambda_0 / 36$ compared to the PEC ground plane.

The parametric study of various ground plane dimensions was carried out in order to optimise the ground plane, without incurring any significant loss in the directivity values and the F/B ratio. The chosen ground plane sizes to be investigated were: 100cm x 100cm; 100mm x 74cm; 100cm x 43cm; 74cm x 100cm, 74cm x 74cm; 74cm x 43cm; 43cmx 100cm; 43cm x 74cm; 43cm x 43cm and 74cm x 43cm PEC.

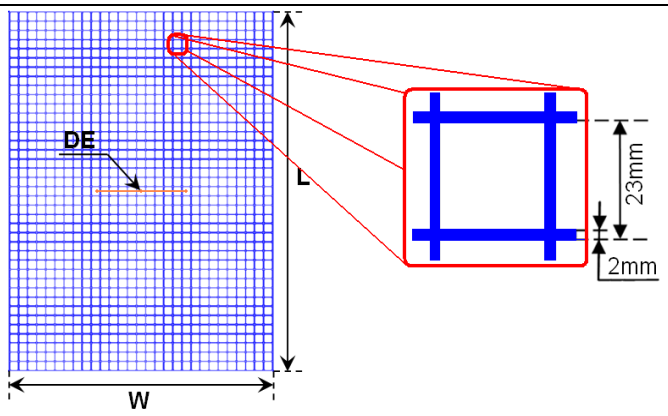

100cm x 74cm

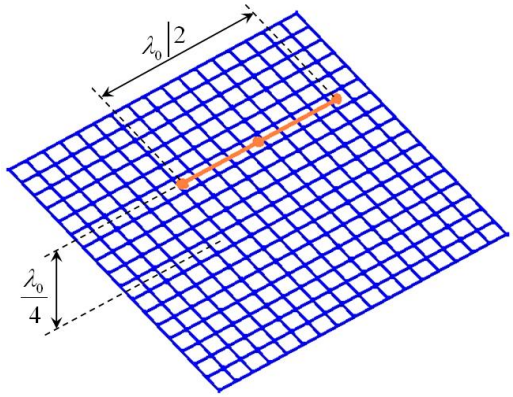

43cm x 43cm

Figure 5.8 The dimensions of the ground planes

The first dimension represents the height of the structure ("L" vertical axis) and the second dimension corresponds to its width ("W" horizontal axis), see Figure 5.8. The ground planes were placed $\lambda_0/4$ apart from the radiating element. In order to speed up the simulation, the chosen driven element (DE) was the $\lambda_0/2$ wire dipole (Figure 5.8). The effect of the ground plane size change on the return loss is illustrated in Figure 5.9.

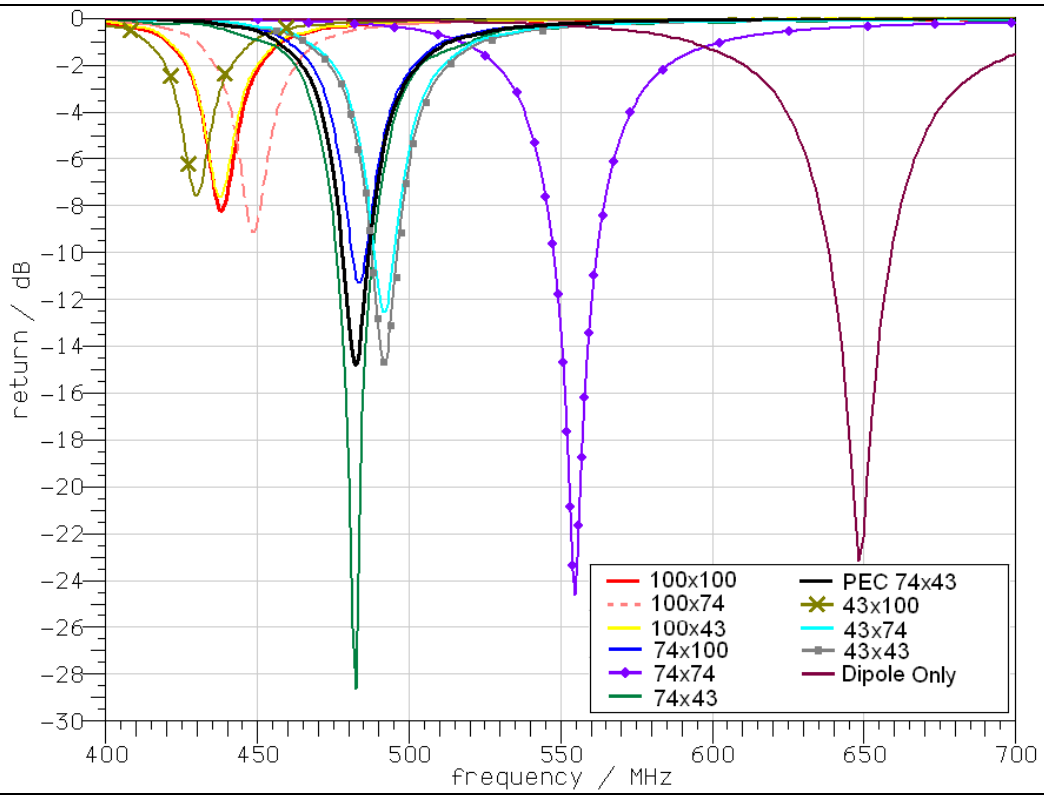

Figure 5.9 Simulated return loss of the dipoles placed over different size ground plane

The $\lambda_0/2$ wire dipole is designed to resonate at the centre frequency of the PDA operation band, i.e. 650MHz. However, the resonant frequency is shifted by placing the ground plane at $\lambda_0/4$ distance from the dipole (Figure 5.9). This can be explained by the fact that the ground plane is loading the dipole, and consequently it is operating in a

much lower frequency. The best return loss value (i.e. -28dB), achieved from simulations, was accomplished from the periodic structure with dimensions 74cm x 43cm (30cells x 17cells).

The effect of the ground plane size change on the E-plane and H-plane co-polar radiation patterns is illustrated in Figure 5.10. This figure contains ten different radiation pattern graphs for various ground planes. The radiation patterns shape are quite similar in all cases, however the small changes are visible in the HPBW, in the F/B ratio and in the directivity values. The results containing the HPBW values for various ground planes are shown in Table 5.1.

Ground plane	**Half Power Beam Width (HPBW)**	
	E-plane co-polar	**H**-plane co-polar
Dipole only	78°	180°
100cm x 100cm	59°	81°
100cm x 74 cm	59°	79°
100cm x 34cm	67°	67°
74cm x 100cm	73°	80°
74cm x 74cm	58°	85°
74cm x 43cm	68°	70°
PEC 74cm x 43cm	69°	71°
43cm x 100cm	62°	105°
43cm x 74cm	68°	89°
43cm x 43cm	66°	87°

Table 5.1 The HPBW values for various ground plane

The most directional beam has the dipole placed over the ground plane with dimensions of 100cm x 43cm (E, H-plane was 67°). The widest achieved beam width was 62° at E-plane and 105° at H-plane by the dipole placed over the ground plane with dimensions of 43cm x 100cm.

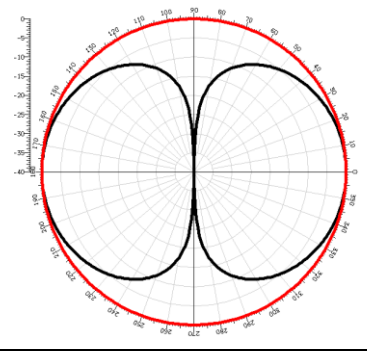

Dipole only

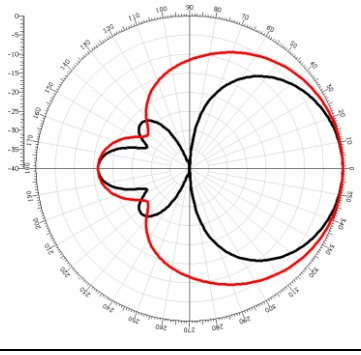

100cm x 100cm

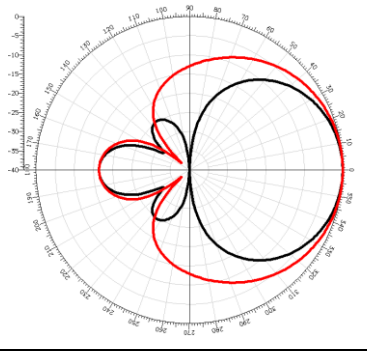

100cm x 74cm

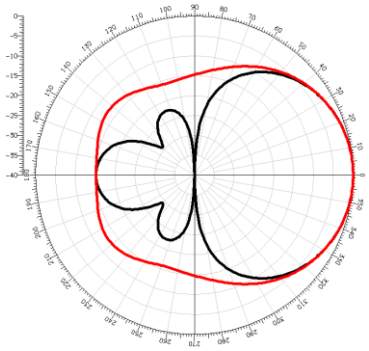

100cm x 43cm

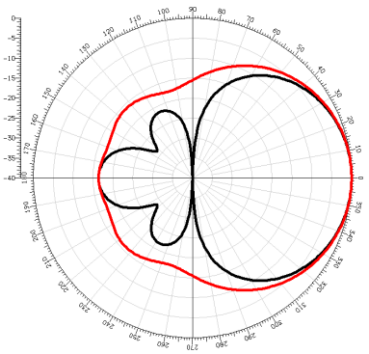

74cm x 100cm

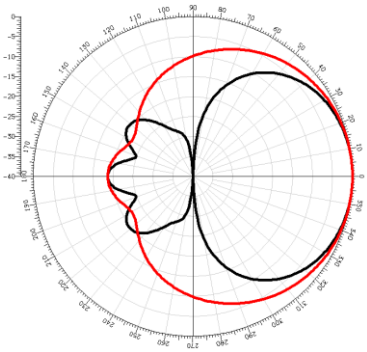

74cm x 74cm

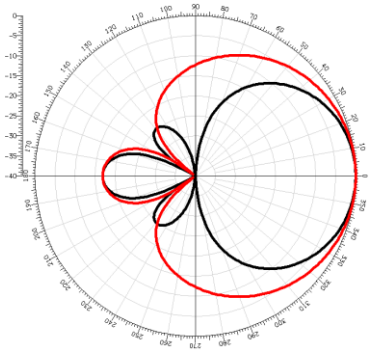

74cm x 43cm

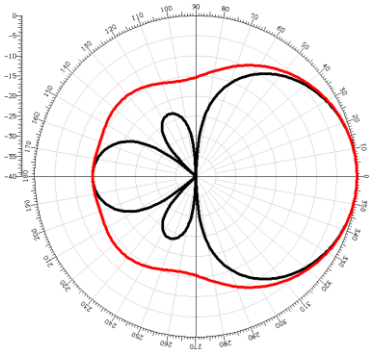

PEC 74cm x 43cm

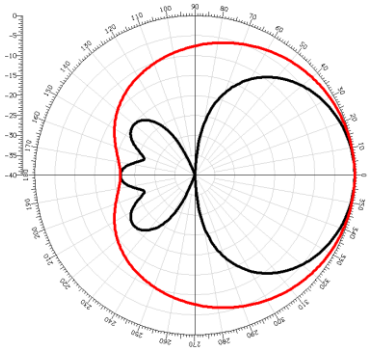

43cm x 100cm

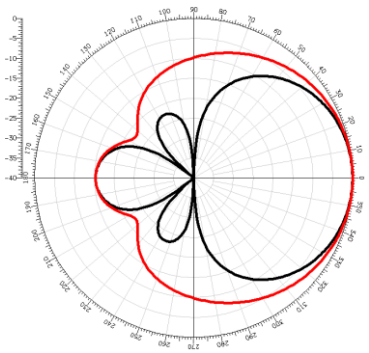

43cm x 74cm

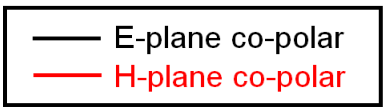

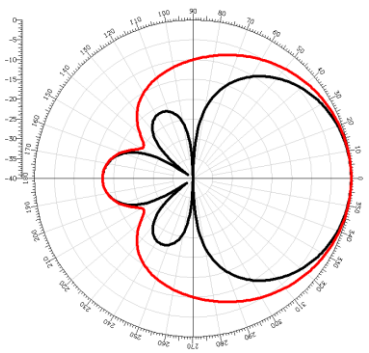

43cm x 43cm

Figure 5.10 E,H-planes co-polar radiation patterns of the dipole placed over various ground planes

It can be noticed from Figure 5.11 that the F/B ratio varies for different ground plane structures. The best F/B ratio (21dB) is achieved when the ground plane size is 43cm x 100cm. Although in comparison, the ground planes with sizes of 43cm x43cm, 74cm x 43 and 74cm x 74cm have higher than 17dB F/B ratio.

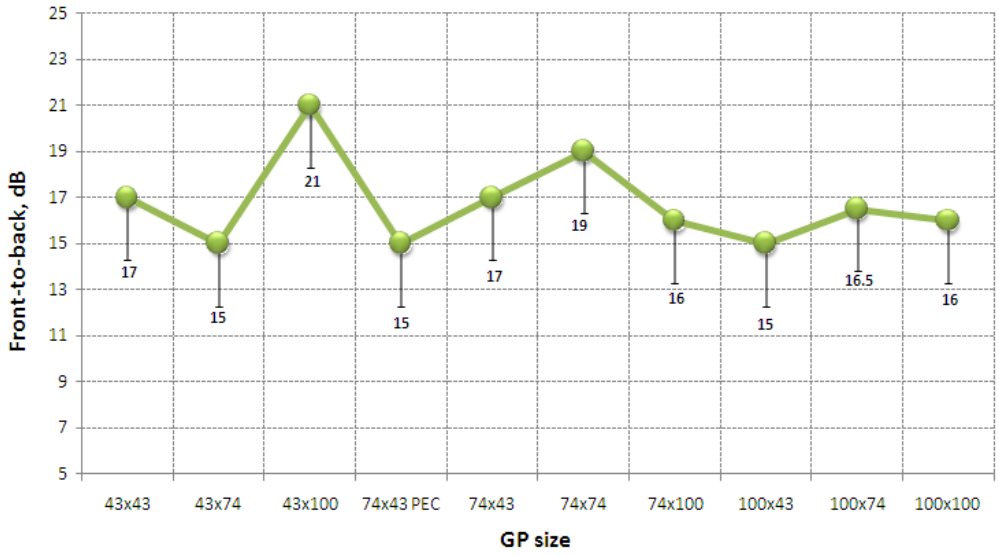

Figure 5.11 Simulated F/B results of the dipole placed over various size ground planes

The directivity values at the resonant frequencies are illustrated in Figure 5.12. The maximum achieved directivity is 9dBi, when the reflector has the dimensions of 74cm x 43cm. The second highest directivity is achieved with the reflector size of 74cm x 43cm. It is only 0.15dBi smaller than the 100cm x 43cm surface and is equal to 8.9dBi. The ground planes with the width of 43cm ("W") have higher directivity in comparison to the other widths (i.e. 100cm and 74cm). This pattern of behaviour is common for all ground planes with different height dimensions.

Taking into account that the structure with the best directivity (i.e. 100cm x 43cm) is $0.43m^2$ and with the 74cm x 43cm ground plane is only $0.318m^2$, the optimum ground plane size would be a ground plane with dimensions of 74cm x 43cm.

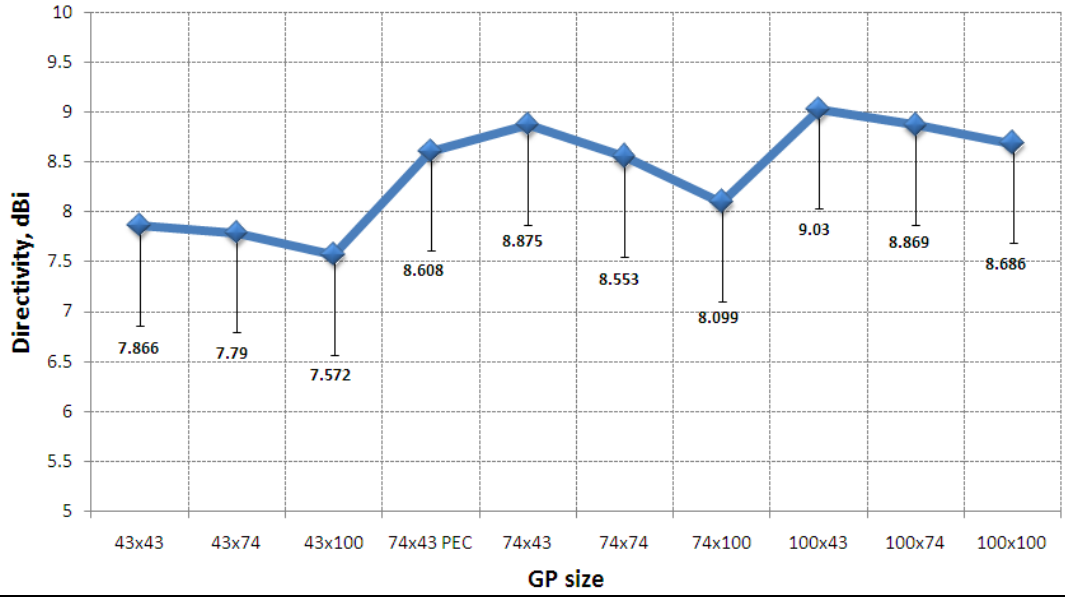

Figure 5.12 Simulated directivity values for the dipole placed over various ground planes

It can be concluded from the performed simulations that the optimum ground plane dimensions is 74cm x 43cm.

5.2.3 Elliptical ground plane

Previous section described the analysed reflector with the following features: low weight, low wind loading, produced from a cost effective material, with a strong overall structure, the flat plate, resilient to oxidisation in outdoor weather conditions and having low profile with a good overall performance. To improve the ground plane shape, the simulated surface currents of the PEC were analysed at various phases, as illustrated in Figure 5.13 (a-d). It should be noticed that the surface current density along the ground plane decreases by increasing the distance away from the centre, where the dipole is placed. The surface current distribution is the same in both cases: over the PEC ground plane with 74cm x43cm dimensions and over the periodically perforated metallic sheet with 74cm x 43cm dimensions (Figure 5.13 e-h). It should be noted that the surface currents propagate in an elliptical shape.

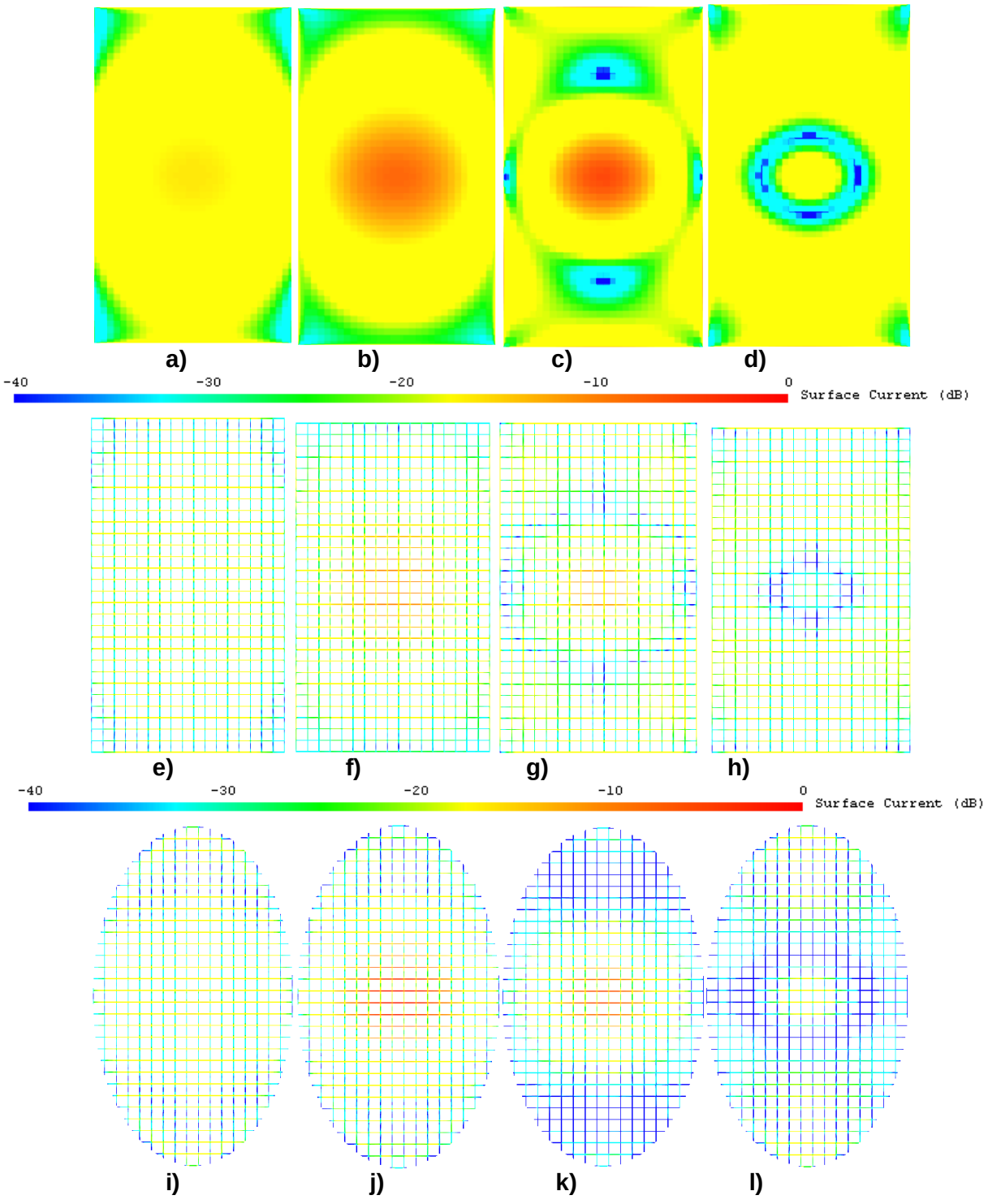

Figure 5.13 Surface current distribution at various phases

To improve the low profile and enhance the reflection performance, the ground plane corners were cut off to make its shape elliptical. The surface currents distribution for this type of structures is illustrated in Figure 5.13 (i-l).

The directivity of the dipole, placed over the ellipse wire mesh ground plane with a size of 74cm x 43cm, is 0.2dB higher than the directivity of the dipole placed over the rectangular wire mesh ground plane with same dimensions at the resonant frequency. The elliptical ground plane with periodically rectangular air perforations will be used in next investigations of the PDA placed over reflector because this ground plane was proved to be the optimum one.

5.3 Results for PDA with ground plane

In order to show the ground plane performance for the PDA system the radiation patterns were investigated. Two types of the PDA were analysed: the PDAwP and the OPDAwP. Moreover, two types of the PDA placements over the ground plane were analysed: above the reflector and parallel to the reflector both at $\lambda_0/4$ distance. The geometries of the various PDA configurations are shown in Figure 5.14.

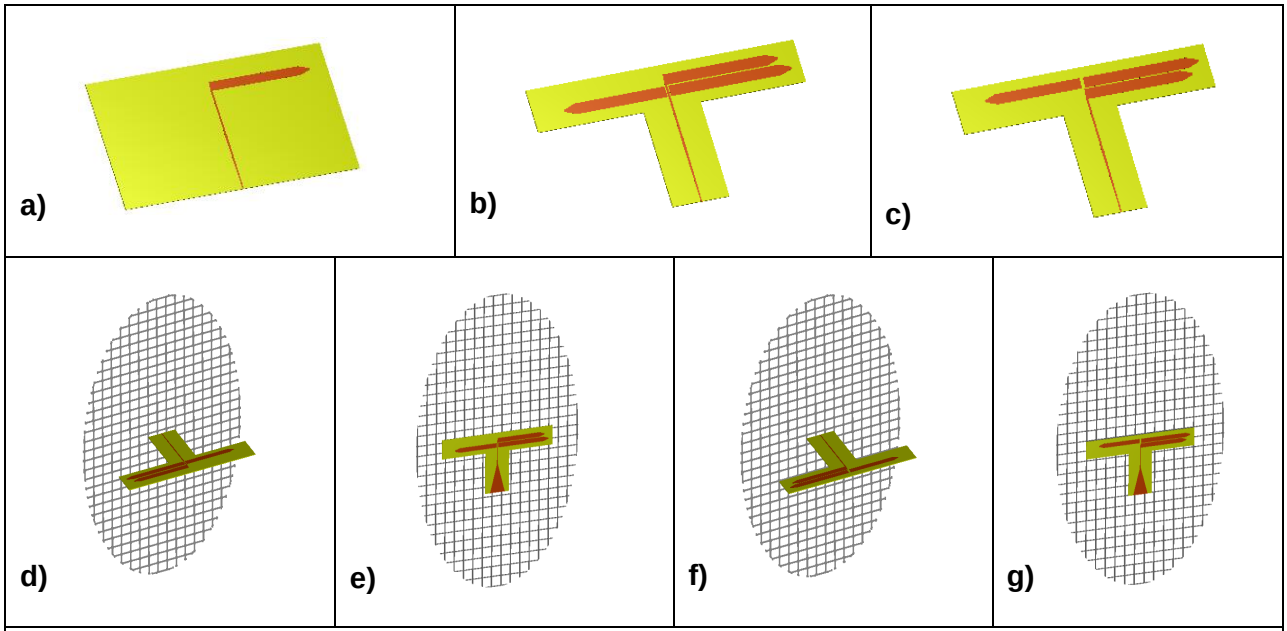

Figure 5.14 Structure of various PDA: a) PDA; b) PDAwP; c) OPDAwP d)PDAwP $\perp$ GP; e) PDAwP $\parallel$ to GP; f) OPDAwP $\perp$ GP; g) OPDAwP $\parallel$ to GP

5.3.1 Results for PDAwP placed over ground plane

The predicted PDAwP results placed over the metamaterial inspired ground plane are shown in Figure 5.15.

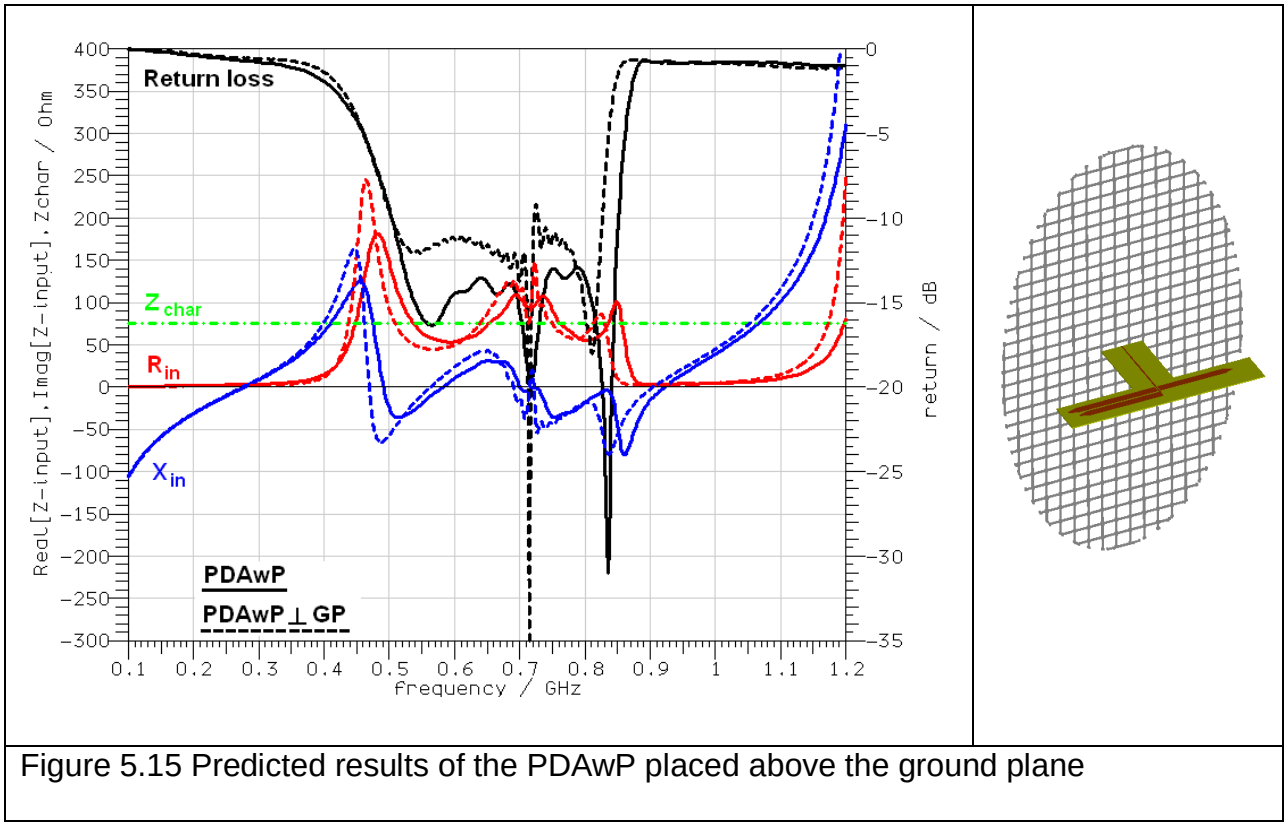

Figure 5.15 Predicted results of the PDAwP placed above the ground plane

Solid lines correspond to the PDAwP and dotted lines represent the PDAwP placed above the reflector. The graph contains the real part (R_{in}) and the imaginary part (X_{in}) of the input impedance. Z_{char} is the impedance characteristic at the input to the antenna, which is design to be equal to 75Ω. The resonance of the PDAwP alone in the return loss appears at 550MHz, 715MHz and 840MHz frequencies, when the real part is close to the 75Ω and the imaginary part is being close to zero or equal to zero.

The results for the E, H-planes co-polar and x-polar radiation patterns of the predicted PDAwP, placed above the ground plane, are shown in Figure 5.16. The radiation patterns are described at five different frequencies: 470MHz, 550MHz, 650MHz, 750MHz and 850MHz.

The F/B ratio varies from 17dB (550MHz) to 27dB (750MHz). The radiation performances of the PDAwP placed above the ground plane throughout the 470MHz – 750MHz frequency range remains unchanged. The antenna radiation from 800MHz to 850MHz interferes with a parasitic element (placed below the radiating element) and deteriorates the wave propagation by redirecting the front beam toward the ground plane.

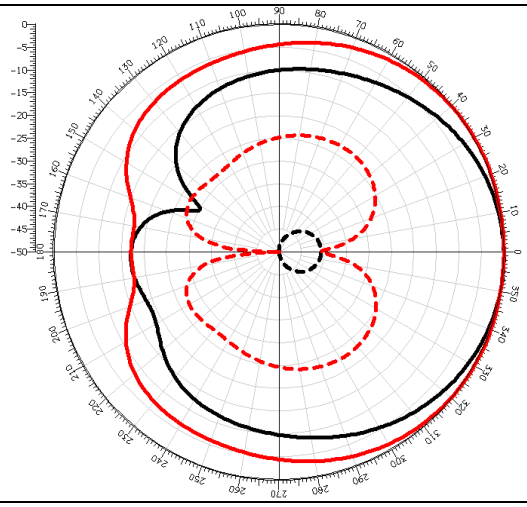

470 MHz

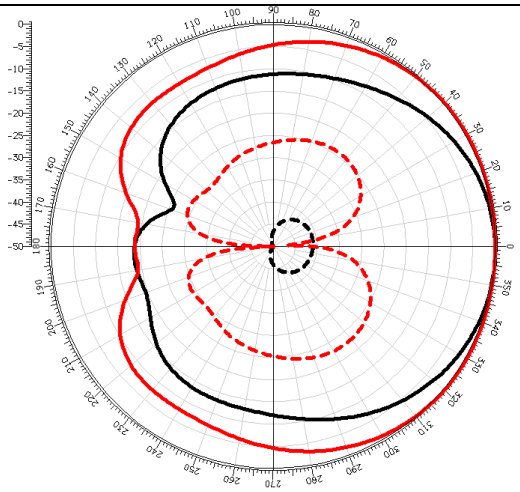

550 MHz

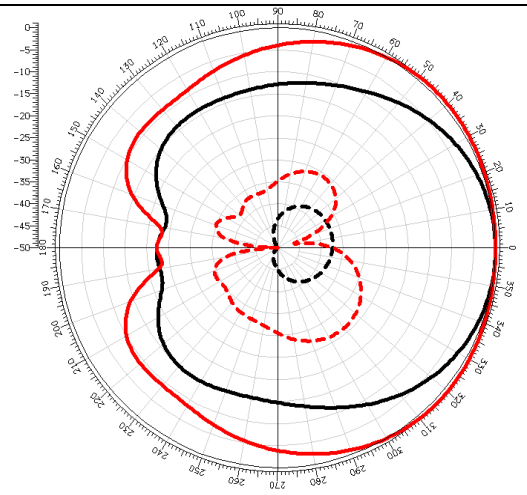

650 MHz

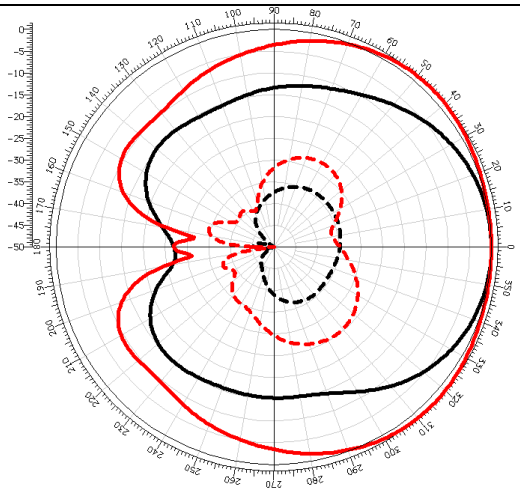

750 MHz

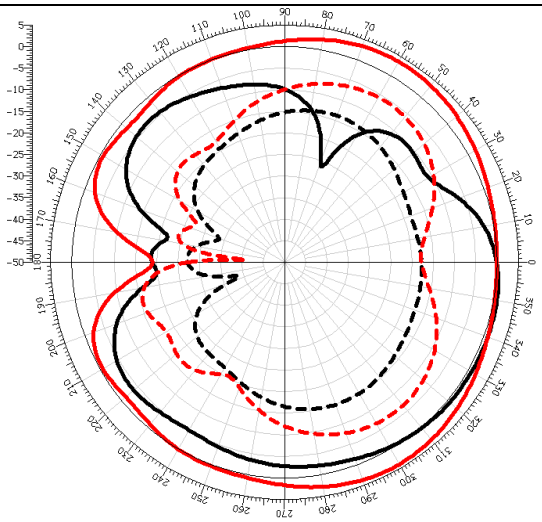

850 MHz

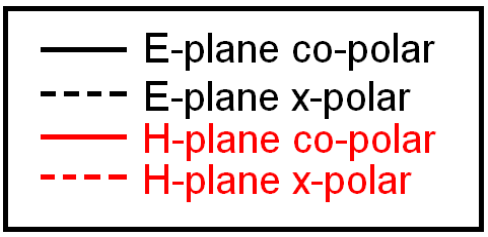

Figure 5.16 Radiation patterns of the PDAwP placed over the ground plane

The simulation results for the PDAwP, placed in parallel to the ground plane, are shown in Figure 5.17. The return loss results are very similar to results for the PDAwP placed above the ground plane.

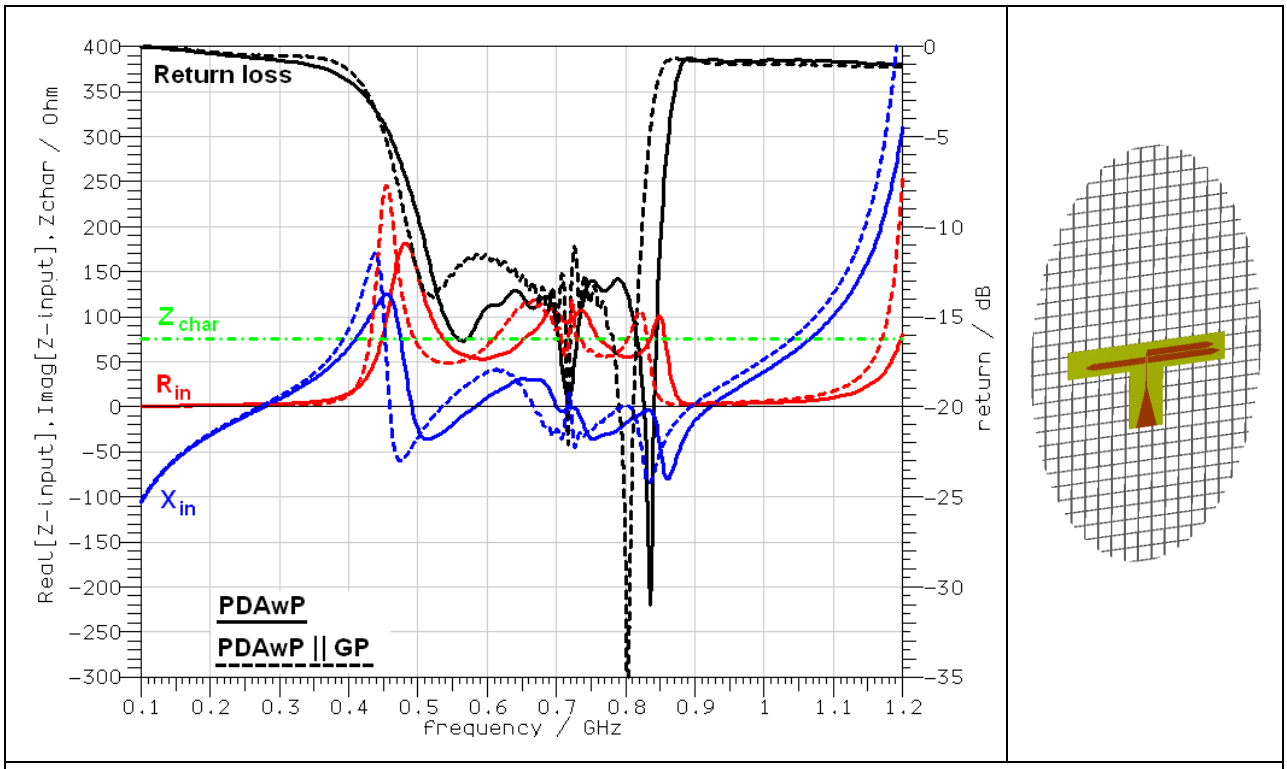

Figure 5.17 Predicted results of the PDAwP placed parallel to the ground plane

However, the radiation patterns are more directive, particularly in the H-plane of the PDAwP placed in parallel to the reflector compared to the PDAwP placed above the reflector, (see Figure 5.18).

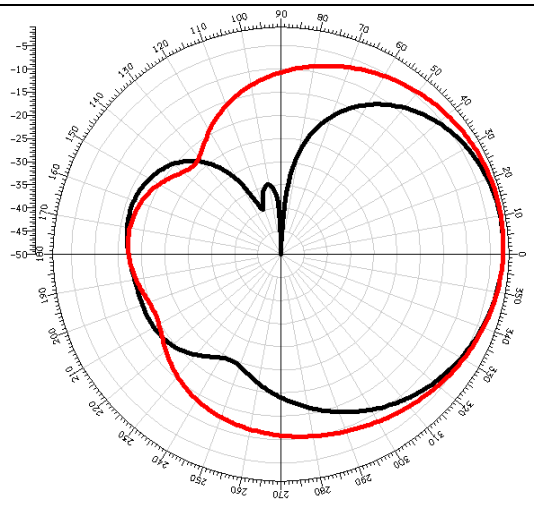

470 MHz

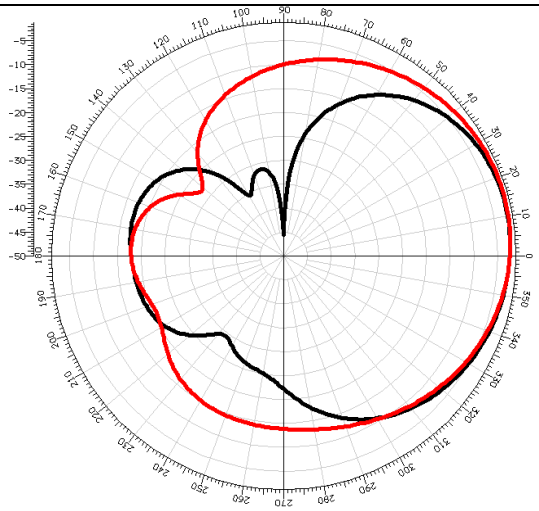

550 MHz

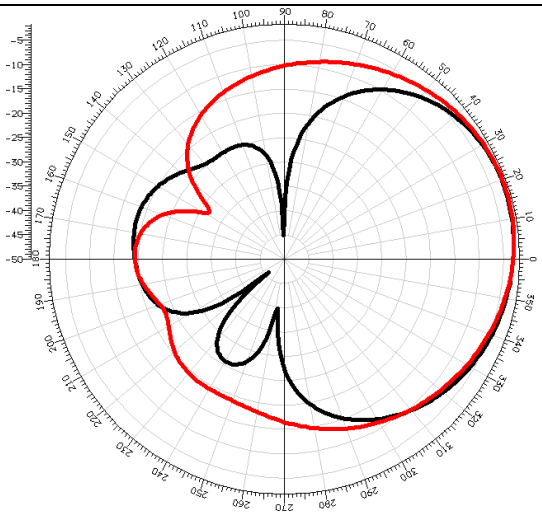

650 MHz

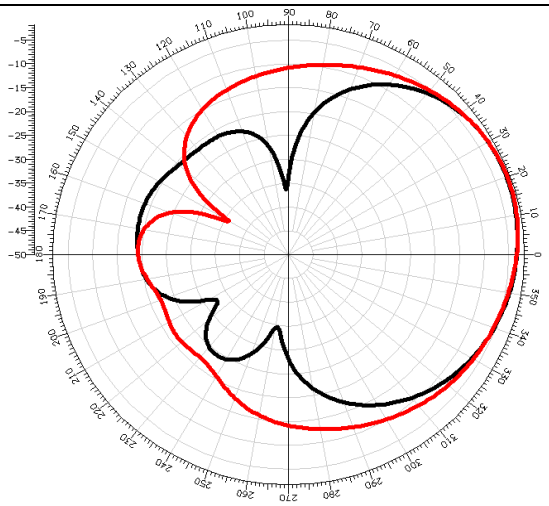

750 MHz

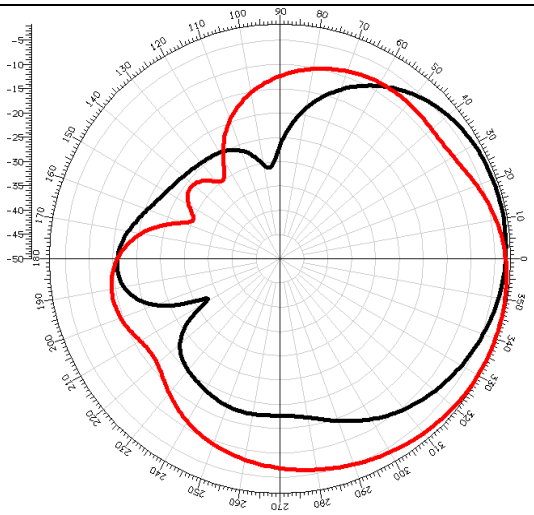

850 MHz

Figure 5.18 Radiation patterns of the OPDAwP placed parallel to the ground plane

The HPBW of the various PDAwP configurations (the PDAwP alone {Figure 5.14 b)}, the PDAwP placed above the ground plane {Figure 5.14 d)} and the PDAwP placed parallel to the ground plane {Figure 5.14 e)}) are shown in Table 5.2

HPBW, deg	**470MHZ**		**550MHz**		**650MHz**		**750MHz**		**850MHz**	
	E-plane	**H**-plane	**E**-plane	**H**-plane	**E**-plane	**H**-plane	**E**-plane	**H**-plane	**E**-plane	**H**-plane
PDAwP	84°	180°	80°	180°	75°	180°	70°	180°	59°	180°
PDAwP ⊥ GP	75°	149°	71°	147°	65°	155°	59°	155°	88°	140°
PDAwP || to GP	65°	90°	71°	80°	72°	76°	67°	72°	66°	84°

Table 5.2 HPBW values of the various PDAwP configurations

In order to validate the simulated return loos results, measurements were carried out. The ANRITSU 37397D Vector Network Analyzer 40MHz - 65GHz [5] was used to take measurements during this experiment. A comparison of the measured and simulated results of the PDAwP alone and over the ground plane is illustrated in Figure 5.19 a). Simulated and measured results of the PDAwP alone and placed in parallel to the reflector are shown in Figure 5.19 b). The bandwidth values of the these PDAwP configurations are shown in Table 5.3

Antenna system	**Bandwidth, %**	
	Simulated	**Measured**
PDAwP {Figure 5.14 b)}	52	54.8
PDAwP ⊥ GP {Figure 5.14 d)}	49.4	57.5
PDAwP || to GP {Figure 5.14 e)}	52.4	60.2

Table 5.3 The bandwidth values of the various PDAwP configurations

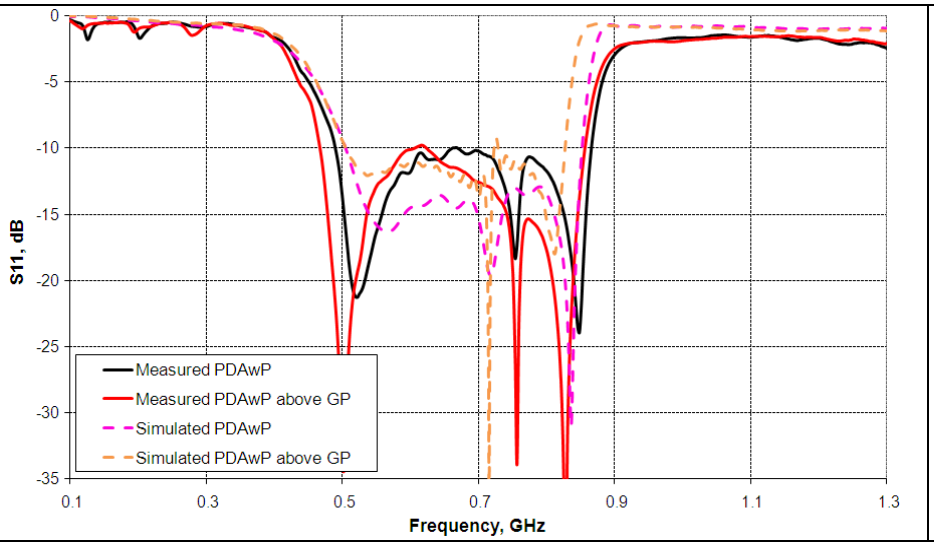

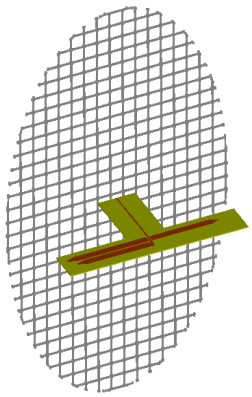

a) The PDAwP with and without ground plane placed above

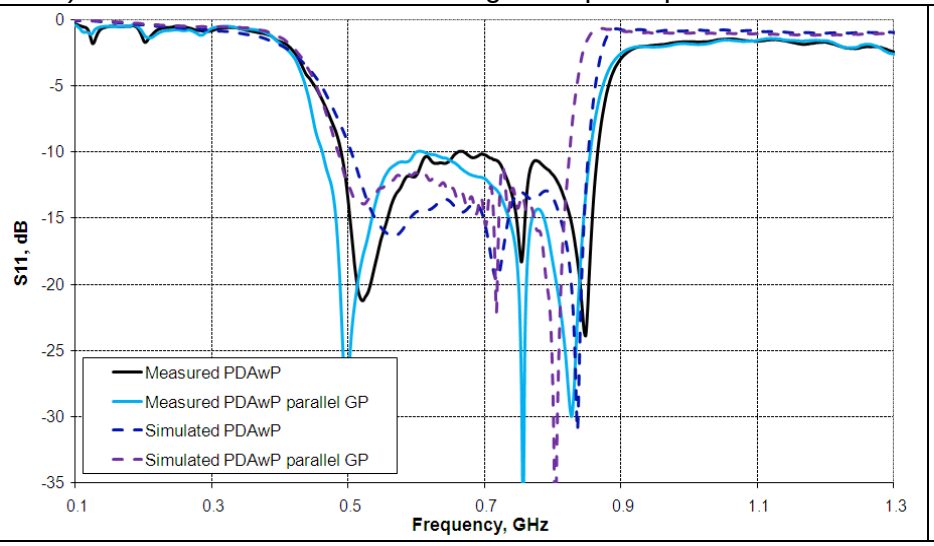

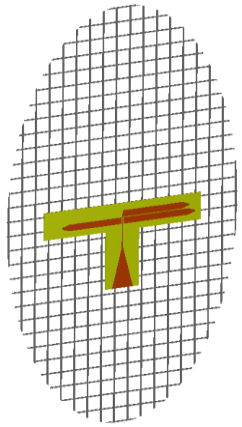

b) The PDAwP with and without groundplane placed parallel

Figure 5.19 Comparison of the simulations and measurements

The measurement results show wider bandwidth than the simulation results. The measured PDAwP alone achieves 2.8% broader bandwidth than simulated one. The measured PDAwP placed above the GP and in parallel to GP achieves as well increased bandwidth of 7.8% and 8.1% respectively. However, both the simulated and measured return loss results have same trends.

5.3.2 Results for OPDAwP placed over ground plane

The performance of the OPDAwP placed above the ground plane was investigated. The return loss results are shown in Figure 5.20. Solid lines represent results for the OPDAwP alone and dotted lines correspond to the OPDAwP placed above the ground plane.

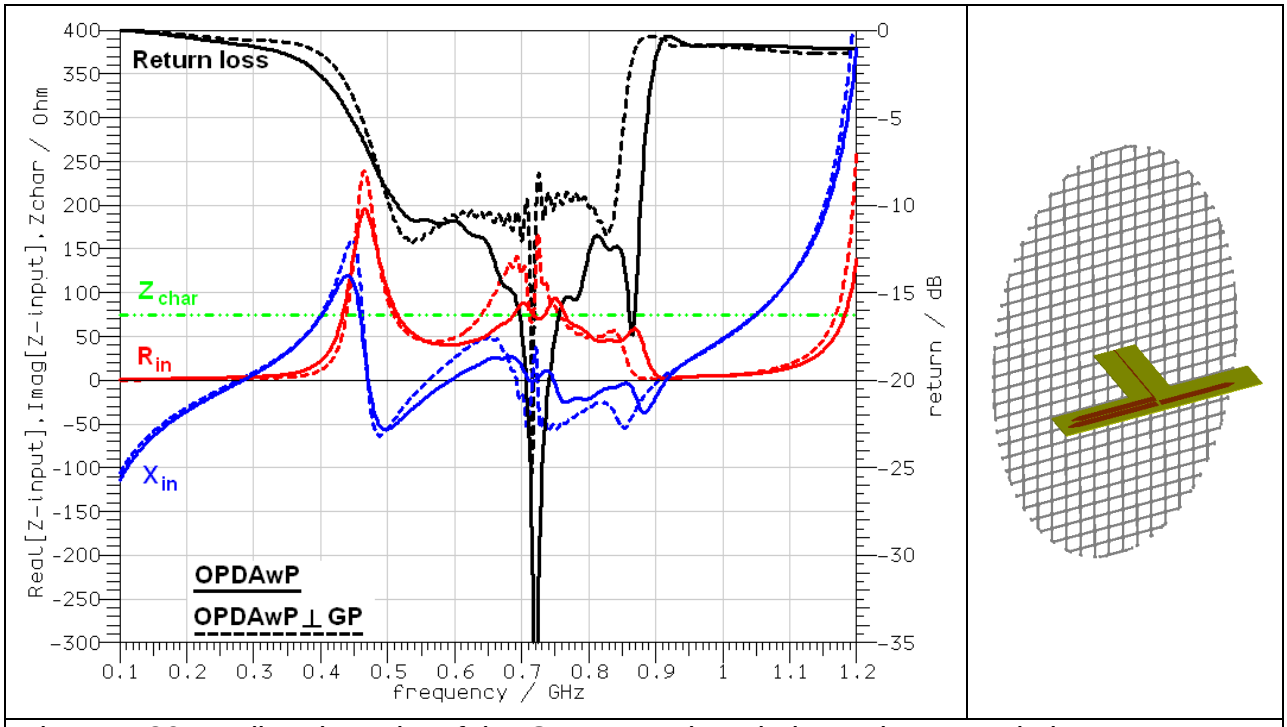

Figure 5.20 Predicted results of the OPDAwP placed above the ground plane

The radiation patterns of the OPDAwP placed above the ground plane are illustrated in Figure 5.21. Comparing these results to the ones described previously (i.e. PDAwP placed over the ground plane Figure 5.16), the OPDAwP placed above the ground plane is far superior. It has more directive beams in both the E and the H planes and the negative effect of the redirected main beam backwards disappears at 800MHz - 850MHz frequencies.

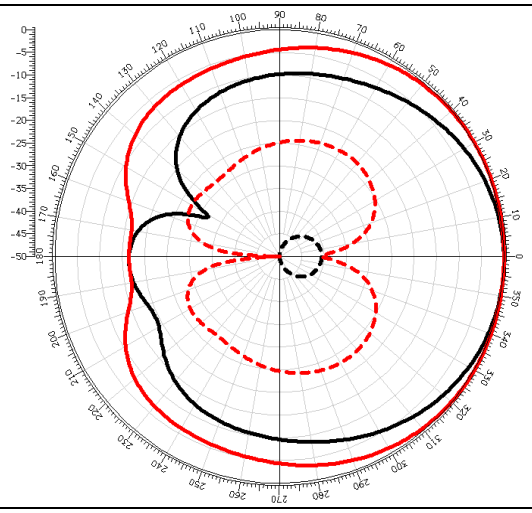

470 MHz

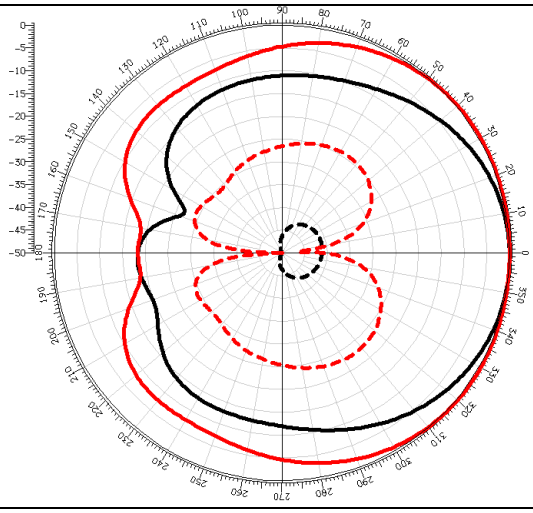

550 MHz

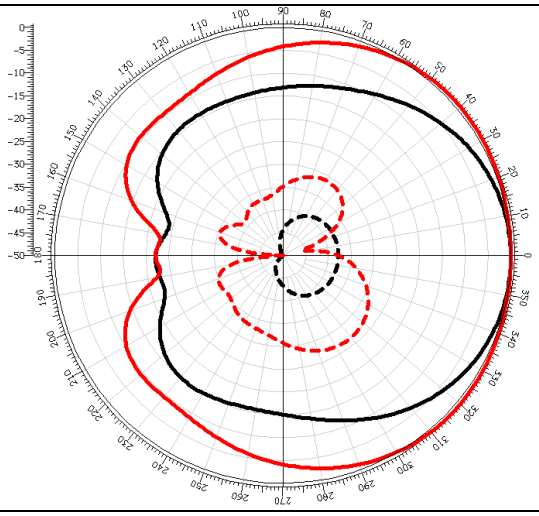

650 MHz

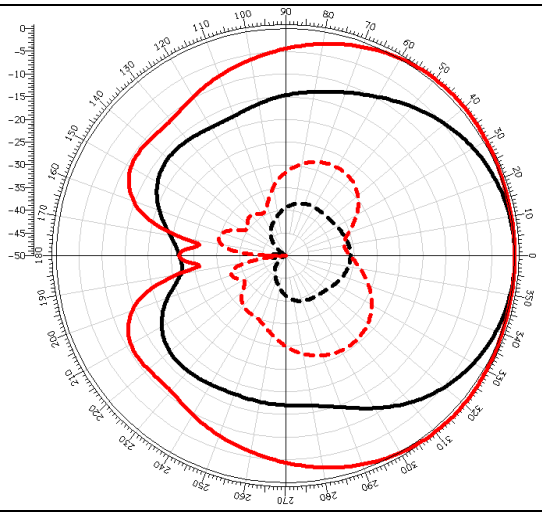

750 MHz

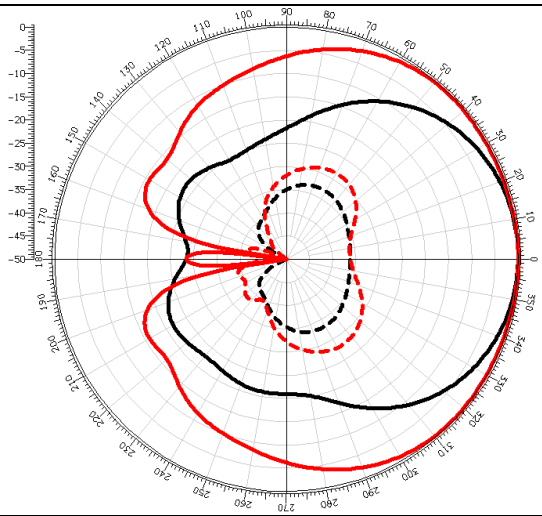

850 MHz

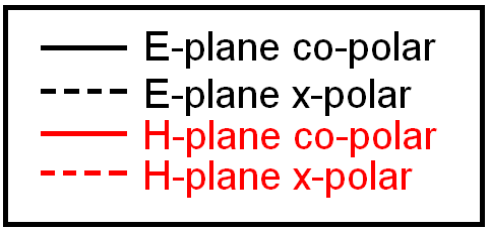

Figure 5.21 Radiation patterns of the OPDAwP placed over the ground plane

Finally, Figure 5.22 illustrates the return loss results when the OPDAwP is placed in parallel to the ground plane. These are the best results achieved in the simulation, during the research, for the radiating antenna placed over the ground plane. The predicted OPDAwP bandwidth is 54%, and the bandwidth of the OPDAwP, placed in parallel to the ground plane, is 52%.

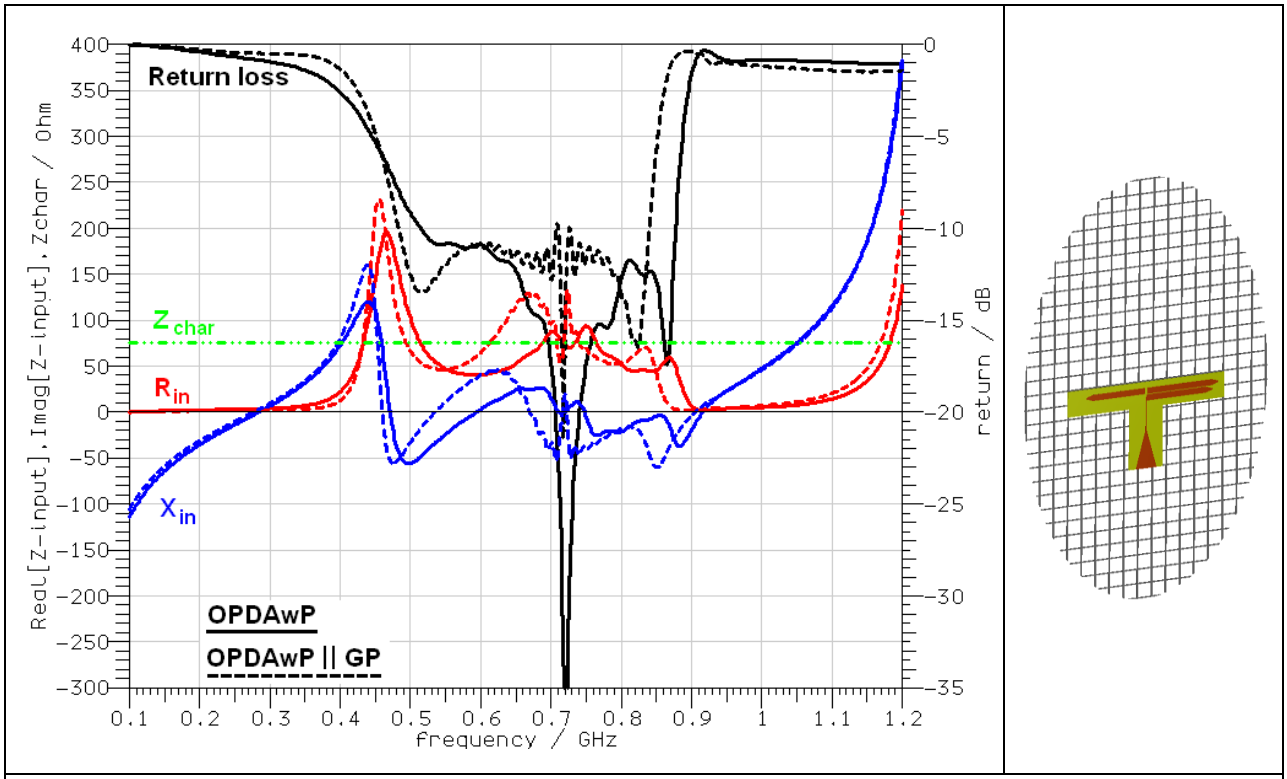

Figure 5.22 Predicted results of the OPDAwP placed parallel to the ground plane

The predicted radiation patterns are shown in Figure 5.22. The Front-to-Back ratio varies from 16dB to 21dB (470MHz - 850MHz).

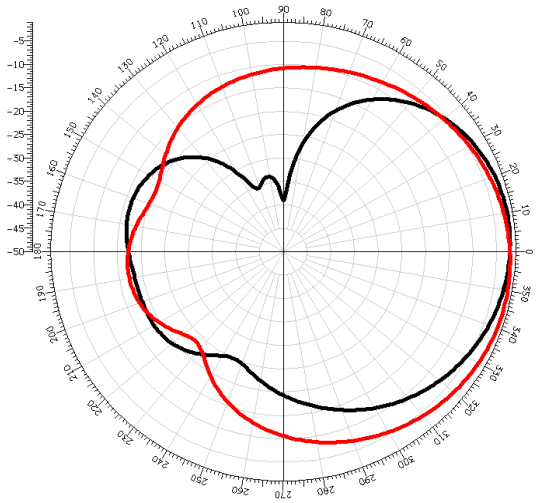

470 MHz

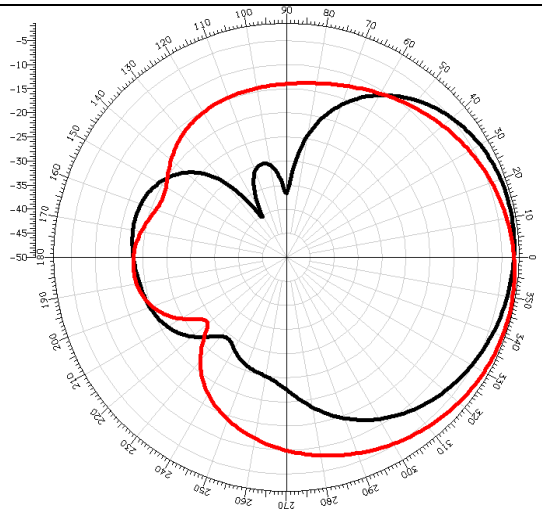

550 MHz

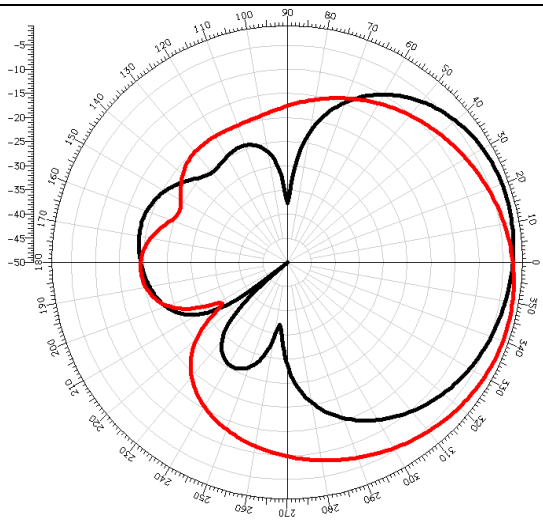

650 MHz

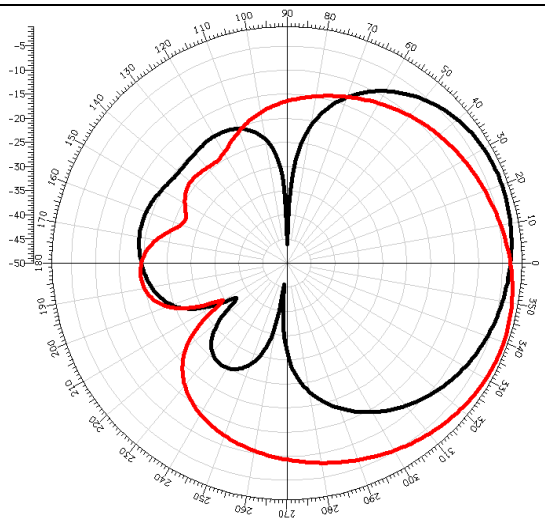

750 MHz

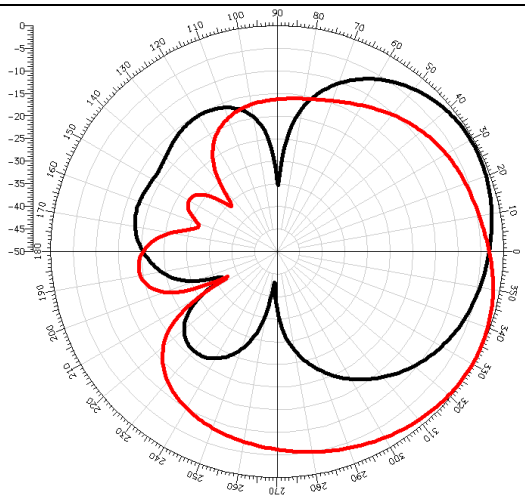

850 MHz

Figure 5.23 Radiation patterns of the OPDAwP placed parallel to the ground plane

The half power beam width values for the various OPDAwP configurations (the OPDAwP alone {Figure 5.14 c)}, the OPDAwP placed above the ground plane {Figure 5.14 f)} and the OPDAwP placed parallel to the ground plane {Figure 5.14 g)}) are shown in Table 5.4.

HPBW, deg	**470MHZ**		**550MHz**		**650MHz**		**750MHz**		**850MHz**	
	E-plane	**H**-plane	**E**-plane	**H**-plane	**E**-plane	**H**-plane	**E**-plane	**H**-plane	**E**-plane	**H**-plane
OPDAwP	82°	180°	80°	180°	74°	180°	71°	180°	63°	180°
OPDAwP ⊥ GP	77°	152°	70°	151°	65°	154°	62°	153°	60°	148°
OPDAwP || to GP	65°	87°	70°	75°	70°	61°	66°	61°	54°	64°

Table 5.4 HPBW values of the various OPDAwP configurations

To validate the return loss simulated results, measurements were carried out. The comparison between the simulation and measurement results is shown in Figure 5.24. The bandwidth values are represented in Table 5.5

Antenna system	**Bandwidth, %**	
	Simulated	**Measured**
OPDAwP {Figure 5.14 b)}	52.9	56.8
OPDAwP ⊥ GP {Figure 5.14 d)}	50.3	61.4
OPDAwP || to GP {Figure 5.14 e)}	53.8	62.2

Table 5.5 The bandwidth values of the various OPDAwP configurations

The measured OPDAwP alone achieves 3.9% broader bandwidth in comparison to the simulated one. However, the measured OPDAwP placed above the GP achieves 11.1% broader bandwidth compared to the predicted one.

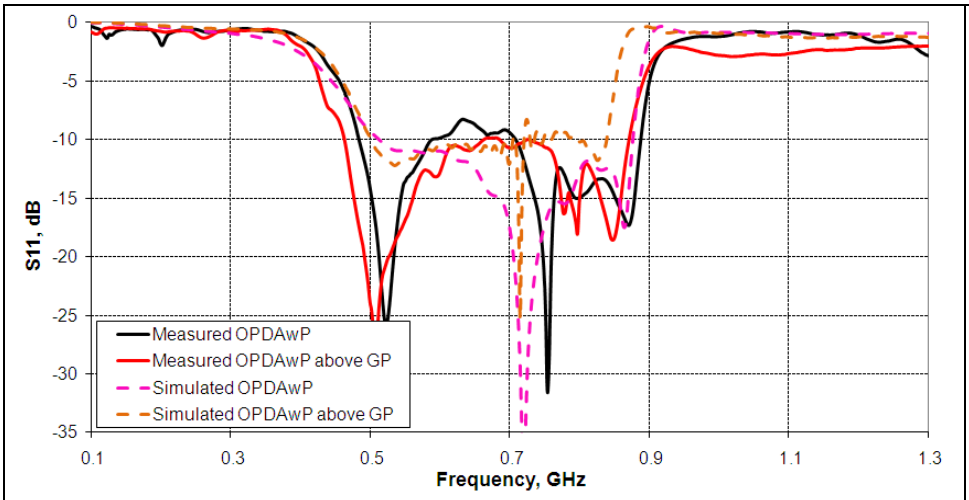

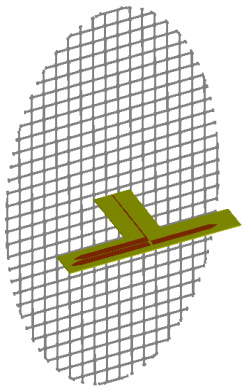

a) The OPDAwP alone and the OPDAwP placed above the ground plane

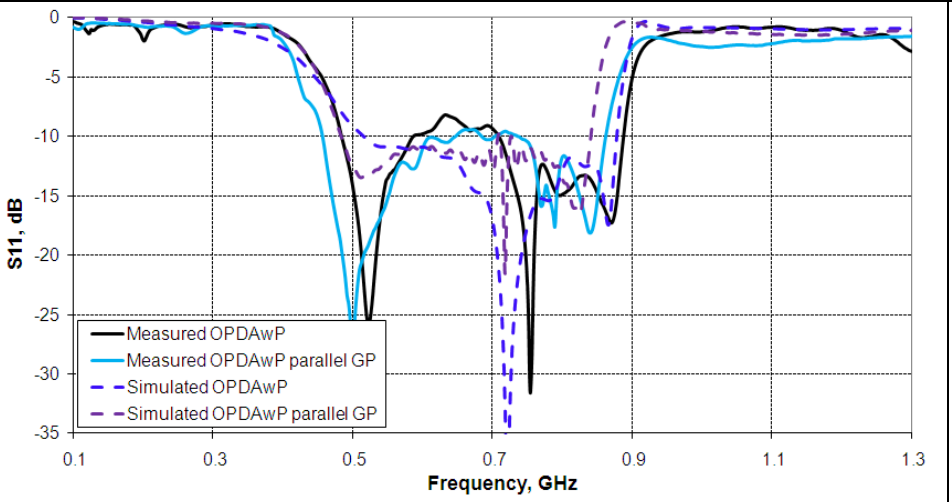

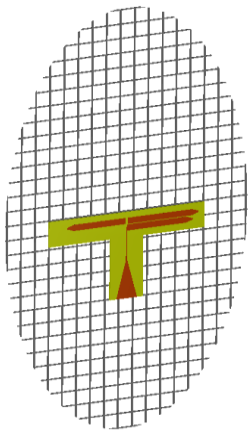

b) The OPDAwP alone and the OPDAwP placed parallel to the ground plane

Figure 5.24 Comparison of the simulations and measurements

Results showed that measurements performed even better than the simulation. The OPDAwP match was slightly worse in comparison to the PDAwP match at 610MHz ~-8dB, but the trend of the higher operating frequency band increased. On the other hand, the resonance at 610MHz was improved (-10dB) by placing the ground plane above/ in parallel to the OPDAwP.

5.3.3 Directivity results for various PDA configurations

The predicted directivity results for various printed dipole antenna configurations with and without ground plane are shown in Table 5.6.

Frequency, / Antenna type	Directivity, dBi				
	470 MHz	**550 MHz**	**650 MHz**	**750 MHz**	**850 MHz**
PDA	2.24	2.34	2.5	2.69	2.91
PDAwP	2.2	2.28	2.42	2.75	5.14
PDAwP ⊥ GP	4.85	5.2	5.6	6.01	4.39
PDAwP ‖ to GP	8.02	8.34	8.77	9.09	7.24
OPDAwP	2.32	2.47	2.73	3.08	4.4
OPDAwP ⊥ GP	5.07	5.47	5.81	6.14	6.48
OPDAwP ‖ to GP	8.05	8.42	8.90	9.42	10.45

Table 5.6 Predicted directivity results of the various PDA

The predicted directivity results from Table 5.5 for various PDA configurations are illustrated in Figure 5.25.

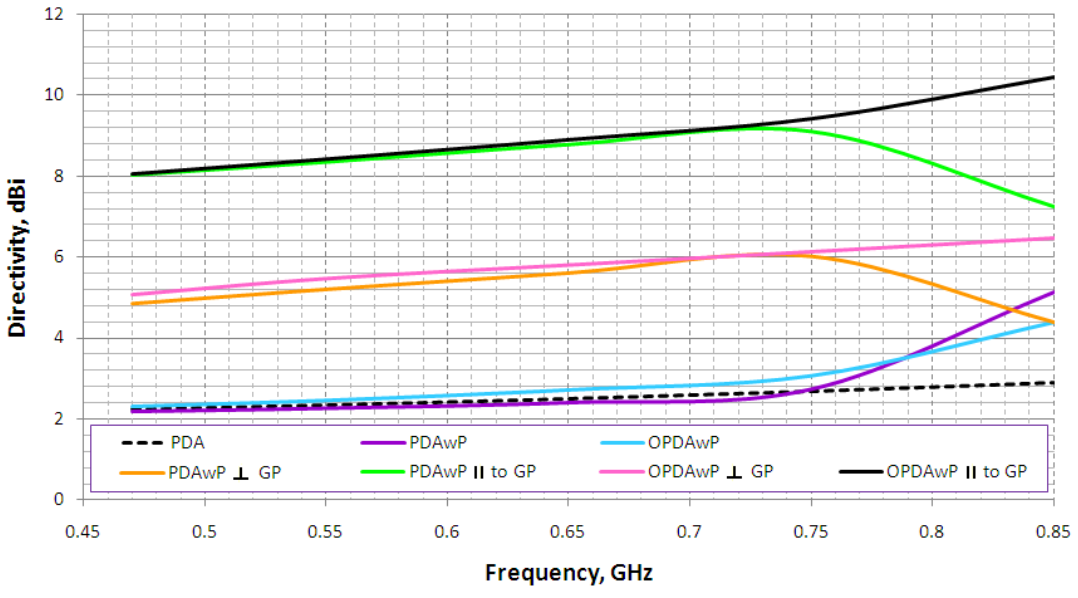

Figure 5.25 Predicted directivity results of the various PDA

The graph (Figure 5.25) compares seven different directivity results for various PDA configurations: the PDA alone {Figure 5.14 a)}, the PDAwP alone {Figure 5.14 b)}, the OPDAwP alone {Figure 5.14 c)}, the PDAwP placed above the GP {Figure 5.14 d)}, the PDAwP placed in parallel to the GP {Figure 5.14 e)}, the OPDAwP placed above the GP {Figure 5.14 f)} and the OPDAwP placed in parallel to the GP {Figure 5.14 g)}. The directivity values of the PDA alone increase slightly when frequency increases, i.e. from 2.2dBi to 2.9dBi. The PDA, the PDAwP and the OPDAwP have similar directivity values from 470MHz to 750MHz. However, due to a parasitic element, the PDAwP and the OPDAwP achieve more directional beams at 800MHz -850MHz (see Chapter 4). This results in the increase of directivity values to 5.14dBi and 4.4dBi for the PDAwP and the OPDAwP respectively.

When two PDA's (the PDAwP and the OPDAwP) are placed over the ground plane, the directivity values increase by more than 2.5dBi. However, the PDAwP placed over the GP at a higher frequency has a negative impact on the antenna radiation due to the parasitic element. This phenomenon was reported in previous chapter (section 4.3.4).

The best directivity values were achieved in case when the OPDAwP is placed in parallel to the GP. The directivity values are as high as 8.05dBi and 10.45dBi at 470MHz and 850MHz respectively.

5.4 Outdoor measurements

In order to validate the predicted radiation pattern results, measurements were made for the prototype antenna. The available anechoic chamber was not suitable for the UHF (470MHz – 850MHz) antenna measurements. The anechoic chamber is designed for the frequency band from 900 MHz to 6 GHz. The roof of the Electronic and Electrical Engineering Department building was the only suitable place to carry out the measurements. The antenna under test (AUT) was a printed dipole antenna with a parasitic element (PDAwP), placed above an ellipse shaped ground plane with a periodically rectangular perforations (Figure 5.14d). The radiation patterns (the E-plane co-polar, x-polar and the H-plane co-polar) were measured at various frequencies. Five main frequencies were chosen at constant intervals through the 470MHz -850MHz frequency band (i.e. 470MHz, 550MHz, 650MHz, 750MHz, 850MHz). For calibration purposes five pairs of the balanced $\lambda_0/2$ dipoles were manufactured at the chosen frequencies. They were tested and used for outdoors measurements as testing antennas.

Three types of the commercial high gain Yagi Uda antennas were bought from the German Company “Kathrein” [1] (3 elements, 6 and 11 elements), to compare the measurement technique and the performance of the novel PDAwP placed above the reflector.

5.4.1 Dipole Calibration

Five sets of dipole pairs were manufactured. The dipoles were used to measure the gain and the radiation patterns of the AUT. The $\lambda_0 / 4$ balun was used for a balanced dipole [6, 7]. The diagram, representing this structure, is shown in Figure 5.26. In this figure **A** corresponds to the input to the antenna and **B** is the shorted outer at $\lambda_0 / 4$ distance. However, considering the velocity of propagation inside the cable, the inner is cut at distance C, which is equal to $\frac{\lambda_0}{4\sqrt{\varepsilon_r}}$ (ε_r is the cable substrate permittivity value). **Port1** and **Port2** are in balanced.

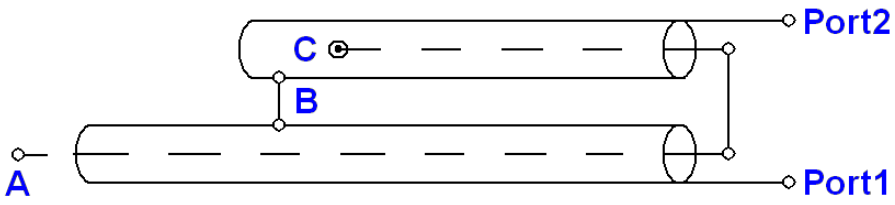

Figure 5.26 Diagram of the balun

The structure of the manufactured balanced dipole, designed to resonate at 470MHz, is shown in Figure 5.27. The same variables (A, B, C, Port 1 and Port 2) from Figure 5.26 are represented in Figure 5.27.

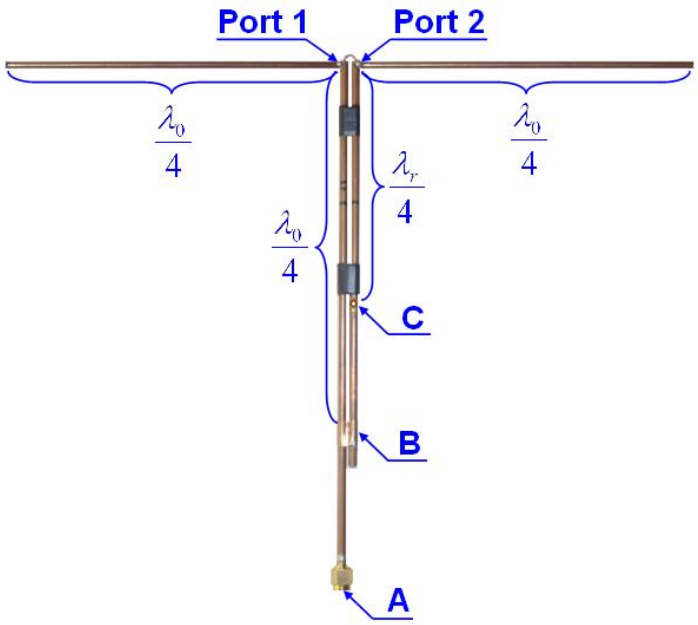

Figure 5.27 Manufactured dipole at 470MHz frequency

The image of all manufactured dipoles is shown in Appendix D (Figure A4). It was necessary to design a dipole pair (Rx, Tx) which would match at the same frequency. The measurement results show that there is a neglectable discrepancy of the return loss values between the dipoles in a pair. The measured return loss of five sets of dipole pairs is shown in Figure 5.28. A semi rigid coaxial cable of 50Ω with a SMA male connector of 50Ω was used to manufacture dipole antennas.

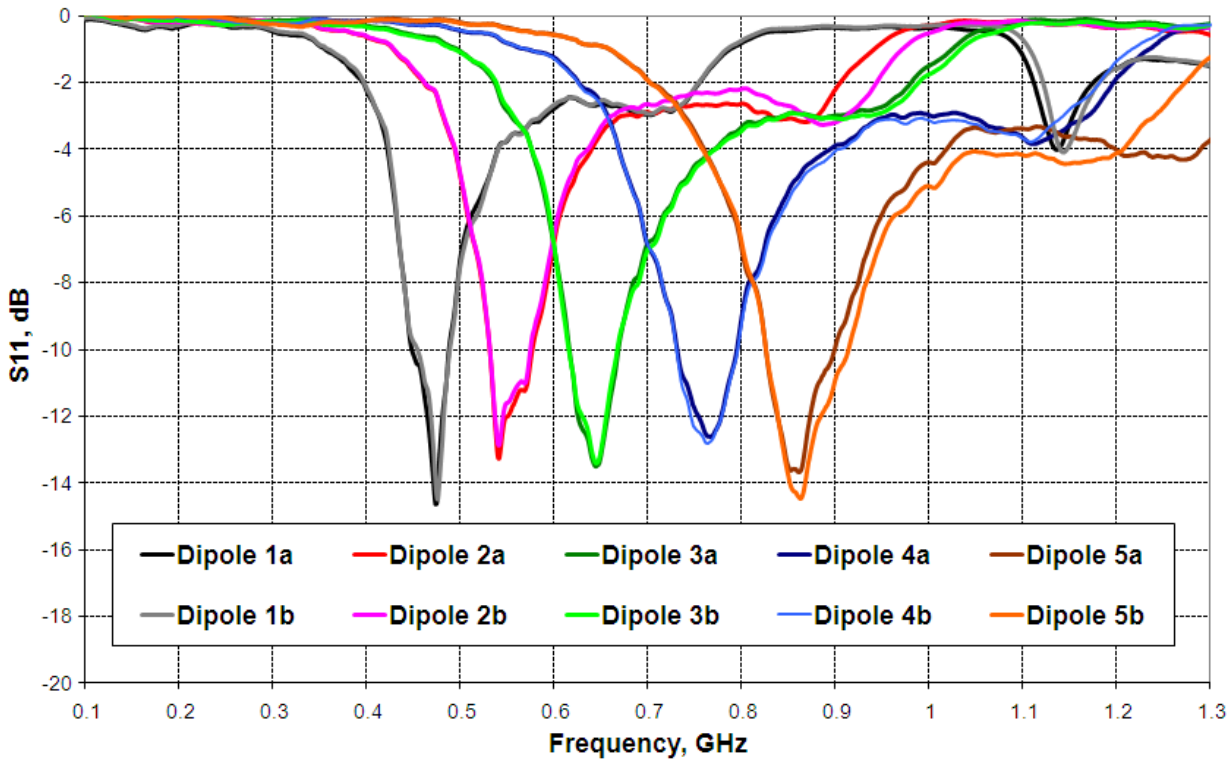

Figure 5.28 Measured return loss of the five dipole set of pairs

The bandwidths for the manufactured dipoles were calculated at 10dB of the return loss in the following way:

$$BW_{Dipole\ 1a,b} = \frac{40MHz}{470MHz} \cdot 100\% = 8.51\%; \qquad BW_{Dipole\ 2a,b} = \frac{43MHz}{553.5MHz} \cdot 100\% = 7.77\%$$

$$BW_{Dipole\ 3a,b} = \frac{52MHz}{642MHz} \cdot 100\% = 8.1\%; \qquad BW_{Dipole\ 4a,b} = \frac{63MHz}{763MHz} \cdot 100\% = 8.65\%$$

$$BW_{Dipole\ 5a} = \frac{74MHz}{863MHz} \cdot 100\% = 8.57\%.$$

The largest bandwidth was achieved for the fourth dipoles pair, $BW_{Dipole\ 4}$ and is equal to 8.65%

The comparison of the simulated and measured radiation patterns for the $\lambda_0/2$ balanced dipole is shown in Figure 5.29.

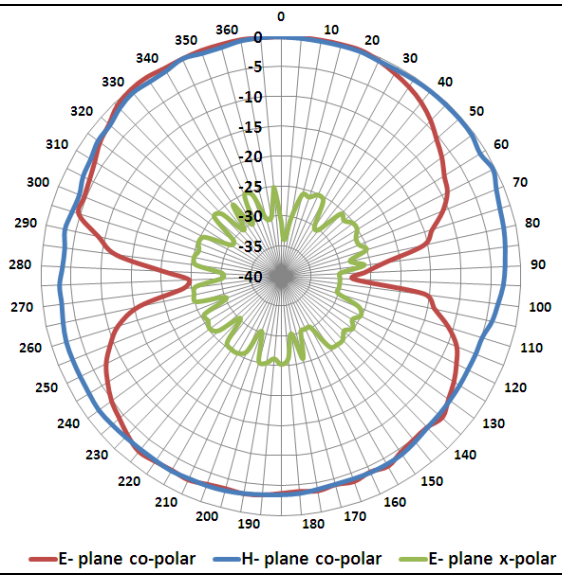

Measured @ 470MHz

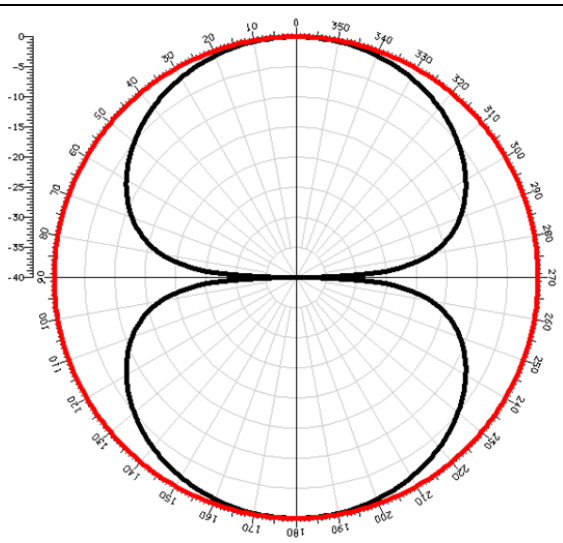

Simulated @ 470MHz

Figure 5.29 Simulated and measured dipole radiation patterns

The measured radiation patterns at 470MHz (E, H-planes co-polar) for the $\lambda_0/2$ balanced dipole are very similar to the simulated results. The dynamic range (DR) was varying from 40dB to 53dB through all outdoor measurements.

5.4.2 Measurements setup

The outdoors measurements setup structure is shown in Figure 5.30. The length of the antenna range is important, if it is too short, there will be significant phase difference over the aperture of the antenna being tested, resulting in low measured gain. The minimum range length to avoid this error is the Far Field (FF) distance:

$$FF = \frac{2 \cdot D^2{}_a}{\lambda_0} \qquad \text{eq.5.1}$$

Where D_a is the largest dimension of the aperture. The D_a varies from 0.16m (850MHz balanced dipole) to 1.34m (13 element Yagi-Uda) for the all antennas measured outdoors.

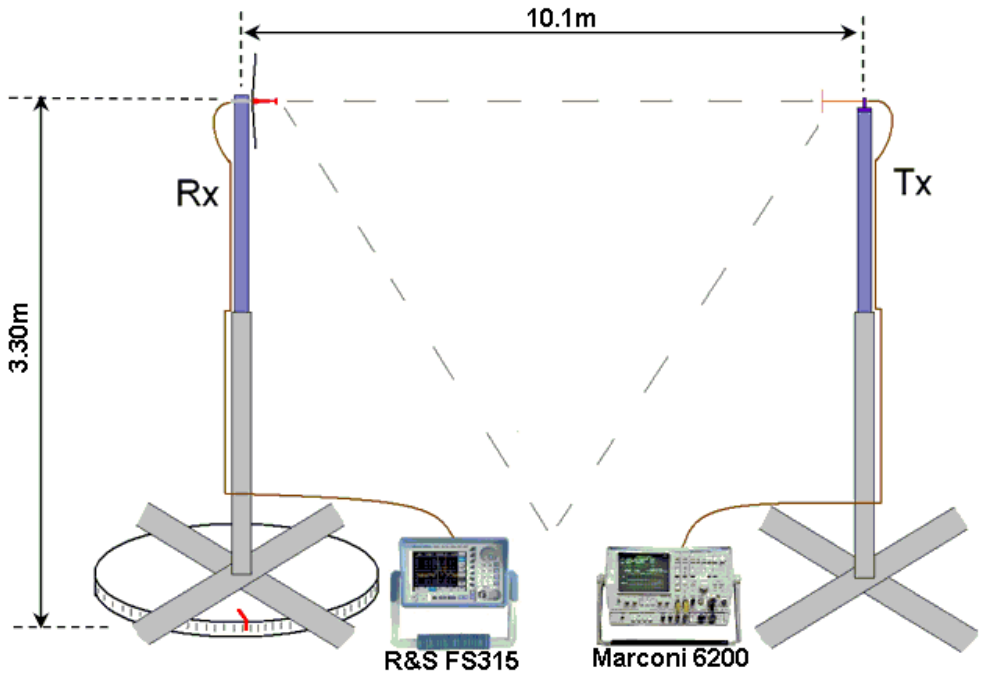

Figure 5.30 Measurement set up on the roof of a three storey building

The far field distance for 13 element Yagi UDA antenna at 850MHz is equal to 5.1m. The transmitter and receiver were placed 10 meters apart, see Figure 5.30. The antenna stands consisted of two materials: a lower part made from a 2 metre high metallic stand and a higher part made from a plastic material (1.3metres).

The receiver was placed on the revolving platform, which performs 360° rotation and a MARCONI INSTRUMENTS Reflection Analyzer (10MHz - 20GHz Marconi Test Set 6200) [8] was used to generate a continuous wave (CW) signal for the transmission. A ROHDE & SCHWARZ FS315 Spectrum Analyzer (9 kHz - 3 GHz) [9] was used for the signal reception, as a standalone receiver. The picture of the roof, where the measurement took place, is shown in Figure 5.31.

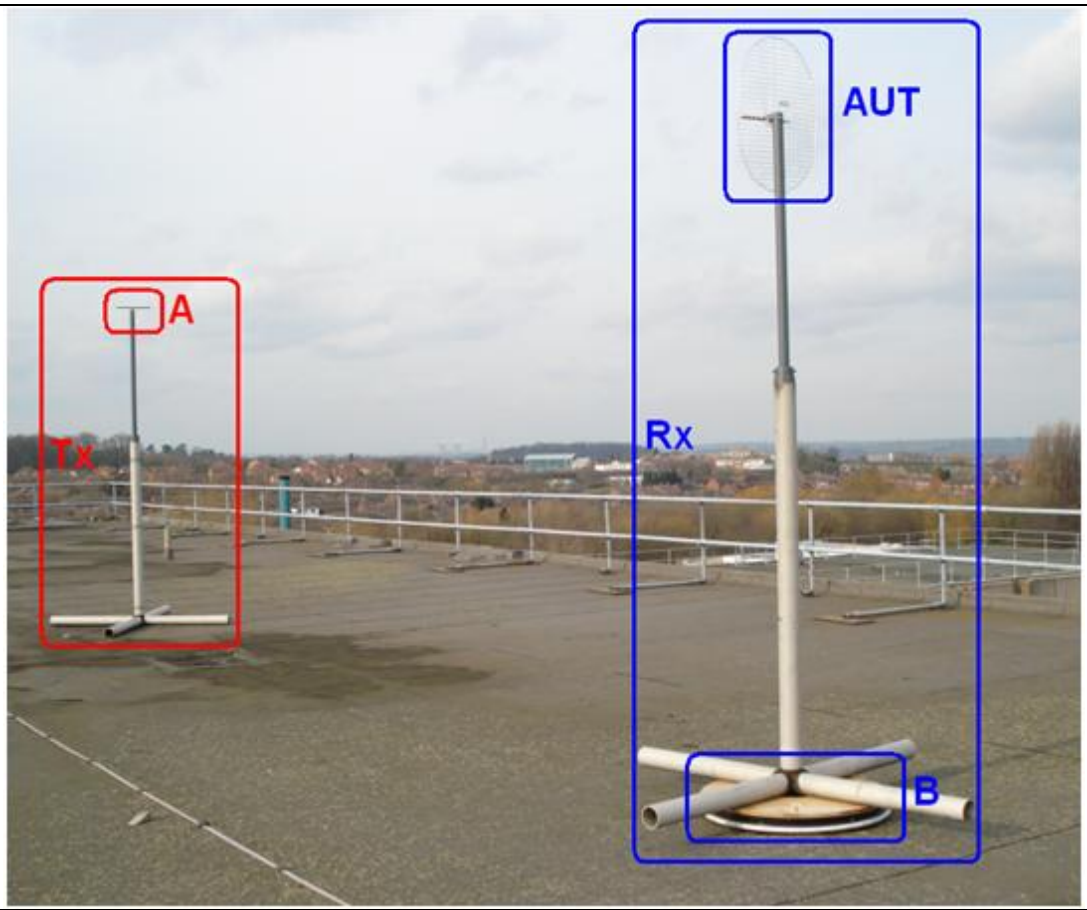

Figure 5.31 The outdoor measurements setup

In Figure 5.30 **A** represents the measuring antenna (the balanced $\lambda_0/2$ dipole) and **B** is the turn table for the receiver (Rx).

Special mechanical adapters were added to both top ends of the stands in order to connect and hold dipoles and cables (see Figure 5.32).

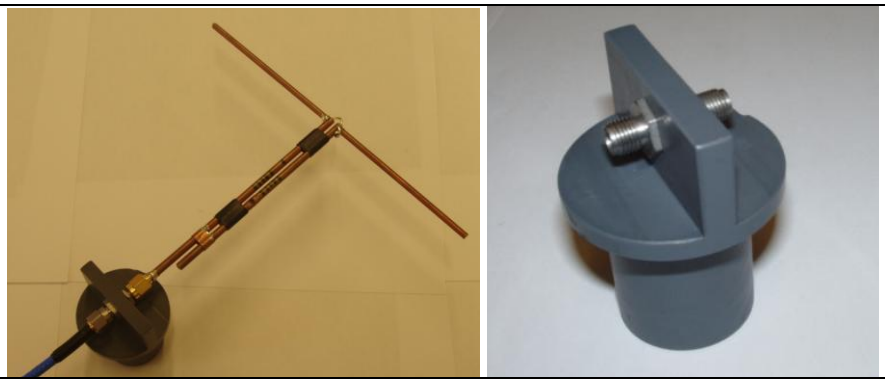

Figure 5.32 Adapter which holds and connects the dipole and the cable

A 5m RHOFLEX [10] R402 cable with a diameter of 4.14mm and 50Ω impedance was used for the dipole gain measurements. It connected the transmitter to the wave generator and the receiver to the spectrum analyser. A semi rigid coaxial cable of 75Ω reference was used to connect AUT to the spectrum analyser, for the PDAwP placed above the ground plane measurements. For measured frequencies the attenuation losses of cables are shown in Figure 5.33.

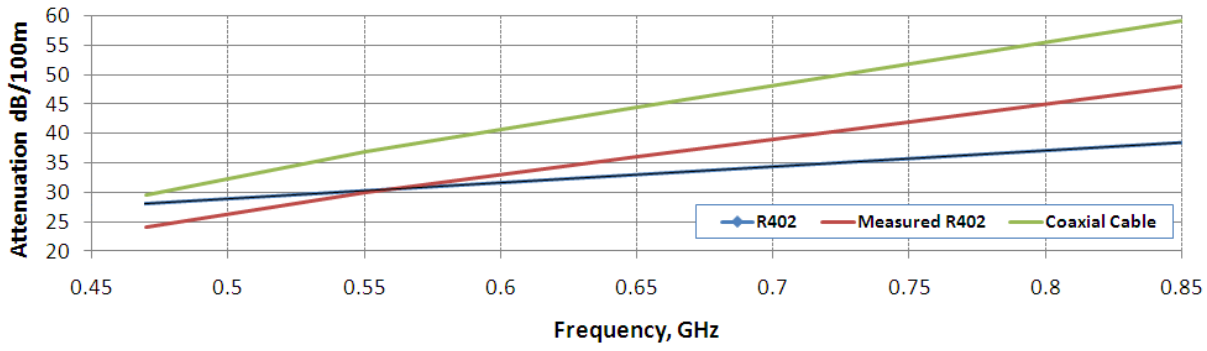

Figure 5.33 Attenuation results in the outdoors measurements

The attenuation results for cables used in outdoors measurements and for the free space path loss (FSPL) are shown in Table 5.7.

Frequency / Attenuation, dB	470MHz	550MHz	650MHz	750MHz	850MHz
5m cable R402	1.43	1.51	1.68	1.79	1.93
Measured 5m cable R402	1.2	1.5	1.8	2.1	2.4
Measured 5m Coaxial cable	1.48	1.85	2.22	2.59	2.96
FSPL	45.6	47.1	48.5	49.8	50.9

Table 5.7 Attenuation results in measurements

The attenuation losses of cables were measured by using the HP 438A Power Meter [11]. The connectors and cables used in outdoors measurements are shown in Figure 5.34.

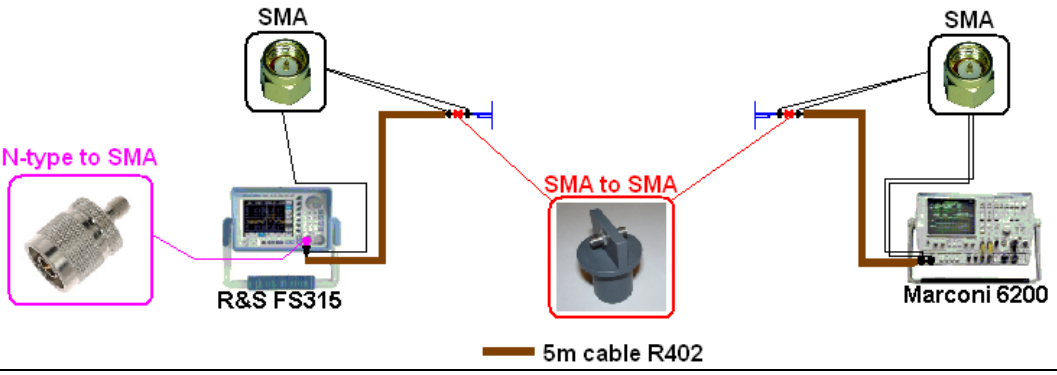

Outdoors measurement setup for two dipoles

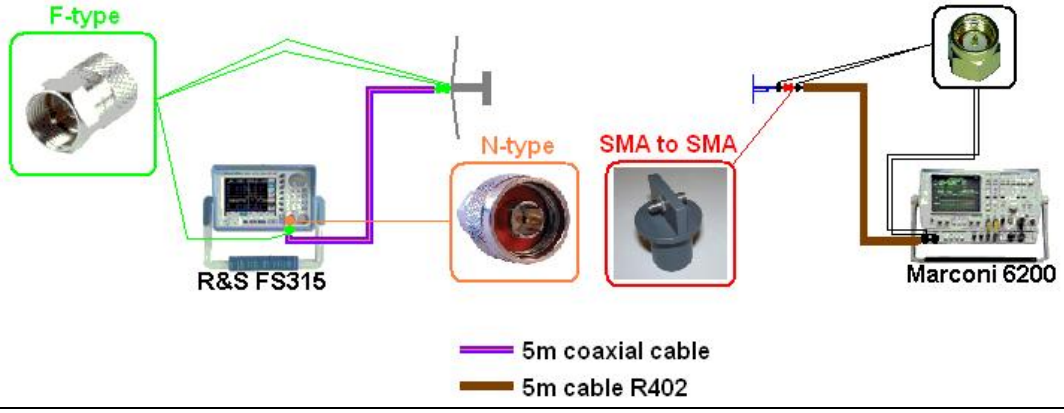

Outdoors measurement setup for PDAwP+GP and dipole

Figure 5.34 Connectors and cables used in outdoors measurements

The measured five meter cable (R402) included two male SMA connectors at the ends of the cable and the measured 5m coaxial cable attenuation included two F-type male connector losses.

In the beginning of the outdoor measurements the received power (P_{Rx}) was measured of the five pairs of the dipoles. The transmitted power (P_{Tx}) was the generated continuous wave of 5 dBm. In order to estimate the gain from measurements, Friis transmission equation [12] was used (see eq. 5.2)

$$\frac{P_{Rx}}{P_{Tx}} = G_{Rx} \cdot G_{Tx} \left(\frac{\lambda}{4 \cdot \pi \cdot R} \right)^2 \qquad \text{eq.5.2}$$

By assuming that the dipoles have the same electromagnetic propagation performances ($G_{Rx} = G_{Tx}$), a single dipole gain would be equal to:

$$G_{Dipole} = \sqrt{\frac{P_{Rx}}{P_{Tx} \left(\frac{\lambda}{4 \cdot \pi \cdot R} \right)^2}} \qquad \text{eq.5.3}$$

To calculate the antenna under test (AUT) gain values the following equation was used:

$$G_{Rx} = \frac{P_{Rx}}{P_{Tx} \cdot G_{Dipole} \cdot \left(\frac{\lambda}{4 \cdot \pi \cdot R} \right)} \qquad \text{eq.5.4}$$

The concrete of a floor of buildings is typically made up of a wire mesh embedded in a thick layer of concrete cement for structural reinforcement. The mesh may consist of straight wires joined perpendicular to give planar periodic array of square grid for structural reinforcement. When the array is illuminated by EM waves, its periodicity would exhibit certain reflection characteristics depending on the size of the

grid and the concrete properties [4, 13]. The Ground reflection from the floor concrete could be calculated only if detailed structure of the concrete would be known. However the incidence angle (θ) on the ground and the path phase difference (ϕ) can be easily calculated (Figure 5.30):

$$\theta = \tan^{-1}\left(\frac{H_1 + H_2}{d}\right) = \tan^{-1}\left(\frac{3.3m + 3.3m}{10.1m}\right) = 33° \qquad \text{eq.5.5}$$

$$\phi = k(R - D) \qquad \text{eq.5.6}$$

Where $D = \sqrt{d^2 + (H_1 - H_2)^2}$; $R = \sqrt{d^2 + (H_1 + H_2)^2}$; $k = 2\pi/\lambda_0$

The path phase difference (ϕ) for all outdoor measured antennas are shown in Appendix E. It is varying in all cases, because the different antennas represent different distance between the receiver and the transmitter.

5.4.3 Measurements

The return loss results were carried out indoors in the anechoic chamber for the PDAwP with and without the ground plane and for the OPDAwP with and without the ground plane.

The outdoor radiation pattern measurements were done only for the PDAwP placed above the ground plane (see Figure 5.35). The adverse weather conditions within the slot, allocated for the outdoor measurements, prevented a systematic repeat of measurements as well as the testing of the OPDAwP placed above the ground plane.

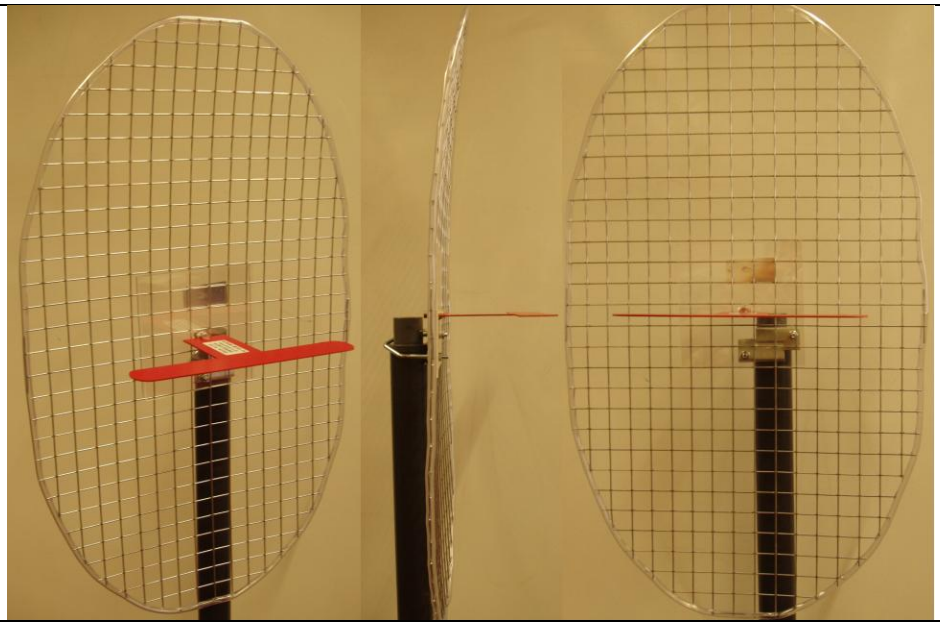

Figure 5.35 The PDAwP placed above the ground plane front, side and corner views

However, the boresight gain measurements were a lot less time consuming compared to each 5° radiation pattern measurement. Therefore, they were performed for the PDA with three different ground planes.

5.4.3.1 Return loss measurements

The comparison of the indoor measured return loss results for the PDAwP and the OPDAwP are shown in Figure 5.36.

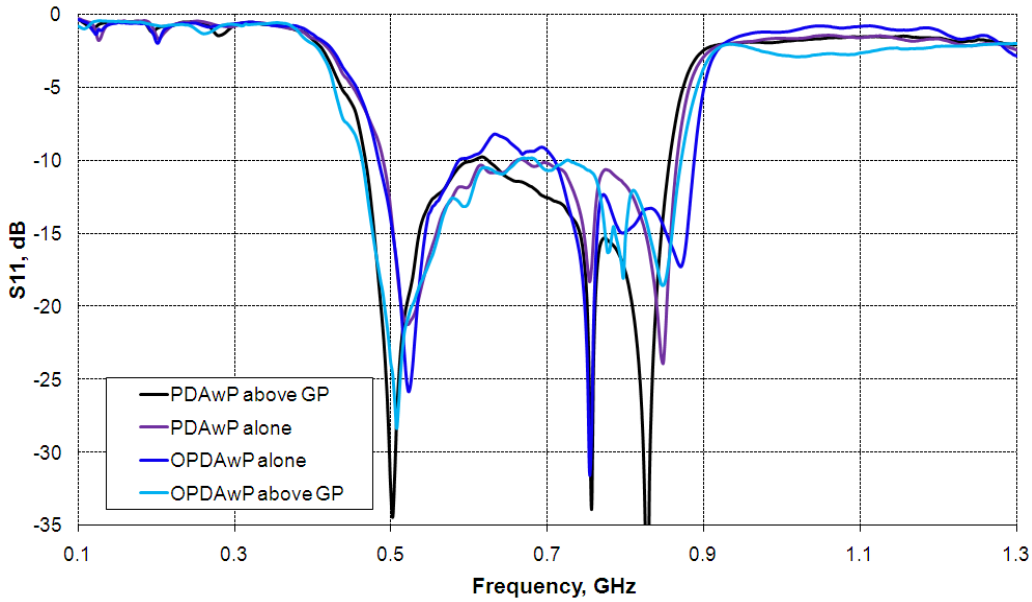

Figure 5.36 Indoor measured results of the various PDA systems

The PDAwP placed above the ground plane achieved a better match than the OPDAwP. However, the larger operating bandwidth is achieved by the OPDAwP placed over the ground plane. $BW_{PDAwP+GP} = 59.8\%$ $BW_{OPDAwP+GP} = 61.6\%$

5.4.3.2 Radiation patterns measurements

The outdoor measured radiation patterns (E-plane co-polar, x-polar and H-plane co-polar) at five different frequencies are shown in Figure 5.37 and Figure 5.38.

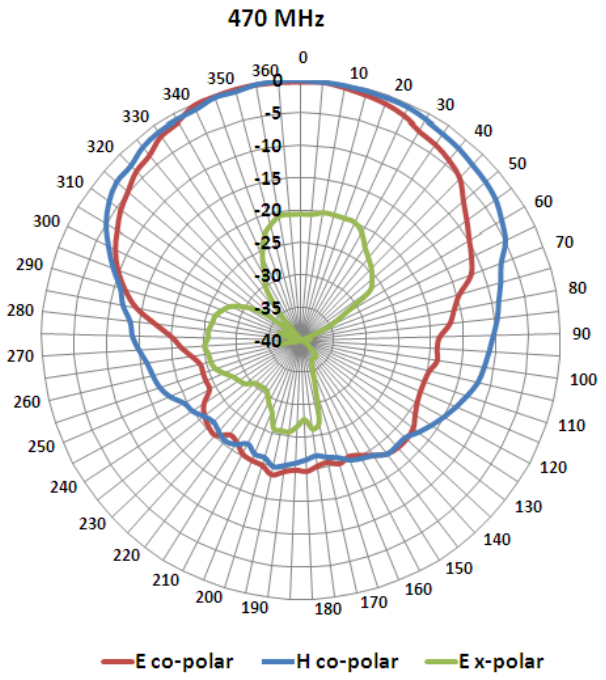

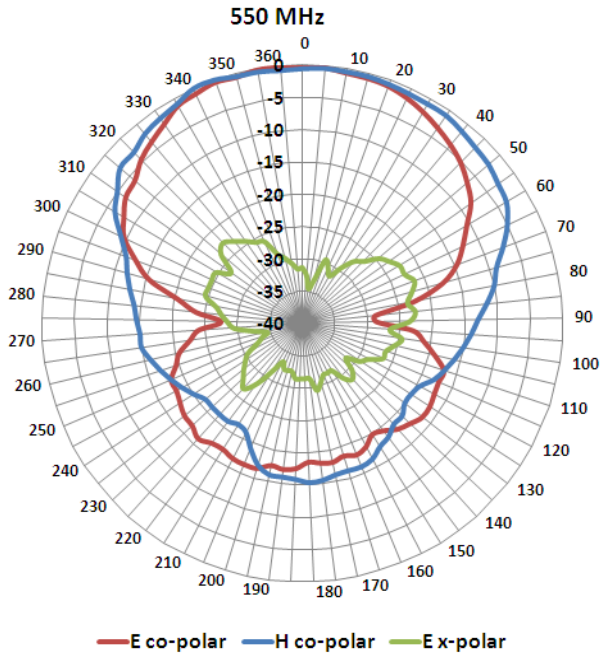

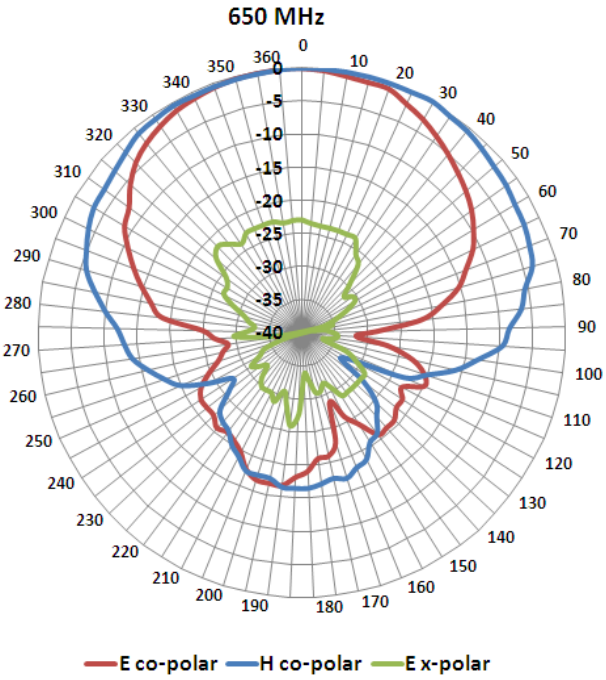

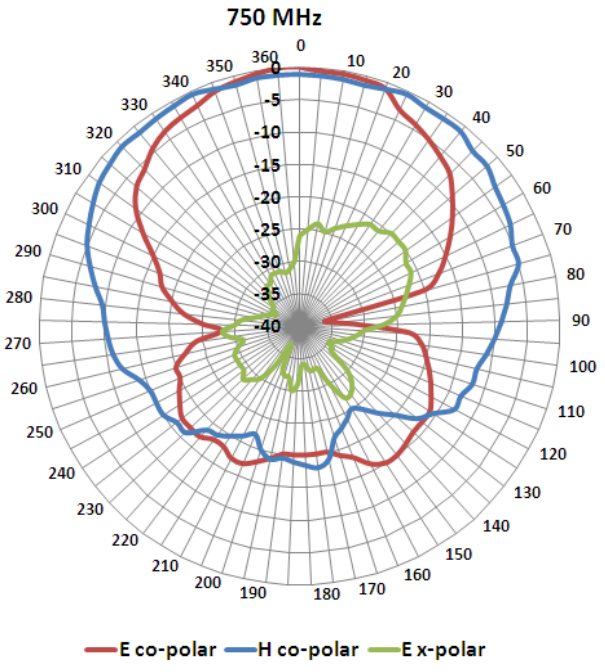

Figure 5.37 Measured radiation patterns for the PDAwP placed above the ground plane at 470MHz, 550MHz, 650MHz and750MHz

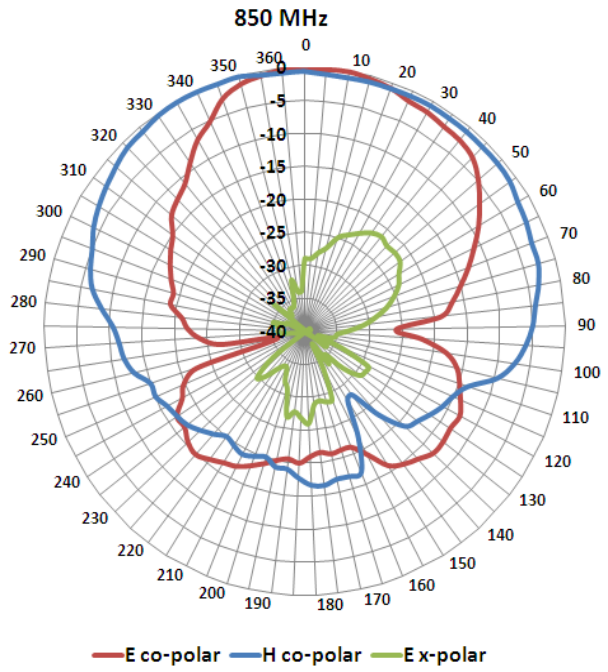

Figure 5.38 Measured radiation pattern for the PDAwP placed above the ground plane at 850MHz

The F/B ratio varies from 16dB to 20dB throughout the operating band. The comparison of the measured and the simulated HPBW results of the PDAwP placed above the ground plane, is shown in Table 5.8.

HPBW, deg	**470MHZ**		**550MHz**		**650MHz**		**750MHz**		**850MHz**	
	E-plane	**H**-plane	**E**-plane	**H**-plane	**E**-plane	**H**-plane	**E**-plane	**H**-plane	**E**-plane	**H**-plane
Simulated	75°	149°	71°	147°	65°	155°	59°	155°	88°	140°
Measured	71°	112°	68°	105°	67°	125°	50°	128°	70°	142°

Table 5.8 The HPBW values of the PDAwP⊥GP

The predicted E-plane half power beam widths are very close to the measured ones, in the frequency range of 470MHz-750MHz. The bigger discrepancy between the predicted and the measured HPBM occurs at the H-plane in a lower frequency range.

5.4.3.3 Gain measurements

The received power was measured at various frequencies for the PDAwP placed above the three different ground planes, i.e. the flat GP (Figure 5.35), the $20°$ inclined GP (Figure 5.39) and the $45°$ inclined GP (Figure 5.40).

Figure 5.39 PDAwP $\perp$ GP $\angle$ 20°

Figure 5.40 PDAwP $\perp$ GP $\angle$ 45°

The corner reflector achieved greatly increased gain values in comparison to the flat plate ground plane, due to a more directional beam form shape. The gain values for the measured and the predicted results for different PDA system variations are shown in Table 5.9.

Frequency / Antenna type	Gain, dBi				
	470MHz	**550MHz**	**650MHz**	**750MHz**	**850MHz**
Simulated					
PDA	0.51	2.26	2.07	1.89	0.59
PDAwP	2.05	2.17	2.23	2.53	4.78
PDAwP ⊥ GP	4.37	4.68	5.04	5.4	3.95
PDAwP || to GP	8.02	8.34	8.77	9.09	7.24
OPDAwP	2.08	2.24	2.45	2.77	3.97
OPDAwP ⊥ GP	4.81	5.19	5.39	5.65	6.18
OPDAwP || to GP	7.8	8.14	8.57	9.11	10.19
Measured					
PDAwP over GP	7.26	9.28	8.21	7.12	5.16
PDAwP ⊥ GP ∠20°	7.95	10.98	9.55	9.21	8.22
PDAwP ⊥ GP ∠45°	7.75	10.68	10.8	10.2	9.12

Table 5.9 Predicted and measured results of the different PDA systems variations

The PDAwP placed above the ground plane measured gain values are about 2dB's larger than the simulated ones. A possible reason for this discrepancy could be interference with the multi reflections from the concrete. Another reason could be the miscalculations caused by the simulation software (rectangular mesh, etc.).

The boresight gain results from the Table 5.9 for various PDA systems are illustrated in a graphical form in Figure 5.41.

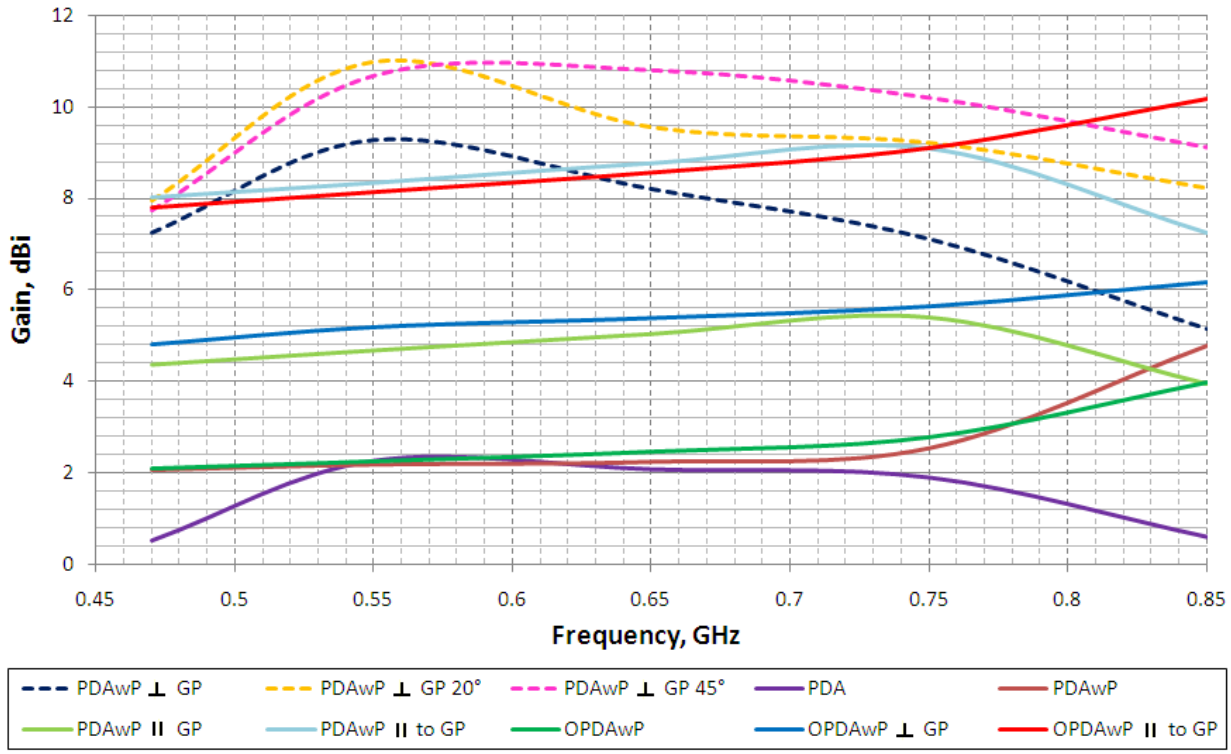

Figure 5.41 Gain results of the PDA system

The measured results are represented by dotted lines and the predicted results of the gain values are shown in solid colours. The measured gain of the PDAwP placed above the ground plane varies from 4.8dBi to 9.2dBi. However, the best measurement results were achieved for the PDAwP placed above the ground plane inclined at $45°$, i.e. from 8dBi to 11dBi.

The best PDA system configuration would be the OPDAwP placed in a parallel to the ground plane. The antenna in this case would be more directive without side lobes at the higher frequency band of 800MHz-850MHz.

5.4.4 Comparative measurements

Finally, in order to compare the novel compact and broadband antenna system at UHF, three types of commercially available Yagi Uda antennas were bought from Kathrein Company [1]. They were: the 5 elements - AOI65, the 8 elements - AON65 and the 13 elements - AOP65. The gain values of these antennas were measured and compared with the available data sheets to evaluate the measuring method and the novel PDA system (Table 5.10).

				
Type (Kathrein code)	AOI 65	AON 65	AOP 65	PDAwP$_{\perp}$GP$_{\angle}$45°
Manufacturers Gain, dBi	7-9.5	8.5-13.5	9.5-15	
Measured Gain, dBi	6.7-9.6	7.4-13.1	8.8-15.2	7.8-11
Mean Gain	8.15	10.25	12	9.4
Front-to-back-ratio	20-25	21-26	22-28	18-22
Length, cm	41cm	81cm	134cm	15cm
Unit weight, kg	1	1.8	2.4	0.72

Table 5.10 Data of the bought UHF antennas and PDAwP placed above the GP

Even the smallest AOI 65 five elements Yagi antenna is more than two times longer and 300g heavier than the novel PDA. The F/B ratio values are similar for all antennas. The manufactures gain values were taken from the data sheets which were included with the antennas. The gain values from the data sheets and the values, measured during this research, are very close. For example, the 5 element Yagi

antenna (AOI 65) gain values vary from 7dBi to 9.5dBi according to the manufactures. However, these research measurements resulted in a gain value range from 6.7dBi to 9.6dBi. The highest gain value difference obtained in this research between the manufactures stated and the measured is 1.1dB in the lower trend of the AON 65 gain values (Table 5.10). However, the measurement errors are $\pm 1dB$. Therefore, it can be concluded that the outdoors measurements, performed in this research, are comparable with the Kathrein's measurements. The gain calculation data for the measured received power is illustrated in Appendix F. The gain values from Table 5.10 are represented in a graphical form in Figure 5.42.

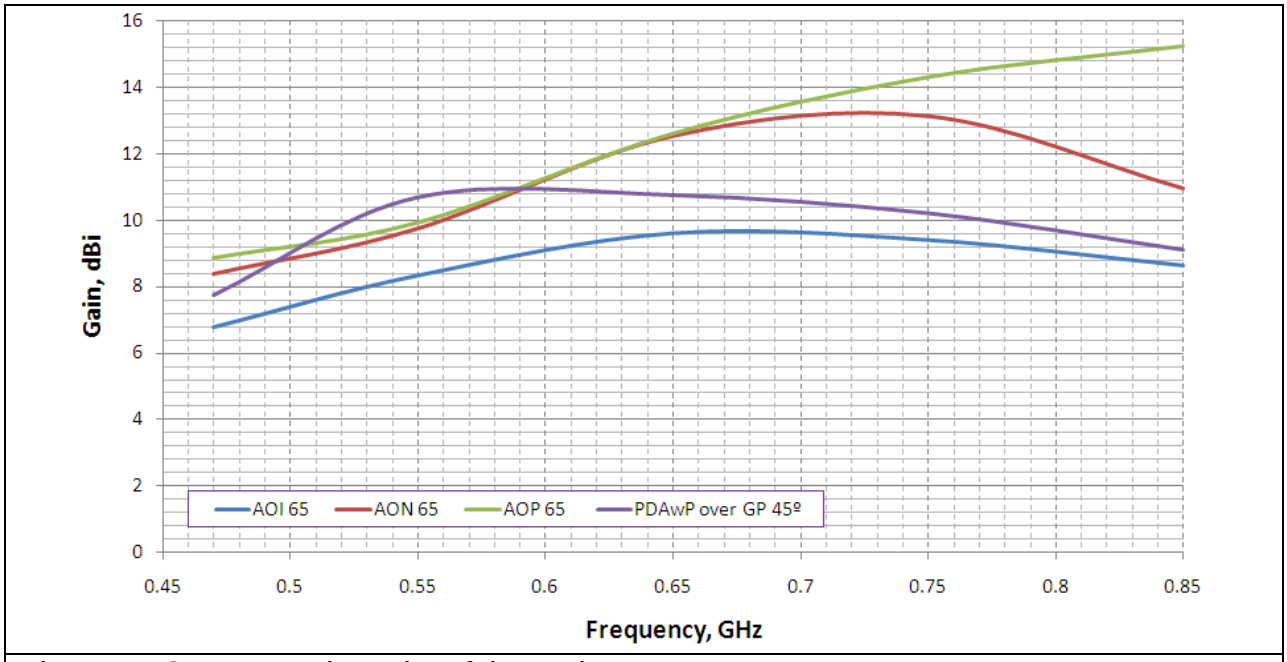

Figure 5.42 Measured results of the various antenna

The PDAwP, placed above the ground plane inclined at $45°$, performs well in comparison to the Kathrein Yagi UHF antennas. The novel PDA achieves a 1dB higher gain at 550MHz compared to all Kathrein Company Yagi antennas (AOI65, AON65 and

AOP65). At other frequencies the achieved gain values range is between the AOI65 (5 elements Yagi) and the AON65 (8 elements Yagi).

The measured return loss is shown in Figure 5.43 for the following antennas: the driven element of the AOI Yagi Uda antennas, the 5 element antenna (AOI65), the 8 elements antenna (AON65), the 13 elements antenna (AOP65) and the PDAwP placed above the ground plane. It should be noted that the ground plane inclination of 20° and 45° angle had no effect on the return loss results.

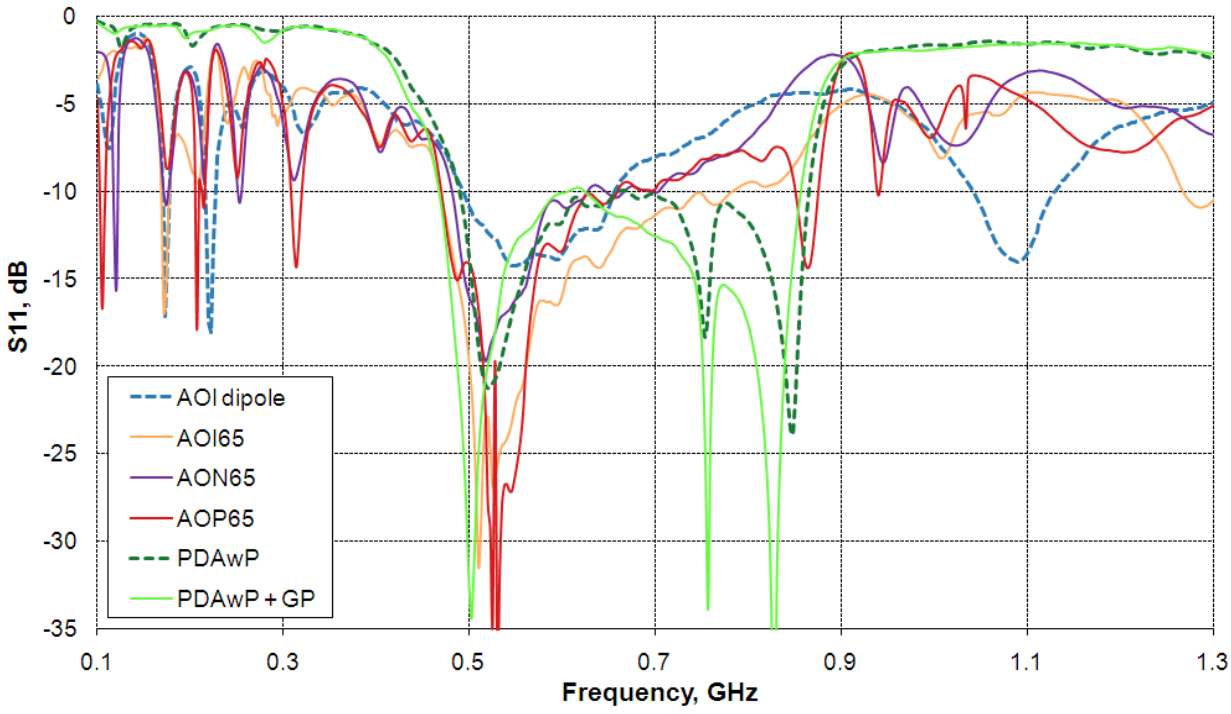

Figure 5.43 Measured return loss of the various UHF antennas

The return loss result of the driven element (DE) of the Yagi Uda antenna system is poor in comparison to the novel PDAwP alone. The calculated bandwidths (at 10dB of

the return loss) for the AOI dipole, AOI65, AON65, AOP65 and for the PDAwP placed above the ground plane are shown in Table 5.11.

Antenna	**AOI DE**	**PDAwP**	**AOI65**	**AON65**	**AOP65**	**PDAwP + GP**
Bandwidth, %	28.9	55.6	49.7	34.8	38.9	59.8

Table 5.11 The bandwidth results for varies UHF antenna systems

The return loss performance of the Yagi Uda antenna systems is low compared to the novel PDAwP system. The largest bandwidth of 49.7% was achieved by the Kathrein Company Yagi Uda antenna system (AOI65). The PDAwP placed above the ground plane had the bandwidth of 59.8%.

5.5 Conclusions

The broadband and low profile PDA with the reflector system for the UHF was proposed and analysed. The performance of the printed dipole antennas over the ground planes was investigated.

The parametric study was carried out in order to optimise the ground plane. The elliptical shape reflector with periodically rectangular air perforations and dimensions of the 74cm x 43cm showed fairly good overall performance. Therefore, it was chosen to be used it in the next research steps.

Two types of the PDA were analysed: the PDAwP and the OPDAwP. Moreover, two types of the PDA placements over the ground plane were analysed: i.e. above the reflector and in parallel to the reflector, both at the $\lambda_0 / 4$ distance. The radiation patterns of the parallel ground plane placement were more directive and the achieved directivity was as high as 10.45dBi at 850MHz of the OPDAwP.

In order to validate the predicted results, measurements were made on the prototype PDAwP placed over the ground plane. Measurements took place on the roof of a three storey building. However, the return loss was measured in the anechoic chamber. The measured return loss had 11% wider bandwidth compared to the simulated one, when the OPDAwP was placed above the GP. The measured gain values of the PDAwP, placed above the ground plane, varied from 4.8dBi to 9.2dBi (mean gain was 7dBi). However, the best measurement results were achieved for the PDAwP placed above the ground plane inclined at $45°$. In this case the mean gain was equal to 9.4dBi.

Furthermore, to compare the measurement technique and the performance of the novel PDAwP placed above the reflector, three commercial Yagi UHF antennas were analysed and measured. The comparison of the manufacturers' data to the measured gain values showed a good match. For the measured PDAwP placed over the ground plane, the bandwidth at 10dB of the return loss is equal to 59.8%. Therefore, it outperformed all other commercial antenna designs.

5.6 References

[1] Kathrein Ltd web page: http://www.kathrein.com/.

[2] C. Balanis, “Antenna Theory, Analysis and Design”, 2nd ed. New York, Wiley, 1997.

[3] D. Sievenpiper, Lijun Zhang, R. F. J. Broas, N. G. Alexopolous and E. Yablonovitch, "High impedance electromagnetic surfaces with a forbidden frequency band," IEEE Trans. Microwave Theory and Techniques, vol. 47, pp. 2059 -2073, November, 1999.

[4] CST’s MicroStripes website: http://www.cst.com/.aspx.

[5] Anritsu 37397D Series Vector Network Analyzer Operation Manual, 30 September 2007, UK; Anritsu 37397D Series Vector Network Analyzer Programming Manual, 30 September 2007, UK.

[6] Willmar K. Roberts “A New Wide-Band Balun”, proc. IRE, pp. 1628-1631, June 17, 1957.

[7] E.G.Fubini and P.J. Sutro, “A wide-band transformer from an unbalanced to a balanaced line”, Proc. IRE, vol. 35, pp. 1153-1155, October, 1947.

[8] Marconi Instruments RF and Microwave Test Sets 6200A Series Operating Manual, 1 May 1996, UK; Marconi Instruments RF and Microwave Test Sets 6200A Series GPIB Operating Manual, 6 June 1996, UK.

[9] R & S FS315 Spectrum Analyzer Operating Manual, August 2007, Germany.

[10] Rhophase company website: http://www.rhophase.co.uk/.html.

[11] HP 435B Power Meter Operating and Service Manual, 1980, USA.

[12] A.W. Rudge, K.Milne, A.D. Olver, P.Knight “The handbook of antenna design”, volumes1 and 2, Page Bros Ltd, Norfolk,1986.

[13] Tang, Y, Sobol, H, “Microwave Propagation in Multi-room Buildings for PCS”, IEEE GLOBECOM 1993, VOI 2 pp 1232-1236.

Chapter 6

Conclusions and future work

6.1 Review of the research study

This thesis has described the theory and practical analysis of a novel, balanced, low weight, low profile and broadband antenna in the UHF band (470MHz - 850MHz). The main contributions to this work were the investigation of a linearly polarised UHF antenna system and the employment of the printed dipole antenna (PDA), which resolved all disadvantages of the conventional antennas discussed in this research. The PDA structure's simplicity would be anticipating the overall product cost to be low.

The research started from the analysis of the commercial available UHF antennas: the Vertically Stacked Dipoles Antenna (VSDA) system and the Yagi-Uda antenna (YUA) system.

Chapter 2 summarised the research on one of the most popular and high gain commercially available UHF antennas. The VSDA system performance was investigated in terms of the return loss, the input impedance and the surface currents. The equivalent circuit was created by using lumped elements in order to better understand the balun operation. It was perfectly working between the frequencies of 420MHz and 920MHz. A good agreement of the return loss between the predicted and simulated results was achieved. The VSDA system bandwidth was equal to 48% at –10 dB in the return loss.

The simulated radiation patterns revealed the VSDA systems radiation performance. The radiation patterns remained relatively consistent over the frequency band. The VSDA system achieved high directionality pencil beams in E and H planes. However, large side lobes appeared in the lower frequency band (470MHz-520MHz), since the ground plane was placed too close (at $\lambda_0/8$) towards the radiating element.

The best performance of this antenna system was achieved in the middle band of 550MHz - 750MHz, when the radiation patterns were very directional and the return loss was very low (from -10dB to -28db). At the higher frequency band of 800MHz-850MHz the VSDA system lost the match and the return loss increased up to -7dB (in measurements). The best HPBW values (for the VSDA system placed over the ground plane) were: 28° for the E-plane and 31° for the H-plane at 850MHz.

The VSDA system placed above the ground plane achieved a medium overall performance with a mean gain value of 9.5dBi over the frequency band of 470MHz-850MHz. Some of these results have been published [1].

In chapter 3 the performance of the YUA system was discussed. The YUA system balun achieved a better match over the desired UHF frequency band than the VSDA system balun, analysed in chapter two. Therefore, it was decided to carry out the parametric study in order to improve the bandwidth and the directivity of the YUA system. The first parametric study stage commenced with the analysis of changing the parasitic element dimensions. The return loss results showed that it is possible to move the second resonant frequency by 100 MHz towards the lower frequency by adding the parasitic element. A constant change of the air gap separation distance between the balun and the radiating element added an extra capacitance value to the input impedance of the antenna, therefore, changing its return loss performance. The first resonant was shifted to the higher band and the second resonate was shifted to the lower frequency band by increasing the separation distance. The achieved optimum air gap separation was 1mm and the YUA system with the parasitic achieved the bandwidth of 64.4%. A 78% bandwidth was achieved during the YUA systems parametric study, when the balun was loaded with a V-shape dipole with an air gap separation of 1.0mm without the parasitic element. A reasonable agreement between the predicted and the measurement results was obtained.

The next stage was a parametric study done by changing the arm angle of the YUA system. Different arm angles influenced the return loss, the radiation patterns and the directivity values. The achieved optimal YUA system V-shape dipole arm angle was $25°$ with a maximum directivity of 5.1dBi at the higher frequency band.

The last stage of the investigation was performed by changing the dipole base length. The optimised base length was found to be x+11cm with a directivity value of

8.2dBi. Further increase in the base length revealed the large side lobes increase by 37° (in the H-plane). As a result, the optimal YUA system without the parasitic element had the following configuration: the air gap separation of 1mm, the dipole arm angle equal to $25°$ and the base length equal to x+12cm. Some of these results have been published in [1-4].

Chapter 4 commenced with the methodology for the innovation of the balanced, broadband and the low cost radiating element for the UHF band. The printed dipole antenna (PDA) structure was analysed and the main PDA parts explained. To improve the PDA performance a parametric study was carried out. The first PDA prototype acquired the dual resonance at 550MHz and at 790MHz.

In order to simplify the PDA connection with the ground plane (at $\lambda_o / 4$) the next prototype was created, i.e. the PDA with the extended feeding. The parametric study was carried out to improve the PDA bandwidth. The PDA with the stretched balun achieved a bandwidth of 26%. The PDA maintained relatively consistent radiation patterns in the frequency interval from 470MHz to 850MHz. They were similar to the radiation patterns of the $\lambda_o / 2$ wire dipole. The directivity was equal to 2.2dBi and 2.9dBi at 470MHz and 850MH respectively.

The radiation patterns, the directivity and the return loss were improved by implementing the passive element to the PDA structure. The use of the parasitic element in a close proximity to the dipole arms resulted in a PDAwP bandwidth increase to 52%. The directivity of the PDAwP achieved 5.2dBi value at 850MHz, which is 3.3dB higher than the conventional PDA directivity value at same frequency. On the other

hand, the parasitic element had a negative effect on the radiation patterns. This phenomenon appeared in the frequency band from 800MHz to 850HMz in the radiation patterns. However, this issue was resolved by performing numerous simulations. The identical parasitic element was placed at 1mm above the resonant element. This improved the radiation patterns at higher frequency (800MHz - 850MHz) and also resulted in the bandwidth increase by 0.9%. The simulated antenna efficiency varied from 88% to 97.7%, which was a very good performance. The obtained OPDAwP directivity and gain values at 850MHz were as high as 4.3dBi and 4.1dBi respectively.

The return loss results for the manufactured prototypes (the PDAwP and the OPDAwP) were better than the simulated ones. The PDAwP bandwidth was improved by 2.8% and the OPDAwP bandwidth was improved by 3.9%. Antennas were covered in antioxidant material which initially resulted in the loading effect on the PDA. The antennas matching band was shifted to a lower frequency by 10-15MHz.

Chapter 5 described the methodology for optimisation of the ground plane and its placement under the PDAwP and the OPDAwP, in order to improve the antenna systems directivity, gain and bandwidth values.

The parametric study was carried out to optimise the ground plane. The elliptical shape reflector with periodically rectangular air perforations and dimensions of the 74cm x 43cm showed fairly good overall performance. Therefore, it was chosen to be used in the next research steps as a reflector. Two types of the PDA were analysed: the PDAwP and the OPDAwP. Moreover, two types of the PDA placements over the ground plane were analysed: i.e. above the reflector and in parallel to the reflector, both at the

$\lambda_0 / 4$ distance. The radiation patterns of the parallel ground plane placement were more directive and the achieved directivity was as high as 10.45dBi at 850MHz of the OPDAwP placed in parallel to the ground plane.

For validation of the predicted results, measurements were made on the prototype PDAwP placed over the ground plane. Measurements took place on the roof of a three storey building. The measured gain values of the PDAwP, placed above the ground plane, varied from 4.8dBi to 9.2dBi (mean gain was 7dBi). However, the best measurement results were achieved for the PDAwP placed above the ground plane inclined at 45°. In this case the mean gain was equal to 9.4dBi.

Furthermore, to compare the measurement technique and the performance of the novel PDAwP placed above the reflector, three commercial Yagi UHF antennas were measured and analysed. The comparison of the manufacturers' data to the measured gain values showed a good match. For the measured PDAwP placed over the ground plane, the bandwidth at 10dB of the return loss was equal to 59.8%. The proposed antenna performed better than the commercial counterparts.

6.2 Future work

This research has produced the original work, containing a variety of innovative results. Nevertheless, the future work would involve measurements of the radiation patterns and the gain of the OPDAwP placed over various ground planes. Another stage of the future work would be to improve the directivity and the gain values by either implementing a vertically stacked PDA array or by introducing directors to the PDA structure.

A pilot study was undertaken to investigate the potential applications for the OPDAwP. As a result, the following areas could be researched in future:

- The indoor DTV antenna with a higher permittivity substrate and a smaller ground plane to improve the low profile (DVB-T) [5].
- The PDA for Wi-Fi and WiMAX applications [5-10].
- The PDA array for the Satellite communication for the X band with a dual polarisation (DVB-S) [11- 14].

6.3 References:

[1] N. Riauka, A. Chauraya, and J. C. Vardaxoglou, “Compact antenna integrated into flat plate FSS”, IEEE APS 2008, 5-11 July 2008, San Diego, CA, AP-S/URSI 2008, pp1-4.

[2] N. Riauka, A. Chauraya, and J. C. Vardaxoglou, “Wideband Planar Metamaterial Inspired Antenna Analysis and Design”, IEEE International Symposium on Antennas and Propagation - June 2009, North Charleston, South Carolina, USA.

[3] Yiannis (J) Vardaxoglou, R. D. Seager, N. Riauka, A. Chauraya, and P deMaagt, “Metamaterial Based Antennas with Super- and Sub-strates” 3rd European Conference on Antennas and Propagation (EUCAP) - March 2009 in Berlin, Germany.

[4] J.(Yiannis) C. Vardaxoglou, A.Chauraya, R.D.Seager, N.Riauka, G.K.Palikaras and P. deMaagt, “Towards Metasurfaces for Wideband Systems” 39th European Microwave Conference (EuMC) - August 2009, Rome, Italy.

[5] Tecpoyotl-Torres, M.; Vera-Dimas, J.G.; Vargas-Chable, P.; Damian-Morales, J.A.; Torres-Cisneros, M.; Sanchez-Mondragon, J. "Antenna prototypes for indoor and outdoor Wi-Fi communication", University of Guanajuato IEEE Students Chapter (IEEExPO), 2009 III Conference of, vol., no., pp.37-41, 24-26 Nov. 2009.

[6] Tawk, Y.; Kabalan, K.Y.; El-Hajj, A.; Sadek, S.; Al-Husseini, M. "A Modified Bowtie Antenna Design for Wi-Fi and WiMAX Applications", Wireless Communications and Mobile Computing Conference, 2008. IWCMC '08. International, vol., no., pp.729-732, 6-8 Aug. 2008.

[7] "A socio-economic analysis of WiMAX", Application of Information and Communication Technologies, 2009. AICT 2009. International Conference on, vol., no., pp.1-6, 14-16 Oct. 2009.

[8] Yue Li; Kouvatsos, D.; Weixi Xing "Performance modeling and bandwidth management of WiMAX systems", Wireless Communication, Vehicular Technology, Information Theory and Aerospace & Electronic Systems Technology, 2009. Wireless VITAE 2009. 1st International Conference on, vol., no., pp.485-491, 17-20 May 2009.

[9] Garber, L. "Mobile WiMax: The Next Wireless Battle Ground", Computer, vol.41, no.6, pp.16-18, June 2008.

[10] Fan Wang; Ghosh, A.; Sankaran, C.; Fleming, P.; Hsieh, F.; Benes, S. "Mobile WiMAX systems: performance and evolution", Communications Magazine, IEEE, vol.46, no.10, pp.41-49, October 2008.

[11] Chair, R.; Kishk, A.A.; Lee, K.F. "Wideband dual polarized dielectric resonator antennas at X-band", Antennas and Propagation Society International Symposium, 2005 IEEE, vol.4B, no., pp. 214- 217 vol. 4B, 3-8 July 2005.

[12] Rostan, F.; Heidrich, E.; Wiesbeck, W. "Dual polarized multilayer aperture-coupled patch antennas for spaceborne application in C- and X-band", Antennas and Propagation Society International Symposium, 1994. AP-S. Digest, vol.1, no., pp.476-479 vol.1, 20-24 Jun 1994.

[13] Tiezzi, F.; Vaccaro, S. "Hybrid phased array antenna for mobile KU-band DVB-S services", Antennas and Propagation, 2006. EuCAP 2006. First European Conference on, vol., no., pp.1-4, 6-10 Nov. 2006.

[14] Bennett, Bruce; Hannan, Daniel; Marshall, James; Gibbons, Richard "GBS over WGS Using DVB-S and DVB-S2 (#1546)", Military Communications Conference, 2007. MILCOM 2007. IEEE, vol., no., pp.1-7, 29-31 Oct. 2007.

Appendix A

Transforming 50Ω to 75 Ω

The conversion of a 50Ω referenced S-parameter to 75Ω begins with eq.1 [1, 2]. Both the S-parameter and input impedance are complex numbers *(R+jX)*, where R represents the real component, and the *X* represents the imaginary component. Z_0 is a real impedance.

$$S_{11} = \frac{Z_{in} - Z_0}{Z_{in} + Z_0} \qquad \text{eq.1}$$

The rearrangement of equation 1 gives an input impedance Z_{in} expression (eq.2):

$$Z_{in} = Z_0\left(\frac{1+S_{11}}{1-S_{11}}\right) \qquad \text{eq.2}$$

Replacement of the S_{11} with *R+jX* results in eq.3

$$Z_{in} = Z_0\left(\frac{1+R+jX}{1-R-jX}\right)$$

Multiplication of the denominator of eq.3 with its complex conjugate separates the real and imaginary components:

$$Z_{in} = Z_0\left(\frac{1+R+jX}{1-R-jX}\right)\cdot\left(\frac{1-R+jX}{1-R+jX}\right) \qquad \text{eq.4}$$

$$Z_{in} = Z_0\left(\frac{1-R^2-X^2+j2X}{\left(1-R^2\right)^2+X^2}\right) \qquad \text{eq.5}$$

Equation 6 is the real component of the input impedance,

$$Z_{in}(\mathrm{Re}\,al) = Z_0\left(\frac{1-R^2-X^2}{\left(1-R^2\right)^2+X^2}\right) \qquad \text{eq.6}$$

Eq. 7 is the imaginary component of the input impedance

$$Z_{in}(\mathrm{Im}\,aginary) = Z_0\left(\frac{j2X}{\left(1-R^2\right)^2+X^2}\right) \qquad \text{eq.7}$$

Once the complex input impedance is obtained, eq. 1 is used again to convert the impedance back to a 75Ω-referenced S-parameter. Eq. 8 is the same as eq.1, except Z_{in} is replaced with *R+jX*:

$$S_{11} = \frac{R+jX-Z_0}{R+jX+Z_0} \qquad \text{eq.8}$$

Multiplication of the denominator of eq.8 with its conjugate separates the real and imaginary components:

$$S_{11} = \left(\frac{R-Z_0+jX}{R+Z_0+jX}\right)\cdot\left(\frac{R+Z_0-jX}{R+Z_0-jX}\right) \qquad \text{eq.9}$$

$$S_{11} = \frac{R^2-{Z_0}^2+X^2+j2XZ_0}{\left(R+Z_0\right)^2+X^2} \qquad \text{eq.10}$$

Eq. 11 is the real component of the input return loss (S_{11}),

$$S_{11}(\mathrm{Re}\,al) = \frac{R^2-{Z_0}^2+X^2}{\left(R+Z_0\right)^2+X^2} \qquad \text{eq.11}$$

Eq. 12 is the imaginary component of the input return loss (S_{11}),

$$S_{11} = \frac{j2XZ_0}{\left(R+Z_0\right)^2+X^2} \qquad \text{eq.12}$$

The software program MATLAB [3] was used to convert of a 50Ω-referenced S-parameter to 50Ω. The developed program code is represented bellow:

```
f=deg2rad(F);
A=power(10,S11/20);
Za=A.*(cos(f)+i*sin(f));
S11R=real(Za);
S11X=imag(Za);
Zo=50;
R=Zo*(1-(S11R.^2)-(S11X.^2))./(1-S11R).^2+(S11X.^2);
X=Zo*(2*S11X)./((1-S11R).^2+S11X.^2);
Zo=50;
S11R=((R.^2-Zo^2)+(X.^2))./(((R+Zo).^2)+(X.^2));
S11X=(2*X*Zo)./(((R+Zo).^2)+(X.^2));
S11M=sqrt(S11R.^2+S11X.^2);
S1150=20*log10(S11M);
Zo=75;
S11R=((R.^2-Zo^2)+(X.^2))./(((R+Zo).^2)+(X.^2));
S11X=(2*X*Zo)./(((R+Zo).^2)+(X.^2));
S11M=sqrt(S11R.^2+S11X.^2);
S1175=20*log10(S11M);
```

Appendix B

Microstrip transition to parallel strip line

Figure A1 shows the structure of the microstrip transmission line and Figure A2 shows the structure of the parallel transmission line with the conductor thickness *(t)* and width *(w)*, the substrate height *(h)* and relative permittivity (ε_r).

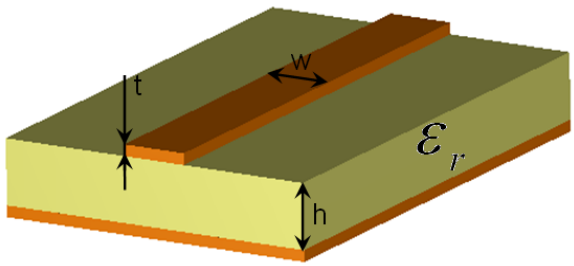

Figure A1 Structure of microstrip transmission line

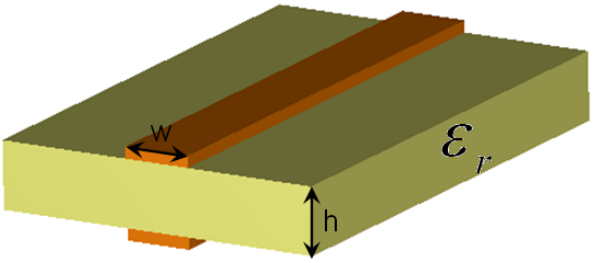

Figure A2 Structure of parallel strips transmission line

The main equation for the characteristic impedance Z_m of the microstrip transmission line [4] calculation is attributable to Harold A. Wheeler [5]. For $\frac{w}{h}<1$ Wheeler's basic result for Z_m is:

$$Z_m = \frac{377}{\pi\sqrt{2}\sqrt{\varepsilon_r+1}}\left\{\ln\left(\frac{8h}{w}\right)+\frac{1}{32}\cdot\left(\frac{w}{h}\right)^2-\frac{1}{2}\cdot\left(\frac{\varepsilon_r-1}{\varepsilon_r+1}\right)\cdot\left(\ln\frac{\pi}{2}+\frac{1}{\varepsilon_r}\ln\frac{4}{\pi}\right)\right\} \quad \text{eq.13}$$

For $\frac{w}{h}>1$

$$Z_m = \frac{377}{2\sqrt{\varepsilon_r}}\left\{\frac{w}{2h} + 0.441 + 0.082\cdot\left(\frac{\varepsilon_r - 1}{{\varepsilon_r}^2}\right) + \left(\frac{\varepsilon_r + 1}{2\pi\varepsilon_r}\right)\left\{1.451 + \ln\left(\frac{w}{2h} + 0.94\right)\right\}\right\}^{-1} \quad \text{eq.14}$$

Where effective permittivity is (due to Schneider) [6]

$$\varepsilon_r = \frac{1}{2}\left\{\varepsilon_r + 1 + (\varepsilon_r - 1)\cdot\left(1 + \frac{10h}{w}\right)^{-\frac{1}{2}}\right\} \quad \text{eq.15}$$

Some corrections for the strip thickness can be made as well by substituting an effective width w' for w

$$w' = w + \frac{t}{\pi}\left(1 + \ln\left(\frac{2x}{t}\right)\right) \quad \text{eq.16}$$

With $x = h$ for $w > \left(\frac{h}{2\pi}\right) > 2t$ eq.17

and $x = 2w\pi$ for $\left(\frac{h}{2\pi}\right) > w > 2t$ eq.18

Parallel strip lines can be used as a feed line for the double sided printed dipole. The field distribution remains unchanged if an infinite sized electric conductor is placed at any plane inside the substrate in parallel to the strips. The characteristic impedance (Z_m) of the parallel strip line with the substrate of separation (d) is two times bigger than the microstrip line with a twice thinner thickness *(h)* [7].

$Z_m(parallel-srips) = 2Z_m(microstrip)$, when $\left(h = \frac{d}{2}\right)$ eq.19

$\varepsilon_r(parallel-stips) = \varepsilon_r(microstrip)$, when $\left(h = \frac{d}{2}\right)$ eq.20

Appendix C

EM field distribution in microstrip and in parallel strip transmissions lines

Figure A3 shows the electromagnetic field distribution between the parallel strip line and the microstrip line is very similar. Therefore, the transition between them is not complicated.

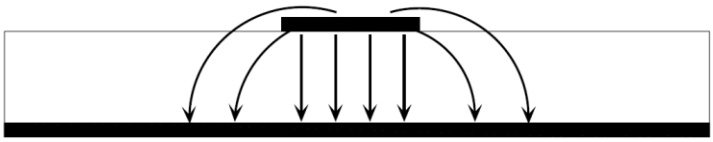

a) Microstrip transmission line

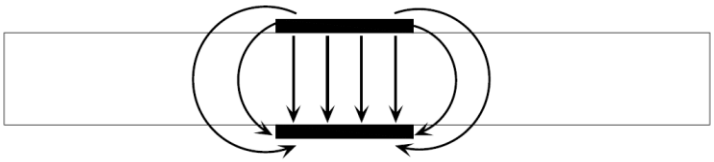

b) Parallel strip transmission line

Figure A3 E-field distribution

The main concern is the impedance matching, which can be calculated and designed by using previously shown formulas: eq.13 – eq.20.

Appendix D

Manufactured dipoles

A five pairs of the manufactured dipoles are shown in Figure A4.

Figure A4 Picture of the manufactured dipoles

Appendix E

The path phase difference (ϕ)

Dipoles										
Freq, Hz	λ, m	d, m	H1, m	H2, m	D, m	R, m	k	total ϕ,rad	total ϕ, deg	**ϕ, deg**
470000000	0.6382979	9.68	3.3	3.3	9.68	11.7159	9.843657	20.040738	1148.25067	68.25067
550000000	0.5454545	9.78	3.3	3.3	9.78	11.79866	11.51917	23.253305	1332.31735	252.3173
650000000	0.4615385	9.8	3.3	3.3	9.8	11.81524	13.61357	27.434667	1571.89195	131.892
750000000	0.4	9.84	3.3	3.3	9.84	11.84844	15.70796	31.548548	1807.60017	7.600169
850000000	0.3529412	9.88	3.3	3.3	9.88	11.88168	17.80236	35.634685	2041.71877	241.7188
PDAwP+GP										
Freq, Hz	λ, m	d, m	H1, m	H2, m	D, m	R, m	k	total ϕ,rad	total ϕ, deg	**ϕ, deg**
470000000	0.6382979	9.74	3.3	3.3	9.74	11.76553	9.843657	19.938582	1142.39758	62.39758
550000000	0.5454545	9.79	3.3	3.3	9.79	11.80695	11.51917	23.233612	1331.18901	251.189
650000000	0.4615385	9.8	3.3	3.3	9.8	11.81524	13.61357	27.434667	1571.89195	131.892
750000000	0.4	9.81	3.3	3.3	9.81	11.82354	15.70796	31.628614	1812.1876	12.1876
850000000	0.3529412	9.84	3.3	3.3	9.84	11.84844	17.80236	35.755021	2048.61352	248.6135
AOI 65										
Freq, Hz	λ, m	d, m	H1, m	H2, m	D, m	R, m	k	total ϕ,rad	total ϕ, deg	**ϕ, deg**
470000000	0.6382979	9.48	3.3	3.3	9.48	11.55121	9.843657	20.388258	1168.16215	88.16215
550000000	0.5454545	9.53	3.3	3.3	9.53	11.59228	11.51917	23.755733	1361.10437	281.1044
650000000	0.4615385	9.65	3.3	3.3	9.65	11.69113	13.61357	27.78705	1592.08206	152.0821
750000000	0.4	9.56	3.3	3.3	9.56	11.61695	15.70796	32.310544	1851.25938	51.25938
850000000	0.3529412	9.58	3.3	3.3	9.58	11.63342	17.80236	36.555672	2094.4875	294.4875
AON 65										
Freq, Hz	λ, m	d, m	H1, m	H2, m	D, m	R, m	k	total ϕ,rad	total ϕ, deg	**ϕ, deg**
470000000	0.6382979	9.076	3.3	3.3	9.076	11.22202	9.843657	21.124704	1210.35739	130.3574
550000000	0.5454545	9.126	3.3	3.3	9.126	11.2625	11.51917	24.610698	1410.0903	330.0903
650000000	0.4615385	9.136	3.3	3.3	9.136	11.2706	13.61357	29.059566	1664.99189	224.9919
750000000	0.4	9.156	3.3	3.3	9.156	11.28682	15.70796	33.470863	1917.74083	117.7408
850000000	0.3529412	9.176	3.3	3.3	9.176	11.30305	17.80236	37.866535	2169.59449	9.594488
AOP 65										
Freq, Hz	λ, m	d, m	H1, m	H2, m	D, m	R, m	k	total ϕ,rad	total ϕ, deg	**ϕ, deg**
470000000	0.6382979	8.545	3.3	3.3	8.545	10.79708	9.843657	22.168743	1270.1765	190.1765
550000000	0.5454545	8.595	3.3	3.3	8.595	10.8367	11.51917	25.822508	1479.52197	39.52197
650000000	0.4615385	8.605	3.3	3.3	8.605	10.84463	13.61357	30.489371	1746.91378	306.9138
750000000	0.4	8.625	3.3	3.3	8.625	10.86051	15.70796	35.115271	2011.95853	211.9585
850000000	0.3529412	8.645	3.3	3.3	8.645	10.8764	17.80236	39.72414	2276.02749	116.0275

Appendix F

Gain calculation data

Dipoles							
Freq Hz	Tx, dBm	Rx, dBm	R, m	lamb	sq-lamb/4*pi*R	Gain 1dip	Gain 1dip, dBi
4.7E+08	3.2461	-38.72	9.68	0.638	2.75345E-05	1.22569548	0.883825831
5.5E+08	2.9461	-35.55	9.78	0.545	1.96979E-05	2.19113078	3.406683003
6.5E+08	2.6461	-38.38	9.8	0.462	1.40457E-05	1.97663749	2.959270284
7.5E+08	2.3461	-43.91	9.84	0.4	1.04643E-05	1.28669054	1.094741063
8.5E+08	2.0461	-43.94	9.88	0.353	8.08111E-06	1.56244166	1.938038113

PDAwP +GP (0°)								
Freq Hz	Tx, dBm	Rx, dBm	R, m	lamb	sq-lamb/4*pi*R	1Dipole Gain	Gain	Gain, dBi
4.7E+08	3.246	-33.6751	9.74	0.638	2.71963E-05	1.22569	6.095308515	7.849957
5.5E+08	2.946	-30.7283	9.79	0.545	1.96577E-05	2.1911	9.962576366	9.983717
6.5E+08	2.646	-34.4692	9.8	0.462	1.40457E-05	1.9766	6.998620349	8.450124
7.5E+08	2.346	-38.4273	9.81	0.4	1.05284E-05	1.28669	6.177744475	7.908299
8.5E+08	2.046	-41.2919	9.84	0.353	8.14695E-06	1.56244	3.642638787	5.614161

PDAwP + GP (20°)								
Freq Hz	Tx, dBm	Rx, dBm	R, m	lamb	sq-lamb/4*pi*R	Dipoles Gain	Gain	Gain, dBi
4.7E+08	3.246	-33.5751	9.74	0.638	2.71963E-05	1.22569	6.237286489	7.949957
5.5E+08	2.946	-29.7283	9.79	0.545	1.96577E-05	2.1911	12.54214055	10.98372
6.5E+08	2.646	-33.3692	9.8	0.462	1.40457E-05	1.9766	9.015969527	9.550124
7.5E+08	2.346	-37.1273	9.81	0.4	1.05284E-05	1.28669	8.333547994	9.208299
8.5E+08	2.046	-38.6919	9.84	0.353	8.14695E-06	1.56244	6.628512929	8.214161

PDAwP + GP (45°)								
Freq Hz	Tx, dBm	Rx, dBm	R, m	lamb	sq-lamb/4*pi*R	Dipoles Gain	Gain	Gain, dBi
4.7E+08	3.246	-33.7751	9.74	0.638	2.71963E-05	1.22569	5.956562354	7.749957
5.5E+08	2.946	-30.0283	9.79	0.545	1.96577E-05	2.1911	11.70500661	10.68372
6.5E+08	2.646	-32.1692	9.8	0.462	1.40457E-05	1.9766	11.88536258	10.75012
7.5E+08	2.346	-36.1273	9.81	0.4	1.05284E-05	1.28669	10.49131534	10.2083
8.5E+08	2.046	-37.7919	9.84	0.353	8.14695E-06	1.56244	8.154852454	9.114161

AOI 65								
Freq Hz	Tx, dBm	Rx, dBm	R, m	lamb	sq-lamb/4*pi*R	Dipoles Gain	Gain	Gain, dBi
4.7E+08	3.246	-34.52	9.48	0.638	2.87085E-05	1.22569	4.753448419	6.770088
5.5E+08	2.946	-32.15	9.53	0.545	2.07449E-05	2.1911	6.804966935	8.32826
6.5E+08	2.646	-33.18	9.65	0.462	1.44858E-05	1.9766	9.131446665	9.605396
7.5E+08	2.346	-36.71	9.56	0.4	1.10862E-05	1.28669	8.712472565	9.401414
8.5E+08	2.046	-38.04	9.58	0.353	8.59516E-06	1.56244	7.300331118	8.633426

AON 65								
Freq Hz	Tx, dBm	Rx, dBm	R, m	lamb	sq-lamb/4*pi*R	Dipoles Gain	Gain	Gain, dBi
4.7E+08	3.246	-32.52	9.076	0.638	3.13212E-05	1.22569	6.905276693	8.391811
5.5E+08	2.946	-30.35	9.126	0.545	2.26223E-05	2.1911	9.444982268	9.752011
6.5E+08	2.646	-29.78	9.136	0.462	1.61616E-05	1.9766	17.9059407	12.52997
7.5E+08	2.346	-32.61	9.156	0.4	1.20862E-05	1.28669	20.54173901	13.12637
8.5E+08	2.046	-35.34	9.176	0.353	9.36868E-06	1.56244	12.47149022	10.95918

AOP 65								
Freq Hz	Tx, dBm	Rx, dBm	R, m	lamb	sq-lamb/4*pi*R	Dipoles Gain	Gain	Gain, dBi
4.7E+08	3.246	-31.52	8.545	0.638	3.53348E-05	1.22569	7.7057736	8.868162
5.5E+08	2.946	-29.65	8.595	0.545	2.55039E-05	2.1911	9.843101876	9.93132
6.5E+08	2.646	-29.18	8.605	0.462	1.82177E-05	1.9766	18.23839887	12.60987
7.5E+08	2.346	-30.91	8.625	0.4	1.36202E-05	1.28669	26.96148734	14.30744
8.5E+08	2.046	-30.54	8.645	0.353	1.05549E-05	1.56244	33.43039713	15.24142

References:

[1] J.A. Stratton “Electromagnetic Theory”, First edition, New York:1941, McGraw-Hill.

[2] J.D. Kraus, R.J. Marhefka **“**Antennas for all applications**”** ,Third Edition, 2002, McGraw-Hill.

[3] MATLAB webpage: http://www.mathworks.com/products/matlab/

[4] J.R. James, P.S. Hall, C. Wood “Microstrip Antenna Theory and Design” Peter Peregrinus, 1981.

[5] Harold A. Wheeler “Transmission-line properties of a strip on a dielectric sheet on a plane", IEEE Tran. Microwave Theory Tech., vol. MTT-25, pp. 631-647, Aug. 1977.

[6] M. V. Schneider, "Microstrip lines for microwave integrated circuits," Bell Syst Tech. J., vol. 48, pp. 1422-1444, 1969.

[7] Ramesh Garg, Prakash Bhartia, Inder Bahl, Apisak Ittipiboon “Microstrip Antenna Design handbook” Norwood, 2000.